UNIVERSITY OF CALIFORNIA
Santa Barbara

Nanometer-scale engineering of shallow spins in diamond

A dissertation submitted in partial satisfaction
of the requirements for the degree of

Doctor of Philosophy

in

Materials

by

Kenichi Ohno

Committee in charge:

Professor David D. Awschalom, Co-Chair

Professor Christopher J. Palmstrøm, Co-Chair

Professor Arthur C. Gossard

Professor Chris G. Van de Walle

December 2014

The dissertation of Kenichi Ohno is approved:

Arthur C. Gossard

Chris G. Van de Walle

Christopher J. Palmstrøm, Committee Co-Chair

David D. Awschalom, Committee Co-Chair

October 2014

Nanometer-scale engineering of shallow spins in diamond

Copyright © 2014

by

Kenichi Ohno

To my parents, Kazuo and Junko
my grandparents, Hisao and Sayoko
and my wife, Tomomi

Acknowledgments

It was a major decision for me to attend a graduate school abroad in the U. S. as no one assures that I can manage as a graduate student, even that I can adjust myself to a different culture. Looking back now, I am very happy to say that my graduate student life is full of exciting scientific challenges, friends/collaborators always nice to me, and fun.

I couldn't acquire experiences and insights to this extent without Professor David Awschalom's academic advice. He always knows my direction ahead of me, and pushes me towards the most challenging researches with his smile or "David's optimism" (which means that a student will suffer from an "easy" project for the next half a year, according to his advisor). Most importantly, I learned that finding a good problem is much more difficult than solving a problem.

If it were not for interactions with such talented labmates, I couldn't raise myself as a Ph.D student and make achievements. Joe Heremans introduced me to the lab, helped me setting up FML, and later, he always converted tons of raw data I threw out to him to presentation-grade figures with appropriate error bars. He was always happy to polish "Kenglish" in paper drafts. David Toyli gave me many thoughtful questions on my data, and talking with Lee Bassett about idea or data usually ended up an endless discussion, both of which were always useful for moving onto to the next step. Whenever I asked Bob Buckley questions about the measurement setup, he always answered with his hand-writing figures on a white board. Discussion with Greg Fuchs inspired me a lot of new idea that I wanted to test. Abram Falk taught me cleanroom techniques, and I used Brian Maertz's legacy setup. I had a good team with Bryan Myers and Claire McLellan, sharing the diamond CVD machine and having active discussion with them

in biweekly CVD meetings.

Labmate interactions are not necessarily limited to the scientific ones. I had many cultural and social interactions with my friends nearby. I did a lot of hiking in the local area as well as national parks with Chris Yale, who was also my good room mate, and he taught me many American TV shows including Jon Stewart's The Daily Show. I may have more Japanese cultural influence on David Christle than I had American cultural influence from him. Will Koehl's questions about Japanese culture were sometimes too deep that I couldn't answer. Viva Holowitz's humming song was good background music in the CNSI lab. Mark Nowakowski was always happy showing me his great setup in his lab next door, and Shawn Mack was a great front runner ahead of me as he was the only other Materials student in our group. I never forget Andwer Yeats' smile with a coffee cup in his hand sitting in front of his lab. Talking about Jazz with Greg Calsine was always fun and he took me to Jazz concerts many times at Lobero theater. He and I were the last Santa Barbara Awschalomers. Friday evening dance time in the CNSI lab with Paolo Andrich and Benji Aleman were refreshing moments welcoming weekends. I wish good luck to younger students in our group, Paul Klimov, Chalres de las Casas, Steve Brown (he used to be a team CVD diamond), and all new Chicago kids.

I cannot say enough thanks to CNSI staffs. Holly Woo is my "Mom" in Santa Barbara helping my HVPO and payrolls as well as more personal stuff including how to choose a car insurance company and write a thank you note after my job interview. Peter Duda is always a skillful and reliable cleanroom engineer helping me installing and maintaining the CVD machine. Bob Hanson is a very careful building manager and he offered me a lot of technical support regarding with the machine. I will never forget my first day working with him unpacking the machine and a control tower fell on to him breaking his leg. I had

really comfortable days in my office in CNSI with friendly staffs including Eva Deloa, Lynne Leininger, Daniel Daniels, Teddy Thomas, Alycia Lewis, Paul Weakliem, Marissa Guillen, Neysa Gleason, Anna-Marie Nuila-Chae, Sonya Perez, and a couch at the end of the hall way: my best place for taking a nap.

The MBE lab was what attracted me to UCSB when I first visited here a year before my application, and I realized that their activity was even more exciting than I thought after joining the lab. This is all thanks to the well organization of Professor Art Gossard and the engineer of no-substitute, John English. Although my research has been rather independent from the MBE lab, John always taught me useful techniques, and lent me tools from the lab. Learning diverse research projects running in the lab by sitting in the weekly MBE meetings and interacting with people in the lab always motivated me. I adapted many equipment and vacuum tricks learned in the meeting to the CVD machine. I am very happy to join this world's best grower team. I want to express my best thank to the all former and current MBE lab members who shared their time with me.

Professor Chris Palmstrøm is my thesis co-advisor and he gave me a lot of growth insight especially in the early stage of my research. Talking about crazy idea with him in his office was always a nice time. My original plan was to make a hybrid metal/diamond structure using his MBE, but my research direction was shifted and I regret I hadn't enough time playing with his jungle/space station/monster MBE system. I wish good luck to the younger students in his lab.

I cannot say enough thank to Professor Ania Jayich for her welcoming me to her lab as a semi-group member. She always coordinated my measurement time and she gave me timely advice while I was working on my last project. Her support is valuable, especially after our entire group moved to Chicago. I had

a very comfortable and thrilling time working in the Jayich lab with her group member, Preeti Ovartchaiyapong, Kenny Lee, Matt Pelliccione, Laetitia Pascal, in addition to Bryan and Claire.

Of course, my research was not productive without staffs/engineers supporting me. Engineers in the Nanofab, Jack Whaley, Don Freeborn, Tony Bosch, Aidan Hopkins, and Brian Lingg always came into the cleanroom whenever I called them having troubles with the equipments. Without assistance of Mark Cornish, Youli Li, and Tom Mates, I couldn't make my sample characterization so quick, which would delay my growth cycle. Jeff Dutter and Doug Rehn at the machine shop always tried to put my work order on top of others to get my parts done faster. Special thanks go to the Materials office staffs represented by Oura Neak. They made my Ph.D life social and comfortable. Especially, I enjoyed the visiting day every year they organized, which is, in my opinion, not only welcoming new graduate students but also an annual department-wide festival. I can't forget mentioning Constance Callinicos although she retired from the Materials office a couple of years ago, because without her warmest welcome and assistance during my first visit to UCSB, I wouldn't apply for this school.

I couldn't imagine better collaborators than Dr. Dan Rugar and his team members, John Mamin, Moonhee Kim, and Mark Sherwood at the IBM Almaden research center. They were always fast in taking data and giving me feedback, and they made the most of the samples that I grew. It was also my great honor to have a chance to work with Professor Evelyn Hu at Harvard University and her group member, Jonathan Lee and Shanying Cui, on a very challenging project. I am very glad that our project finally works very well. It was one of my best lucks in my Ph.D career to work with such nice and talented collaborators.

I learned many things from classrooms. Among them, Professor Omar Saleh's thermodynamics course was one of the best courses that I have ever sat in, and Steve Denbaars' MOCVD and wide-bandgap courses gave me a good introduction to work on a CVD machine. Professor Chris Van de Walle always gave me the toughest questions during my exam, and I always realized later that they were very thoughtful and gave me a new perspective on my research.

I thank all of my Japanese friends who shared their time with me on the campus. I hung out with Kosuke Ono, Hiroyuki Ishii, Masakazu Kondo, and Tsuyoshi Yamamoto in the early years in my Ph.D life. I learned many CVD tricks from visiting MOCVD researchers including Junichi Sonoda, Shinichi Tanaka, Yoshinobu Kawaguchi, and Kohei Kubota. Friends in my generation, Sayaka and Hironori Okumura, Emi and Yukiya Kitayama, Tamami and Shinji Matsushita encouraged me to get married and bring my wife here. Talking with visiting polymer chemistry researchers, Momoko and Tomoya Arai, Yoko and Satoshi Shibui, and Kazuhiko Tsurui inspired me a lot of multidisciplinary ideas. Great thanks go to Professor Toshiro Tanimoto and his wife Hiroko, Maki and Tetsuro Oishi, Asako and Takaaki Sokabe for both my wife and my social lives in Santa Barbara.

Finally, I want to express my greatest gratitude to my parents, Kazuo and Junko, for raising me up, sending me abroad, as well as their continuous support and love throughout my life. I am also grateful for my grandparents, Hisao and Sayoko, who are always looking forward to my weekly e-mails and returning home for the Christmas vacations. And of course, I couldn't make any success during my Ph.D career without my wife, Tomomi's patience, support and her greatest love.

Vitæ

Kenichi Ohno

Education

2007 B.S., Electronic Engineering, The University of Tokyo.

2009 M.S., Electronic Engineering, The University of Tokyo.

2012 M.S., Materials Science, University of California, Santa Barbara.

2014 Ph.D., Materials Science, University of California, Santa Barbara.

Patents

"Diamond crystal with engineered depth and thickness control of nitrogen enriched layers for atomic scale magnetic field, electric field and thermometric sensors," K. Ohno, F. J. Heremans, L.C. Bassett, B. A. Myers, A. C. Bleszynski Jayich, C. J. Palmstrøm, and D. D. Awschalom, US Patent pending

Publications

"Engineering shallow spins in diamond with nitrogen delta-doping," K. Ohno, F. J. Heremans, L. C. Bassett, B. M. Myers, D. M. Toyli, A. C. Bleszynski Jayich, C. J. Palmstrøm, and D. D. Awschalom, *Appl. Phys. Lett.* **101**, 082413 (2012).

"Nanoscale nuclear magnetic resonance with a nitrogen-vacancy spin sensor," H. J. Mamin, M. Kim, M. H. Sherwood, C. T. Rettner, K. Ohno, D.D. Awschalom, and D. Rugar, *Science* **339**, 557 (2013).

"Probing surface noise with depth-calibrated spins in diamond," B. A. Myers, A. Das, M. C. Dartiailh, K. Ohno, D. D. Awschalom, and A. C. Bleszynski Jayich, *Phys. Rev. Lett.* **113**, 027602 (2014).

"Multipulse double-quantum magnetometry with near-surface nitrogen-vacancy centers," H. J. Mamin, M. H. Sherwood, M. Kim, C. T. Rettner, K. Ohno, D.D. Awschalom, and D. Rugar, *Phys. Rev. Lett.* **113**, 030803 (2014).

"Three-diemnsional localization of spins in diamond using ^{12}C implantation," K. Ohno, F. J. Heremans, C. F. de las Casas, B. M. Myers, B. J. Alemán, A. C. Bleszynski Jayich, and D. D. Awschalom, *Appl. Phys. Lett.* **105**, 052406 (2014).

"Engineered micro- and nanoscale diamonds as mobile probes for high-resolution sensing in fluid," P. Andrich, B. J. Alemán, J. C. Lee, K. Ohno, C. F. de las Casas, F. J. Heremans, E. L. Hu, and D. D. Awschalom, *Nano. Lett.* **14**, 4959 (2014).

"Proton magnetic resonance imaging with a nitrogen-vacancy spin sensor," D. Rugar, H. J. Mamin, M. H. Sherwood, M. Kim, C. T. Rettner, K. Ohno, and D.D. Awschalom, to be published in *Nature Nanotechnology*.

"Resonance enhancement of delta-doped NV centers in diamond coupled to photonic crystal cavities," J. C. Lee, D. O. Bracher, S. Cui, K. Ohno, C. McLellan, X. Zhang, P. Andrich, B. J. Alemán, K. J. Russell, A. P. Magyer, I. Aharonovich, A. C. Bleszynski Jayich, D.D. Awschalom, and E. L. Hu, in preparation.

Fields of study

Major field: Materials

Nanometer-scale engineering of shallow spins in diamond

Professor David D. Awschalom

Abstract

Nanometer-scale engineering of shallow spins in diamond

by

Kenichi Ohno

A crystal growth technique enabling to control the depth of a single nitrogen-vacancy (NV) center at nanometer scale in diamond is developed. This nitrogen delta-doping technique during the plasma-enhanced chemical vapor deposition (PE-CVD) of diamond enables to create near-surface NV centers whose depths ranging from about 100 nm down to less than 2 nm while preserving their spin coherence times.

These shallowly doped, long-coherence NV centers are used as an atomic-scale magnetic sensor that enables to detect nuclear spin signal from an organic sample of a nanometer-scale volume *external* to the diamond crystal. Extension of this nanometer-scale nuclear magnetic resonance (nanoNMR) to two-dimensional nanometer-scale magnetic resonance imaging (2D nanoMRI) is also presented.

The nitrogen delta-doping technique is combined with shallow ^{12}C ion implantation through lithographically-patterned apertures to demonstrate three-dimensional (3D) localization of single NV centers at nanometer scale. The demonstrated long spin coherence times of 3D-localized NV centers pave a way towards quantum applications by maximizing their interactions to the diamond-based nanostructures.

Contents

Chapter 1 Introduction **1**

Chapter 2 The nitrogen-vacancy (NV) center **4**

2.1 The nitrogen-vacancy (NV) center 4

2.2 Spin coherence of the NV center 9

2.3 Applications of the NV center 12

2.3.1 Sensitive nanometer-scale magnetometry applications . 12

2.3.2 NV center-based metrology 16

2.3.3 Quantum applications of the NV center 17

2.4 Conclusion and Organization 22

Chapter 3 Crystal growth of high-purity diamond **24**

3.1 Thermodynamics of diamond synthesis 24

3.2 PE-CVD growth of diamond 27

3.3 Substrates 29

3.4 Growth theory 31

3.4.1 General theory for step-flow growth 32

3.4.2 Growth strategy for PE-CVD diamond 34

3.5 Crystal growth of high-quality diamond film 35

3.5.1 Temperature dependence of hydrogen etching 35

3.5.2 Crystal growth of diamond with atomically flat surface . 39
3.6 Material properties of CVD-grown diamond film 42
3.6.1 Nitrogen impurity and growth rate 42
3.6.2 Surface termination 43
3.6.3 Surface reconstruction 46
3.7 Diamond growth on (111) plane 48
3.8 Increasing growth rate using high microwave power 53
3.8.1 Increasing growth rate 53
3.8.2 Growth system and procedure 54
3.8.3 Growth results 56
3.8.4 Growth-incorporated NV centers: possibilities 59
3.9 Conclusion 60

Chapter 4 The nitrogen delta-doping technique 63
4.1 Introduction 63
4.2 Challenges 64
4.2.1 Magnetic dipole coupling 64
4.2.2 Shallow NV center creation 67
4.3 Concept of the nitrogen delta-doping 69
4.4 Sample preparation 70
4.4.1 Crystal growth conditions 70
4.4.2 Nitrogen doping 71
4.4.3 Post growth vacancy creation process 73
4.4.4 Residual gas analysis 74
4.5 Measurement setup 75
4.5.1 Optical setup 76
4.5.2 Electrical setup 79

4.6 Isotopic identification of doped NV centers 83
4.7 Nanometer-scale depth confinement of doped NV centers 85
4.7.1 Sample structure 86
4.7.2 Isotopic signatures in ESEEM 87
4.7.3 Experimental results 88
4.7.4 Nanometer-scale depth dispersion of doped NV centers . 90
4.7.5 Coupling length to ^{13}C-enriched layers 91
4.8 Spin coherence properties of shallowly doped NV centers 98
4.8.1 Sample structure 98
4.8.2 Hahn echo measurements 99
4.8.3 Hahn echo measurements for doped NV centers ("node" method) 101
4.8.4 Spin coherence times of doped NV centers 105
4.8.5 Doped NV density 108
4.9 Sensitivity calculations of doped NV centers 109
4.10 Conclusion and outlook 116

Chapter 5 Nanometer-scale nuclear magnetic resonance (nanoNMR) 119
5.1 Introduction 119
5.2 Background 123
5.2.1 Sample preparation 123
5.2.2 Statistical polarization 127
5.2.3 Measurement protocol 129
5.3 nanoNMR results 132
5.3.1 nanoNMR 132
5.3.2 nanoNMR spectrum by Fourier transform method 133
5.4 Analysis 136

5.4.1 Estimation of proton magnetic field signal 136
5.4.2 Proton sensitivity of NV center 139
5.4.3 Detection volume 143
5.4.4 Towards single proton spin detection 147
5.5 Conclusion 149

Chapter 6 Three-dimensional position control of a single NV center 152
6.1 Introduction 152
6.2 Challenges 153
6.3 ^{12}C implantation technique: concept and sample preparation . . 156
6.4 NV center activation via vacancy diffusion 158
6.5 Effects of ^{12}C implantation dose and $^{15}N_2$ doping gas flow . . . 160
6.5.1 Effects on the NV density 160
6.5.2 Effects on the spin coherence 163
6.6 3D localization of a single NV center using nanoscale apertures 166
6.6.1 Aperture sample preparation 167
6.6.2 Localized NV center number vs aperture diameter . . . 169
6.6.3 Spin coherence of a localized single NV center 173
6.7 Localization volume estimation 174
6.7.1 Vacancy diffusion length 174
6.7.2 Localization volume 181
6.8 Nanopillar approach for 3D localization 185
6.8.1 Nanoplillar sample preparation 185
6.8.2 Average NV center number localized in the nanopillar . 187
6.8.3 Spin coherence of NV centers localized in the nanopillar 191
6.9 Conclusion and outlook 192

Chapter 7 Recent results **195**

7.1 Nanometer-scale magnetic resonance imaging (nanoMRI) 195

7.1.1 Sample preparation 195

7.1.2 Scanning the sample 196

7.1.3 Spin echo measurements 199

7.1.4 Proton NMR measurements 199

7.1.5 2D nanoMRI 201

7.1.6 Proton magnetic signal 203

7.1.7 Thickness of the proton containing layer 206

7.1.8 Outlook 209

7.2 Extremely shallowly doped NV centers 211

7.2.1 Sample preparation 211

7.2.2 Spin coherence of extremely shallow NV centers 212

7.2.3 Figure of merit 215

7.3 Deterministic depth control of NV emitters in photonic cavities . 216

7.3.1 Sample preparation 216

7.3.2 Photonic cavity design 218

7.3.3 Estimation of the Purcell enhancement 219

7.3.4 Outlook 222

7.4 Sub-micron-scale diamond particle sensor in fluidic environment 223

7.4.1 Sample preparation 224

7.4.2 Position and motion stability of diamond particles in microfluidic channel 226

7.4.3 Outlook 227

7.5 Conclusion 228

Chapter 8 Conclusion **230**

Appendix A Seki AX6300 Diamond CVD Operation Procedure with 1.5 kW Microwave Head **233**

Appendix B Growth resources **252**

List of figures

2.1 Schematic of the NV center. 5
2.2 PL spectrum of the NV center. 5
2.3 Ground state enegry levels of the NV center. 7
2.4 Energy diagram of the optical transition of the NV center. 8
2.5 Hahn echo decay curve displaying $T_2 \sim 1.8$ ms at room temperature. 11
2.6 Scanning electron microscopy (SEM) image of an diamond-based atomic force microscopy (AFM) tip. 14
2.7 Scanning confocal microscopy image of a living cell containing nanodiamond thermometer. 17
2.8 NV center-based quantum register. 19
2.9 Phonon-mediated spin coupling. 20

3.1 Energy diagram of carbon allotropes. 26
3.2 Phase diagram of carbon. 27
3.3 Picture of the PE-CVD machine. 28
3.4 Schematic of the PE-CVD system. 30
3.5 Schematic of the step-flow growth. 32

3.6 AFM images of the hydrogen (H)-etched diamond surface ($T = 330 - 650$ ^{o}C). 36
3.7 AFM images of the H-etched diamond surface ($T = 700 - 750$ ^{o}C). 37
3.8 AFM images of the H-etched diamond surface ($T = 800 - 900$ ^{o}C). 38
3.9 Time-dependent surface morphology of the H-etched diamond. . 39
3.10 AFM sufrace morphologies of the H-etched diamond and the grown film. 40
3.11 Secondary ion mass spectrometry (SIMS) profile of the PE-CVD grown film. 41
3.12 X-ray photoelectron spectra of the diamond substrate and the grown film. 44
3.13 Low energy electron diffraction (LEED) pattern of the H-terminated CVD-grown film. 46
3.14 Interpretation of the LEED pattern. 47
3.15 AFM images of the H-etched (111) diamond substrate 48
3.16 Temperature-dependent surface morphorogy of the (111) diamond surface. 50
3.17 AFM image of the (111) diamond film. 51
3.18 Picture of the “high power” microwave head. 55
3.19 Differential interference contrast microscope (DICM) images of the sample surface ($CH_4 = 4$ %). 56
3.20 SIMS profile of the diamond grown by using a high-power microwave. 58
3.21 DICM images of the sample surface ($CH_4 = 7$ %). 59

4.1 Dipole coupling prefactor and required spin coherence times as a function of the target-NV center distance. 66
4.2 Concept of the nitrogen delta-doping. 69
4.3 SIMS profile of the nitrogen-doped film. 72
4.4 Residual gas analysis (RGA) of the nitrogen partial pressure of the growth chamber. 74
4.5 Optical setup 77
4.6 Electrical setup 81
4.7 Continuous-wave electron spin resonance (CWESR) spectra of a substrate and the doped NV center 84
4.8 $^{13}C/^{12}C/^{13}C$ isotopically layered sample structure. 86
4.9 Electron spin echo envelope modulation (ESEEM) pattern of a substrate and the doped NV center. 89
4.10 ESEEM pattern of the doped NV center indicative of the ^{13}C coupling. 90
4.11 Schematic geometry of a NV center and a ^{13}C nuclear spin. . . . 93
4.12 Structure of the nitrogen delta-doped sample. 99
4.13 Schematic of the Hahn echo pulse sequence. 100
4.14 “Node” method for the Hahn echo measurement. 103
4.15 Hahn echo results of the doped NV centers at depths $d = 5$ and 52 nm 106
4.16 Summary of T_2 times of the doped NV centers. 107
4.17 Doped NV density as a function of the depth. 108
4.18 Schematic geometry of a NV center and an external target spin. . 112
4.19 Calculated dipole sensitivity as a function of target-NV center distance. 114

5.1 Schematic of magnetic resonance force microscopy (MRFM). . 122
5.2 Structure of the sample for the nanoeter-scale nuclrear magnetic resonance (nanoNMR). 124
5.3 Hahn echo data of the NV center usesd for nanoNMR. 125
5.4 Schematic of statistical polarization. 128
5.5 Schematic of the nanoNMR pulse sequence. 130
5.6 nanoNMR results. 133
5.7 nanoNMR results by a Fourier transform method. 135
5.8 Three-dimensional plot of the target protons. 147
5.9 Root-mean-square field from a cubic volume of proton as a function of its side length. 148

6.1 Surface confocal scan of an electron irradiated sample displaying spars NV centers. 154
6.2 Surface confocal scan of an electron irradiated sample displaying both substrate and doped NV centers. 155
6.3 Concept of ^{12}C implantation technique. 156
6.4 Results of the time-dependent annaling study. 158
6.5 NV density as functions of doping gas flow and ^{12}C implantation dose. 161
6.6 Spin coherence times as a functions of doping gas flow and ^{12}C implantation dose. 164
6.7 Concept of the three-dimensional (3D) localization using aperture implantation. 167
6.8 Surface confocal scan of the aperture implantation sample. . . . 170
6.9 Histogram of the number of NV centers localized per aperture. . 171

6.10 Average number of NV centers per aperture as a function of diameter. 172
6.11 Photon antibunching and Hahn results fo the 3D-localized NV center. 173
6.12 Vacancy distribution after a certain annealing time. 176
6.13 Probability distribution of doped and substrate NV centers. . . . 179
6.14 Calculated distribution of the diffusion length. 180
6.15 Schematic of the sample structure used for the localized volume calculation. 182
6.16 Conversion efficiency and localization volume as a function of vacancy diffusion length. 184
6.17 Concept of the nanopillar sample. 185
6.18 SEM image of an array of the nanopillars. 187
6.19 Surface confocal scan of an array of the nanopillars. 188
6.20 Histogram of NV centers per nanopillar. 189
6.21 Measured T_2 times of single NV centers localized within a nanopillar. 191

7.1 Experimental setup of two-dimesional nanomete-scale magnetic resonance imaging (2D nanoMRI). 197
7.2 Proton NMR measurements. 200
7.3 Line scans of the NMR signal (1D nanoMRI). 202
7.4 2D nanoMRI. 204
7.5 Root mean squre (RMS) proton magnetic signal as a function of NV center depth. 209
7.6 Hahn echo results of the extremely shallowly doped NV centers. 212

7.7 Summary of T_2 times of the extremely shallowly doped NV centers. 213
7.8 Figure of merit as a function of NV center depth. 214
7.9 Sample preparation process of the photonic crystal nanobeam containing nitrogen delta-doped layer. 217
7.10 SEM image of the phoronic crystal nanobeam. 219
7.11 Photonic cavity mode shift as a function of gas injection step. . . 220
7.12 Photon lifetime results of NV centers in the photonic cavity. . . 221
7.13 SEM image of the cylindrical diamond particles (DPs). 225
7.14 Schematic of a microfluidic channel with a laser-trapped single DP. 225
7.15 CW-ESR spectra of DPs. 227

A.1 Photo of the diamond CVD system. 234
A.2 Photo of the diamond CVD rack. 235
A.3 Photo of the main panel of the CVD control software. 235
A.4 Photo of the chase. 236
A.5 Photo of the semi-auto panel of the CVD control software. . . . 239
A.6 Photo of the diamond CVD cage. 239
A.7 Photo of the top part of the diamond CVD system. 240

B.1 Molybdenum sample holder design 254

List of tables

B.1 List of samples 253

Chapter 1

Introduction

The development of the semiconductor process technologies over the last five decades has enabled the materials engineering and the device fabrication at an amazing level of precision. Driven by Moore's law [1], the size of a transistor gate in the modern very-large-scale integration (VLSI) circuits is today less than 20 nm [2]. Sophisticated thin-film deposition techniques have reached the ability to control the synthetic film thickness with atomic level precision [3]. The advancement of the semiconductor technology continues to provide interesting problems for the science community.

Quantum physics in the solid state is driven by the ability to control materials systems using the semiconductor technology, dating back to the discovery of the tunneling effect [4]. This led to the emergence of quantum structures and continues to push the boundaries by exploring the properties of single quanta

such as single electrons, photons and spins.

Moreover, given the continued miniaturization of semiconductor devices now entering the atomic scale, the question becomes: Can we control, image, and manipulate individual atoms using the semiconductor technology?

To better engineer defects and impurities in semiconductor devices, scientists are now challenged with controlling the position of individual atoms. Furthermore, if the size of a transistor gate becomes comparable to that of molecules, the disconnect between the semiconductor technology and the chemical or biological researches might be bridged. This may lead to interesting collaborative ideas, for example, visualizing the atomic behavior within molecules and manipulating atoms to control the chemical synthesis by the future generations of semiconductor devices.

The nitrogen-vacancy (NV) center, which is a point defect in diamond crystal consisting of a substitutional nitrogen with an adjacent vacancy, is an ideal system to test such concepts as it is a defect complex which acts like a virtual atomic system trapped in the solid state. Moreover, the quantum control of a single spin associated with the NV center can be used to detect and image atomic-scale objects. Most importantly, the quantum properties of the NV center can be controlled by materials engineering and nanometer-scale device fabrication.

The goal of this dissertation is to develop materials engineering techniques that precisely control the position of the NV center in the diamond crystal and furthermore, to explore applications of such engineered atoms in the solid state for quantum information processing as well as the atomic-scale sensing and imaging techniques.

Chapter 2

The nitrogen-vacancy (NV) center

2.1 The nitrogen-vacancy (NV) center

The nitrogen-vacancy (NV) center is a point defect in the diamond crystal, consisting of a substitutional nitrogen and an adjacent vacancy [5, 6], which has the C_{3v} point group symmetry with its symmetry axis along the $\langle 111 \rangle$ crystal orientation (Fig. 2.1).

The NV center shows optical emission with the zero phonon line (ZPL) at 637 nm (1.945 eV) [5] corresponding to a $^3A_2$ (ground state) $\rightarrow$ ^3E (excited state) optical transition [7]. In addition, the vibronic sideband emission from around 650 to 800 nm is also observed in the photoluminescence (PL) spectra at room temperature as shown in Fig. 2.2. The NV center's strong optical transition allows for the PL detection from a single NV center [8, 9].

The NV center's $^3A_2$ ground state has a spin triplet ($S = 1$) [11, 12].

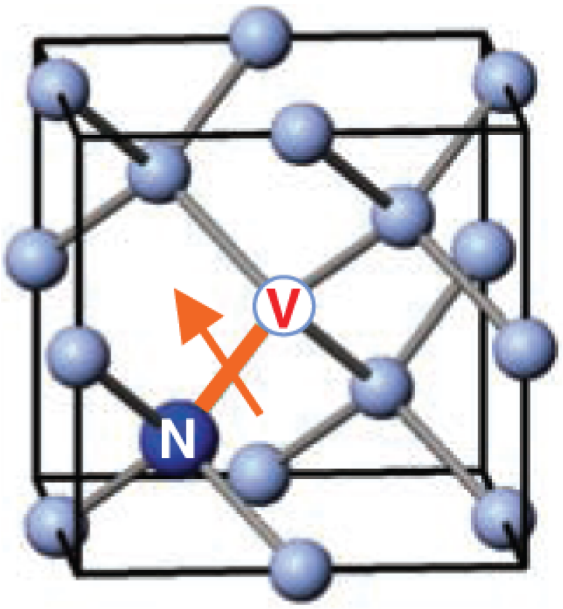


Figure 2.1: Schematic of the nitrogen-vacancy (NV) center in the diamond lattice. Two carbon atoms adjacent to each other are replaced by a nitrogen atom and a vacancy, forming an NV center.

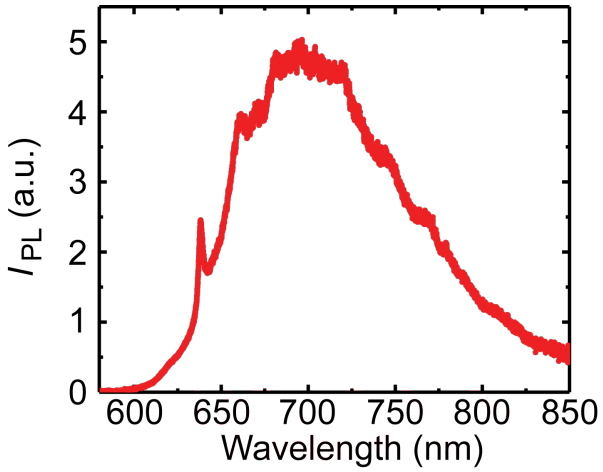


Figure 2.2: Typical photoluminescence spectrum of the NV center at room temperature by using a 532 nm green laser excitation. The zero phonon line (ZPL) at 637 nm and a broad vibronic sideband emission between 650 to 800 nm are observed. Data courtesy of B.B. Buckley and F. J. Heremans. Ref. [10]

The degeneracy between the $m_s = \pm 1$ states and the $m_s = 0$ state is lifted up by the crystal field splitting $D/2\pi$ = 2.88 GHz due to the spin-spin interaction [7]. Each of the $m_s = \pm 1$ spin sublevels is further split by the Zeeman splitting and by the hyperfine coupling to the host nitrogen nuclear spin, which can be expressed by the following ground state Hamiltonian,

$$H = DS_z^2 + g\mu_B BS_z + A\mathbf{S}\cdot\mathbf{I} \tag{2.1}$$

where $\mu_B = 9.27 \times 10^{-24}$ J/T is the Bohr magneton, g = 2.00 is the electron g-factor, $\mathbf{S}$ is the NV center spin, S_z is its z component, B is the external field, A is the hyperfine splitting constant and $\mathbf{I}$ is the nuclear spin. A schematic of the ground state energy level as a function of the external magnetic field applied along the NV center symmetry axis is shown in Fig. 2.3.

The ^3E excited state of the NV center is also a spin triplet. The $^3A_2 \rightarrow {}^3E$ optical transition is a spin-conserving, radiative transition with the excited state lifetime of $\sim$ 10 ns [13]. In addition, the spin singlet $^1A_1$ and ^1E states lying below the ^3E states create an alternative relaxation path through the inter-system crossing, which makes the NV center a unique spin system (Fig. 2.4). The energy relaxation from the ^3E state to the $^1A_1$ state occurs with a much higher probability when the excited state spins are in the $m_s = \pm 1$ states [14]. Furthermore, the non-radiative energy relaxation from the $^1A_1$ state ends preferentially into the $m_s = 0$ ground state [15, 16], ultimately causing the spin flip

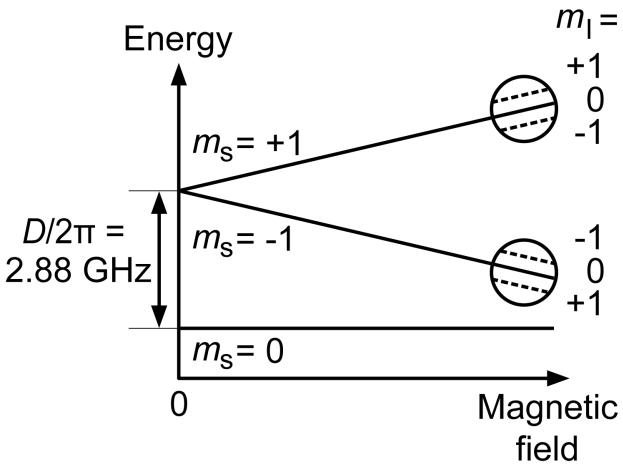


Figure 2.3: Schematic of the ground state energy levels of the NV center as a function of the external magnetic field applied parallel to the NV center symmetry axis. The degeneracy between the $m_s = \pm 1$ states and the $m_s = 0$ state at the zero magnetic field is lifted up by the crystal field splitting $D/2\pi$ = 2.88 GHz. The $m_s = \pm 1$ states are split by the Zeeman splitting when the external magnetic field is applied. Each of the $m_s = \pm 1$ state is further split by the hyperfine splitting. The circles on the right display "close-up" to show the hyperfine splitting due to the host ^{14}N nuclear spin ($I = 1$).

from $m_s = \pm 1$ to $m_s = 0$ during the energy relaxation. This spin-selective relaxation through the intersystem crossing results in two important features for the NV center spin measurement. First, it allows for the laser-induced spin initialization to the $m_s = 0$ state. Even though the initial spin population is in a thermal equilibrium between the $m_s = 0$ and ± 1 states, spins in the $m_s = \pm 1$ states are "optically pumped" into the $m_s = 0$ state through the intersystem crossing during several microseconds of laser illumination, while spins in the $m_s = 0$ state keep undergoing the spin-conserving optical cycle, resulting in the spin align-

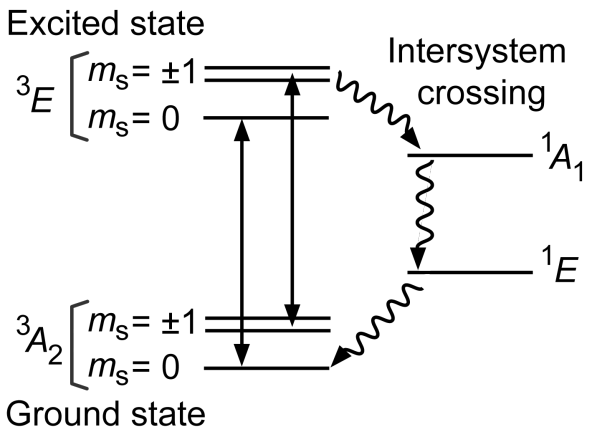


Figure 2.4: Energy diagram showing the spin selective optical transition of the NV center. Spin sublevels of the $^3A_2$ ground state and the ^3E excited state are shown. The $^1A_1$ and ^1E singlet states lying between the $^3A_2$ and ^3E triplet states create an alternative relaxation path through the intersystem crossing. The straight arrows indicate radiative and spin conserving transition, whereas wavy arrows indicate the nonradiative process. The $^3E \rightarrow {}^1A_1$ transition is spin selective, occurring with a higher probability when the ^3E excited state spins are in the $m_s = \pm 1$ states. Energy relaxation through the intersystem crossing occurs preferentially into the $m_s = 0$ ground state.

ment to the $m_s = 0$ state. Moreover, because of the spin-selective nonradiative decay, PL from the $m_s = \pm 1$ states is about 30 % lower than the $m_s = 0$ state, allowing for a simple way to read out spin by measuring the PL intensity.

In addition to the optical spin initialization and read out, an electron spin resonance (ESR) technique allows for spin manipulation via applying microwave (2 – 3 GHz) resonant to the energy splitting between the spin sublevels. An optically detected magnetic resonance (ODMR) technique that combines the ESR spin manipulation and the optical spin read out was first demonstrated on an

ensemble of NV centers at low temperature [17, 18, 19], followed by on a single NV center at room temperature [8]. Furthermore, coherent manipulation of a single electron spin was demonstrated with a single NV center at room temperature [20], which triggered broad interests in this system for the spin-based quantum science and technology.

2.2 Spin coherence of the NV center

Among many solid state spin systems, the NV center stands out because of its exceptionally long electronic spin coherence time T_2 at room temperature, reaching up to the order of milliseconds. A long spin coherence time is one of the critical requirements not only for the quantum information processing enabling a large number of quantum operations and long-lived qubit storage, but also for weak field detection in the nanometer-scale metrology techniques. Improvement of the materials quality to reduce the source of spin noise is therefore an important challenge in order to extend the spin coherence time. In this section, the efforts to improve NV center's T_2 times are overviewed, in order to emphasize the importance of controlling the materials quality.

The Type Ib diamonds containing a high nitrogen impurity concentration larger than $\sim 10^{18}$ cm^{-3} are one of the common materials for the NV center research, which is irradiated by high energy (~ 2 MeV) electron beam to create

vacancies and subsequently annealed (above 650 ^{o}C, typically $\sim$800 ^{o}C, for a few hours) to diffuse them to form NV centers [5]. One of the early reports measured $T_2 \sim 80$ μs at T = 1.5 K in such a material [18]. In these days, T_2 times of NV centers in the Type Ib diamonds range from 0.4 to 7 μs at room temperature [21, 22], which is limited by a large number of the paramagnetic impurities caused by the nitrogen electron spins (P1 centers). Since T_2 is inversely proportional to the nitrogen concentration [23], reducing nitrogen impurities in diamond is an important approach to improve the NV spin coherence. A T_2 time of ~ 60 μs at room temperature was measured in a chemical vapor deposition (CVD) – grown diamond of a nitrogen concentration of 6×10^{16} cm^{-3} [24]. Reducing nitrogen impurities further down to 10^{15} cm^{-3} resulted in $T_2 \sim 600$ μs together with careful magnetic field alignment along the symmetry axis of the NV center [25].

At such a low nitrogen impurity concentration, the ^{13}C nuclear spin bath is a dominant source of the NV spin decoherence. Although the most naturally abundant (98.9 %) carbon isotope ^{12}C has no nuclear spin, the 1.1 % abundant ^{13}C isotope has a nuclear spin $I = 1/2$, which causes spin fluctuation adversely affecting the NV center spin coherence. The T_2 time of NV centers was predicted to be inversely proportional to the ^{13}C concentration [27], which was experimentally confirmed [28]. By reducing the ^{13}C concentration down to 0.3 %

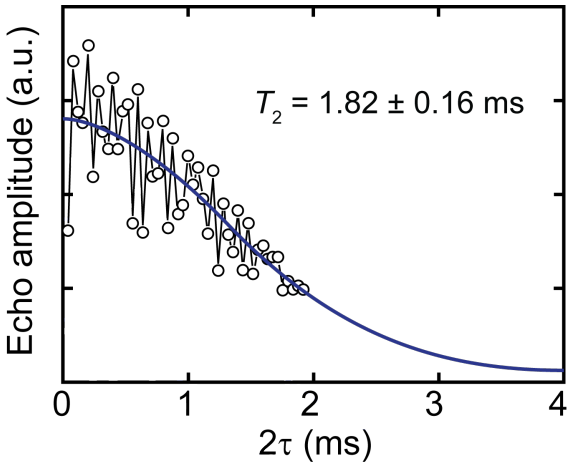


Figure 2.5: Hahn echo decay curve of an NV center in an isotopically purified ^{12}C diamond showing an exceptionally long $T_2 \sim 1.8$ ms at room temperature. Data adapted from Ref. [26].

using an isotopically purified $^{12}CH_4$ source gas during CVD of diamond, along with careful control of nitrogen impurities being less than 10^{13} cm^{-3}, an unusually long T_2 of 1.8 ms at room temperature was demonstrated (Fig. 2.5) [26], which gained considerable attention. Although such a long T_2 was measured in a one-of-a-kind ultrapure material, the development and application of the dynamical decoupling techniques enabled extension of T_2 in less pure materials up to several hundreds of microseconds [29, 30, 31]. Using a pure diamond and creating NV centers by a nitrogen implantation technique [32, 33, 34] is a common way to prepare samples in these days, although T_2 variation due to crystal damage and other issues are important challenges regarding this method, which is discussed in detail in Chapter 4.

The long T_2 of the NV center should be compared to other solid state spin systems. For example, T_2* of III-V semiconductor quantum dots is on the order of 10 ns at T = 100 mK [35]. Although electron spins bound to the phosphorous donor in isotopically purified ^{28}Si display unusually long $T_1 \sim 1$ hour at T = 1.25 K [36] and T_2 = 14 ms at T = 7 K [37], these spin coherence times drop sharply with temperature due to the Orbach process, resulting in $T_1 \sim T_2 \sim 1$ μs at T = 20 K [37]. In addition, electron spins associated with basal and c-axis divacancies in 4H-SiC display $T_2 \sim 180$ μs at T = 20 K and $T_2 \sim 260$ μs at T = 200 K, respectively [38]. Although 4H-SiC displays persisted electron spin coherence at room temperature in a certain type of defects (unidentified), the T_2 is decreased to ~ 40 μs. By comparing to other solid state electron spin systems, a long, room temperature T_2 should be emphasized for considering unique applications of the NV center.

2.3 Applications of the NV center

2.3.1 Sensitive nanometer-scale magnetometry applications

One of the most emerging applications of the NV center is an ultrasensitive magnetic field detection in combination with the nanometer-scale spatial resolution. The field sensitivity of the NV center-based magnetometry technique can be enhanced by the quantum coherent manipulation of the probe NV spin.

The minimum detectable field B_{min} of the NV center, which is limited by its spin coherence and the optical spin read out is given by [39]

$$B_{min} \approx \frac{\hbar}{g\mu_B\sqrt{t\tau}} \tag{2.2}$$

where $\hbar$ is the reduced Planck's constant, t is the total measurement time, and τ is the relevant spin coherence time of the NV center depending on the detection scheme. $\tau = T_2{}^*$ ($\sim 1\ \mu$s) is the relevant time scale for the DC magnetometry scheme, which can be extended to $\tau = T_2$ ($\sim 0.1 - 2$ ms) using the spin echo technique for the AC magnetometry [40], resulting in a sensitivity on the order of a few nT/$\sqrt{\text{Hz}}$ corresponding to the capability of detecting a single electron spin and even a single ^{1}H nuclear (proton) spin at a distance of 10 nm. Moreover, the field sensitivity can be further improved by the advanced multi-pulse echo sequences, at the cost of detection bandwidth. Although the AC magnetometry scheme requires to control the target magnetic source oscillating in synchronous to the spin echo pulses, it is not a significant problem for a single spin detection, as additional pulses can be used to control the target spin in phase. A theoretical framework and a proof-of-concept measurement were reported in 2008 [39, 40], inspiring many efforts to implement the NV center-based magnetometry since then.

In addition to the excellent sensitivity, the most important feature of the NV center-based magnetometry is that the probe spin can be localized within

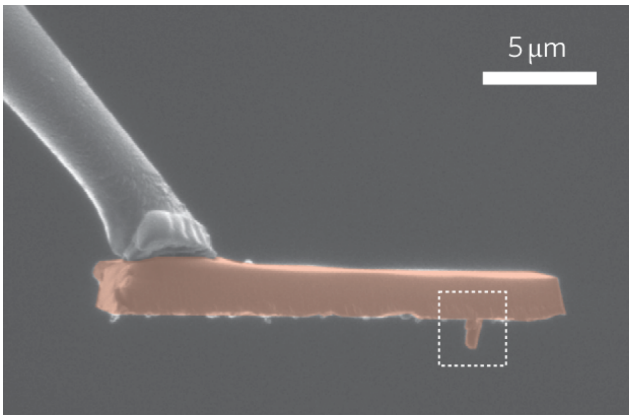


Figure 2.6: Scanning electron microscopy (SEM) image of an diamond-based AFM tip. A single NV center is embedded at the end of the AFM tip in the dotted square. Data adapted from Ref. [41].

a volume of about 10 nm due to the inherent atomic-scale nature of the defect. Moreover, the probe spin can be placed in the direct proximity of the magnetic source within a distance of about 10 nm, enabling nanometer-scale spatial resolution, which can be realized by placing a single NV center near the surface of a bulk diamond, or in a diamond nanocrystal of 10 – 20 nm size. Furthermore, nanometer-scale magnetic imaging using the scanning probe technique was proposed by placing a single NV center at the end of a diamond-based atomic force microscopy (AFM) tip, or by attaching a nanodiamond to a (conventional) AFM tip or tapered optical fiber [41, 42, 43]. An NV-center embedded diamond AFM tip (Fig. 2.6) was utilized to detect and image a single electron spin of a separate target NV center [44]. In addition, a magnetized AFM tip was used to induce

a local magnetic field gradient that allows for imaging and coherent control of a single NV center spin [45] and a single dark spin [46] in an ensemble spin environment.

An outstanding question to realize such nanometer-scale magnetic sensing and imaging schemes is if the NV center's optical and spin properties are preserved within nanometers from the diamond surface. The electronic properties near the surface of the materials are different from the bulk, which can affect the magnetometry performance of the NV center placed in the nanometer proximity of the surface. Controlling positions, in particular depth, of the NV centers at the nanometer-scale accuracy while preserving their optical and spin properties is indeed one of the important questions that is addressed by this dissertation, which is a critical requirement for realizing NV center-based nano-magnetometry.

Finally, an additional advantage of the NV center-based magnetometry is that it can be operated under ambient conditions. This advantage is particularly important for the magnetometry in biological samples such as cells, or molecular structure imaging since most of biological and chemical researches are conducted under ambient conditions. The chemical stability and biological compatibility of diamond are also beneficial for these applications.

The NV center-based magnetometry is strongly motivated by an ultimate

goal of detecting and imaging a single electron and proton spin in the organic and biological samples. The material science and nanotechnology to engineer NV centers in the diamond crystal are critical requirement for enabling these fascinating applications.

2.3.2 NV center-based metrology

The NV center-based metrology is not limited to magnetometry. A wide variety of metrology schemes are actively investigated taking advantages of NV center's long spin coherence, room temperature operation, and coherent spin control.

A single NV center in the bulk diamond was used for sensing electric field via energy shifts of the ground state spin sublevels due to the Stark effect [47]. By applying an oscillating electric field, the AC field sensitivity reached ~ 200 V/cm$\sqrt{\text{Hz}}$, equivalent to a field induced by a single electron charge at a ~ 150 nm distance.

Thermometry is one of the emerging applications of the NV center-based metrology, which was stimulated by a temperature-dependent measurement of the optical read out of the NV center spin [49]. This work demonstrated that the spin-dependent PL contrast was measurable up to more than 600 K, also showing that the temperature-dependent zero-field splitting $D(T)$ [50] can be used for

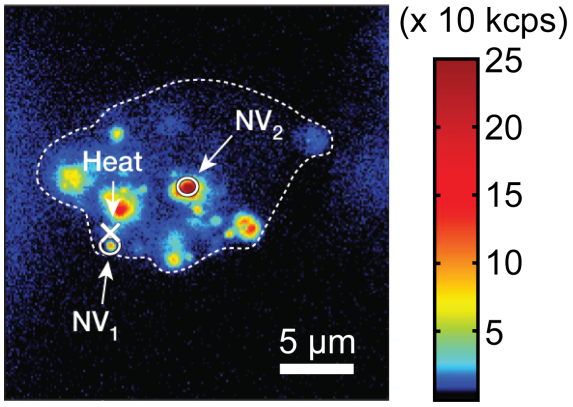


Figure 2.7: Scanning confocal microscopy image of a living cell. Nanodiamonds containing a single NV center are injected into the cell for a local temperature sensing. Data adapted from Ref. [48].

temperature measurements over a wide range of temperature. The thermal sensitivity was calculated to be $\sim$ 100 mK$\sqrt{\text{Hz}}$ using DC measurement schemes, which can be improved by an order of magnitude by applying a coherent spin control to suppress magnetic noise [51]. Combining this thermometry scheme with bio-compatible nanodiamonds [52] enabled local temperature sensing inside a living cell (Fig. 2.7) [48], which offered a combination of good thermal sensitivity and the nanometer-scale spatial resolution, a unique feature arising by using the NV center.

2.3.3 Quantum applications of the NV center

Coherent coupling between qubits is an essential building block for realization of quantum computing, long-distance quantum communication as well

as quantum-enhanced metrology. The electronic spin of the NV center is an excellent candidate for the coupled qubits because of its long spin coherence, optical accessibility and room temperature operation. Moreover, due to its solid state nature, NV centers are advantageous for realizing a scalable quantum system. In this section, various types of coherent coupling between the NV center and other qubits are overviewed.

Coherent coupling between a single NV center spin and other electron spin(s) can be found in literature, such as coupling with a nitrogen spin bath [21], a single nitrogen spin [53], and another single NV center spin [54, 55]. Among these demonstrations, the NV-NV coupling was of particular importance as both qubits are optically addressable. As nitrogen spin is a major source of NV spin decoherence, localization of a pair of nitrogen atoms in the pure material together with a high yield of the nitrogen to NV center conversion are essential for the further upscaling of the NV-NV coupling.

A quantum register, consisting of a long-lived qubit for information storage and a processing qubit for write in and read out, is an essential component for long-distance quantum communication and distributed quantum computation. An NV center spin coupled to one or multiple nuclear spin(s) is an excellent system for the quantum register because nuclear spins are highly isolated from the environment and hence the memory time can be on the order of mil-

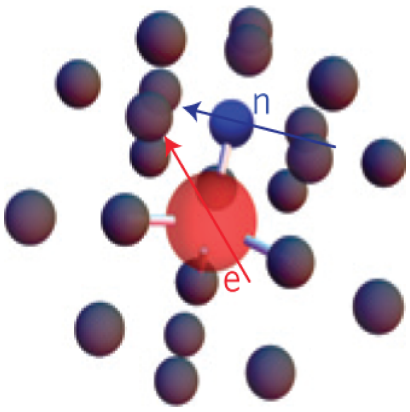


Figure 2.8: Schematic of a quantum register using coherent coupling between an electronic spin of an NV center (red arrow) and a nuclear spin of its host nitrogen (blue arrow). Original figure presented in Ref. [56].

liseconds and up to seconds, much longer than the coherence time of electron spins. Demonstrations of the NV-nuclear spin coupling includes coupling with the host ^{14}N nuclear spin (Fig. 2.8) [56], individual proximal ^{13}C nuclear spins [57, 58], two ^{13}C nuclear spins [59] and a single ^{13}C nuclear spin [60]. In the last example, an NV center in an isotopically ^{12}C -enriched (99.99 %) diamond sample was used in order to mitigate the decoherence due to ^{13}C nuclear spin bath while one of the ^{13}C spin at a distance of $\sim$ 2 nm was weakly coupled to the NV center. High-fidelity, single-shot readout of a single [61] and up to three nuclear spin(s) [62] in the NV center-based quantum registers were also demonstrated.

Coupling solid state qubits to photons is of particular importance for quantum repeater, necessary for long-distance quantum communication. Although

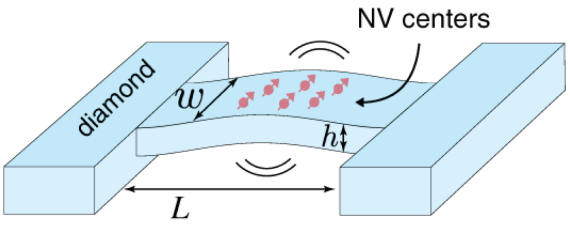


Figure 2.9: Conceptual figure of the phonon-mediated spin coupling in a mechanical resonator. Original figure presented in Ref. [66].

photon is an ideal qubit for transmitting quantum information in a long distance because of its very weak coupling to the environment, quantum repeaters are still necessary to extend the communication distance by refining and amplifing information caused by the optical loss. The NV center is a promising element of the quantum repeater because of its strong optical emission, and the demonstrated spin-light entanglement [63, 64]. Furthermore, two NV centers at a 3-meter distance were coherently coupled through photons [65], displaying potential of the NV center as a building block for long-distance quantum communication. Diamond device engineering at a micrometer scale (such as solid immersion lens) and further at a nanometer scale (such as photonic crystals) is an important part of the photon-mediated entanglement schemes in order to increase the photon collection efficiency for measuring faint signals.

Finally, spin-phonon coupling is an emerging research field that enables coherent spin interactions among multiple NV centers over a long range on

the micrometer scale. The NV center spin coupled to the motion of a magnetized mechanical resonator was used to coherently detect small Brownian motion [67] and projected to sense a quantized motion (a single phonon) [68]. Strain-mediated coupling between an NV center and a diamond monolithic mechanical resonator was demonstrated [69]. Reducing the size of mechanical resonators down to the nanometer scale would enable strong coupling between spins and phonons (Fig. 2.9) [66, 68, 70], allowing for the phonon-mediated spin coupling over a long distance beyond the direct magnetic dipole coupling limited to tens of nanometers. Such nanomechanical coupling requires precise NV center position control in order to maximize the strain effect on the NV center.

Coherent coupling of an NV center spin to other electronic and nuclear spins, as well as photons and phonons are very important for realizing quantum applications as well as for the fundamental test of quantum physics concepts. To meet conflicting requirements of localizing spins while isolating them from a noisy spin environment is an outstanding challenge for coherent coupling of multiple spins, which necessitates fine material tuning for specific measurements. Moreover, strong coupling of NV center spins with photons and phonons requires diamond-based nanostructure engineering. In a reverse manner, development of new materials and nanometer-scale device technologies should drive

new researches on the NV center-based quantum science and its applications. Therefore, the materials science and engineering play important roles for the NV center spin-based quantum science and applications.

2.4 Conclusion and Organization

The optical and spin properties of the NV center are reviewed. Important features of the NV centers include long spin coherence at room temperature, optical initialization and read out of the spin, single spin addressability and inherent atomic scale. The solid state nature of the NV center is greatly exploited as it is compatible to the nanometer-scale engineering. These advantages of the NV center open up a wide variety of applications ranging from nanometer-scale magneto-, electro- and thermometry techniques to quantum computing and quantum communications. For whatever applications, precise control of the material quality and nanometer-scale engineering of the NV centers in diamond are the most important challenges for exploring further potentials of the NV center, which is the main focus of this dissertation. Synthesis of a high-quality diamond film is discussed in the next chapter, followed by presenting a technique that enables nanometer-scale depth control of NV centers in Chapter 4. This technique is extended to the three-dimensional position control of a single NV center as discussed in Chapter 6. Applications of such highly engineered

NV centers for proton spin sensing in organic materials is presented in Chapter 5 as well as other results including proton spin imaging and nanostructure engineering are discussed in Chapter 7.

Chapter 3

Crystal growth of high-purity diamond

3.1 Thermodynamics of diamond synthesis

Diamond is one of the allotropes of carbon consisting of sp^3 bonding, displaying excellent material properties such as extreme hardness, thermal conductivity, chemical stability, and optical transparency over a wide range of wavelength (from deep ultraviolet to infrared). Such properties of diamond are exploited for many applications including industrial cutting tools, polishing powders and optical windows for lasers. Carbon atoms in a diamond forms a diamond crystal structure with a lattice constant of 3.57 Å (with the carbon-carbon bond length of 1.54 Å) showing a bandgap of 5.5 eV, wider than other widegap materials such as GaN (3.4 eV) or 4H-SiC (3.3 eV). Due to emerging interests in

wide bandgap semiconductor materials for the last two decades [71], electronic properties of diamond have gained significant interests as diamond may have potentials comparable or even superior to other wide bandgap materials [72]. For example, diamond displays high breakdown electric field of $\sim$ 10 MV/cm because of its wide bandgap, and it also shows a high carrier mobility of 4500 and 3800 cm^2/Vs for electrons and holes, respectively [73]. These properties along with the extreme thermal conductivity hold a promise of the material for power electronics applications. The promising potentials of the diamond as a semiconductor material draw significant interests for the artificial synthesis of diamond.

However, an outstanding challenge of diamond synthesis arises from graphite, another stable allotrope of carbon consisting of sp^2 bonding, being a thermodynamically more stable phase than diamond at the ordinary pressure and temperature. Figure 3.1 shows an energy diagram of graphite and diamond, exhibiting that graphite has lower enthalpy than diamond (C(diamond) = C(graphite) + 1.9 kJ/mol) [74]. The activation energy between graphite and diamond is very high ($\sim$ 700 kJ/mol) preventing diamond from dissolving into graphite, and hence diamond is a kinetically stable (metastable) phase.

One way to make a diamond phase dominant during synthesis is to use conditions significantly different from the ordinary pressure and temperature.

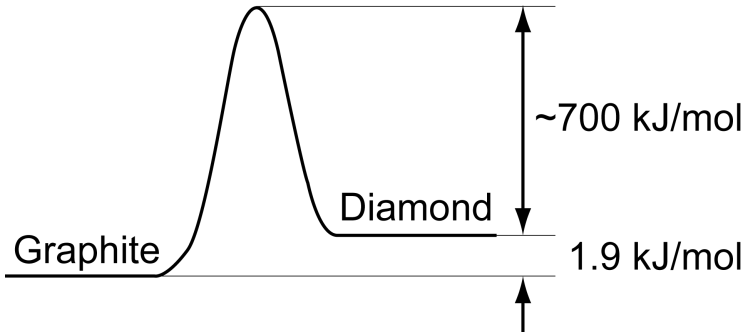


Figure 3.1: Energy diagram of graphite and diamond. Enthalpy difference and activation energy between the two phases are shown (not to scale).

Figure 3.2 shows a phase diagram of carbon [75, 76], suggesting that the diamond phase is most stable at high pressure and high temperature. A high pressure high temperature (HPHT) method is a common way to synthesize artificial diamond. The HPHT method uses synthetic conditions of a pressure ~ 5 GPa and a temperature above 1300 ^{o}C by placing a seed diamond crystal in a high pressure anvil with carbon source [77]. Some catalysts are added in order to mitigate pressure and temperature required for the growth.

Another approach to synthesize artificial diamond is to use a non-equilibrium condition via chemical vapor deposition (CVD) techniques. In particular, a plasma-enhanced chemical vapor deposition (PE-CVD) technique emerges as an established method to artificially synthesize diamond both in laboratories and industrial levels [72], as it is capable of precise growth parameter control while minimizing impurity incorporation during the growth. Both *p*-type [78]

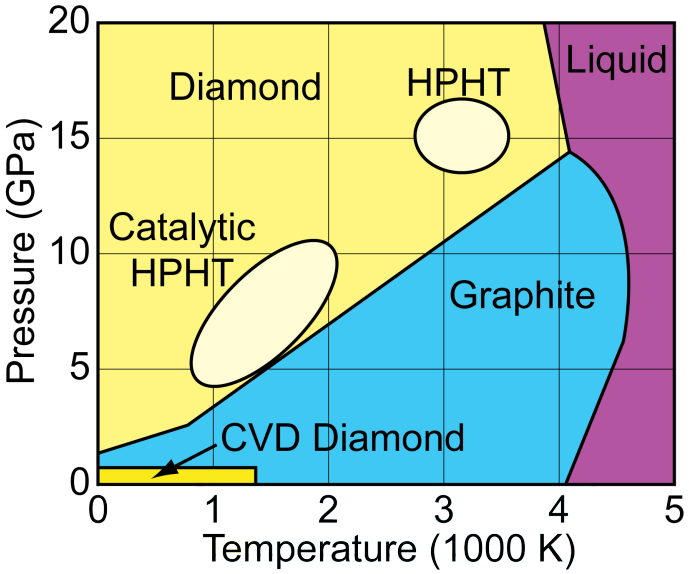


Figure 3.2: Phase diagram of carbon showing diamond, graphite and liquid phases [75, 76]. Pressure and temperature ranges used for diamond synthesis techniques are drawn in the diagram.

and *n*-type [79] doping as well as a *pn* junction [80] and a layered structure growth [81, 82] were established using the PE-CVD technique, widely opening up semiconductor applications of diamond. In the PE-CVD of diamond, hydrogen atoms (radicals) originated from H_2 process gas are activated in the plasma state, which selectively etch sp^2 bonding of carbon suppressing the graphite phase formation while promoting diamond growth.

3.2 PE-CVD growth of diamond

Figure 3.3 shows a picture of a Seki Technotron AX6300 1.5 kW mi-

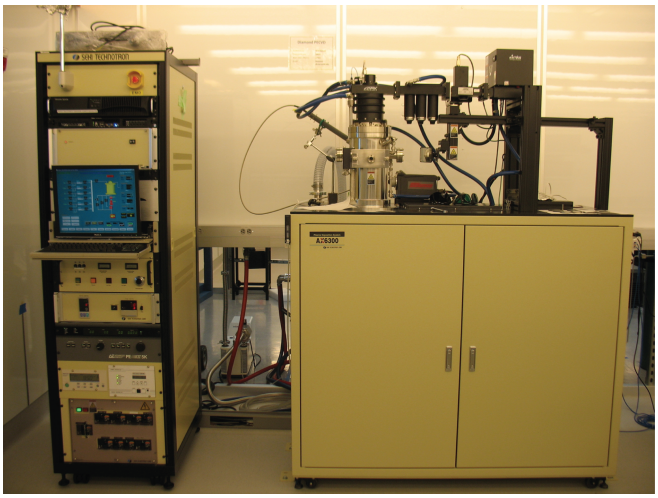


Figure 3.3: Picture of the PE-CVD machine.

crowave PE-CVD system used for the diamond growth. On the left of the picture is a control tower and the growth systems are towards the right. The growth system is schematically shown in Fig. 3.4, namely, a mixture of CH_4 source gas and H_2 carrier gas is introduced into the growth chamber with their gas flows controlled by a separate mass flow controller (MFC). This gas mixture is hit by RF microwave (2.45 GHz) in the growth chamber, forming plasma as seen as a purple ball in the inset of Fig. 3.4. A microwave generator is located on top right of the system and a waveguide leads the microwave into the growth chamber through a quartz window. Three tuners attached to the waveguide are used to match impedances between the waveguide and the chamber. The stainless steel growth chamber itself is an electromagnetic cavity whose conditions can be controlled by the height of a motorized sample stage. The design of a

molybdenum (Mo) sample holder affects the plasma chemistry, which depends on the plasma shape and its power density, and thus it is one of the key details for optimizing growth conditions. A Mo disc of 50 mm in diameter and 5 mm thick that has a sample pocket at the center of the top face is considered to be an optimized design [83] as this design mitigates plasma damage to the sample (see Appendix B). The Mo sample holder is placed on top of a graphite susceptor, which can be heated up by an induction-coupled RF stage heater without changing the plasma condition.

The process gases are pumped out using a dry pump (Adixen, ACP 28i), which mitigates oil back flow contamination to the chamber compared to an oil rotary pump. An Ar ballast gas is introduced into the last stage of the dry pump in order to improve its capability of pumping light gases, particularly H_2.

3.3 Substrates

All the diamond films presented in this dissertation are homoepitaxially grown on diamond substrates. Two types of diamond substrates, Type Ib, HPHT diamond substrates from *Sumitomo Electric Industries*, and electronic-grade, CVD-grown diamond substrates from *Element 6* are used. The nitrogen impurity concentration of the Type Ib substrates is less than 100 ppm ($\sim 2 \times 10^{19}$ cm^{-3}) displaying yellow color, whereas the electronic grade substrates contains

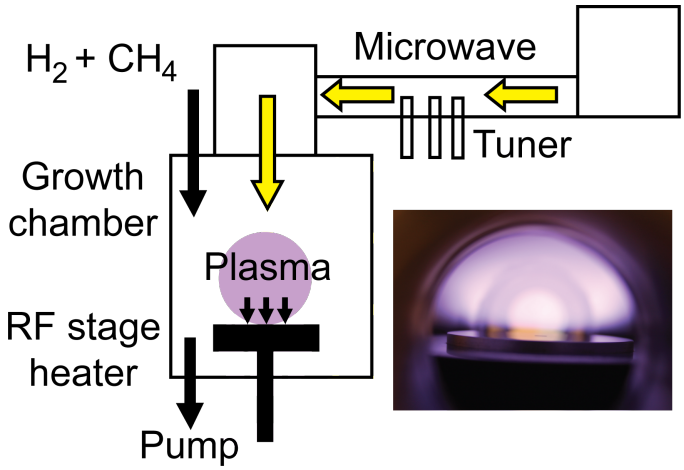


Figure 3.4: Schematic of the PE-CVD system. (inset) View of the chamber through the optical window during the growth. The plasma and the sample holder are seen.

nitrogen impurities less than 5 ppb ($\sim 9 \times 10^{14}$ cm^{-3}) showing colorless transparency. Type Ib substrates are used to optimize the crystal growth conditions while electronic-grade substrates are used for growth-incorporated NV center studies in order to avoid high background luminescence of NV centers in the substrate. All of the CVD films are grown on the (100) plane except growth results on the (111) plane are presented in Section 3.7. The surface miscut angle is $< \pm 1^o$ (3^o) for the Type Ib (electronic grade) substrates according to their specifications. The size of the substrates is typically 3 x 3 x 0.5 mm for the Type Ib and 2 x 2 x 0.5 mm for the electronic grade substrates.

Mechanical polishing marks are usually left on the surface of as-received substrates, which impede flat surface of the grown films [83, 84]. In order to

get rid of these polishing marks, all substrates are sent to *Syntek* for additional mechanical polishing that improves surface roughness (RMS) from 1.6 nm to 0.2 nm, according to the *Syntek*'s specification.

After receiving substrates back from polishing, they are treated with a boiling acid cleaning process (HNO_3 : H_2SO_4 = 30 mL : 20 mL, at 120 ^oC) in order to get rid of a surface graphitic layer. As diamond is highly hydrophobic, contaminating particles cannot be removed by sonication and hence substrate surface is cleaned with a cotton swab in acetone and IPA. Since the number of contaminating particles on the substrate surface increases with a time, it is important to clean a substrate in solvent right before mounting it into the growth chamber. One of the edges of the backside of the substrates is scratched by a diamond pen in order to identify the growth face.

3.4 Growth theory

Step-flow growth is a favorable growth mode for a high-quality PE-CVD diamond film displaying an atomically flat surface. In this growth mode, carbon adatoms that arrive at step terraces diffuse to the step edges, there incorporated into the crystal leading to an advancement of the atomic steps (Fig. 3.5). In this section, a general growth theory for the step-flow growth is introduced (Section 3.4.1) and a modified theory for the case of PE-CVD diamond is presented in

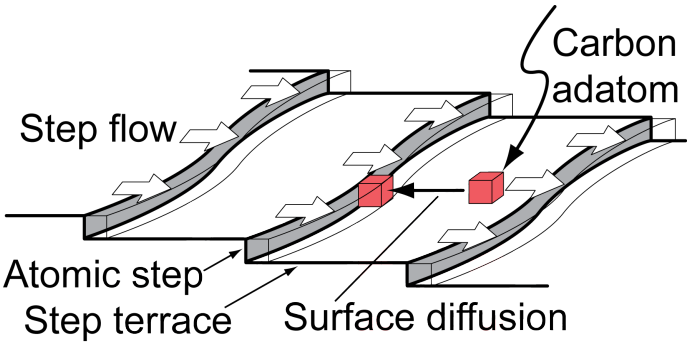


Figure 3.5: Schematic of step-flow growth. A carbon adatom arriving on the step terrace is shown as a cube in red. The adatoms diffuse on the step terrace and incorporated to the diamond crystal at step edges, resulting in advancement of atomic steps. The movement of atomic steps is described as arrows in white.

Section 3.4.2.

3.4.1 General theory for step-flow growth

In order for carbon adatoms to get incorporated at step edges in the step-flow growth mode, the carbon adatom velocity has to be larger than the step velocity. The step edge velocity can be written as [85],

$$v_{step} = jL, \tag{3.1}$$

where j is the deposition rate in the units of monolayer per second and L is the terrace length. The velocity of carbon adatoms can be written as,

$$v_{adatom} = \frac{L}{t} = \frac{L}{(L^2/D)} = \frac{D}{L}, \tag{3.2}$$

where D is the diffusivity, t is the time for a carbon adatom to diffuse to the step edge and a simple form for a diffusion length ($L \approx \sqrt{Dt}$) is used to derive this equation. A condition required for the step-flow growth is

$$v_{step} < v_{adatom}, \tag{3.3}$$

leading to an equation,

$$\frac{jL^2}{D} < 1. \tag{3.4}$$

This equation provides a general strategy for the step-flow growth: decreasing the growth rate via reducing the flow of CH_4 precursor will decrease j, increasing the substrate miscut angle will reduce L, and increasing growth temperature T will increase D as D is proportional to the exponent of T,

$$D = D_0 \exp(-\frac{E_a}{k_B T}), \tag{3.5}$$

where D_0 is a constant, E_a is an activation energy for diffusion, and k_B is the Boltzmann's constant.

On the other hand, when the left hand side of Equation (3.4) is greater than unity, the velocity of carbon adatoms are smaller than the step edge velocity. In such cases, carbon adatoms not reaching the step edges provide additional growth sites on the step terraces, leading to the two-dimensional (2D) nucleation.

3.4.2 Growth strategy for PE-CVD diamond

Although the strategy for the step-flow growth is generally applicable, additional considerations are necessary for PE-CVD of diamond where a hydrogen etching effect plays an important role.

Okushi *et al.*, investigated step-flow growth conditions for homoepitaxial diamond in a low CH_4 concentration less than 2 % [84, 86], where CH_4 concentration is defined as a ratio of CH_4 gas flow to the total gas flow, $[CH_4]/([CH_4] + [H_2])$, which can be reduced to $[CH_4]/[H_2]$ when $[CH_4] \ll [H_2]$. They reported that neither macro-bunching steps nor surface defects such as non-epitaxial crystallites and phyramidal hillocks were observed when the CH_4 concentration is less than 0.15 %. Although the initial substrate has periodic surface mechanical polishing patterns ~ 4 nm high, they observed atomic steps of single- or double-atomic height running along $\langle 110 \rangle$ directions after the growth using an extremely low CH_4 concentration of 0.025 %. They assumed that these results are due to a hydrogen (H) etching effect, since the hydrogen plasma is dominant in such an extremely low CH_4 concentration condition. They also pointed out that an anisotropic H etching effect [87, 88] showing the lowest etching rate for the $\langle 100 \rangle$ direction is the main cause that only substrates with low miscut angles $\theta_{off} < 1.5^{\circ}$ resulted in atomically flat surfaces [89, 90]. They concluded that the balance between the H etching effect and the diamond deposition using an

optimized CH_4 concentration is a key for atomically flat surfaces.

3.5 Crystal growth of high-quality diamond film

3.5.1 Temperature dependence of hydrogen etching

An *in-situ* H etching treatment prior to the diamond growth prepares atomic steps that provide favorable nucleation sites of carbon adatoms for the step-flow growth [83, 84]. As the H etching effect is sensitive to temperature [88, 91] and temperature calibration is necessary for each individual growth system, a temperature dependence of the H etching effect is studied.

For a reliable measurement of growth temperature, the substrate temperature (T_{sub}) is used, which is a temperature reading measured by a thermocouple located beneath the graphite susceptor. Temperature of the sample surface can also be read by a pyrometer, which measures black body radiation of the sample and the sample holder through an optical window of the growth chamber. However, since the pyrometer read is sensitive to the measurement position of the sample holder and it shows inconsistent temperature reading likely due to variations in optical reflectivity of the holder and optical absorption of the source gases, the pyrometer is not used as a measure of the growth temperature. All the temperatures shown hereafter denote the substrate temperature measured by the thermocouple.

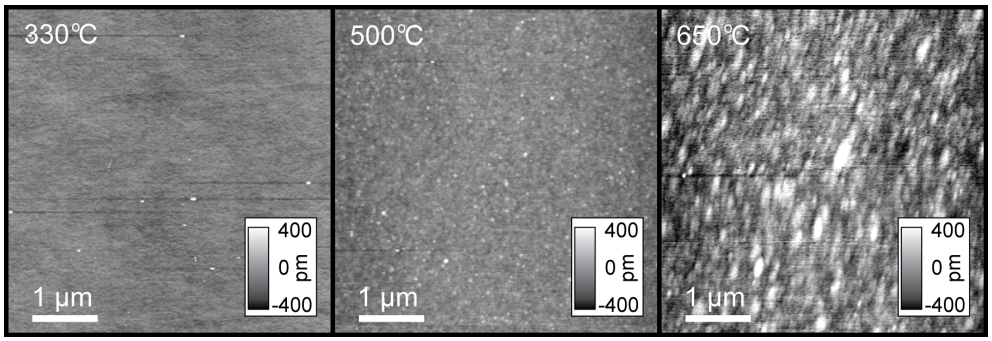


Figure 3.6: 5 μm $\times$ 5 μm AFM images of H-etched diamond surface at 330 (left), 500 (center), and 650 ^{o}C (right).

Once the chamber pressure is stabilized at 25 Torr with a H_2 flow of 500 sccm, H plasma is ignited using a microwave power of 750 W. These parameters are kept constant during an H etching process for an hour. The substrate temperature (T_{sub}) is controlled using an RF heater stage, except for the lowest $T_{sub} \sim 330$ ^{o}C as the power of microwave heats up to that temperature without heating the stage. After the H etching process, the sample is cooled down and taken out from the growth chamber to study surface morphology by atomic force microscopy (AFM). The same sample is used in this cumulative H etching studies, while T_{sub} is gradually increased from 330 ^{o}C up to 900 ^{o}C for each run.

Figure 3.6 shows three 5 μm $\times$ 5 μm AFM images of the sample surface after the H etching process at 330 (left), 500 (center), and 650 ^{o}C (right). The surface morphology after the lowest temperature is quite similar to the substrate before the H etching treatment, suggesting that the H etching causes no effect at

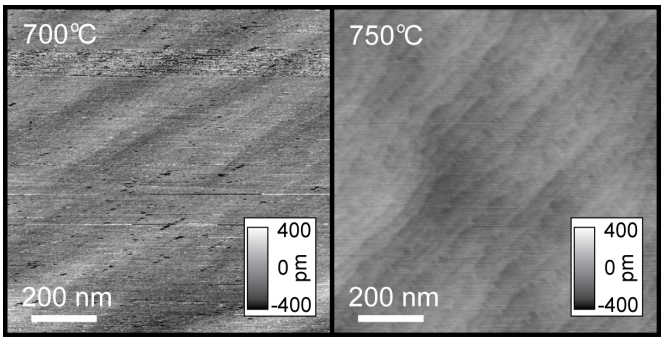


Figure 3.7: 1 μm $\times$ 1 μm AFM images of H-etched diamond surface at 700 (left) and 750 ^{o}C (right).

such a low temperature. On the other hand, grain features are observed at 500 ^{o}C, which become bigger at 650 ^{o}C making the surface rougher, suggesting that carbon atoms diffuse and migrate likely due to the hydrogen-assisted surface diffusion mechanism [92]. The larger size of the grain at a higher temperature suggests that the diffusion length of carbon adatoms increases as temperature is increased.

Figure 3.7 shows 1 μm $\times$ 1 μm AFM images of the surface at higher temperatures of 700 (left) and 750 ^{o}C (right). A drastic change of the surface morphology occurs between these temperatures. The surface displays clear line features at 750 ^{o}C whereas it is almost featureless at 700 ^{o}C. The line features run along the $\langle 110 \rangle$ directions (the diagonal direction in the image), which is consistent with the atomic step direction observed on the (100) diamond surface [84], suggesting that the atomic steps are created by the H etching process

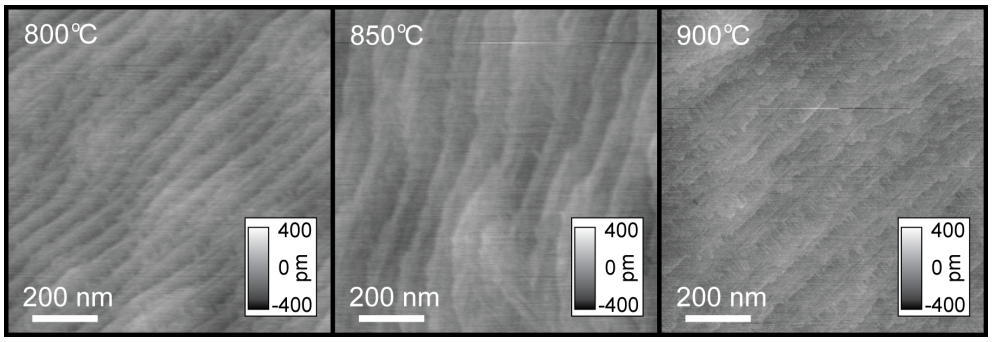


Figure 3.8: 1 μm $\times$ 1 μm AFM images of H-etched diamond surface at 800 (left), 850 (center), and 900 ^{o}C (right).

at a temperature higher than 750 ^{o}C.

Temperature is further increased up to 900 ^{o}C and Fig. 3.8 shows three 1 μm $\times$ 1 μm AFM surface images at 800 (left), 850 (center), and 900 ^{o}C (right). The line features are most clearly observed at 800 and 850 ^{o}C, while they are degraded and step features running in another direction perpendicular to the dominant directions appear at 900 ^{o}C, leading to a conclusion that the best temperature for preparing atomic steps using the H etching treatment is between 750 ^{o}C and 850 ^{o}C.

Next, a time dependence of the H etching effect is investigated. The temperature is fixed at 800 ^{o}C and the H etching time is varied for 5, 15, 30 and 60 minutes. The AFM images over 1 μm $\times$ 1 μm area after each process are shown in Fig. 3.9. Although the atomic step features are observed for the shortest process time of 5 minutes, grain features also remain, which disappear after

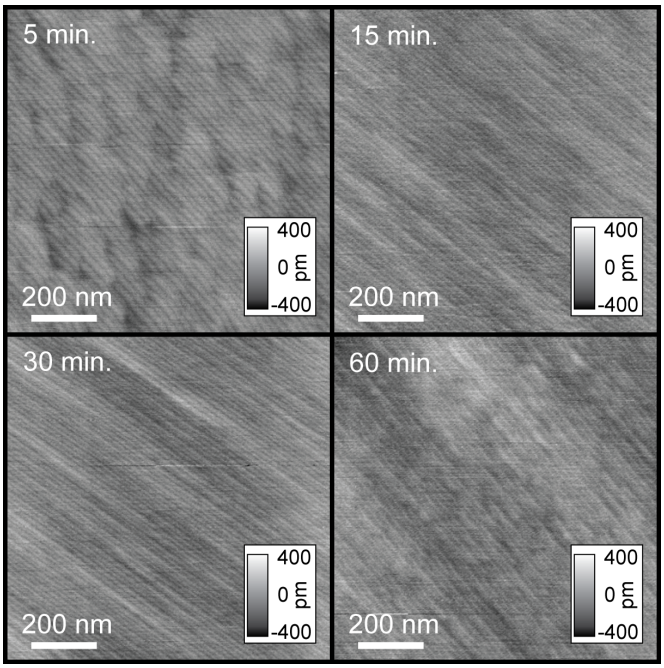


Figure 3.9: 1 μm $\times$ 1 μm AFM images of H-etched diamond surface for 5 (left top), 15 (right top), 30 (left bottom) and 60 min (right bottom).

15 minutes and clear atomic step features are observed at 15 minutes or longer. The atomic step features are somewhat degraded for 60 minutes, hence it is concluded that a 15 minutes of the H etching treatment is an optimized condition for preparing atomic steps.

3.5.2 Crystal growth of diamond with atomically flat surface

Figure 3.10(a) shows a 1 μm $\times$ 1 μm AFM image of the surface after an H etching process with optimized conditions, using a temperature of 800 ^{o}C, pressure of 25 Torr, H_2 flow of 400 sccm, and microwave power of 750 W for

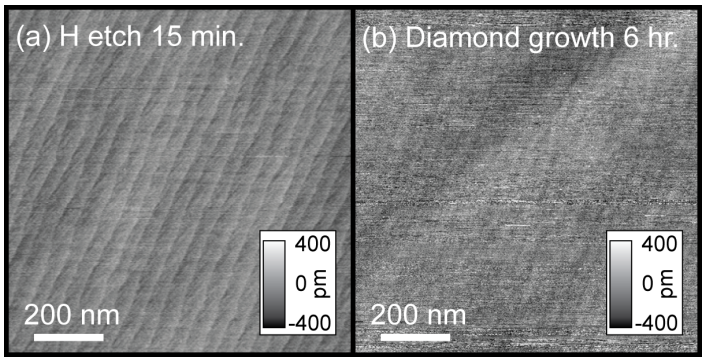


Figure 3.10: 1 μm $\times$ 1 μm AFM images of (a) H-etched diamond surface at 800 ^{o}C for 15 min. (b) After 6 hours of growth using a CH_4 concentration of 0.025 %. The same substrate is used for these experiments.

15 minutes. Clear atomic steps running along $\langle 110 \rangle$ direction is observed. The measured step height is $\sim$ 1 Å, consistent with the height of a single atomic layer.

A diamond thin film is grown using conditions of a temperature of 800 ^{o}C, pressure of 25 Torr, microwave power of 750 W, H_2 flow of 400 sccm, and CH_4 flow of 0.1 sccm (CH_4 concentration of 0.025 %) for 6 hours following an *in-situ* H etching process of 15 minutes. A 1 μm $\times$ 1 μm AFM image of the surface is shown in Fig. 3.10(b). An average of the mean roughnesses from three random points of the surface is computed to be $\sim$ 1 Å demonstrating that the grown film has an atomically flat surface. The direction and spacing of the atomic steps are similar to the H etched surface shown in Fig. 3.10(a), suggesting that the diamond film is grown by the step-flow mode starting from

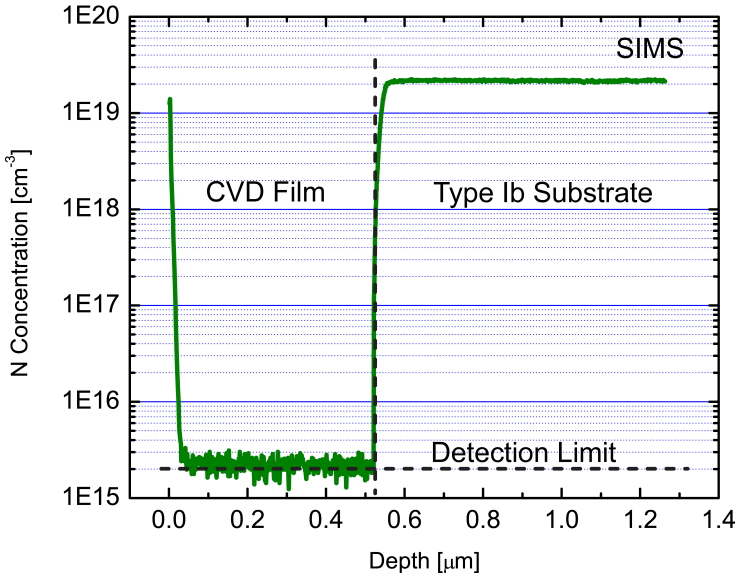


Figure 3.11: Secondary ion mass spectrometry (SIMS) ^{14}N profile of a PE-CVD film grown on top of a commercially available Type Ib (100) diamond substrate. The growth interface and the detection limit of the SIMS measurement are shown by vertical and horizontal dot lines, respectively.

the step edges prepared by the H etching pretreatment. A coincidence of the step spacing between Fig. 3.10(a) and 3.10(b) is because the same substrate is used for these experiments, as the step spacing depends on the miscut angle unique to the substrate.

3.6 Material properties of CVD-grown diamond film

3.6.1 Nitrogen impurity and growth rate

Secondary ion mass spectrometry (SIMS) measures nitrogen impurity concentration as a function of depth. Figure 3.11 shows a SIMS nitrogen (^{14}N) profile of a CVD-grown diamond film grown on top of a Type Ib diamond substrate. A clear increase of nitrogen concentration is observed at $\sim$ 520 nm corresponding to the interface between the substrate and the film. The nitrogen impurity level of the grown films is $\sim 2 \times 10^{15}$ cm^{-3} ($\sim$ 10 ppb), which is four orders of magnitude less than that of the substrate, reaching the detection limit of the measurement system. The result confirms the high-purity of the CVD-grown film.

The film shown in the figure is grown by four separate 6-hour growths using various CH_4 concentrations of 0.025, 0.05, 0.075 and 0.1 %. Assuming that the growth rate is proportional to the CH_4 concentration [72], the nominal growth rate for the 0.025 % CH_4 concentration is calculated to be 8.7 nm / hour.

The growth rate deviates from 5 to 13.4 nm/hour for other five samples grown at CH_4 concentration of 0.025 % computed by SIMS data of each sample. The origin of the growth rate deviation is unclear, but details of growth

conditions and substrate quality fluctuations may sensitively affect the growth rate. An average growth rate is computed to be 8.2 $\pm$ 3.2 nm/hour from these data, which is used hereafter as a calibrated growth rate for a CH_4 concentration of 0.025 %.

3.6.2 Surface termination

Chemical components and the form of atomic bonding near the surface are different from the bulk and hence the surface properties differ from the inherent properties of the material. Surface oxidized layer, termination, and reconstruction are the origins of unique surface phenomena of materials. Since electrical [87, 93, 94] and optical [95, 96] properties of diamond near the surface show different properties from the bulk, it is important to understand the diamond's surface chemistry.

X-ray photoelectron spectroscopy (XPS) is a useful technique to measure the chemical components and their bonding forms within top $\sim$ 10 nm or less from the surface. A material is irradiated by an Al $K\alpha$ x-ray (photon energy E_{photon} = 1486.7 eV) under a ultra high vacuum (UHV) condition, which ionizes and pulls out electrons from the material into the vacuum. The number of emitted electrons is measured as a function of their kinetic energy ($E_{kinetic}$), and because of the energy conservation law, the electron binding energy ($E_{binding}$)

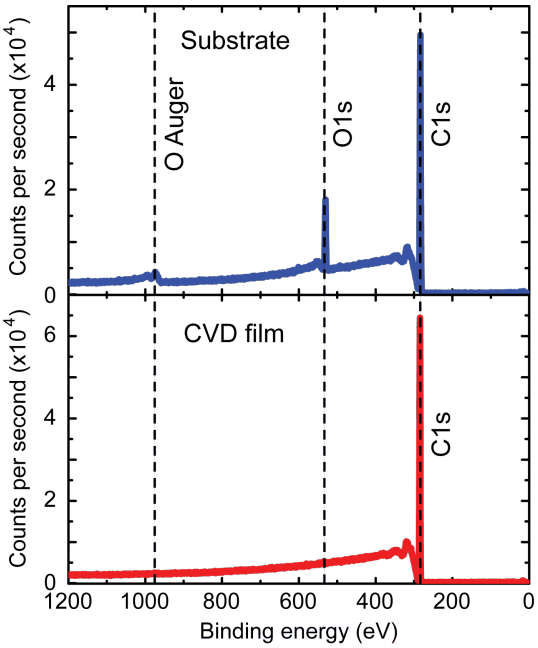


Figure 3.12: X-ray photoelectron spectra of a Type Ib diamond substrate (top) and a PE-CVD film (bottom). Peak positions corresponding to O Auger, O1s and C1s are shown as vertical dot lines.

can be measured as,

$$E_{binding} = E_{photon} - E_{kinetic}, \tag{3.6}$$

if the work function of the detector is aligned with the energy level of the material's surface. Since E_{photon} is known, $E_{binding}$ can be measured by measuring $E_{kinetic}$. In addition, since $E_{binding}$ is known for each chemical component and its bonding form, the atomic components and their chemical states are quantitatively measured.

The detection depth of the measurement is determined by the inelastic

mean free path (IMFP), which is the depth that photo-excited electrons are scattered off by the atoms before reaching to the surface. The IMFP depends on the photoelectron energy but it is less sensitive to the choice of the target materials, following the "universal curve" [97]. The sampling depth is typically 3 – 10 nm for the Al $K\alpha$ x-ray excitation, and therefore the XPS technique is sensitive to the surface. The surface sensitivity can be enhanced by tilting the sample in order to reduce the x-ray incident angle.

Figure 3.12 shows XPS spectra for a Type Ib (100) diamond substrate (top) and a CVD-grown film of $\sim$ 50 nm thick (bottom). The substrate shows three peaks at 284, 531, and 974 eV, corresponding to C1s, O1s, and O Auger peaks, respectively and suggesting that the surface of the diamond substrate is oxygen-terminated. The oxygen atoms terminate the surface carbon atoms rather than forming an oxidation layer [98, 99], which is a unique property of diamond unlike other common semiconductor materials such as Si and GaAs. On the other hand, the CVD film shows only C1s peak at 284 eV without displaying the oxygen-related peaks, suggesting that the surface of CVD films is hydrogen-terminated due to the dominant hydrogen plasma effect during the PE-CVD growth [100] (note that XPS measurements are insensitive to hydrogen atoms). It should be noted that the CVD-grown sample is left in the ambient condition for a week before taking the XPS data, suggesting that the hydrogen termination

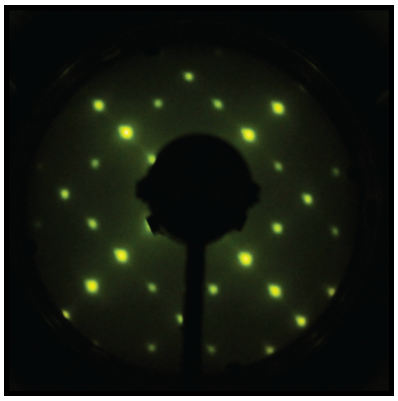


Figure 3.13: LEED pattern of the hydrogen-terminated, CVD-grown film at an acceleration voltage of 160 V. The dark feature at the center is the shade of the electron gun.

of the diamond surface is stable in air, which prevents the surface oxidation.

3.6.3 Surface reconstruction

The surface reconstruction of the hydrogen-terminated diamond is further investigated using a low-energy electron diffraction (LEED) technique. A hydrogen-terminated, CVD-grown film (the same sample used in the XPS measurement) is placed in a UHV chamber, while an electron beam accelerated at 30 – 200 eV is irradiated perpendicular to the sample surface. A diffraction pattern of the backscattered electrons is observed as spots on a phosphor screen. Since the electron beam at these acceleration voltages penetrates only a few nanometer from the surface, the LEED technique measures symmetry of the crystal structure of the surface.

Figure 3.13 shows a LEED pattern of the hydrogen-terminated, CVD-

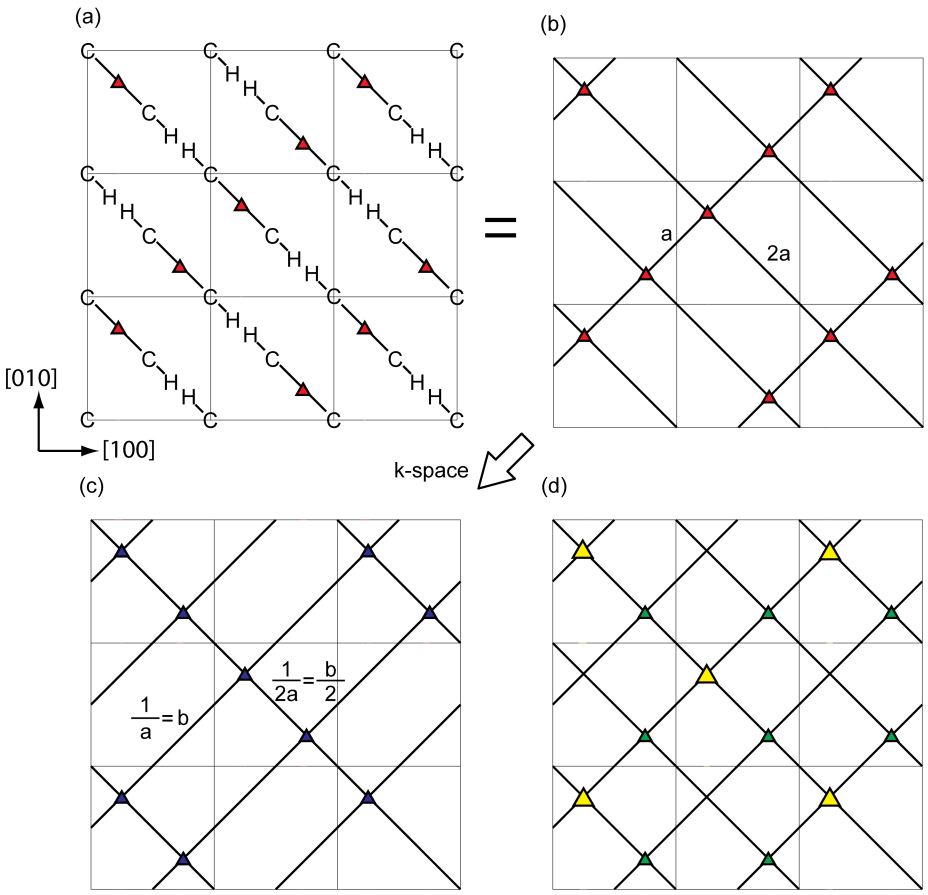


Figure 3.14: Interpretation of the LEED pattern. (a) Schematic of the hydrogen termination of the (100) diamond surface. Each square corresponds to a surface unit cell. Carbon and hydrogen atoms are represented by C and H. Lines connecting C's and H's represent atomic bonds. Note that each carbon atom on the (100) surface has two dangling bonds, one of them forms a bond with another nearest carbon atom and the other is terminated by a hydrogen atom. Red triangles represent the center of periodic units, which are extracted in (b). (b) Schematic showing a periodic structure of the hydrogen-terminated (100) surface. A unit of the period is a rectangle of $a \times 2a$, running parallel to the $\langle 110 \rangle$ directions. (c) k-space representation of the periodic structure shown in (b), showing a (1x2) pattern. Through two-dimensional Fourier transformation, the edge lengths of the periodic unit are transformed to $1/a = b$ and $1/2a = b/2$. (d) Interpretation of the LEED pattern shown in Fig. 3.13. The LEED pattern is constructed by a superposition of (c) and a 90-degree rotated pattern of (c) due to the orthogonal directions of carbon-carbon bonding in alternate atomic layers, and hence it displays a (1x2)/(2x1) pattern. Periodic points coincided in two orthogonal patterns are brighter (triangles in yellow) than those not (green), which is reproduced in the measured LEED pattern shown in Fig. 3.13.

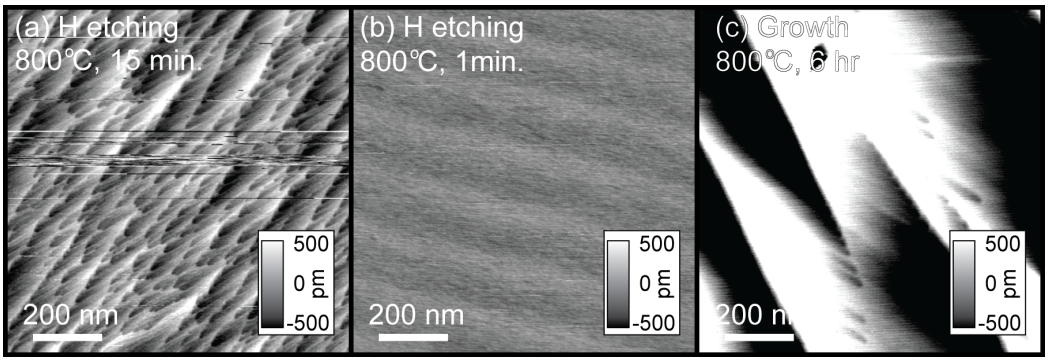


Figure 3.15: 1 μm $\times$ 1 μm AFM images of H-etched, (111) diamond substrate at 800 ^{o}C for 15 (a) and 1 min. (b). (c) After 6 hours of growth at 800 ^{o}C using a CH_4 concentration of 0.025 %.

grown film at an acceleration voltage of 160 V, displaying a (2x1)/(1x2) diffraction pattern. A (2x1) surface reconstruction suggests that one of two dangling bonds of a carbon atom on the top (100) plane is bonded to the nearest carbon atom, while the other dangling bond is terminated by a hydrogen atom as schematically shown in Fig. 3.14 [101]. Coexistence of (2x1) and (1x2) diffraction pattern is due to the direction of carbon-carbon bonding being orthogonal in alternate layers.

3.7 Diamond growth on (111) plane

PE-CVD films of diamond epitaxially grown on (111) substrates have some

advantages for the NV center applications as the NV center symmetry axis can align perpendicular to the surface. Magnetic or electric field induced at the NV center is increased for the (111) plane through a $\cos\theta$ term where $\theta = 54.7^{o}$ is the angle between $\langle 111 \rangle$ and $\langle 100 \rangle$ directions, which enhances NV-based magnetic sensitivity [102] and DC Stark effect of NV centers [103]. In addition, it is recently reported that growth-incorporated NV centers on the (111) plane have their symmetry axis exclusively perpendicular to the surface, allowing for an access to all NV centers in magnetic imaging measurements [104, 105].

The H etching effect on (111) substrates (*Sumitomo Electric Industries*, Type Ib, HPHT) is investigated using a temperature of 800 ^{o}C, microwave power of 750 W, pressure of 25 Torr, and H_2 flow of 400 sccm. A 1 μm $\times$ 1 μm AFM image of the sample (Fig. 3.15(a)) after the H etching treatment for 15 minutes reveals a rough surface of the (111) plane compared to (100) even though the conditions are identical, suggesting that an H plasma effect is stronger for the (111) plane due to an anisotropic H etching effect [88]. In order to mitigate the H plasma damage, the duration of the H etching treatment is reduced to 1 minute, resulting in periodic atomic-step features as shown in Fig. 3.15(b) similar to the (100) result (Fig. 3.10(a)). However, a 6-hour growth using identical conditions optimized for the (100) plane (CH_4 concentration of 0.025 %) following a 1-minute H etching pretreatment results in a completely

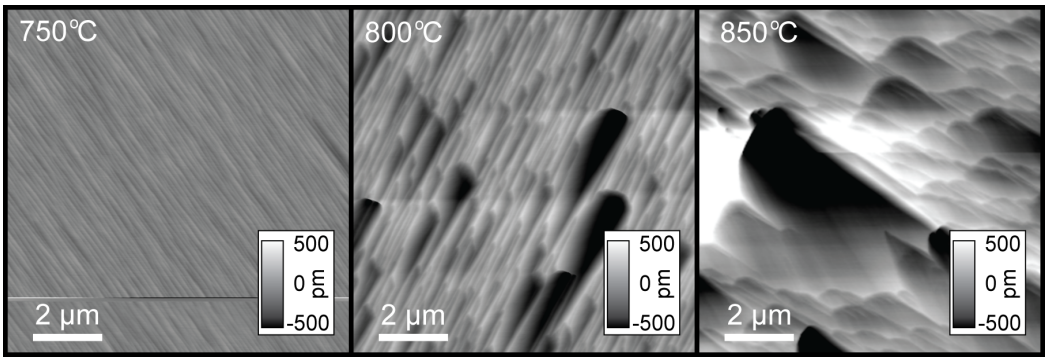


Figure 3.16: 10 μm $\times$ 10 μm AFM images of (111) diamond film grown at 750 (left), 800 (center) and 850 ^{o}C (right) using a CH_4 concentration of 0.015 %.

different surface morphology from the (100) growth result, displaying much rough surface as shown in Fig. 3.15(c). The result suggests that the H etching effect is stronger on the (111) plane, requiring to re-optimize growth conditions to balance the H etching effect and diamond growth specific to this growth plane.

A growth temperature dependence of surface morphology is studied at 750, 800 and 850 ^{o}C with a reduced CH_4 concentration of 0.015 %. Each growth is run for 6 hours following an *in-situ* H etching pretreatment (1 minute) under the same temperature as for each growth. Figure 3.16 shows 10 μm $\times$ 10 μm AFM images for the samples grown at 750 (left), 800 (center) and 850 ^{o}C (right), respectively. The surface of the 850 ^{o}C sample is rough displaying "spoon-cut" features, also observed at 800 ^{o}C whereas they disappear at 750 ^{o}C.

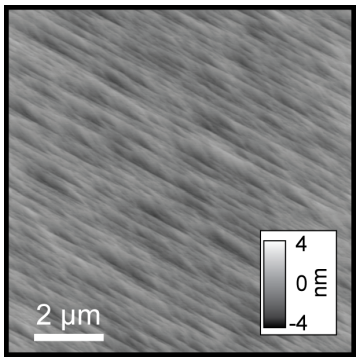


Figure 3.17: 10 μm $\times$ 10 μm AFM image of (111) diamond film grown using a microwave power of 1200 W, pressure of 50 Torr, and CH_4 concentration of 0.025 %. The power of microwave heats substrate temperature (T_{sub}) up to 505 ^{o}C without RF heating.

The surface of the 750 ^{o}C sample is covered with periodic line features, however, their step height is larger than a single atomic step, necessitating a further optimization.

Tokuda *et al*., investigated step-flow growth conditions for (111) diamond films using a microwave power of 1200 W, pressure of 50 Torr, temperature of around 900 ^{o}C, and CH_4 concentration of 0.025 % [106]. They demonstrated an atomically flat surface by suppressing 2D nucleation using a low CH_4 concentration and choosing dislocation-free areas on a lithographically patterned 10 μm $\times$ 10 μm mesa on a Type Ib HPHT substrate, which has a miscut angle of 1.5^{o}.

Inspired by this result, a (111) sample is grown using a microwave power of 1200 W, pressure of 50 Torr, and CH_4 concentration of 0.025 %. These con-

ditions result in a T_{sub} = 505 ^{o}C without RF stage heating due to the power of microwave. An AFM image reveals periodic line features on the surface (Fig. 3.17) although their height is much larger than single- or double- atomic steps. A growth temperature could be increased by active RF stage heating, which could result in a different surface morphology. However, an active heating along with a high power microwave raises concerns about heat damage to the growth system and therefore, the temperature dependence cannot be further investigated. More careful considerations about miscut angle and dislocation densities of substrates may also be required.

With preliminary results, it is concluded that diamond growth on the (111) plane is more difficult than on the (100) plane due to a strong anisotropic H etching effect. It still remains unclear whether CH_4 concentration should be increased to compensate the H etching effect or it should be decreased to etch off irregular nucleation. Careful considerations about the substrate miscut angle and dislocation density are also necessary to achieve an atomically flat surface on the (111) plane.

3.8 Increasing growth rate using high microwave power

3.8.1 Increasing growth rate

The growth mode using an extremely low CH_4 concentration (denoted as the "low-power" growth mode hereafter) results in high-quality diamond films demonstrating a low nitrogen impurity concentration and an atomically flat surface, as described in Section 3.5 and 3.6. However, this growth mode results in a very slow growth rate less than 10 nm per hour, limiting the film thickness of CVD-grown films to a few hundreds of nanometers with a reasonable growth time. Since depth resolution of confocal microscope measurements is a few micrometers, micrometer-thick films are required in order to optically differentiate NV centers in the CVD-film from ones originated in the substrate, necessitating an increased growth rate up to micrometers per hour.

The growth rate of a diamond film is increased generally in proportional to the CH_4 concentration [72, 107]. As increasing the CH_4 concentration, microwave power should be increased simultaneously in order to activate sufficient amount of atomic hydrogen in the plasma for etching off unfavorable growth sites nucleating non-epitaxial crystallines and pyramidal hillocks.

Tallaire, Achard *et al*., systematically investigated diamond homoepitaxy

with a growth rate of micrometers per hour using microwave power of 3200 W, CH_4 concentration of 4 %, pressure of 220 mbar (165 Torr), growth temperature of 850 ^oC, and total gas flow of 500 sccm [108, 109]. With the optimized growth conditions, they observed macroscopically smooth surface without observing defect-related peaks in low-temperature PL measurements, while growth rate is increased up to 6 μm/hr. They also demonstrated that the growth rate can be increased up to $\sim$ 16 μm/hr by either using a higher CH_4 concentration of 7.2 %, or adding a small amount of nitrogen $\sim$ 10 ppm [110].

3.8.2 Growth system and procedure

In order to provide sufficient microwave power for a high growth rate, microwave generator of the system is replaced to the one capable of generating up to 6 kW (Astex FI20111, "high power microwave head", Fig.3.18). Since the increased power of microwave significantly heats up the sample stage, the RF heater stage is replaced to a water-cooled, stainless steel stage. The growth temperature can be controlled by changing the thermal coupling between the cooling stage and the Mo sample holder by inserting copper shims in between. However, all the samples presented in this dissertation are grown with a direct contact of the sample holder to the cooling stage, and hence the growth temperature is not an independent parameter, depending on the microwave power.

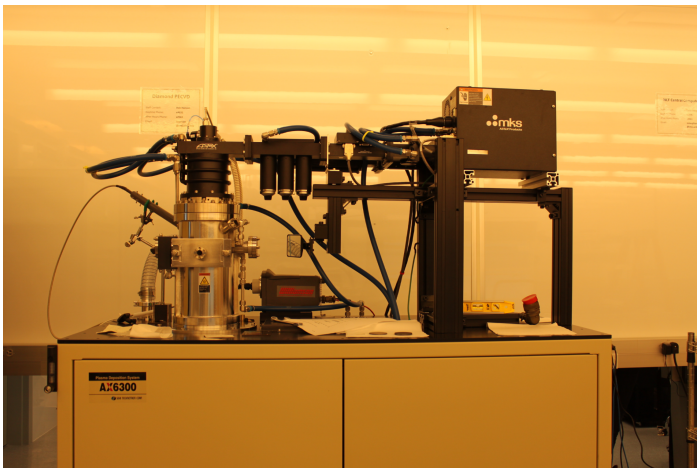


Figure 3.18: Picture of the "high power" microwave head.

These system modifications can easily go back and forth, allowing for switching between the "low-power" and "high-power" growth as necessary.

Inspired by previous works of Tallaire *et al.*, [108, 109] a microwave power dependence of surface morphology is investigated for CH_4 concentrations of 4 and 7 %, while other growth parameters are fixed using pressure of 165 Torr, total gas flow (H_2 + CH_4) of 500 sccm and growth time of 6 hours. All the samples are grown on Type Ib (100) diamond substrates (from *Sumitomo Electric Industries*). While pressure and microwave power are ramped up before starting growth, a 10 sccm flow of O_2 gas is added while H_2 flow is kept at 490 sccm. This H_2-O_2 plasma pretreatment is known to help increasing the surface quality during the high power growth [111]. When the pressure and microwave power becomes stable, the diamond growth is immediately started

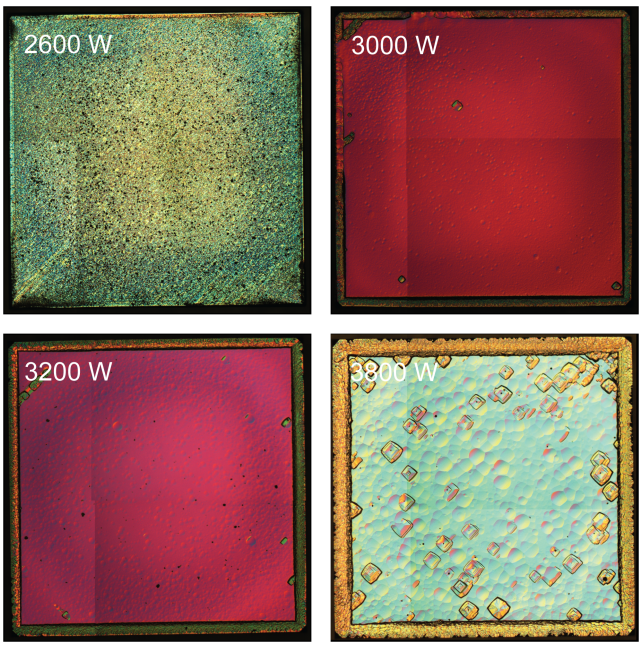


Figure 3.19: Differential interference contrast microscope (DICM) images of sample surface grown by the "high-power" growth mode using microwave powers of 2600, 3000, 3200, and 3800 W (from left top to right bottom) and a fixed CH_4 concentration of 4 %. Different colors of the surface are due to various angles of the polarizer, which is unrelated to the growth results.

by adding CH_4 gas at the calculated flow, while O_2 gas is cut off and H_2 flow is adjusted for a target CH_4 concentration under a fixed total gas flow of 500 sccm.

3.8.3 Growth results

Four samples are grown at a CH_4 concentration of 4 % using various microwave powers of 2600, 3000, 3200, and 3800 W, and their surface is characterized by a differential interference contrast microscope (DICM) as shown in

Fig. 3.19. The read of pyrometer temperature during growth are 890, 880, 970, and 1070 ^{o}C, respectively (note that the pyrometer readings are not reproducible as discussed in Section 3.4). At 2600 W, the entire surface is covered by etch pits caused by decrease in surface reaction rates due to relatively low growth temperature [108, 112]. The surface is smooth without non-epitaxial crystallites and pyramidal hillocks at 3000 and 3200 W, while a higher microwave power of 3800 W results in a surface covered with a number of pyramidal defects originated from surface point defects [108], suggesting that an optimized microwave power is either 3000 or 3200 W.

A growth rate using a microwave power of 3200W and CH_4 concentration of 4 % is measured by SIMS. The sample is grown on a Type Ib substrate and a clear interface between the film and the substrate is seen in the SIMS result shown in Fig. 3.20. The growth rate is calculated to be 1.8 μm/hr by dividing the film thickness of 10.6 μm with a growth time of 6 hours, which is about 200 times lager growth rate than grown by an extremely low CH_4 concentration (Fig. 3.11). The nitrogen impurity level of the CVD film is $\sim 4 \times 10^{15}$ cm^{-3}, or 20 ppb, which is slightly higher than the "low power" growth mode, suggesting that nitrogen atoms may more easily be incorporated into the diamond film with a larger growth rate.

In order to aim for even higher growth rates, CH_4 concentration is in-

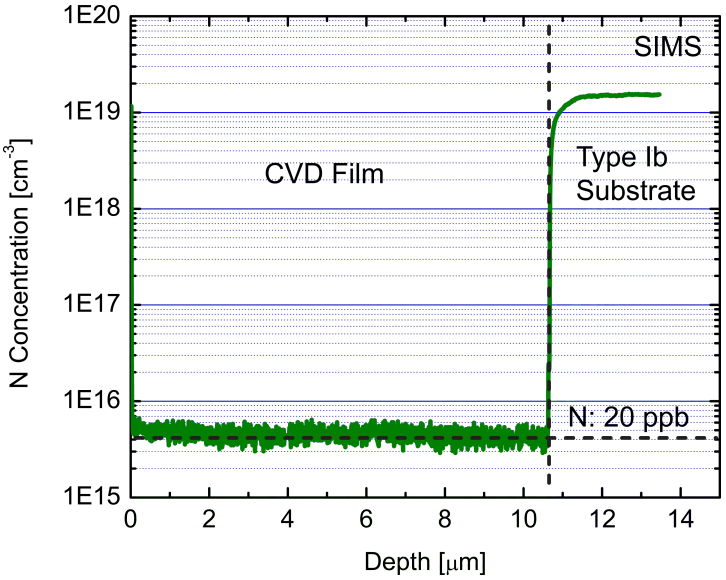


Figure 3.20: SIMS ^{14}N profile of a PE-CVD film grown using a microwave power of 3200 W and CH_4 concentration of 4 % on top of a commercially available Type Ib (100) diamond substrate. The interface between the film and the substrate is shown by a vertical and dot line. The nitrogen impurity level of the film is $\sim$ 20 ppb, as shown in a horizontal dot line.

creased to 7 %. DICM images are taken from the samples grown for 6 hours at various microwave powers of 3000, 3800, 4400, and 5000 W (Fig. 3.21). All samples show macro-bunching structures on the surface, suggesting step-flow growth is a dominant growth mode. At 3000 W, the bunching structures run in parallel lines on most of the surface while at some places they run along the edges of pyramidal hillocks. As increasing the microwave power, the bunching structure results in vortices rather than lines, which is apparent in results above 4400 W. The bunching structures are caused by nitrogen impurities in the substrate, which block the advancement of steps [108]. Pyramidal hillocks

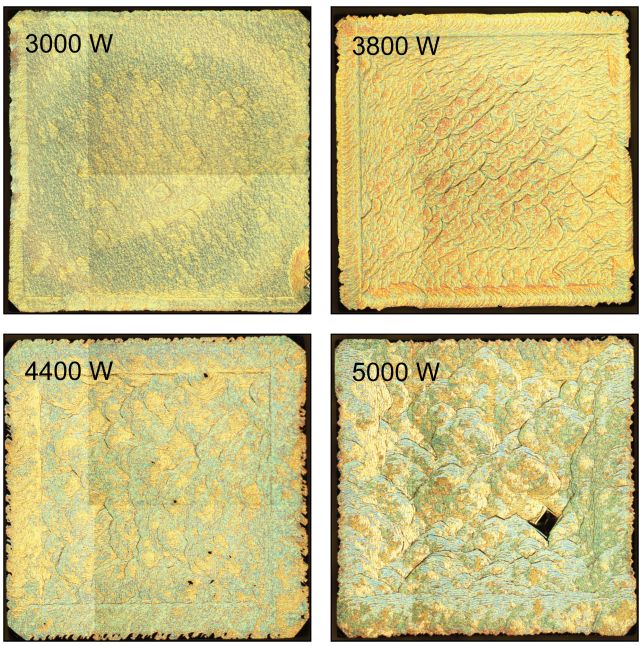


Figure 3.21: DICM images of sample surface grown using various microwave powers of 3000, 3800, 4400, and 5000 W (from left top to right bottom) with a fixed CH_4 concentration of 7 %.

and vortex structures are likely nucleated from substrate dislocations, requiring better control of the substrate quality for a further improvement of the surface morphology.

3.8.4 Growth-incorporated NV centers: possibilities

Finally, possibilities of growth-incorporated NV centers are discussed. Tallaire *et al*, demonstrated that an addition of N_2 gas between 2 to 10 ppm (relative to the total gas flow) during diamond growth (microwave power: 3200 W and CH_4 concentration: 4 %) results in observation of PL peaks at 575 nm and 637

nm corresponding to zero phonon lines of NV^0 and NV^- states [110]. The peak intensities become larger as the nitrogen flow is increased, suggesting that the density of NV centers in the crystal is related to the nitrogen doping amount in the gas phase. In these films, vacancies are likely created by either inherent point defects due to a high growth rate (greater than a micrometer per hour) or high-power plasma damage. Although their growth rate is too large to control film thickness at a nanometer scale using the "high-power" growth mode, these results suggest that it is possible to "dope" NV centers in the diamond crystal during the growth. In the next chapter, a growth technique is presented that constrains the depth of the nitrogen doped layer in the film, which enables to control depth of NV centers at a nanometer scale.

3.9 Conclusion

In this chapter, PE-CVD growth of high-quality, single crystal diamond is studied. Thermodynamics background and a growth theory for the step-flow growth are presented. Details about the growth system and sample preparation processes are also discussed.

The step-flow growth is a key to achieve an atomically flat surface. An *in-situ* H etching treatment prior to the growth is important to prepare atomic steps providing nucleation sites for carbon adatoms. It is shown that the H etching

effect is very sensitive to the temperature, and that the atomic steps are observed only when temperature is ≥ 750 ^{o}C, while the surface becomes rougher as increasing the temperature ≤ 700 ^{o}C.

Optimized growth conditions for (100)-plane, PE-CVD films using a temperature of 800 ^{o}C, microwave power of 750 W, pressure of 25 Torr, H_2 flow of 400 sccm and CH_4 flow of 0.1 sccm (CH_4 concentration of 0.025 %) result in a high purity crystal with an atomically flat surface. These growth conditions lead to a slow growth rate of 8.2 ± 3.2 nm/hr due to a strong H etching effect by using an extremely low CH_4 concentration. Surface characterization techniques such as XPS and LEED reveal that the surface of a CVD-grown film is hydrogen terminated, which is stable in the ambient condition.

Crystal growth conditions on (111) substrates are different from the optimized conditions for (100) substrates due to the anisotropic H etching effect. Further control of miscut angle and dislocation density of substrates are required for an atomically flat surface.

Growth rates of (100)-plane films are significantly increased by using a higher CH_4 concentration and a high power microwave. The "High-power" growth conditions using a CH_4 concentration of 4 %, microwave power of 3000 or 3200 W, pressure of 165 Torr and total gas flow of 500 sccm result in smooth surfaces without non-epitaxial crystallites and pyramidal hillocks. Further en-

hancement of growth rate would be expected by increased CH_4 concentration, although more considerations about dislocation density and impurities of substrates are required.

Growth insights on the bulk, pure materials are very important to develop advanced crystal growth techniques, including doping techniques and creating layered structures. A nanometer-scale growth rate of the "low-power" growth mode would enable controlling thickness of layers in a diamond film at a nanometer scale. A very low nitrogen impurity background in the CVD-grown film would allow for doping nitrogen at the controlled depth in the film. In the next chapter, a nitrogen doping technique is explored that enables to control depth of NV centers at nanometer scale while preserving their spin coherence.

Chapter 4

The nitrogen delta-doping technique

4.1 Introduction

External spin sensing is one of the most important challenges of the NV center-based metrologies, enabling many applications such as hybrid quantum architectures [113] and, most importantly, nanometer-scale magnetic sensing/imaging [39, 40, 42, 114]. A critical challenge to realize the external spin sensing is to create NV centers close to the surface while maintaining their spin coherence, in order to enable reasonable magnetic coupling between a target external spin and the probe NV center spin. In this chapter, a technique based on the crystal growth – the nitrogen delta-doping technique – is presented as a method to engineer shallow spins. Challenges for creating surface-proximal spins are

described in Section 4.2. The concept of the nitrogen delta-doping is presented in Section 4.3. Section 4.4 describes sample preparation process including details of the doping process. Measurement setup is described in Section 4.5 and isotopic identification of doped NV centers are discussed in Section 4.6. Experimental and analytical results showing nanometer-scale confinement of doped NV centers are presented in Section 4.7. Spin coherence properties of shallow NV centers are discussed in Section 4.8. Potentials of doped NV centers for external spin sensing is presented in Section 4.9, and finally, Section 4.10 presents conclusion and outlook.

4.2 Challenges

4.2.1 Magnetic dipole coupling

The magnetic dipole-dipole coupling between an external target spin and the probe NV center electronic spin is described by a following Hamiltonian,

$$H_{dip} = \frac{\mu_0 g g_{ext} \mu_B \mu_{ext}}{4\pi r^3} \left[\hat{S}_{NV}\hat{S}_{ext} - 3(\hat{S}_{NV}\cdot\hat{r})(\hat{S}_{ext}\cdot\hat{r})\right], \tag{4.1}$$

where μ_0 is the vacuum permeability, g (g_{ext}) is the electronic (target spin's) g-factor, μ_B (μ_{ext}) is the Bohr (target spin's) magneton, $\hat{S}_{NV}$ ($\hat{S}_{ext}$) is the spin operator of the NV center (target), r is the distance between the target and the NV center, and $\hat{r}$ is the unit vector connecting them [54, 115]. The terms in

the brackets define the angular dependence and the prefactor determines the strength of the dipole coupling. Figure 4.1(a) plots the prefactor of the dipole coupling (in the units of Hz) as a function of the target-NV distance r, using the following equations for an electron spin (black curve) and a proton (red curve) spin detection, respectively,

$$f_{electron} = \frac{\mu_0 g^2 \mu_B^2}{4\pi h r^3}, \tag{4.2}$$

$$f_{proton} = \frac{\mu_0 g g_p \mu_B \mu_p}{4\pi h r^3}, \tag{4.3}$$

where h is the Planck's constant, g_p = 5.59 is the proton g-factor, and $\mu_p = 1.41 \times 10^{-26}$J/T is the proton magnetic moment. Note that the proton magnetic moment is about 660 times smaller than the Bohr magneton, $\mu_B = 9.27 \times 10^{-24}$J/T, leading to the dipole coupling strength with a proton spin about 3 orders of magnitude smaller than that with an electron spin. For example, the dipole coupling prefactor is 6.5 MHz and 28 kHz for an electron and a proton spin, respectively, at a distance r = 2 nm. Figure 4.1(b) plots $1/f_{electron}$ (black curve) and $1/f_{proton}$ (red curve) as a function of the target-NV distance r, which are equivalent to the spin coherence times (in the units of μs) required for an NV center to detect an electron and a proton spin. These plots summarize the engineering challenges for the external spin sensing, which requires to create

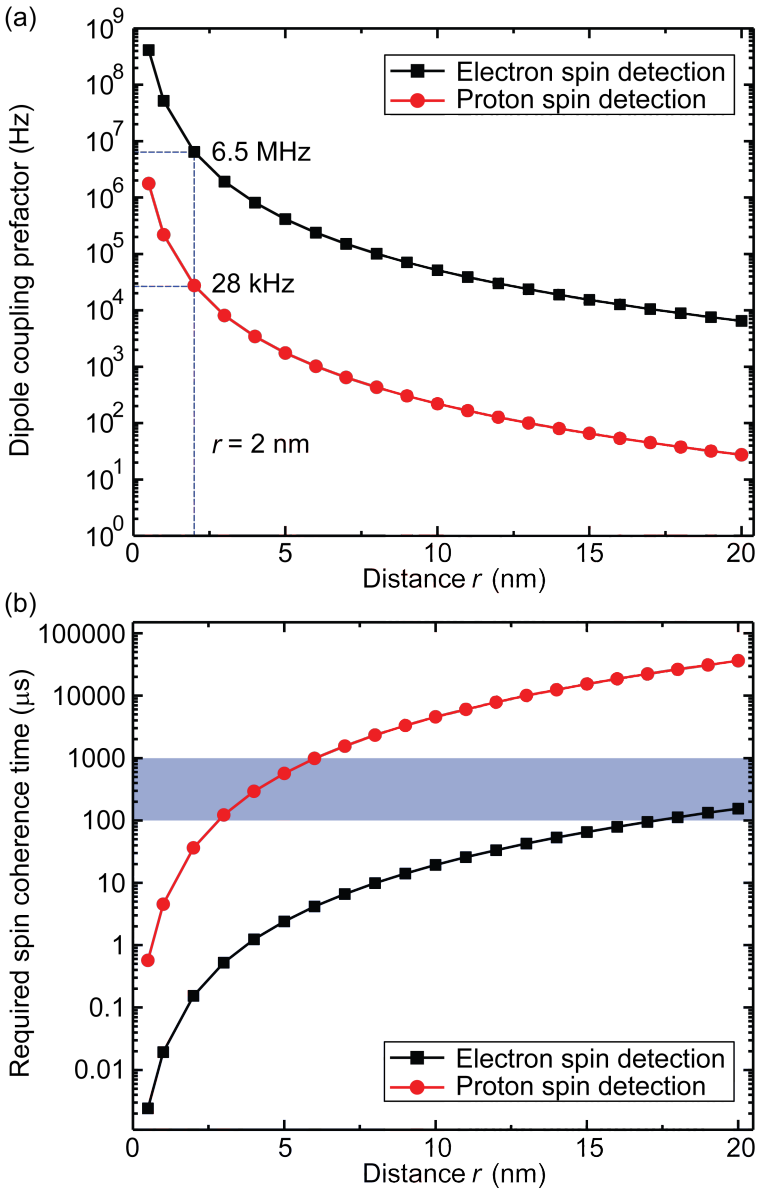


Figure 4.1: (a) Dipole coupling prefactor (in the unit of Hz) and (b) required spin coherence times (in the unit of μs) as a function of target-NV center distance for a single electron (black curve) and proton (red) spin detection. Spin coherence time on the order of 100 μs is shown in blue belt to emphasize the engineering target.

NV centers shallower than 20 nm (ideally 5 nm for a proton spin detection) from the surface while maintaining their spin coherence times on the order of hundreds of microseconds (blue belt in Fig. 4.1(b)). Moreover, since the dipole coupling decays with distance r by $1/r^3$, nanometer-scale depth control of shallow NV centers is also critically important.

It was demonstrated that a single NV center in an isotopically engineered diamond material displayed a long spin coherence time T_2 as long as 1.8 ms [26]. However, the measured NV center was in the bulk and the density of such NV centers was extremely low, necessitating an engineered way to create shallow NV centers.

4.2.2 Shallow NV center creation

A common way to create shallow NV center is to utilize a nitrogen ion implantation technique, which accelerates nitrogen ions and bombard them to a diamond crystal [32, 33, 34]. The nitrogen implantation process creates both nitrogen and vacancies at the same time, and vacancies diffuse to form NV centers during a subsequent annealing process. As the nitrogen diffusion length in diamond is low [116], the mean depth of NV centers can be tuned by an implantation energy. For example, an energy of 6 keV results in the calculated average NV center depth of 10 nm [45], and a use of very low energy of 0.4 keV cre-

ates NV centers at a predicted depth of as shallow as 1.1 nm [117]. However, the measured NV center depth dispersion was usually wider than the expected values from SRIM calculations [118] due to the ion channeling and straggling effects [33]. As an example, the measured NV center depth dispersion is wider than $\pm$10 nm at a 6 keV acceleration energy, much larger than the calculated value of $\pm$3 nm [45]. The depth dispersion would be diminished by reducing the acceleration energy, but the predictable depth control at nanometer-scale is necessary as the magnetic dipole coupling is very sensitive to the depth of NV centers.

Moreover, NV centers created by the nitrogen ion implantation show widely dispersed and usually short spin coherence times T_2, due to non-uniform crystal damage caused by the ion impact [33, 34]. For example, some of the implanted NV centers showed $T_2 > 50$ μs while up to 40 % of measured NV centers resulted in $T_2 < 10$ μs in Ref. [34]. For efficient external spin sensing measurements, creation of NV centers with reproducibly long T_2 is important.

Encouragingly, a growth-incorporated NV centers with millisecond T_2 was located within a top 100 nm layer of a diamond crystal, although the depth dispersion was too large for the target external spin sensing applications [119].

As discussed above, creation of shallow and depth-controlled NV centers with maintained spin coherence remains an outstanding challenge.

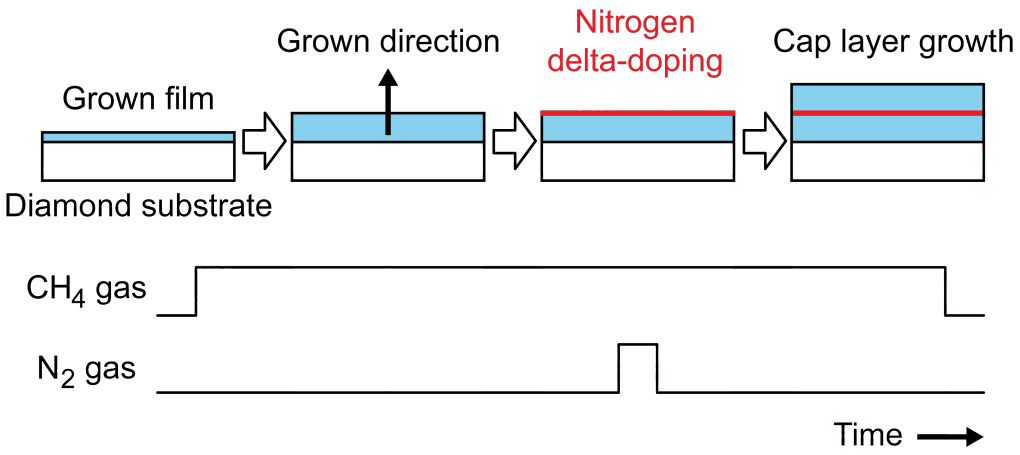


Figure 4.2: Schematic of crystal structure of a nitrogen delta-doped sample (top) and growth sequence showing a timing chart of the source gas introduction (bottom). The time is not to scale.

4.3 Concept of the nitrogen delta-doping

The nitrogen delta-doping technique is a method to create NV centers by using an *in-situ* nitrogen doping during crystal growth of diamond [120]. Figure 4.2 shows a crystal structure of the nitrogen delta-doped sample and a growth sequence showing a timing chart of the source gas introduction. During the diamond growth, N_2 gas is briefly introduced to the growth chamber whose gas flow and timing is controlled by a mass flow controller (MFC). The thickness of the nitrogen doped layer is determined by duration of N_2 gas introduction while the depth of the nitrogen doped layer is defined by the thickness of a subsequently grown cap layer. For nanometer-scale depth control of NV centers,

the growth rate is reduced down to $\sim$0.1 nm/min.

Vacancies are created separately in the post growth process, and they diffuse to form NV centers during a subsequent annealing process. Specifically, an electron irradiation technique is used for the post growth vacancy creation as it causes far less damage compared to the ion implantation, maintaining the high crystal quality of the PECVD-grown diamond film.

The *in-situ* nitrogen doping, reduced growth rate, and the post growth vacancy creation are the key components of the nitrogen delta-doping technique, which provide both nanometer-scale depth control as well as long and reproducible spin coherence times of engineered NV centers, as discussed in the following sections.

4.4 Sample preparation

4.4.1 Crystal growth conditions

All the diamond samples are grown by the plasma-enhanced chemical vapor deposition (PE-CVD) system, using a growth temperature of 800 ^{o}C, microwave power of 750 W, pressure of 25 Torr, H_2 flow of 400 sccm, and $^{12}CH_4$ gas flow of 0.1 sccm, on top of a commercially available, electronic grade (100) diamond substrate from *Element 6* [84]. Prior to the growth, all the substrates are mechanically polished by *Syntek*. These growth parameters

result in a growth rate of 8.2 $\pm$ 3.2 nm/hr calibrated by secondary ion mass spectrometry (SIMS) measurements. The extremely slow growth rate enables to control depth of the nitrogen doped layer at nanometer scale. Isotopically purified $^{12}CH_4$ (99.999 %) source gas (from *Cambridge Isotope Laboratories*) is used in order to deplete ^{13}C nuclear spins in the film, which are know to be a spin decoherence source for NV centers [26].

4.4.2 Nitrogen doping

To dope nitrogen, $^{15}N_2$ gas (10 – 30 sccm) is simply added while keeping all other growth parameters as the same. Nitrogen is typically doped for 10 to 15 minutes during the growth, which forms a nitrogen doped layer of 1-2 nm thick. Isotopically purified $^{15}N_2$ ($>$ 98 %, also from *Cambridge Isotope Laboratories*) is used in order to discriminate NV centers in the nitrogen doped layer from those in the substrate, which will be discussed in Section 4.6.

The nitrogen dopant concentration is estimated by a ^{14}N SIMS profile of a sample containing four nitrogen-doped layers. Each layer is doped with naturally abundant N_2 gas (^{14}N = 99.6 %) for 1 hour using various doping gas flow of 50, 20, 10 and 5 sccm (from bottom to top). Each nitrogen doped layer is separated by pure diamond layers grown for 2 hours, and the entire structure is grown on top of a Type Ib (100) diamond substrate. Three peaks are identi-

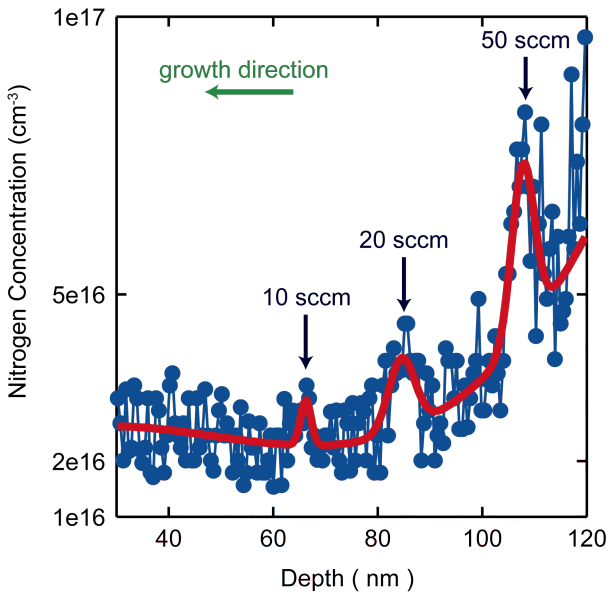


Figure 4.3: ^{14}N SIMS profile of a stack of nitrogen doped layers. The doping N_2 gas flow is varied for 50, 20, 10, and 5 sccm in each layer from bottom to top as indicated by a green arrow showing the growth direction. The red curve is a three Gaussian fit on top of a cubic polynomial to account for the background fluctuations. The nitrogen concentration in the 5 sccm layer is below the noise floor of the measurement. Original data presented in Ref. [120]

fied in the SIMS profile shown in Fig. 4.3, which are attributed to the nitrogen doped layers with 50, 20, and 10 sccm flow, respectively, based on the estimated depth of each layer. A fit to these peaks suggests that the nitrogen dopant concentration increases monotonically with the doping gas flow: $(0.8 \pm 0.6) \times 10^{16}$ cm^{-3}, $(1.3 \pm 0.3) \times 10^{16}$ cm^{-3}, and $(3.1 \pm 0.3) \times 10^{16}$ cm^{-3} for 10, 20 and 50 sccm, respectively. The nitrogen dopant level for the 5 sccm doping gas flow is below the noise floor of the SIMS profile, which is 0.6×10^{16} cm^{-3}.

Given a relatively large N_2/CH_4 gas flow ratio, the nitrogen incorporation

to the diamond crystal is very limited. The insufficient N_2 activation in the plasma state due to relatively low microwave power may account for this low nitrogen incorporation, or the strong hydrogen etching effect may remove nitrogen adatoms before they are incorporated into diamond crystal. Contrary to other reports using high microwave power [110, 121, 122], nitrogen doping does not increase the growth rate, enabling to control the nitrogen doped layer thickness at nanometer scale, which supports the speculation that the hydrogen etching effect may be dominant in the low microwave power growth mode used during the nitrogen delta-doping technique.

4.4.3 Post growth vacancy creation process

After the growth, sample is subject to an electron irradiation process for vacancy creation using an acceleration energy of 2 MeV and a dose of 10^{14} cm^{-2} at the NEO beam facility in Kent State University. The vacancies diffuse to form NV centers during a subsequent annealing process using a quartz tube furnace at 850 ^{o}C for 2 hours in a H_2/Ar forming gas atmosphere. Note that the high energy electron beam penetrates the diamond crystal creating vacancies also in the substrate forming background NV centers, requiring to discriminate NV centers in the nitrogen doped layer from substrate NV centers, which is discussed in Section 4.6.

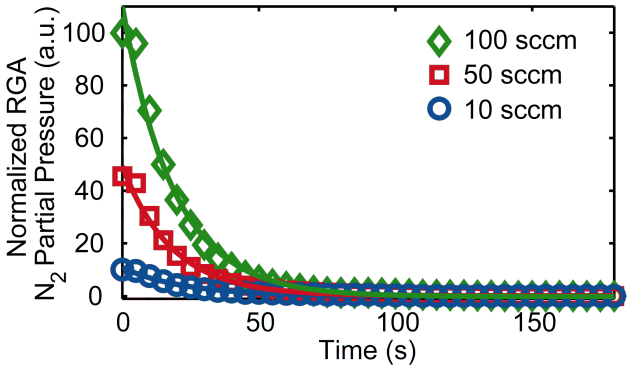


Figure 4.4: Residual gas analysis (RGA) of the nitrogen partial pressure of the growth chamber after shutting off the N_2 gas of 100 (green), 50 (red), and 10 (blue) sccm flows. Each data are fitted by a single exponential decay shown as lines of each color. Original data presented in Ref. [120]

After the annealing process, the sample is cleaned using a perchloric acid mixture ($HClO_4$: H_2SO_4: HNO_3 = 10 mL : 10 mL : 10 mL, at 200 ^oC for 30 min.) in order to remove a graphitic layer, as well as to oxidize the surface for promoting the negatively charged state of the NV centers [95, 96].

4.4.4 Residual gas analysis

The sharpness of the nitrogen doped layer interface is a key for the nanometer-scale depth confinement of NV centers. It is generally believed that the molecular beam epitaxy (MBE) technique allows for abrupt interfaces using ultra high vacuum and mechanical shutters to alternate the source, compared to the chemical vapor deposition (CVD) technique, which requires a transition time to wash out the prior gas after switching source gases. Although the di-

amond growth is based on the CVD technique, the situation is different as the growth rate is extremely low.

A residual gas analysis (RGA) is performed to estimate the sharpness of the nitrogen doped layer. The chamber gas condition is kept consistent with the growth conditions (pressure of 25 Torr and H_2 flow of 400 sccm), and N_2 gas is added with various gas flow of 10, 50 and 100 sccm. The nitrogen partial pressure after cutting off the N_2 flow is monitored using an RGA probe inserted into the growth chamber through a port. Figure 4.4 shows decay curves of the nitrogen partial pressure with various N_2 flows. The lines in the figure show fits to the data, resulting in a decay time constant of 19.8 ± 1.7 sec consistent across the three different nitrogen gas flows. This transition time defines the thickness of a transient layer, the sharpness of the nitrogen doped layer interfaces. Given the growth rate of 8.2 ± 3.2 nm/hr, the thickness of the interfacial layer is estimated to be < 0.5 Å, which is less than one monolayer thickness of the diamond lattice.

4.5 Measurement setup

Spin properties of NV centers originated in the nitrogen doped layer are measured using a home-build confocal microscope setup. This section describes the measurement setup used in this dissertation [10, 123, 124, 125]. All mea-

surements are performed in the ambient conditions.

4.5.1 Optical setup

Figure 4.5 schematically shows the optical measurement setup. A continuous wave (CW), monolithic diode-pumped solid-state (DPSS) laser from *Oxxius* (SLIM-532S-150-COL-OE) is used for an excitation laser source. The wavelength of the laser is 532 ± 1 nm (green) and the output power is 150 mW. The laser excitation power to the sample can be changed by an attenuator in front of the laser.

An acousto-optic modulator (AOM; *Isomet* 1250C) is inserted in the laser path at the focal point of a lens pair. The crystal used in the AOM ($PbMoO_4$) has a damage threshold of 10 W/mm^2, which is large enough for an estimated power density at the focal point of the laser. The AOM is controlled by an RF driver whose output power is adjusted to provide an optimized extinction ratio. Another trick to enhance the extinction ratio is to insert a "tank circuit" between the AOM and the RF driver. It consists of a hand-coiled wire in parallel with two parallel *pin* diodes pointing opposite directions working as a band-block filter at the operating RF frequency when the input voltage is below the *pin* diode threshold.

The laser beam is expanded using another lens pair such that the Gaussian

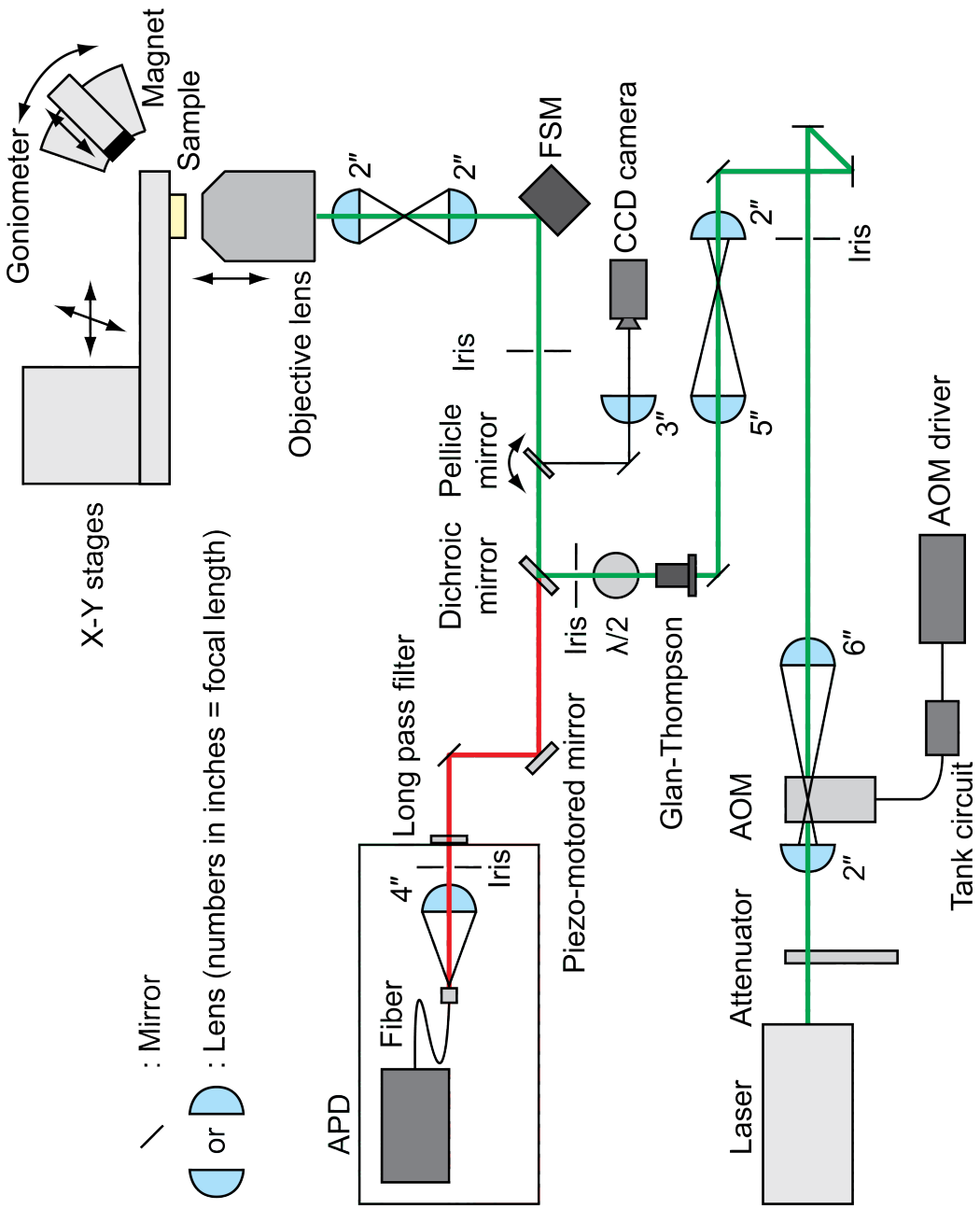


Figure 4.5: Schematic of the optical setup

beam covers the back iris of objective lens. The laser polarization is refined by a Glan-Thompson polarizer and a half-wave plate is used to rotate the polarization. A dichroic mirror (*Semrock* LPD01-532RU-25) reflects the excitation beam at 532 nm wavelength, while transmits the wavelengths of the PL from NV centers. A fast steering mirror (FSM; from *Newport*) is used to raster the beam for two-dimensional imaging. A lens pair of the identical focal length is inserted between the FSM and the objective lens in order to compensate the beam shift due to the raster of the beam. Finally, the laser beam is focused by an objective lens (*Olympus*, LMPLFLN) that has a magnification of x100, a Numerical Aperture (NA) of 0.80 and a working distance of 3.4 mm. Some data are taken by a separate, similar setup in the Jayich lab, which uses an oil immersion lens (*Olumpus* APON 60XOTIRF) with an NA of 1.49.

A lithographically patterned Ti (10 nm) / Pt (90 nm) coplanar waveguide (CPW) on the sample is wirebonded to a brass holder, which is mounted at the end of an aluminum part attached to motorized stages. The in-plane position of the sample is controlled by a combination of a vertical and a horizontal stages (*Newport*, PM500), and the focus is changed by a separate motorized linear stage (also *Newport*, PM500) that the objective lens is mounted on.

A bar magnet is mounted on a custom-made goniometer for magnetic field alignment (for experiments discussed in this chapter, the external magnetic field

is usually off by a few degrees from the NV center symmetric axis [115, 125]). The magnet can be moved along an axis either manually or using a CMAX stepper motor (*Advanced Micro Systems*) in order to change the magnetic field at the sample in a range of several tens to a few hundred Gauss.

The photoluminescence of NV centers is collected by the same objective lens used for excitation. The collection path passes through the dichroic mirror as well as a longpass filter (*Omega Optical*, 3RD630LP), which cuts off wavelengths $\leq$ 630 nm. The collection path is aligned by a pair of mirrors, one of which is mounted on a piezomotor-driven optical mount (*Newport* Agilis series, AG-M100N) allowing for a fine alignment. Finally, the path is coupled to an optical fiber, which is connected to an avalanche photo diode (APD, *Perkin Elmer* SPCM-AQR-13-FC) to count photons. The APD and the fiber coupler are placed inside a dark box in order to prevent accidents when excess amount of light causing damage to the APD.

4.5.2 Electrical setup

Figure 4.6 summarizes an RF electrical setup used to manipulate NV center electronic spins. The pulse patterns are generated by an arbitrary waveform generator (AWG; *Tektronix* 7102. The maximum sampling rate is 10 GS/s). Four output channels of the AWG are used; the *Analog* channel is for controlling

RF microwave, the *Channel 1 Marker 1* (*Ch1M1*) as well as *Channel 1 Marker 2* (*Ch1M2*) are used to control switches for demultiplexing output signals to separate DAQ ports, and *Channel 2 Marker 1* (*Ch2M1*) is used to control the AOM. All channels have complementary outputs that are used to monitor the pulse pattern by using an oscilloscope.

The RF microwave for NV center spin manipulation is generated by a signal generator (*Agilent Technologies*, E8257D). The RF frequency that induces electron spin transition between m_s = 0 and ± 1 states is given by a following equation ($\hbar = 1$),

$$f_{0\rightarrow\pm1} = D \pm \gamma_e \cdot B, \tag{4.4}$$

where $D/2\pi = 2.88$ GHz is the crystal field splitting, $\gamma_e/2\pi = 2.8$MHz/G is the electron gyromagnetic ratio and B is the external field. All measurements discussed in this chapter use the m_s = 0 to -1 transition with the magnetic field of less than 300 G, and therefore the RF frequencies used in the experiments are in a range of 2 – 3 GHz.

The RF sine-wave signal is mixed with patterned pulses from the AWG using a mixer (*MITEQ*, BMA0208LW2MD). The mixed signal is amplified using a microwave amplifier (*Amplifier Research*, 25S1G4A) when necessary. In particular, the signal needs to be amplified when a gold wire loop (instead of CPW) is used to generate microwave on to the sample, as the wire interferes

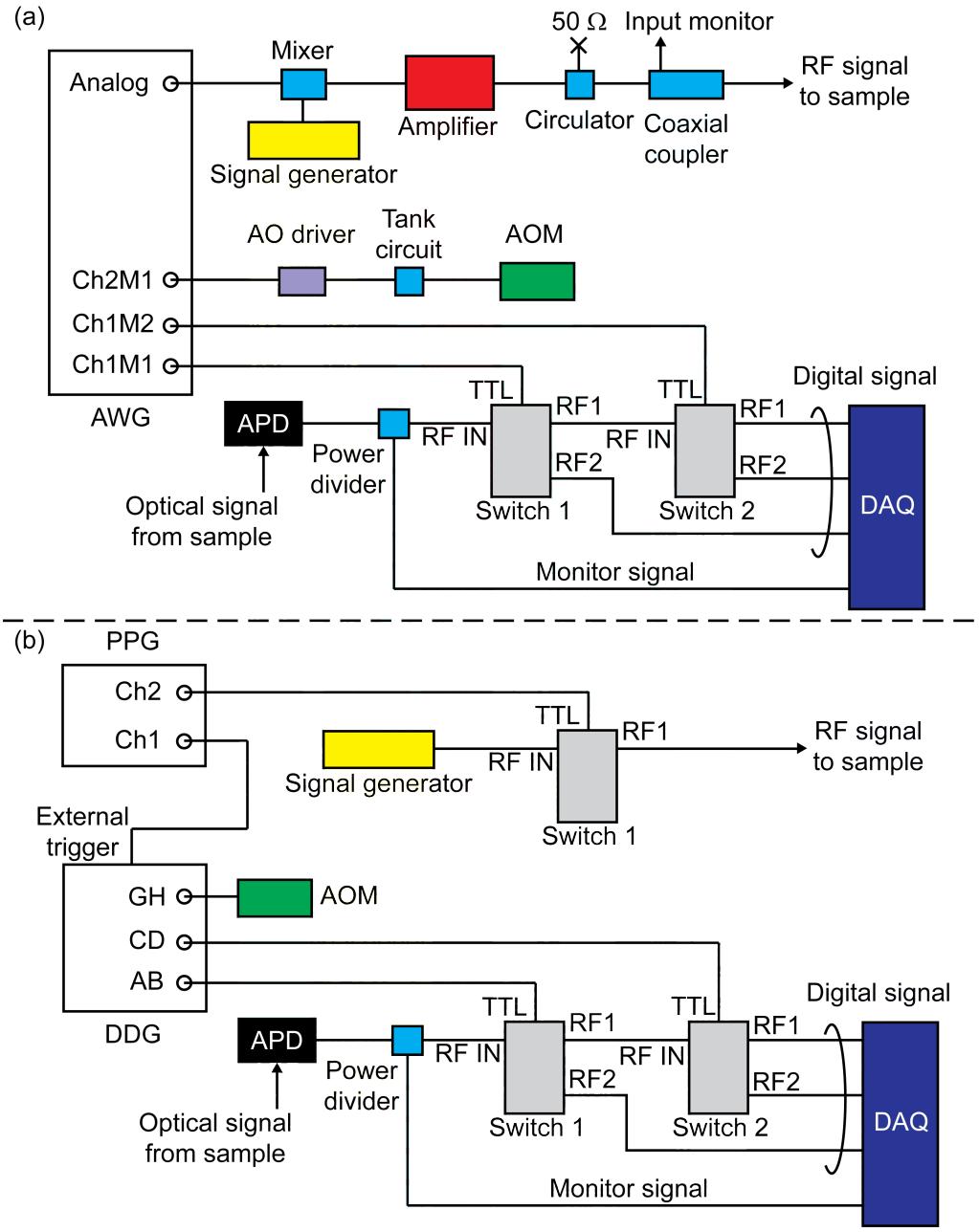


Figure 4.6: Schematic of the electrical setup. (a) and (b) represent two separate setups.

the laser path and it cannot be placed less than $\sim 20\ \mu$m from NV centers, reducing the RF power applied to them. The RF signal is led to the sample after the signal passing through a circulator (*NARDA*, 4923) and a coaxial coupler (*NARDA*, 4216-20), which is used to monitor the input power of the signal. The monitored signal power is converted to a DC output using a zero-bias Schottky diode detector (*Herotek*, DZM185AB), which is read by a multimeter.

The *Ch2M1* port of the AWG is connected to the AOM driver (*Isomet*, 525C), which is further connected to the AOM through the tank circuit (see previous subsection).

The last two ports of the AWG, *Ch1M1* and *Ch1M2*, are used to control switches (*MiniCircuits*, ZASWA-2-50DR) for the output signal (see Fig. 4.6(a)). The APD outputs a train of digital pulses when it detects photons. The output signal is led to the RF IN port of the RF switch, which goes out through either "RF1" or "RF2" port depending on the AWG signal ("Low or High") inputted into the TTL port. The RF IN port of the second switch is connected to the RF1 port of the first switch to make a cascade. The two outputs of the second switch are connected to separate ports of the DAQ (*National Instruments*, BNC-2110). The use of two identical switches, controlled by two separate channels of the AWG, enables two-channel measurements with short data acquisition windows (~ 400 ns). For continuous-wave electron spin resonance (CWESR)

measurements, another DAQ port is used that monitors the raw APD signal.

A separate electrical seup is also used in some measurements, which uses a combination of a pulse pattern generator (PPG) and a digital delay generator (DDG) as shown in Fig. 4.6(b). The *Channel 1* (*Ch1*) of the PPG (*Agilent Technologies*, 81130A; 1.32 Gb/s) is used to modulate RF microwave generated by an signal generator (*Agilent Technologies*, E8257D) using an RF electrical switch (*MiniCircuits*, ZASWA-2-50DR). The *Channel 2* (*Ch2*) of the PPG is used to trigger the DDG (*Stanford Research Systems*, DG645). Two ports of the DDG (*AB* and *CD*) are used to control switches for demultiplexing the output signal to different DAQ ports allowing for two-channel measurements, and the third port (*GH*) is used to control the AOM driver.

4.6 Isotopic identification of doped NV centers

The depth resolution of a confocal microscope is worse than a micrometer, much larger than the thickness of the CVD grown film (typically less than 150 nm), necessitating a way to discriminate NV centers in the nitrogen doped layer from the ones in the substrate. Isotopic discrimination is used during the optically detected magnetic resonance (ODMR) measurements, in order to identify doped NV centers.

Isotopically purified $^{15}N_2$ gas is used to dope ^{15}N isotopes in the grown

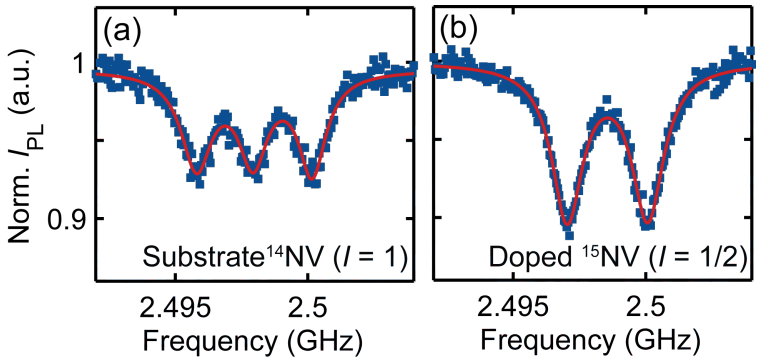


Figure 4.7: CWESR spectra of a substrate ^{14}NV center (a) and a doped ^{15}NV center (b). The red curves show three- and two- Lorentzian fits to the respective data. Original data presented in Ref. [120]

film. Since natural abundance of ^{15}N is only 0.4 %, it is very rare that the naturally incorporated nitrogen impurities in the substrate are ^{15}N isotopes, which further suggests that if the ^{15}N isotopic signature is measured, it is highly likely (with 99.6 % probability) that the measured NV center is originated from the ^{15}N doped layer.

The isotopic signatures are originated from the hyperfine interactions between the electronic spin of NV centers and the nitrogen nuclear spins of their host nitrogen, which are measured in low excitation CWESR measurements. Both the laser excitation power and the microwave power are reduced to resolve the hyperfine structure in the CWESR measurements. Since ^{14}N isotopes have a nuclear spin $I = 1$, they show a three-fold hyperfine splitting each separated by $|A_{14}| = 2.16$ MHz [126, 127, 128], whereas ^{15}N isotopes show a two-fold hy-

perfine splitting as they have a nuclear spin $I = 1/2$, separated by $|A_{15}| = 3.05$ MHz [32].

Figure 4.7 shows measured CWESR spectra of a substrate ^{14}NV (a) and a doped ^{15}NV (b) centers. As expected, the substrate ^{14}NV center shows a three-fold hyperfine splitting, while the doped ^{15}NV center shows a two-fold splitting. The red curves in the figures are three- and two-Lorentzian fits, resulting in the expected hyperfine splitting of ~ 3 MHz and ~ 2 MHz for the ^{14}NV and ^{15}NV centers, respectively.

This isotopic discrimination during the CWESR measurements provides a reliable manner to identify doped ^{15}NV centers from substrate ^{14}NV centers, which is routinely measured prior to any further spin manipulation measurements with the doped NV centers.

4.7 Nanometer-scale depth confinement of doped NV centers

Nanometer-scale hyperfine interactions between the doped NV center electronic spin and the carbon nuclear spins in the diamond crystal probes the depth confinement of doped NV centers in an isotopically layered ^{13}C/^{12}C/^{13}C sample structure. In this section, experimental results demonstrating the depth dispersion of doped NV centers being less than $\pm$ 4 nm are discussed. A model to

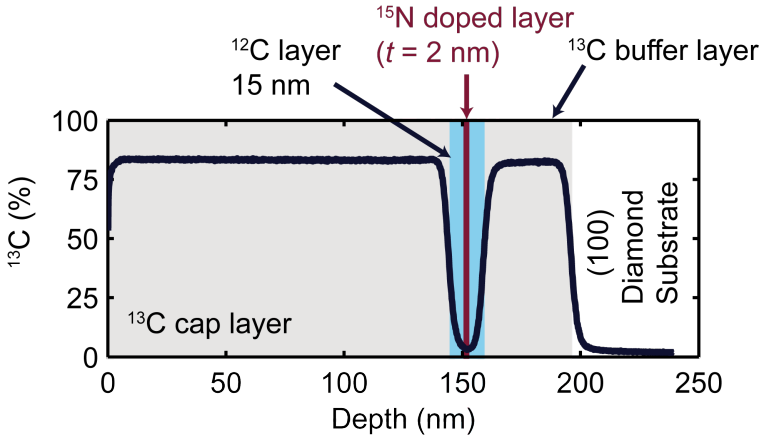


Figure 4.8: Schematic of $^{13}C/^{12}C/^{13}C$ isotopically layered sample structure. A ^{15}N doped layer of 2 nm thick is located at the center of a 15-nm-thick ^{12}C-enriched layer. The black curve shows measured ^{13}C SIMS profile of the sample showing the ^{13}C concentrations of each isotopic layer. Original data presented in Ref. [120]

calculate a length scale of hyperfine coupling between an NV center spin and a ^{13}C nuclear spin is also presented.

4.7.1 Sample structure

An isotopically layered sample consisting of a ^{13}C buffer layer (37 nm) / ^{12}C layer (15 nm) / ^{13}C cap layer (144 nm) structure is grown on top of an electronic grade (100) diamond substrate. The carbon isotopic layers are continuously grown by switching the source gases between $^{12}CH_4$ and $^{13}CH_4$ (99.99 %, from *Cambridge Isotope Laboratories*). The flow of each isotopic carbon source gas is calibrated and nominally identical gas flows (0.1 sccm) are used. A ^{15}N doped layer (2 nm, doped with a 10 sccm $^{15}N_2$ flow) is formed at the

center of the ^{12}C layer. Figure 4.8 is a schematic of the sample structure, superposed with a depth profile of the fraction of the ^{13}C isotopes in diamond measured by SIMS (black curve), showing that ^{13}C is depleted in the ^{12}C layer. The thickness of the ^{12}C layer is estimated by measuring the width of a layer displaying $^{13}\mathrm{C} < 50$ % in the SIMS scan.

4.7.2 Isotopic signatures in ESEEM

The depth dispersion of the NV centers originated from the ^{15}N doped layer is measured using nanometer-scale hyperfine interactions between an NV center electronic spin and environmental nuclear spins. The hyperfine interactions are measured by probing the electron spin echo envelope modulation (ESEEM) [129] in the Hahn echo measurements, consisting of a microwave pulse sequence of $\pi/2 - \tau - \pi - \tau - \pi/2$, where τ is free precession time.

The hyperfine couplings of an NV center spin with different nuclear species result in different frequency components in the ESEEM. The coupling of a doped NV center spin with its host ^{15}N nuclear spin induces modulations at frequencies f_{ms}^{15N}, corresponding to the ^{15}N Larmor precession frequencies depending on the NV center electronic spin state $m_s = 0$ or ± 1. For relatively weak magnetic fields used in this study, $f_{\pm 1}^{15N} \approx 3$ MHz is the hyperfine coupling frequency, and f_0^{15N} is proportional to the magnetic field component perpendicular

to the symmetry axis of an NV center [130]. In addition, a weak coupling of a NV center spin to ^{13}C nuclear spins induces the third frequency component in the modulation, f^{13C}, corresponding to the bare ^{13}C Larmor precession frequency, which is proportional to the external magnetic field [57].

^{12}C atoms do not produce modulations as ^{12}C has no nuclear spin, nor does the ^{14}N nuclear spin since it has a large quadrupolar splitting [57].

Since NV center spins couple only to ^{13}C nuclei within a few nanometer distance [131], the ESEEM measurements provide a nanometer-precision probe of the location of a doped NV center in the ^{12}C layer sandwiched by the two ^{13}C layers, allowing for measuring depth dispersion of NV center originated from the ^{15}N doped layer.

4.7.3 Experimental results

Figure 4.9(a) shows a Hahn echo result of a ^{14}NV center found ~ 15 μm deep in the substrate. A collapse-and-revival feature with a period of ~ 7 μs is an ESEEM due to coupling with an ensemble spins of ^{13}C nuclei naturally abundant (1.1 %) in the substrate. A ^{13}C Larmor frequency of f^{13C} = 145 $\pm$ 1 kHz is extracted from the oscillation period , corresponding to an external field of 136 $\pm$ 1 G calculated using the ^{13}C gyromagnetic ratio of 1.071 kHz/G [57].

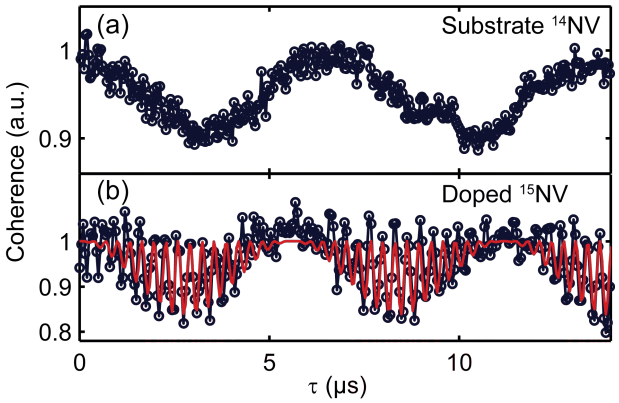


Figure 4.9: Hahn echo signal of (a) a substrate ^{14}NV center and (b) a doped ^{15}NV center. A red curve in (b) is a fit according to an ESEEM model with two ^{15}N Larmor frequency components f_0^{15N} and f_{-1}^{15N} depending on the electronic spins state of the NV center. Original data presented in Ref. [120]

A Hahn echo result of a doped ^{15}NV center measured at the same magnetic field is shown in Fig. 4.9(b), displaying an ESEEM pattern distinct from the substrate ^{14}NV center. Two frequency components are extracted from the fit (red curve), which are 3.15 $\pm$ 0.01 MHz and 179 $\pm$ 3 kHz. These frequencies are consistent with the ^{15}N hyperfine coupling frequency ($f_{\pm1}^{15N}$) and the ^{15}N Larmor precession frequency (f_0^{15N}) at 30 G of the perpendicular component of the magnetic field, respectively. The errors in the frequencies are quoted at 95 % confidence. These frequencies are clearly different from f^{13C}, and no trace of oscillation indicative of a coupling with ^{13}C nuclei is observed in the result. Therefore, this doped ^{15}NV center must be well localized in the ^{12}C layer, away enough from the ^{13}C layer.

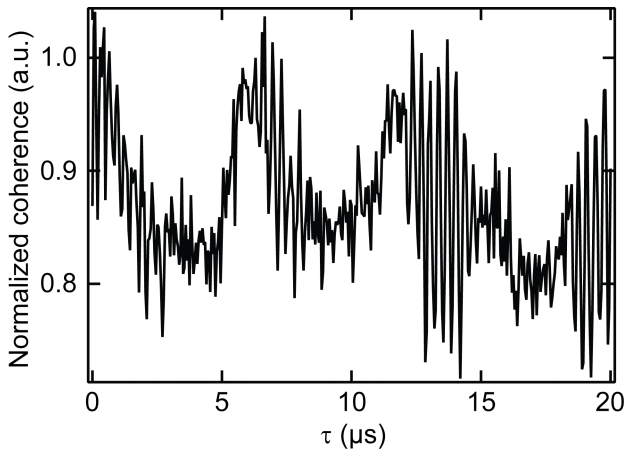


Figure 4.10: Hahn echo result of a doped ^{15}NV center, showing three frequency components f_{-1}^{15N}, f_{0}^{15N} and f^{13C} of ESEEM, indicative of coupling to ^{13}C nuclear spins. Note that the coupling to ^{13}C results in collapse of the ESEEM pattern as apparent in the first 5 μs of the data.

4.7.4 Nanometer-scale depth dispersion of doped NV centers

Of 29 doped NV centers measured, 23 show no evidence of coupling to ^{13}C nuclei and they must be located within the ^{12}C layer. A calculation model (see next subsection) suggests that NV centers located more than ~ 2 nm away from the ^{13}C layer do not display detectable coupling to ^{13}C nuclei. Assuming a normal distribution for doped NV centers' depth, and given 79 % (=23/29) of doped NV centers showing no coupling to ^{13}C nuclear spins, the depth dispersion of the doped NV centers is calculated to be $\sigma \sim 4$ nm.

The remaining 6 doped NV centers display three frequency components $f_{\pm 1}^{15N}$, f_{0}^{15N} and f^{13C} of ESEEM in their Hahn echo result (Fig. 4.10), indicating

coupling with ^{13}C nuclear spins. However, the shortest T_2 time of these NV centers is 70 ± 10 μs, while the other 5 show $T_2 > 250$ μs. Assuming that T_2 times are inversely proportional to the ^{13}C concentration [27, 28], the expected T_2 time for NV centers in the ^{13}C-enriched layer (> 80 %) is ~ 8 μs. The measured T_2 times of the ^{13}C-coupled doped NV centers are much longer than the expected value for being in the ^{13}C layer, and therefore, these doped NV centers must also be located within the ^{12}C layer. The observed ^{13}C coupling is due to the NV centers' location in proximity to the ^{12}C/^{13}C interface, or a coupling to residual ^{13}C atoms in the ^{12}C layer. If latter is the case, these ^{13}C-coupled doped NV centers could also be well localized near the center of the ^{12}C layer, and the depth dispersion could be as small as 2 nm, inferred from the thickness of the ^{15}N doped layer.

4.7.5 Coupling length to ^{13}C-enriched layers

In this subsection, a model to estimate the distance s between a NV center and the ^{12}C/^{13}C interface without detecting a ^{13}C modulation signal is presented. Since NV centers are confined in the ^{12}C-enriched layer of a fixed thickness of 15 nm, a calculated distance s estimates the depth dispersion of doped NV centers.

Assuming a nanometer-scale distance, the interaction between an NV cen-

ter and an individual ^{13}C nuclear spin is very weak and described by the following Hamiltonian ($\hbar = 1$),

$$H = DS_z^2 + \mu_e BS_z + (\mu_n \mathbf{B} + m_s \mathbf{A}) \cdot \mathbf{I}, \tag{4.5}$$

where $D/2\pi = 2.88$ GHz is the crystal field splitting, **S** (**I**) is the electron (nuclear) spin operator, μ_e (μ_n) is the electron (nuclear) magnetic moment, m_s is the electron spin state, **B** is the external magnetic field vector, and **A** is the hyperfine interaction vector.

The coupling between an NV center spin and each ^{13}C nuclear spin produces ESEEM in the Hahn echo signal, and the modulation signal can be described by a pseudo spin. For the j^{th} ^{13}C nuclear spin, the pseudo spin can be written as

$$S_j(\tau) = 1 - 2C_j \sin^2\left(\pi f_0^j \tau\right) \sin^2\left(\pi f_{\pm 1}^j \tau\right), \tag{4.6}$$

where f_{ms}^j is the ^{13}C Larmor frequency due to an m_s-dependent effective magnetic field,

$$\mathbf{B}_{ms} = \mathbf{B} + \frac{m_s}{\mu_n}\mathbf{A}, \tag{4.7}$$

and C_j is the amplitude of the modulation,

$$C_j = \frac{|\mathbf{B}_0 \times \mathbf{B}_{\pm 1}|^2}{|\mathbf{B}_0|^2 |\mathbf{B}_{\pm 1}|^2}. \tag{4.8}$$

Assuming the point-dipole approximation, the hyperfine field caused by the NV

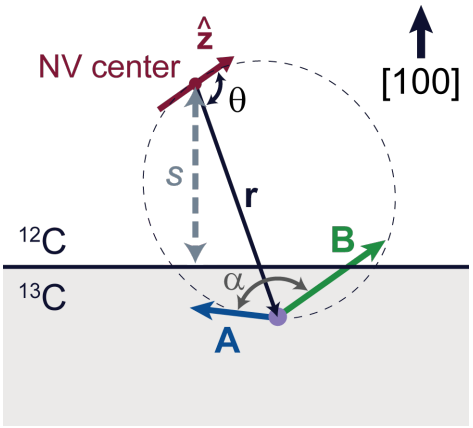


Figure 4.11: Schematic geometry of a NV center and a ^{13}C nuclear spin considered in a model. The origin is set at the NV center and a vector $\mathbf{r}$ is pointing to the ^{13}C nuclear spin. A vector $\hat{\mathbf{z}}$ is parallel to the NV center symmetry axis (// [111]), and θ is the angle between $\mathbf{r}$ and $\hat{\mathbf{z}}$. Vectors $\mathbf{A}$ and $\mathbf{B}$ are the hyperfine and the external magnetic field respectively, and α is the angle between the two. s is the distance between the NV center and the ^{12}C/^{13}C interface. Original data presented in Ref. [120]

center spin on the j^{th} nuclear spin is given by

$$\mathbf{A}(\mathbf{r}_j) = \frac{\mu_0 \mu_n \mu_e}{4\pi r_j^3}(3\hat{\mathbf{r}}\cos\theta_j - \hat{\mathbf{z}}), \tag{4.9}$$

where μ_0 is the vacuum permeability, $\mathbf{r}_j$ is the displacement vector from the NV center to the j^{th} nucleus, $\hat{\mathbf{r}}$ ($\hat{\mathbf{z}}$) is the unit vector in the $\mathbf{r}_j$ direction (NV center symmetry axis) and θ_j is the angle between $\hat{\mathbf{r}}$ and $\hat{\mathbf{z}}$ (see Fig. 4.11). The point-dipole approximation will be ultimately justified by the conclusion that $r >\sim 2$ nm. Using the ^{13}C gyromagnetic ratio ($\mu_n/2\pi = 10.705$ MHz/T), $|\mathbf{A}|$ is estimated to be ~ 2.5 kHz for $r = 2$ nm and $\mu_n\mathbf{B} = 145$ kHz at the experimental condition of $B = 136$ G, satisfying a condition that $\mu_n\mathbf{B} \gg |\mathbf{A}|$. Then, Equations

(4.7) and (4.6) can be approximated as

$$S_j(\tau) \simeq 1 - 2C_j \sin^4(\pi f_L \tau), \tag{4.6'}$$

$$|\mathbf{B}_0| \approx |\mathbf{B}_{\pm 1}| \approx B, \tag{4.7'}$$

where f_L is the ^{13}C Larmor frequency at the magnetic field calculated by $f_L =$ 1.071 (kHz/G)$\times B$(G). Under this approximation,

$$\begin{aligned} C_j &\simeq \frac{|\mathbf{A}(\mathbf{r}_j)|^2 \sin^2(\alpha_j)}{\mu_n^2 B^2} \\ &= \left(\frac{\mu_0 \mu_n \mu_e}{4\pi r_j^3 B}\right)^2 \left[3\cos^2\theta_j + 1 - (3\cos\theta_j \hat{\mathbf{r}}_j \cdot \hat{\mathbf{e}} - \hat{\mathbf{z}} \cdot \hat{\mathbf{e}})^2\right], \end{aligned} \tag{4.10}$$

where a_j is an angle between $\mathbf{A}(\mathbf{r}_j)$ and $\mathbf{B} = B\hat{\mathbf{e}}$ (see Fig. 4.11). Note that the following equation is used to derive this equation,

$$\mathbf{B}_0 \times \mathbf{B}_{\pm 1} = \mathbf{B} \times \left(\mathbf{B} + \frac{1}{\mu_n}\mathbf{A}\right) = \frac{1}{\mu_n}\mathbf{B} \times \mathbf{A} = \frac{1}{\mu_n} B|\mathbf{A}|\sin\alpha. \tag{4.11}$$

If the magnetic angle is applied parallel to the NV center symmetry axis, $\hat{\mathbf{e}} \| \hat{\mathbf{z}}$, Equation (4.10) can be simplified to

$$C_j = \left(\frac{3\mu_0 \mu_e}{8\pi r_j^3 B}\right)^2 \sin^2(2\theta_j). \tag{4.12}$$

The total modulation due to an ensemble of ^{13}C nuclear spins (neglecting the decoherence decay) can be written as

$$S_{bath}(\tau) = \prod_j (1 - 2C_j) \simeq 1 - 2\sum_j C_j, \tag{4.13}$$

to lowest order with $C_j \ll 1$. Hence $S_{bath}(\tau)$ can be approximated as

$$S_{bath}(\tau) \simeq 1 - 2\int dV n(\mathbf{r}) C(\mathbf{r}) = 1 - C_{bath}, \tag{4.14}$$

where $n(\mathbf{r})$ is the density distribution of ^{13}C nucleus and C_{bath} is the total contrast of the ESEEM due to an ensemble ^{13}C nuclear spin. Assuming a uniform ^{13}C distribution,

$$n(\mathbf{r}) = x n_0, \tag{4.15}$$

where $n_0 = 176$ nm^{-3} is the carbon atomic density in diamond, and x is the concentration of ^{13}C ($x = 0.011$ for the natural ^{13}C abundance).

From Equation (4.12), the individual ^{13}C contribution to the ESEEM can be simply written as

$$C(r,\theta) = c_0 \frac{\sin^2(2\theta)}{r^6}, \tag{4.16}$$

where

$$c_0 = \left(\frac{3\mu_0\mu_e}{8\pi B}\right)^2. \tag{4.17}$$

The ESEEM contrast from an ensemble ^{13}C nuclear spins in a shell with $r > r_0$ is given by

$$\begin{aligned} C_{shell}(r_0) &= 2\int dV n(\mathbf{r}) C(\mathbf{r}) \\ &= 2x n_0 c_0 \int_0^{2\pi} d\phi \int_{r_0}^{\infty} \int_0^{\pi} \frac{\sin^2(2\theta)}{r^6} r^2 \sin\theta \, d\theta \, dr \\ &= \frac{64\pi x n_0 c_0}{45 r_0^3}. \end{aligned} \tag{4.18}$$

From this equation, the critical coupling distance r_c can be calculated, beyond which the ensemble signal of ^{13}C nuclear spin is negligible. That is,

$$r_c = \left(\frac{64\pi x n_0 c_0}{45 C_{min}} \right)^{1/3}, \tag{4.19}$$

where C_{min} is the minimum detectable contrast. Plugging in the magnetic field $B = 136$ G for Equation (4.17), $c_0 = 0.01$ nm^6. Assuming the experimentally observable contrast of $C_{min} \sim 10$ % and using the natural ^{13}C abundance of $x = 0.011$, Equation (4.19) implies $r_c = 1.0$ nm, which is consistent with previous studies in Ref [131]. In a case of a ^{13}C-enriched matrix, r_c is increased by a factor of $(x/x_{nat})^{1/3}$, up to 4.3 nm for $x = 1$.

This consideration can be applied to the ^{13}C/^{12}C/^{13}C isotopically layered structure. The minimum distance s between an NV center spin in the ^{12}C layer and an interface of ^{12}C/^{13}C layers without detecting the ^{13}C ESEEM signals is calculated. For simplicity, and since the coupling is dominated by the closest ^{13}C nuclear spins to the NV center, $C(r,\theta) \simeq C(r,\theta_0)$, where $\theta = 54.7^{\circ}$ is the angle between the NV center symmetry axis (//[111]) and the axis normal to the layers (//[100]). The ESEEM contrast from an ensemble of nuclear spins in the ^{13}C-enriched layer ($r > s$) can be derived by modifying Equation (4.18) using a spherical coordinate system of (r, ϕ', θ'), where θ' is an angle relative to the

[100] axis, (see Fig. 4.11)

$$
\begin{aligned}
C_{layer}(s) &= 2\int dV n(\mathbf{r}) C(\mathbf{r}) \\
&\simeq 2xn_0c_0 \int_0^{2\pi} d\phi' \int_s^{\infty} \int_0^{\cos^{-1}(s/r)} \frac{\sin^2(2\theta_0)}{r^6} r^2 \sin\theta' d\theta' dr \\
&= 4\pi xn_0c_0 \sin^2(2\theta_0) \int_s^{\infty} \frac{1}{r^4}\left(1-\frac{s}{r}\right) dr \\
&= \frac{\pi xn_0c_0}{3s^3} \sin^2(2\theta_0). \qquad (4.20)
\end{aligned}
$$

Hence, the minimum distance for the negligible ^{13}C contribution to the ESEEM can be calculated by

$$
s = \left[\frac{\pi xn_0c_0}{3C_{min}} \sin^2(2\theta_0)\right]^{1/3}. \qquad (4.21)
$$

Again, assuming the minimum detectable contrast of $C_{min} \sim 10$ % and using the measured ^{13}C concentration $x = 0.8$ in the ^{13}C-enriched layer, Equation (4.21) implies that $s = 2.4$ nm.

This result implies that 23/29 = 79 % of the measured NV centers are localized around the center of the ^{12}C layer (thickness: 15 nm) and they are at least 2.4 nm away from the ^{12}C/^{13}C layer interface in order to display no measurable ESEEM signal due to ^{13}C nuclear spins. Assuming a normal distribution for NV centers' depth, the depth dispersion of the doped NV center σ can be calculated as

$$\sigma = \frac{(15/2 - 2.4)\text{nm}}{\sqrt{2}erf^{-1}(23/29)} = 4.1\text{nm}. \tag{4.22}$$

As discussed at the end of the previous subsection, the ^{13}C ESEEM signals detected by the 6 doped NV centers could be due to coupling to residual ^{13}C nuclear spins in the ^{12}C-enriched layer, suggesting that the depth dispersion could be as small as 2 nm implied by the thickness of the ^{15}N doped layer.

4.8 Spin coherence properties of shallowly doped NV centers

4.8.1 Sample structure

In order to investigate spin coherence properties of shallowly doped NV centers, four samples each containing a single ^{15}N doped layer at various depths (5 – 103 nm) are grown. The sample structure, as schematically shown in Fig. 4.12, consists of a ^{12}C buffer layer of 32 $\pm$ 12 nm, a ^{15}N doped layer (thickness: t) and a ^{12}C cap layer of thickness $c = 4$ – 100 nm. The average doped NV center depths $d = c + t/2$ of the four grown samples are 5.1 $\pm$ 2.6, 21.0 $\pm$ 8.7, 52 $\pm$ 21, and 103 $\pm$ 41 nm, respectively. The film thicknesses and their uncertainties are estimated by the calibrated growth rate from the SIMS measurements. For the samples with $d > 20$ nm, the thickness of the ^{15}N doped

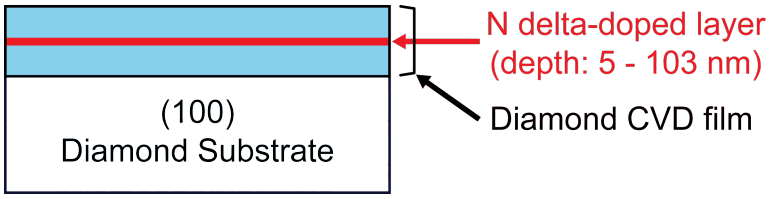


Figure 4.12: Schematic of a delta-doped sample structure. A PECVD-grown film is represented in blue and a ^{15}N doped layer is in red. Four samples with various depths d of the ^{15}N doped layer ($d = 5$ – 103 nm) are grown by varying the thickness of a ^{12}C cap layer.

layer is $t = 1.3 \pm 0.5$ nm using a 10 sccm $^{15}N_2$ gas flow, whereas for the $d = 5$ nm sample, $t = 2.0 \pm 0.8$ nm with a 30 sccm $^{15}N_2$ gas flow. The increased doping gas flow and the doped layer thickness presumably help increasing the chance to find doped NV centers in the very shallow regime (see Section 4.8.5). All the samples have a ^{12}C diamond matrix in order to mitigate spin decoherence of NV centers caused by ^{13}C nuclear spin fluctuations [26].

4.8.2 Hahn echo measurements

A schematic of the Hahn echo measurement sequence is shown in Fig. 4.13 [20]. The NV center electronic spin is initialized to the $m_s = 0$ state with the 532 nm green laser excitation for ~ 1 μs. Then, the superposition state $(|m_s = 0\rangle + |m_s = \pm 1\rangle)/\sqrt{2}$ is prepared by applying a $\pi/2$ pulse. After a free evolution time τ, a π pulse is applied to flip the direction of the spin evolution, followed by another free evolution time τ. In this way, the magnetic fluctuations whose time scale is slower than τ is cancelled out [20]. The phase of the spin

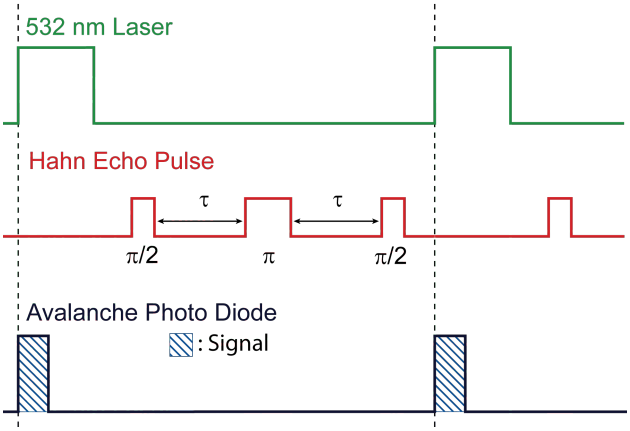


Figure 4.13: Schematic of Hahn echo pulse sequence. Original data presented in Ref. [120]

after a total evolution time of 2τ is projected to the population of $m_s = 0$ and ± 1 states by applying a $\pi/2$ pulse, which is measured by the photoluminescence (PL) intensity from the NV center.

Some data are taken by the differential measurements, in which two identical pulse sequences are run in a one measurement cycle besides a -(π/2) instead of (π/2) pulse is applied at the end of the second sequence. The data in each sequence is recorded and the difference between the spin populations of $m_s = \pm 1$ states is plotted. The differential measurement makes signal more tolerant to the background noise and also helps determining the full decay point as the data should be converged to the zero difference at long τ.

The NV center PL is detected by an avalanche photodiode (APD) typically for 400 ns detection window while illuminating the green laser. The pulse sequence is repeated many times to accumulate the signal while sweeping the

total evolution time 2τ.

Fits to the Hahn echo decay curve reveals the spin coherence time T_2 of the NV center. Many recent studies report that the spin coherence time of NV centers can be extended via dynamical decoupling techniques with increasing the number of π pulses (N) applied during the total evolution time [29, 30, 31]. Still, the Hahn echo T_2 times provide a good probe of the materials quality as they are the simplest case $N = 1$ of the dynamical decoupling technique, which set the lower limit of the spin coherence time.

4.8.3 Hahn echo measurements for doped NV centers ("node" method)

One complexity of the Hahn measurements in the nitrogen-doped samples is the ESEEM caused by coupling to the ^{15}N nuclear spin. The faster frequency component of ESEEM, $f_{\pm 1}^{15N} \approx 3$ MHz, is undersampled with a measurement time step much longer than 1 μs, necessary when the total evolution time 2τ is extended up to several hundreds of microseconds in order to measure T_2. In order to get around this undersampling issue, a "node" technique presented below is developed.

The Hahn echo signal $p(\tau)$, measuring the probability that the NV center electronic spin is in the $m_s = 0$ state at the end of the sequence, can be described

as

$$p(\tau) = \frac{1+S(\tau)}{2}, \tag{4.23}$$

where $S(\tau) \in [0,1]$ is the pseudo spin, which measures the coherence of the electronic spin. In the case of NV centers only coupled to a ^{15}N nuclear spin, $S(\tau)$ can be written as a product of the pseudo spin for the ^{15}N nuclear spin $S_{15N}(\tau)$ and a dephasing term $D(\tau)$,

$$S(\tau) = S_{15N}(\tau)D(\tau), \tag{4.24}$$

where

$$D(\tau) = \exp\left[-\left(\frac{2\tau}{T_2}\right)^2\right]. \tag{4.25}$$

The power factor n depends on the mechanism of the doped NV center spin decoherence. Since the decoherence mechanism of the doped NV center is not well understood, n is left to be a fitting parameter.

$S_{15N}(\tau)$ describes the ESEEM due to interaction with the ^{15}N nuclear spin,

$$S_{15N}(\tau) = 1 - 2C\sin^2\left(\pi f_0^{15N}\tau\right)\sin^2\left(\pi f_{\pm1}^{15N}\tau\right), \tag{4.26}$$

where C is a constant related to the effective magnetic field vector $\mathbf{B}_{ms}$ depending on the NV center spin state

$$C = \frac{|\mathbf{B}_0 \times \mathbf{B}_{\pm1}|^2}{|\mathbf{B}_0|^2|\mathbf{B}_{\pm1}|^2}, \tag{4.27}$$

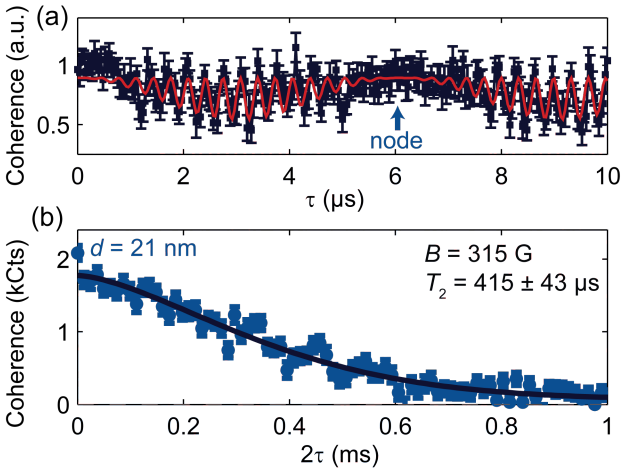


Figure 4.14: (a) Hahn echo signal of a doped ^{15}NV center at depth $d = 21$ nm for free evolution time τ between 0 – 10 μs with a 25 ns measurement time step. The red curve is a fit to data, from which a node period $1/f_0^{15N} = 6.17$ μs is extracted. (b) Hahn echo decay curve of the same NV center measured in a $2\tau = 12.34$ μs time step up to $2\tau \sim 1$ ms. The black curve is a fit to the data, from which spin coherence times $T_2 = 415 \pm 43$ μs is measured. Original data presented in Ref. [120]

and f_0^{15N} ($f_{\pm1}^{15N}$) are the Larmor precession frequency of the ^{15}N nuclear spin when the NV center electronic spin states are in $m_s = 0$ (±1). Although the hyperfine coupling frequency $f_{\pm1}^{15N}$ is a constant value at 3 MHz, $f_0^{15N}$is typically on the order of $\sim$ 100 kHz much slower than $f_{\pm1}^{15N}$, and moreover, $f_0^{15N}$is experimentally controllable as it is proportional to the magnetic field component perpendicular to the NV center symmetry axis.

When τ is equal to a multiple of $1/f_0^{15N}$, the Equation (4.26) simply reduces to $S_{15N}(\tau) = 1$. Under such condition, $S(\tau) = D(\tau)$, allowing for a direct measurement of T_2. Figure 4.14(a) shows a Hahn echo result of one of the doped

NV centers from the d = 21 nm sample. The data is taken in 25 ns time steps of the spin evolution time τ from 0 to 10 μs, displaying the characteristic ^{15}N ESEEM. The modulation pattern is fitted by Equation (4.26) (red curve) and the "node" position where $\tau_0 = 1/f_0^{15N}$ is extracted from this fit. In order to measure the T_2 time, the Hahn echo measurement is extended up to a total evolution time of $2\tau \sim 1$ ms as shown in Fig. 4.14(b) with the time step a multiple of τ_0 (in this case, $2\tau_0 = 12.34$ μs). It should be noted that all the measurement conditions should be kept as same for the two Hahn echo measurements of different time scale, as f_0^{15N} is sensitive to the perpendicular component of the external magnetic field and thus the position of the magnet. Figure 4.14(b) shows a vanished ESEEM pattern via the "node" method, and a fit to the Hahn echo decay data (black curve) gives a direct measurement of T_2, which is 415 $\pm$ 43 μs in this specific case.

A precise measurement of the node position is critical as an error in the estimation of the node position is accumulated when the total measurement time is extended, resulting in an unwanted ESEEM beating occurring again. By measuring and fitting several nodes with τ up to several tens of microseconds, the node position can be more precisely measured. Measuring ESEEM beating away from $\tau = 0$ (e.g. 50 μs $< \tau <$ 60 μs) also helps reducing the error, as the errors are accumulated after several nodes.

All the Hahn echo data for the T_2 measurement shown in this chapter (also in Chapter 6) are taken by this "node" method. Another way to get around the ^{15}N ESEEM beating is to align the magnetic field perfectly along the NV center symmetry axis. f_0^{15N} becomes smaller as the external field close to aligned with the NV center axis, and finally, $C = 0$ when it is perfectly aligned (see Equation (4.27)), also leading to $S_{15N}(\tau) = 1$. This method has an advantage that an arbitrary free evolution time (τ) can be chosen for measurements, while the "node" method is constrained to a multiple of $1/f_0^{15N}$. This requirement constrains some quantum metrology measurements, and in such a case, magnetic field has to be perfectly aligned. The Hahn echo data shown in Chapter 5 is taken by this magnet-alignment method.

4.8.4 Spin coherence times of doped NV centers

Spin coherence times of doped NV centers are measured using Hahn echo sequences. Figure 4.15 shows Hahn echo decay curves of NV centers from the $d = 5$ nm (a) and 52 nm (b) samples, respectively. Each decay curve is fitted by a following equation,

$$F(\tau) = A_0 \exp\left[-\left(\frac{2\tau}{T_2}\right)^n\right] + y_0, \tag{4.28}$$

where the amplitude A_0, the base line y_0, as well as the power factor n are left to be fitting parameters. Despite proximity to the surface, several NV centers

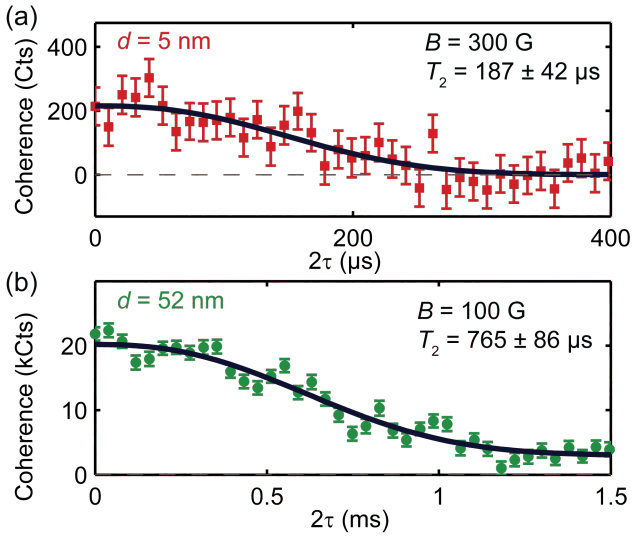


Figure 4.15: Hahn echo signal of a doped NV center at depths $d = 5$ (a) and 52 (b) nm. The black curves are fits of the form $A_0 \exp[-(2\tau/T_2)^n] + y_0$. Uncertainties in T_2 are quoted in 95 % confidence. Original data presented in Ref. [120]

in the 5 nm sample show $T_2 > 100$ μs, which is about an order of magnitude improvement compared to the ion implantation technique [34]. The T_2 times of the doped NV centers are as long as > 600 μs for a deeper sample at $d = 52$ nm.

T_2 results of total 16 doped NV centers from the four samples ($d = 5 - 103$ nm) are summarized in Fig. 4.16. All of the measured NV centers show long T_2 times on the order of hundreds of microseconds. Moreover, the T_2 results are consistent and reproducible in each sample, unlike the implanted samples showing wide deviation of T_2 results [34]. Doped NV centers in the deep samples ($d > 50$ nm) show saturating $T_2 \sim 700$ μs whereas shallower samples show

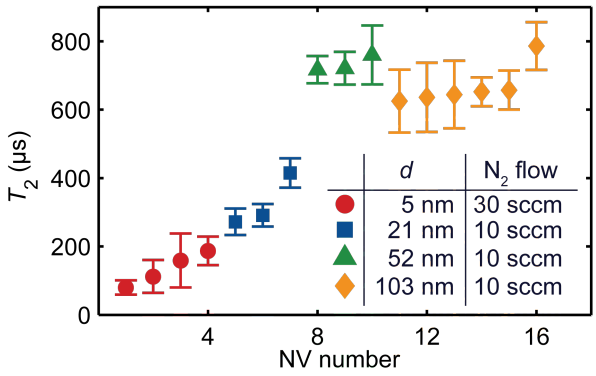


Figure 4.16: Summary of T_2 data of 16 doped NV centers from four different samples with various depths $d = 5$(red), 21(blue), 52(green), and 103(orange) nm. A $^{15}N_2$ doping gas flow of 30 sccm is used for the $d = 5$ nm sample, and 10 sccm for the other three samples. Uncertainties in T_2 are quoted in 95 % confidence. Original data presented in Ref. [120]

shorter T_2 when $d \leq 21$ nm, suggesting that surface effects degrade the spin coherence of shallow NV centers [132].

Since ^{13}C nuclear spins are depleted in the ^{12}C diamond grown film, the primary factor limiting the spin coherence of deeper NV centers are likely the residual nitrogen dopants that do not turn into NV centers. According to Ref. [23], T_2 times of NV centers are inversely proportional to the nitrogen (P1 center) concentration in diamond crystal, and they measure $T_2 \sim 30$ μs for the 1 ppm nitrogen concentration (1.8×10^{17} cm^{-3}). Assuming nitrogen is the only source of decoherence for NV centers, the estimated T_2 time for the nitrogen concentration of the doped layer (0.8×10^{16} cm^{-3}) is ~ 675 μs, which is consistent with the measured T_2 times for the deeper doped NV centers, supporting

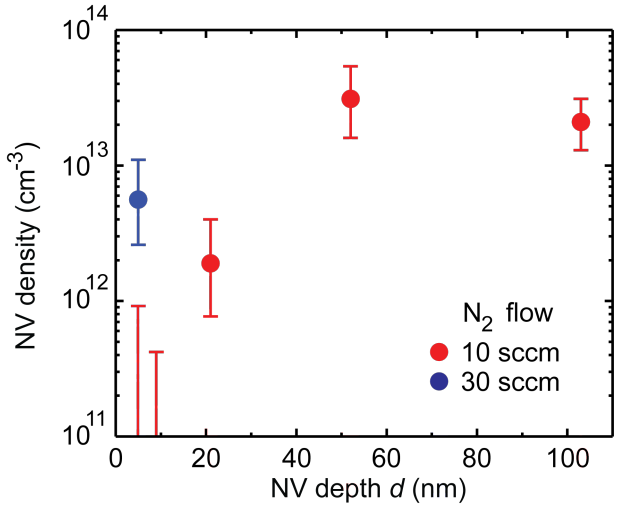


Figure 4.17: Doped NV density as a function of depth. Data in red are samples doped with 10 sccm $^{15}N_2$ flow, and blue is with 30 sccm. Since no doped NV centers are found in the shallowest two samples with 10 sccm $^{15}N_2$ flow, the upper limit of the NV density is shown for each sample.

the assumption that nitrogen is the primary decoherence source.

4.8.5 Doped NV density

Shallowly doped samples display very low doped NV density as shown in Fig. 4.17 plotting the measured doped NV density as a function of the NV center depth. The data points in red are for the 10-sccm doped samples, and blue is for the 30-sccm doped sample. The doped NV density is computed by the average number of NV centers found per scanned area assuming the thickness of the ^{15}N doped layer (1.3 or 2 nm). For a series of 10-sccm doped samples, the doped NV density is consistent at $(2-3)\times 10^{13}$ cm^{-3} for $d > 50$ nm, while

it decreases by an order of magnitude in the $d = 21$ nm sample ($\sim 2 \times 10^{12}$ cm^{-3}) with further decrease in the $d = 5$ and 9 nm samples. For the two shallowest samples ($d < 10$ nm), the doped NV density is too low that no doped NV centers are found over the scanned areas. The reduction of the density for shallow NV centers may be explained by annihilation of mobile vacancies at the surface, or the surface charge potential preventing vacancies from diffusing to form NV centers.

Another sample is grown to dope at $d = 5$ nm with an increased $^{15}N_2$ doping gas flow of 30 sccm resulting in a doped NV density of 6×10^{12} cm^{-3}. The increased doped NV density is presumably due to the increased nitrogen incorporation with larger $^{15}N_2$ flow (see Section 4.4.2). However, later studies discussed in Chapter 6 reveal that the nitrogen incorporation is weakly dependent on the $^{15}N_2$ doping gas flow. Other effects such as substrate quality variation and the surface miscut angle could also affect the nitrogen incorporation and hence NV density. The relationship between doping gas flow and the NV density is still unclear and more study is necessary to fully understand its mechanism.

4.9 Sensitivity calculations of doped NV centers

In order to motivate using shallowly doped NV centers for external spin

sensing applications, the external spin sensitivity is calculated using measured parameters of doped NV centers.

Assuming that the external spin can be initialized and driven resonantly at their Larmor frequency ν, the ac sensing schemes as described in Ref. [39, 40, 133] can be applied. These schemes are adopted for shallowly doped NV centers. The ac magnetic sensitivity is given by the following equation,

$$\eta_B = \frac{\pi\hbar}{g\mu_B C\sqrt{2\tau}F(\tau)}, \tag{4.29}$$

where $\hbar$ is the reduced Planck's constant, $g \sim 2$ is the electron g-factor, μ_B is the Bohr magneton, C is the parameter estimating the measurement efficiency of the NV center spin readout, 2τ is the total spin evolution time, $F(\tau)$ is the envelope function of the spin echo decay curve.

In the ac magnetic sensing schemes, the external spin precession period $1/\nu$ has to coincide with 2τ in order to make a positive phase accumulation of the probe NV center spin for the two halves of the total free evolution times. Since spin initialization and read out time $\tau_m \sim 2\ \mu$s is much shorter than the free evolution time τ,

$$\tau_m + 2\tau \approx 2\tau = \frac{1}{\nu}. \tag{4.30}$$

For the doped ^{15}NV center in the ^{12}C diamond matrix, the ESEEM due to coupling to the ^{15}N nuclear spin has to be taken into account, which obscures the spin signal from the external spin. In order to get around the ^{15}N ESEEM,

the free evolution time τ has to be a multiple of $1/f_0^{15N}$ (see Section 4.8.3), which together with Equation (4.30) leads to

$$\tau = \frac{m}{f_0^{15N}} = \frac{1}{2\nu}, \tag{4.31}$$

where m is an integer and f_0^{15N} is the "node" frequency. For these discrete numbers of τ satisfying Equation (4.31), the ^{15}N ESEEM beating vanishes and the envelope function of the echo decay curve is simply written as

$$F(\tau) = \exp\left[-\left(\frac{2\tau}{T_2}\right)^n\right]. \tag{4.32}$$

The best sensitivity is acquired when $\sqrt{2\tau}F(\tau)$ (see Equation (4.29)) is maximized. For the doped NV centers in the $d = 5$ and 21 nm samples, the experimental values of f_0^{15N} are plugged in to Equation (4.31) to compute τ and ν, which are further used to calculate the maximum value of $\sqrt{2\tau}F(\tau)$. For the $d = 5$ nm sample as an example, $\sqrt{2\tau}F(\tau)$ is maximized with experimental parameters of T_2 = 187 μs, $n = 2.442$ and $f_0^{15N} = 95.4$ kHz, along with the calculated ac field frequency of $\nu = 9.54$ kHz.

The C parameter ($C \leq 1$) estimates the measurement efficiency constrained by the PL contrast between m_s = 0 and ± 1 states, which can be written as [40]

$$C = \left[\sqrt{1 + 2\frac{a_0 + a_1 + a_0 a_1}{(a_0 - a_1)^2}}\right]^{-1}, \tag{4.33}$$

where the a_0 and a_1 are the photon counts for the $m_s = 0$ and ± 1 states in a single measurement duty cycle. For the doped NV center in the $d = 5$ nm sample,

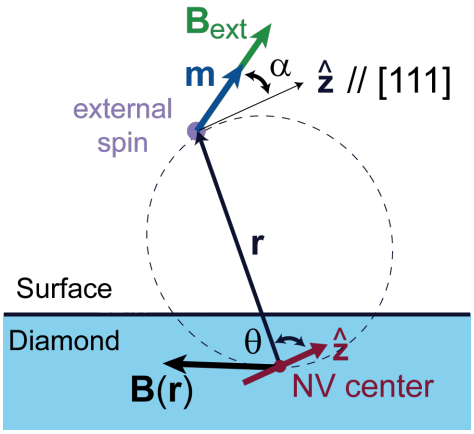


Figure 4.18: Schematic geometry of a NV center and an external target spin. The origin is set at the NV center and a vector $\mathbf{r}$ points from the NV center to the external spin $\mathbf{m}$ in the $x-z$ plane. The NV center symmetric axis is $\hat{\mathbf{z}}$ and the angle between $\mathbf{r}$ and $\hat{\mathbf{z}}$ is θ. The angle between $\mathbf{m}$ and the external magnetic field vector $\mathbf{B}_{ext}$ is α. $\mathbf{B}(\mathbf{r})$ is the magnetic field caused by the external spin at the location of the NV center.

the experimental values are $a_0 = 0.0056$ and $a_1 = 0.0038$, leading to $C = 0.013$. For a current measurement setup, the average number of photons detected during the spin readout window of ~ 400 ns is much less than 1, and therefore the readout sensitivity is limited by the photon shot noise. C could be improved by increasing the photon collection efficiency using oil immersion lenses, photonic cavities, or solid immersion lenses.

By plugging in all the experimental parameters into Equation (4.29), a field sensitivity is calculated to be 172 nT/$\sqrt{\text{Hz}}$ for a NV center in the $d = 5$ nm sample.

In order to convert the magnetic field sensitivity to the external spin sensi-

tivity, a magnetic field generated by an external dipole **m** at the location of NV center is calculated. A schematic of the external and NV center spins as well as the coordination system is shown in Fig. 4.18. Define a vector **r** connecting from the NV center to the external spin dipole, and $\hat{\mathbf{z}}$ parallel to the NV center symmetry axis along [111] direction. Assuming **r** is in the x-z plane, making an angle θ to $\hat{\mathbf{z}}$, leading to $\mathbf{r} = r \begin{pmatrix} \sin\theta \\ \\ \cos\theta \end{pmatrix}$. The magnetic dipole of the external spin, **m**, is assumed to be parallel to the external magnetic field, $\mathbf{B}_{ext}$, which can be written as $\mathbf{m} = m \begin{pmatrix} \sin\alpha \\ \\ \cos\alpha \end{pmatrix}$, where α is an angle between $\mathbf{B}_{ext}$ and $\hat{\mathbf{z}}$. The magnetic field generated by the external spin dipole at the position of the NV center is given by

$$\begin{aligned} \mathbf{B}(\mathbf{r}) &= \frac{\mu_0 m}{4\pi r^5}\left[3\mathbf{r}\,(\mathbf{m}\cdot\mathbf{r}) - \mathbf{m}r^2\right] \\ &= \frac{\mu_0 m}{4\pi r^3}\begin{bmatrix} (3\cos\theta\sin\theta)\cos\alpha + (3\sin^2\theta - 1)\sin\alpha \\ \\ (3\cos^2\theta - 1)\cos\alpha + (3\cos\theta\sin\theta)\sin\alpha \end{bmatrix}. \end{aligned} \tag{4.34}$$

For small values of B_{ext} (relative to the NV center zero field splitting $D/2\pi \sim$ 2.88 GHz), the NV center is sensitive to the projection of the dipole magnetic field along the NV center symmetry axis parallel to $\hat{\mathbf{z}}$, given by

$$B_z = \frac{\mu_0 m}{4\pi r^3}\left[(3\cos^2\theta - 1)\cos\alpha + (3\cos\theta\sin\theta)\sin\alpha\right]. \tag{4.35}$$

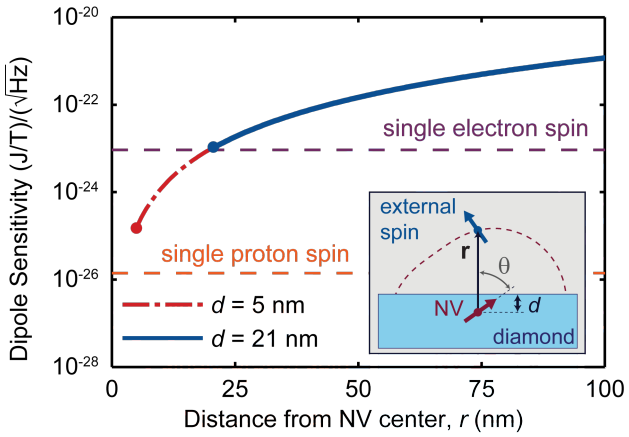


Figure 4.19: Calculated dipole sensitivity as a function of target-NV center distance. The result for a NV center at $d = 5$ (21) nm is represented by a red dash-dot (blue solid) curve. Magnetic dipole of a single electron and proton spin is also shown in the figure for comparison. (inset) Schematic geometry of a NV center (depth: d) and an external spin. A vector $\mathbf{r}$ points from the NV center to the external spin and θ is the angle between $\mathbf{r}$ and the NV center symmetric axis. The dashed curve is an iso-sensitivity contour. Original data presented in Ref. [120]

For fixed θ, B_z takes the maximum value of

$$B_z = \frac{\mu_0 m}{4\pi r^3}\sqrt{3\cos^2\theta + 1}, \tag{4.36}$$

when the external field $\mathbf{B}_{ext}$ is applied at the angle α_0 such that $\tan\alpha_0 = (3\cos\theta\sin\theta)/(3\cos^2\theta - 1)$. Combining Equations (4.29) and (4.36) gives an external magnetic dipole sensitivity,

$$\eta_m(r,\theta) = \frac{\pi\hbar}{g\mu_B C\sqrt{2\tau}F(\tau)} \cdot \frac{4\pi r^3}{\mu_0\sqrt{3\cos^2\theta + 1}}. \tag{4.37}$$

Figure 4.19 plots the dipole sensitivity (which is equivalent to the minimum detectable dipole moment for 1 second averaging) represented by Equation (4.37)

as a function of distance from the NV center r. The plots are calculated for the longest spin coherence NV centers in the $d = 5$ (red, dash-dot curve) and 21 (blue, solid curve) nm samples, respectively, by plugging in the experimental values for C, τ, and $F(\tau)$, as well as an optimized value of ν. Assuming that the external spin is located straight above the NV center, θ is fixed to be 54.7^{o}, an angle between the NV center symmetry axis (// [111]) and the axis normal to the sample surface (// [100]). Also plotted (as dotted lines) in the figure are the magnetic dipole of a single electron spin and a single proton spin. The calculated results suggest that a single electron spin within ~ 15 nm of the surface can be detected by the doped NV center 5 nm below the surface with only 1 second averaging. Moreover, it could detect a single proton spin with 1 minute averaging. Even though the NV centers in the $d = 5$ nm sample shows shorter T_2, it shows a sensitivity two orders of magnitude better than that in the $d = 21$ nm sample. This is because of the proximity enhancement effect scaled as distance r by $1/r^3$, motivating to create shallow NV centers for external spin sensing applications.

The inset of the Fig. 4.19 plots the iso-sensitivity contour (dotted line) given by

$$r_{iso}(\theta) = \left(\frac{\mu_0 m}{4\pi B_0} \sqrt{3\cos^2\theta + 1} \right)^{1/3}. \tag{4.38}$$

The asymmetric shape of the contour reflects the NV center symmetric axis

tilted by 54.7^{o} from the [100] direction.

Considering Equation (4.37), several improvements can be made to achieve better sensitivity. An increase of photon collection efficiency via an oil immersion lens or a high NA objective can improve the C parameter up to ~ 0.05 [40], a factor of five improvement compared to the current measurement setup. The spin coherence factor $\sqrt{2\tau}F(\tau)$ can be improved by using the dynamical decoupling techniques to extend the spin coherence times of NV centers. Placing NV centers even close to the surface gains the sensitivity through the $1/r^3$ factor. Additional improvement by a factor of $\sqrt{2}$ can be made by growing on top of (111) substrates. Each parameter should be considered well and some or all of these improvements should be combined in order to further improve the external spin sensitivity of shallowly doped NV centers.

4.10 Conclusion and outlook

The nitrogen delta-doping technique is discussed as a means to engineer NV centers near the surface. $^{15}N_2$ source gas is briefly introduced into the growth chamber with the controlled timing and duration, forming a nitrogen doped layer that defines the depth of NV centers. Vacancies are created during the post growth process and a subsequent annealing diffuses them to form NV centers. Doped ^{15}NV centers are discriminated from substrate ^{14}NV cen-

ters by measuring the hyperfine coupling with the host nitrogen nuclear spin during CWESR measurements. The nanometer-scale hyperfine coupling to the environmental ^{13}C nuclear spins is used to confirm the nanometer-scale depth confinement of doped NV centers. Finally, despite proximity to the surface, the shallowly doped NV centers display long spin coherence times $T_2 > 100$ (600) μs at depth $d = 5$ (52) nm.

A sensitivity calculation shows that the shallow NV centers with long spin coherence times are advantageous for sensing electron/proton spins external to the diamond crystal. Applications of the delta-doped materials for external nuclear spin sensing will be intensively explored in the next chapter.

Also, the nitrogen delta-doping technique allows for a separate creation of nitrogen and vacancies, opening up a degree of freedom for vacancy engineering. The ability to control NV center density and three-dimensional position control of single NV centers via vacancy engineering will be discussed in Chapter 6.

The spin coherence properties of NV centers are degraded as the doped NV centers are created closer to the surface, suggesting that the surface spins are major source of decoherence for shallow NV centers. To understand the origin and the mechanism of the surface spins is very important as it provides directions to improve external spin sensitivity. Also, the emergence of nanometer-

scale engineering of diamond structures demonstrates the enhancement of NV center functionalities. Eventually, the delta-doped diamond materials will be incorporated into the diamond-based nanostructures in order to combine the advantages of both technologies. Preliminary results in this direction are presented in Chapter 7.

Finally, a continuous improvement of the delta-doping technique is still very important. Although spin coherence and density results of the doped NV centers are statistically consistent, they always show deviations since the diamond film growth and the defects creation processes are very sensitive to the details of process parameters. Some parameters can be controlled but others, such as substrate quality variations, cannot. There might be more optimized process parameters to achieve better NV center properties, i.e. longer spin coherence times, higher NV density, etc. Engineering efforts are necessary to handle details of the process parameters in order to achieve even more reproducible and better results, which is a key to open up practical applications of NV centers.

Chapter 5

Nanometer-scale nuclear magnetic resonance (nanoNMR)

5.1 Introduction

Magnetic resonance imaging (MRI) is a powerful technique that nondestructively visualizes three-dimensional (3D) structures inside a human body, which is widely used as a medical diagnostic tool in modern hospitals [134]. The MRI technique detects magnetic signals from nuclear spins while its spatial information is encoded by the magnetic field gradient that resonantly excites nuclear spins at specific positions. Although a typical spatial resolution in the clinical use for whole-body imaging is a millimeter scale, a sub-millimeter-scale MRI [135] opened up biological applications of the MRI technique as its length scale is comparable to cells whose size are typically on the order of

$\sim 100\ \mu$m. A gradual improvement in the spatial resolution of conventional "induction-coupling" detection in MRI has been made through increasing receiver sensitivity via micro coils [136], using higher magnetic field gradient [137] and a use of dynamic nuclear polarization (DNP) [138], pushing the sensitivity down to $\sim(3\ \mu\text{m})^3$ [137].

Although a moderate estimation of the resolution limit of the conventional MRI technique is $\sim(1\ \mu\text{m})^3$ assuming a reasonable field gradient and an acquisition time [139], there is a continuously increasing desire for pushing this resolution limit down to a nanometer-scale, the size comparable to macromolecules. A strong motivation for the nanometer-scale MRI, or the "nanoMRI" is to image 3D structures of proteins, which remains an outstanding challenge in the modern structural biology [140]. The 3D structures of proteins are the origin of their functionalities, which are determined by either a nuclear magnetic resonance (NMR) or an x-ray diffraction (XRD) technique. However, the NMR technique is applicable only to the proteins of small sizes. Moreover, the structure determination using XRD requires crystallization of the target molecules, which is usually very challenging limiting choice of proteins. Given these limitations of the standard techniques, the nanoMRI possesses a potential of being a complementary technique for the structure determination of certain types of proteins.

An ultimate resolution of MRI, and also NMR, is limited by a small magnetic signal of nuclear spins. Both techniques detect difference in spin populations of different orientations, which follows a Boltzmann distribution and hence a fraction of the population difference can be written as

$$\frac{\Delta N}{N} \approx \frac{\Delta E}{k_B T}, \tag{5.1}$$

where k_B is the Boltzmann's constant, T is temperature, and ΔE is the energy difference between the two spin states due to the Zeeman splitting,

$$\Delta E = \gamma \hbar B, \tag{5.2}$$

where γ is the gyromagnetic ratio, $\hbar$ is the reduced Planck's constant, and B is the external magnetic field. Plugging in representative numbers of $\gamma = 2\pi \times 42.576$ MHz/T (gyromagnetic ratio of ^{1}H nuclear spins), $T = 300$ K and $B = 11.75$ T (used in conventional 500 MHz NMR) results in $\Delta N/N = 8.0 \times 10^{-5}$, suggesting that only a small fraction of the total nuclear spins in the sample is used for the signal detection, requiring a volume of the sample ultimately limiting the spatial resolution. This constraint is inherent as far as the detection scheme relies on the photon irradiation corresponding to the Zeeman splitting ΔE, motivating alternative approaches for the nuclear spin sensing.

Among many schemes proposed and demonstrated, including techniques based on a superconducting quantum interference device (SQUID) [142] and a

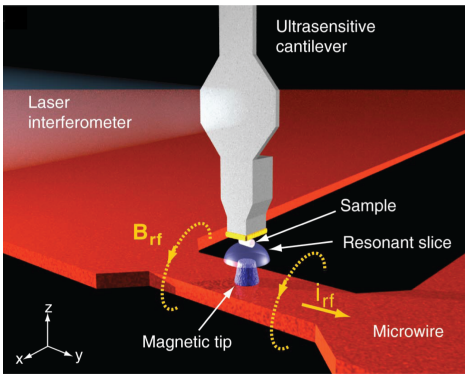


Figure 5.1: Schematic of magnetic resonance force microscopy (MRFM). A sample is attached at the end of an ultrasensitive cantilever. The magnetic interaction between spins in the sample and a magnetic tip causes small vibration of the cantilever, which is sensed by laser interferometer. Only spins in a small volume of the sample intersecting a resonant slice, which is defined by the external field and the magnetic tip, are excited by the RF magnetic field generated by the current through microwire. Three-dimensional spatial information is encoded by scanning the cantilever. Original data presented in Ref. [141].

micrometer-size Hall sensor [143], magnetic resonance force microscopy (MRFM) stands out because of its recently demonstrated spatial resolution ≤ 10 nm and compatibility with a biological sample [141]. MRFM [144] detects tiny vibration of an ultra-sensitive cantilever caused by a magnetic interaction between spins in the sample attached to the cantilever and a separate magnetic tip (Fig. 5.1). Only spins in the sample intersecting a resonant slice, which is defined by the magnetic tip and a static external field, are excited by the RF microwave generated by the current through microwire. The spatial information is acquired by scanning the cantilever in the three-dimensional directions. The recent achievements using MRFM include detection of a single electron spin [145], elemental

selectivity of nuclear species (^{1}H, ^{13}C and ^{31}P) in organic materials [146], and 3D imaging of a biological sample with a spatial resolution $\leq$ 10 nm [141]. Although the MRFM-based MRI technique sets important milestones for the nanoMRI, a major drawback is that it requires an ultra high vacuum (UHV) and a cryogenic temperature less than a few K down to hundreds of millikelvins, in order to reduce thermal noise of the cantilever. Since most of the biological and chemical researches are conducted at ambient conditions, it is highly desired to build a nanoMRI technique that can be operated at room temperature.

The NV center holds a promise as a candidate for the room-temperature nanoMRI. As discussed in the previous chapter (Section 4.9), NV centers located very close to the surface can display magnetic sensitivity capable of detecting a single proton spin on the surface. The goal of this chapter is to present a nanometer-scale detection scheme of an ensemble nuclear spin signal using a shallow single NV center as a spin probe [102]. This nanometer-scale NMR (nanoNMR) is a first important step for the NV-based nanoMRI that can be operated at room temperature.

5.2 Background

5.2.1 Sample preparation

Although several groups used a single NV center to detect spin signals

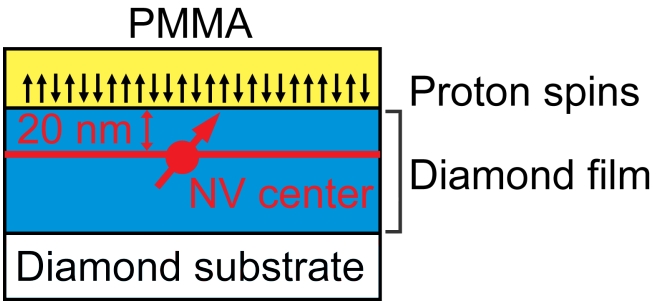


Figure 5.2: Schematic of the sample structure. The sample has a single nitrogen delta-doped layer at 20 nm from the surface. The sample surface is spin coated with organic polymer, PMMA, containing protons of a density of $\rho_N = 57$ nm^{-3}.

from an ensemble [57] and a single nuclear spin(s) [147, 148, 149] *within* a diamond crystal, the nanoNMR scheme requires detection of nuclear spins *external* to the diamond. This requirement demands to create a single NV center in a nanometer-proximity from the surface while maintaining its spin coherence, and therefore, a sample is grown using the nitrogen delta-doping technique.

The sample contains a single 1.3-nm-thick ^{15}N doped layer 20 nm deep from the surface (Fig. 5.2). The $^{15}N_2$ doping gas flow is 10 sccm, and the entire diamond film consists of ^{12}C matrix, grown on top of an electronic-grade (100) diamond substrate from *Element 6*. See Section 4.4.1 for detailed growth conditions. After growth, the sample is electron irradiated at 2 MeV with a dose of 10^{14} cm^{-2} to create vacancies, which diffuse to form NV centers during a subsequent annealing process at 850 ^{o}C for 2 hours in a H_2/Ar forming gas atmosphere. The sample is then treated in a perchloric acid process to make the

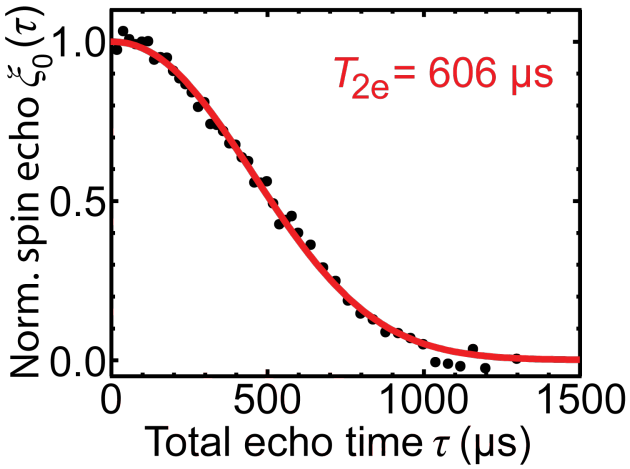


Figure 5.3: Hahn echo decay curve for the NV center used in the measurements, displaying spin coherence time $T_{2e} = 606\ \mu$s. The figure plots normalized spin echo amplitude $\xi_0(\tau)$ as a function of total echo time τ. Original data presented in Ref. [102].

surface oxidized and to remove a graphitic layer. Finally, a 4 μm wide, 140 nm thick gold microwire is patterned using electron-beam lithography and lift-off in order to generate RF and microwave magnetic field to manipulate nuclear and NV center electronic spins.

One of the doped, single NV centers is used as a probe of the nuclear spin signal, which displays a spin coherence time $T_{2e} = 606\ \mu$s measured by a Hahn echo sequence. A resulting Hahn decay curve along with a fit to a form of $\xi_0(\tau) = \exp[-(\tau/T_2)^n]$ is shown in Fig. 5.3, where n is a power factor fitted to be 2.17. Note that the data does not show ESEEM induced by the hyperfine coupling with a host ^{15}N nuclear spin as the external magnetic field is aligned within 0.25° from the NV center symmetry axis (see Section 4.8.3).

The target spins are ^{1}H nuclear (proton) spins within organic polymer poly(methyl methacrylate), or PMMA (molecular weight of 950k, from *MicroChem Corp.*), which is dissolved in methyl isobutyl ketone (MIBK) with 2 % by weight and spin-coated on the diamond sample at 5000 rpm (Fig. 5.2). The polymer film is baked in a vacuum oven for 2 hours at 115 ^{o}C in a flowing nitrogen atmosphere of 100 mTorr. The thickness of the PMMA layer is not measured specifically on the diamond sample, however, it is estimated to be $\sim$ 60 nm based on a similar film prepared on a silicon wafer. The proton density in the polymer layer is estimated to be $\rho_N \sim 57$ nm^{-3}. On the course of measurements, the photon count of a single NV center gradually increases from $\sim$ 25 kilo counts per second (kcps) to $\sim$ 80 kcps due to slow migration of PMMA forming a micro lens, which is also observed by an optical microscope after the measurement. Although origin and mechanism of this PMMA migration is unclear, the NV center photon count returns to $\sim$ 25 kcps after removal of the PMMA layer.

All the measurements are carried out using a home-built confocal microscope setup similar to the one described in Section 4.5.1, using an x100 objective lens with 0.8 NA and a 12 mm diameter NdFeB permanent magnet to produce an external magnetic field in a range of 70 to 80 mT. Microwave and RF signals are generated by a vector signal generator and a function generator,

respectively, which are combined using passive filters and drive the microwire on the sample [102].

5.2.2 Statistical polarization

As detection volume of nuclear spins approaches to nanometer scale, a certain type of polarization different from the Boltzmann polarization becomes dominant: the statistical polarization.

The spin polarization of an ensemble of nuclear spins is defined by the difference in populations of different spin orientations. Although a mean value of the net polarization of nuclear spins is zero at ordinary temperature and low magnetic field, an instantaneous polarization can take non-zero values due to random fluctuation of nuclear spins and their incomplete cancellation. Assuming that the nuclear spin is a spin-1/2 system (up or down) with a total number of spin $N = N_{\uparrow} + N_{\downarrow}$, where $N_{\uparrow}$ and $N_{\downarrow}$ are the population of each spin state, the difference in the up and down spin population $\Delta N = N_{\uparrow} - N_{\downarrow}$ can fluctuate and take either a positive or a negative value on the time scale defined by the spin correlation time τ_c, such as a spin-lattice relaxation time T_1 (Fig. 5.4). As the statistical properties of an ensemble spin-1/2 system can be described by a binomial distribution, a variance of the spin population difference can be written as

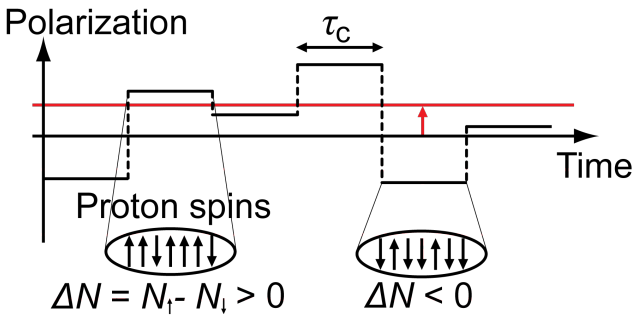


Figure 5.4: Schematic of statistical polarization. The spin polarization of an ensemble of proton spins is defined by the population difference of up and down spins, $\Delta N = N_\uparrow - N_\downarrow$, which can take random values each constant for a short time scale characterized by the spin correlation time τ_c. Black arrows represent proton spin configuration in each "snap shot" of the spin system. A red line and arrow represent a standard deviation of the random spin polarization over a long course of time, which is proportional to a square root of the number of total spin $\sqrt{N}$.

$$\sigma^2_{\Delta N} = N\left[1 - \left(\frac{\overline{\Delta N}}{N}\right)^2\right], \tag{5.3}$$

where $\overline{\Delta N}$ is a mean value of ΔN. For the cases of small mean polarization ($\overline{\Delta N} \sim 0$), the variance is simply reduced to $\sigma^2_{\Delta N} = N$, leading to a standard deviation of the polarization $\sigma_{\Delta N} = \sqrt{N}$ and hence the statistical polarization is proportional to a square root of the total number of the spins, $\sqrt{N}$.

Now, it is shown that the statistical polarization can exceed the Boltzmann polarization for a small sample volume on the nanometer scale. From Equations (5.1) and (5.2), the Boltzmann polarization can be written as

$$\Delta N_{Boltzmann} = N\frac{\gamma\hbar B}{k_B T}, \tag{5.4}$$

while the statistical polarization is expressed as

$$\Delta N_{Statistical} = \sqrt{N}. \tag{5.5}$$

A condition to be set is

$$\Delta N_{Statistical} > \Delta N_{Boltzmann}, \tag{5.6}$$

which derives an equation

$$V < \left(\frac{\gamma\hbar B}{k_B T}\right)^{-2} \rho^{-1}, \tag{5.7}$$

where V is the sample volume and ρ is the nuclear spin density in the sample. Plugging in parameters reflecting the experimental condition of $\gamma = 2\pi \times 42.576$ MHz/T (gyromagnetic ratio of ^{1}H nuclear spins), $T = 300$ K and $B = 80$ mT, and $\rho \sim 57$ nm^{-3}, the "critical" volume below which the statistical polarization exceeds the Boltzmann polarization is calculated to be (3.9 μm)^3, suggesting that the statistical polarization signal dominates for the nanometer-scale volume detection of nuclear spins under the experimental conditions.

5.2.3 Measurement protocol

The proton spin signal is detected by coupling the NV center spin to the statistical polarization of the longitudinal magnetization of proton spins, which is governed by the spin-lattice relaxation time T_{1n} on the order of seconds, much

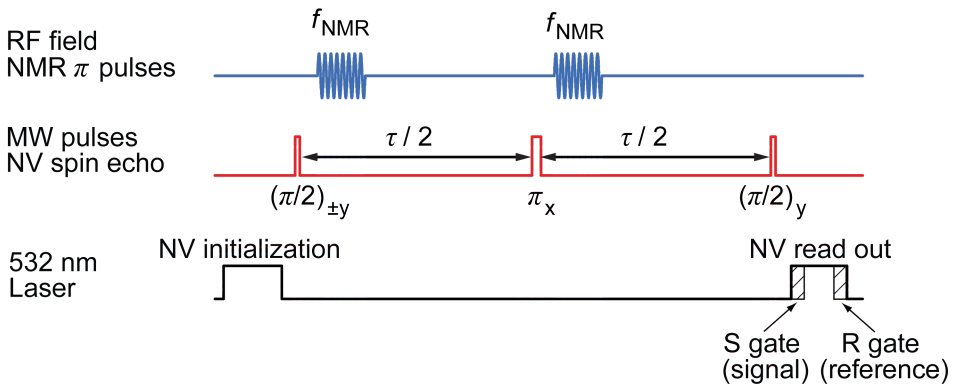


Figure 5.5: Schematic of pulse sequence used for the nanoNMR measurements. A top blue line represents RF π pulses to manipulate proton spins applied in synchronous with microwave pulses (red line) for the NV center spin control. The microwave pulses form a $(\pi/2)_{\pm y} - \tau/2 - (\pi)_x - \tau/2 - (\pi/2)_y$ Hahn echo sequence. The initial $(\pi/2)_{+y}$ pulse leaves the NV center spin in the dark state ($m_s = \pm 1$) at the end of the total echo time of τ, whereas the $(\pi/2)_{-y}$ pulse leaves it in the bright state ($m_s = 0$), allowing for differential measurements. 532 nm laser pulses are used to initialize and read out the NV center spin state. The S and R gates synchronized with the NV read out pulse collect photon counts for the spin signal and the reference. The sequence is repeated for many times to accumulate statistical signal. The NV center photon count is measured while sweeping RF frequency f_{NMR}, enabling NMR spectroscopy measurements. Original data presented in Ref. [102].

longer than the total echo time τ of hundreds of microseconds. The full advantage of long T_{1n} can be taken by using a pulse sequence analogous to the double resonance. Due to the long T_{1n}, the proton field is essentially constant over the Hahn echo measurement of NV center, and the proton field is inverted in synchronous with the Hahn echo π pulse for the NV center spin control, maximizing the proton field sensed by the NV spin.

Figure 5.5 describes a measurement protocol of the nanoNMR scheme.

The NV center spin is initialized into $m_s = 0$ state using a 4-μs pulsed green laser excitation. A $(\pi/2)_{\pm y}$ microwave pulse prepares the NV center spin state into a superposition of $m_s = 0$ and ± 1 sates. The longitudinal proton magnetic field is detected by the NV center spin using a Hahn echo microwave pulse sequence consisting of $(\pi/2)_{\pm y} - \tau/2 - (\pi)_x - \tau/2 - (\pi/2)_y$, where τ of 300 or 440 μs is the total echo time. The initial $(\pi/2)_{+y}$ pulse leaves the NV center spin in the dark state ($m_s = \pm 1$) whereas $(\pi/2)_{-y}$ pulse in the bright state ($m_s = 0$) at the end of the echo sequence, allowing for a differential measurement. After the final $(\pi/2)_y$ pulse, a green laser is shined in order to measure the population of the NV center spin state. The PL signal in each sequence is normalized by the reference signal measured simultaneously during the spin read out pulse in order to minimize the systematic fluctuation of the PL signal.

During the microwave pulse sequence, two RF π pulses are synchronously applied to manipulate proton spins. The first RF pulse sets an initial random longitudinal polarization of the proton spins for the first half of the echo sequence, while the second RF pulse inverts the proton spin polarization for the second half when the RF frequency f_{NMR} is in resonance with the proton Larmor frequency. The inversion of the proton spin polarization reverses the proton magnetic field acting on the NV center, which disturbs the equivalence of the spin evolution for the two halves of the echo sequence. This disturbance re-

duces the spin population in the $m_s = 0$ state at the end of the sequence, which is measured as a decrease in the echo amplitude. The RF frequency f_{NMR} is swept while running the pulse sequence, which allows for a spectroscopic measurement of the nanoNMR.

The two RF pulses are exactly identical consisting of 30 sine wave cycles in order to minimize tedious errors such as "cross talk" of the RF and microwave signals, as the unexpected magnetic field disturbance on the NV center caused by the RF pulse would be cancelled out for the two halves of the echo if the pulses are identical.

5.3 nanoNMR results

5.3.1 nanoNMR

The key results of the nanoNMR measurement are shown in Fig. 5.6(a). The NV center's echo amplitude is measured as a function of f_{NMR} under a static external field of B_0. The three scans correspond to different B_0 of 79.5 (blue), 76.9 (red) and 74.2 (black) mT. As expected, the echo amplitude in each scan decreases when f_{NMR} is in resonance with the proton Larmor frequency at given B_0 showing a dip around the resonant frequency. The dip frequency is plotted as a function of B_0 in Fig. 5.6(b). A linear fit to the data results in a slope of 42.6 MHz/T consistent with the proton gyromagnetic ratio of 42.576

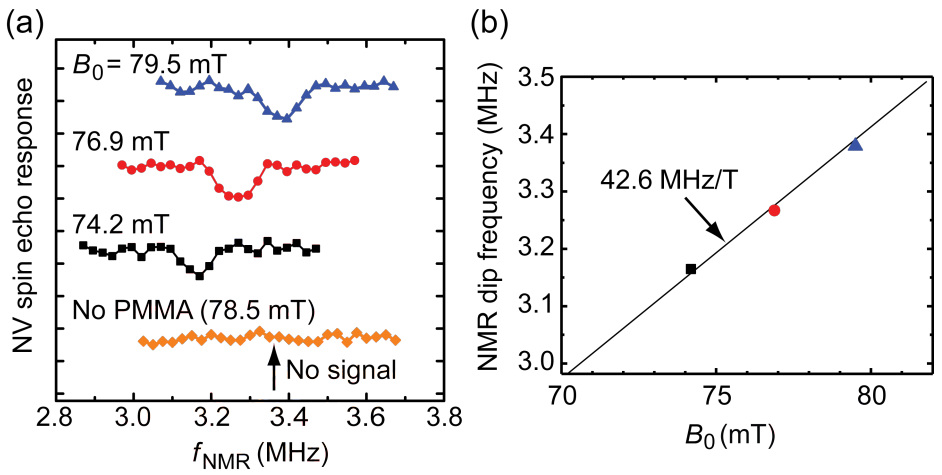


Figure 5.6: Results of nanoNMR measurements. (a) NV spin echo response as a function of frequency f_{NMR}. Curves in blue, red and black are data for the different external magnetic field $B_0 = 79.5$, 76.9 and 74.2 mT, respectively. These curves show dips when f_{NMR} is in resonance with the proton Larmor frequency at given B_0. A curve in orange is the data after removing the PMMA layer, displaying no dip at the expected Larmor frequency corresponding to $B_0 = 78.5$ mT indicated by a black arrow. (b) NMR dip frequency measured by the data shown in (a) as a function of B_0. The line is a fit to the three data resulting in 42.6 MHz/T, consistent with the gyromagnetic ratio of proton spin. Original data presented in Ref. [102].

MHz/T, providing an evidence of detecting proton spins. When the PMMA layer is removed by an acid cleaning, no dip is observed at the expected Larmor frequency (orange curve in Fig. 5.6(a)), confirming that the signal is originated from the organic polymer layer *external* to the diamond.

5.3.2 nanoNMR spectrum by Fourier transform method

Although the data shown in Fig. 5.6(a) demonstrates the spectroscopic feature of the nanoNMR scheme, the dip is broadened $\sim$ 100 kHz due to the

amplitude of RF pulses. The spectral resolution can be improved by applying a Fourier transform technique where a time domain free induction decay (FID) data is Fourier transformed to obtain a NMR frequency data.

To obtain a time domain data, the RF π pulses are split into two identical $\pi/2$ pulses consisting of exact 15 sine wave cycles as shown in Fig. 5.7(a). The spacing between the two $\pi/2$ pulses τ_n is incremented while spin echo amplitude data is taken. This scheme is similar to the Ramsey experiment except that the RF frequency is in resonance with the proton frequency. The resulting data is shown in Fig. 5.7(b), displaying a clear oscillation with a period consistent with the proton Larmor frequency. No oscillation is observed when the RF frequency is off resonance by 600 kHz (data not shown).

In order to obtain a longer time record, a coarser time step of τ_n is used, which speeds up the measurement but results in undersampling of the Larmor frequency oscillation leading to an aliasing effect that shifts the Larmor frequency to the lower. Despite the undersampling, the spin echo amplitude decays for the first ~ 15 μs as shown in Figure 5.7(c), which is consistent with the T_{2n}* of ~ 14 μs for proton spins in PMMA. Some oscillation persisting for a longer time scale up to ~ 50 μs is also observed in the data, whose origin is unclear, but proton spins in some residual solvent may display long T_{2n}*.

The time domain data is cosine transformed to obtain a spectrum data,

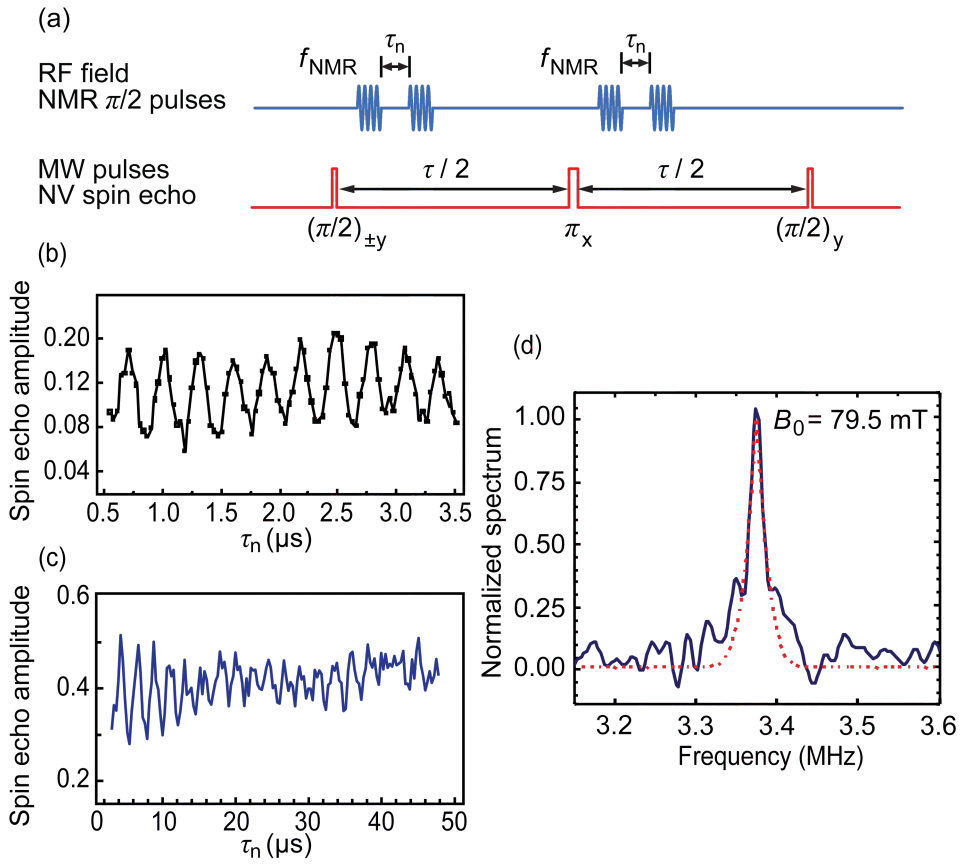


Figure 5.7: nanoNMR results by a Fourier transform method. (a) Schematic of the pulse sequence. The RF pulses are split into two identical $\pi/2$ pulses whose spacing τ_n is incremented while NV center spin echo response is recorded. The RF frequency f_{NMR} is fixed at the proton Larmor frequency. The time domain free induction decay (FID) data for a shorter and a longer time scale are shown in (b) and (c). To obtain a longer time record, a coarser τ_n is used in (c), resulting in undersampling of the Larmor frequency oscillation causing an aliasing effect. (d) Spectrum data obtained by a cosine transformation of the FID data shown in (c). The external field is $B_0 = 79.5$ mT. Frequencies are shifted in order to compensate the aliasing effect. A red dotted curve represents a spectrum of PMMA taken by a conventional 500 MHz NMR using a magnetic field of 11.75 T. Original data presented in Ref. [102].

which is shown in Fig. 5.7(d). The data shows a single narrow peak at the Larmor frequency of the proton spin after compensating the aliasing effect. The peak width is $\sim$ 20 kHz, comparable to a conventional 500 MHz NMR data of proton spins in PMMA, which is overlay in the same figure. The external magnetic field used to take the time domain data in the nanoNMR scheme is B_0 = 79.5 mT, which is orders of magnitude smaller than the magnetic field of 11.75 T used in the conventional 500 MHz NMR, demonstrating an advantage of the nanoNMR scheme that does not require a high magnetic field to obtain spectral resolution comparable to the conventional NMR.

5.4 Analysis

5.4.1 Estimation of proton magnetic field signal

The amplitude of the proton magnetic field, B_{rms}, can be calculated by the depth of dips in the nanoNMR signal shown in Fig. 5.6(a). In this subsection, an equation that relates the experimental results with the proton magnetic field is derived, which is used to estimate the proton signal.

The phase accumulated by the NV center during the total echo time of τ in the Hahn sequence can be expressed as [150]

$$\delta\phi = \gamma \int_0^{\tau/2} B_N(t)dt - \gamma \int_{\tau/2}^{\tau} B_N(t)dt, \tag{5.8}$$

where $\gamma = 2\pi \times 28$ GHz/T is the gyromagnetic ratio of the NV center electronic spin, and $B_N(t)$ is the proton magnetic field. For a specific case used in the experiment where the proton spins are inverted synchronously with the microwave π pulse in the middle of the echo (see Fig. 5.5), Equation (5.8) is reduced to

$$\delta\phi = \gamma \int_0^\tau B_N(t) dt. \tag{5.9}$$

Assuming that the accumulated phase $\delta\phi$ is a normally distributed variable with zero mean, the spin echo response can be written as[1],

$$\begin{aligned} \xi(\tau) &= \xi_0(\tau) \langle \cos(\delta\phi) \rangle \\ &= \xi_0(\tau) \exp\left[-\frac{\langle (\delta\phi)^2 \rangle}{2} \right], \end{aligned} \tag{5.10}$$

where $\xi_0(\tau)$ is the echo response in the absence of proton magnetic field and $\langle \cdots \rangle$ indicates the mean value. From this equation, a mean square phase is

[1]For normally distributed variable x with zero mean and σ^2 variance, the mean of $\cos x$ is calculated as

$$\int_{-\infty}^{\infty} \frac{1}{\sqrt{2\pi\sigma^2}} \exp\left(-\frac{x^2}{2\sigma^2} \right) \cos x dx = \exp\left(-\frac{\sigma^2}{2} \right).$$

This equation is used to derive Equation (5.10).

computed by the spin echo response through a following equation[2],

$$\begin{aligned}\left\langle (\delta\phi)^2 \right\rangle &= -2\log\frac{\xi(\tau)}{\xi_0(\tau)} \\ &= 2\cdot\frac{\xi_0(\tau)-\xi(\tau)}{\xi_0(\tau)} \\ &= 2\cdot\frac{\Delta\xi}{\xi_0(\tau)},\end{aligned} \tag{5.11}$$

where $\Delta\xi/\xi_0(\tau)$ is the fractional change in spin echo amplitude caused by the proton magnetic field.

On the other hand, the mean square phase can also be derived by computing the phase accumulated by the NV center,

$$\begin{aligned}\left\langle (\delta\phi)^2 \right\rangle &= \left\langle \left[\gamma\int_0^\tau B_N(t)dt\right]^2 \right\rangle \\ &= \left\langle \left[\gamma\int_0^\tau B_N(t)dt\right]\left[\gamma\int_0^\tau B_N(t)dt\right] \right\rangle \\ &= \gamma^2\left[\int_0^\tau\int_0^\tau \left\langle B_N(t)B_N(t')\right\rangle dtdt'\right].\end{aligned} \tag{5.12}$$

Since longitudinal polarization of proton spins have a spin correlation time T_{1n} much longer than the total echo sequence time τ ($T_{1n} \gg \tau$), the proton magnetic field is essentially constant during the echo sequence, resulting in

$$\left\langle B_N(t)B_N(t')\right\rangle = \left\langle B_N^2\right\rangle, \tag{5.13}$$

[2]Using the Taylor expansion, $\log(1+x)\approx x$, or $-\log(1-x)\approx x$ for small x ($|x|<1$). The latter equation is used to derive Equation (5.11) by substituting $x=\Delta\xi/\xi_0(\tau)$. The validity of the Taylor expansion is ultimately confirmed from the experimental result $x=\Delta\xi/\xi_0(\tau)=0.2<1$.

which further leads to

$$\left\langle (\delta\phi)^2 \right\rangle = \gamma^2 \left\langle B_N^2 \right\rangle \tau^2. \tag{5.14}$$

By comparing Equations (5.11) and (5.14), a square proton field can be written as

$$\left\langle B_N^2 \right\rangle = \frac{2}{\gamma^2 \tau^2} \frac{\Delta\xi}{\xi_0(\tau)}. \tag{5.15}$$

The results shown in Fig. 5.6(a) display dip depths roughly $\Delta\xi/\xi_0(\tau) \approx 0.2$, which according to Equation (5.15) leads to the proton root-mean-square (rms) field of

$$B_{rms} = \sqrt{\left\langle B_N^2 \right\rangle} = 12\text{nT} - \text{rms}. \tag{5.16}$$

This is the proton magnetic field signal estimated by the experimental results.

5.4.2 Proton sensitivity of NV center

The NV center's proton field sensitivity is constrained by its spin coherence time and the optical read out of the spin states, which can be estimated by finding a minimum rms field B_{min} leading to a unity signal-to-noise ratio (SNR) assuming that the NV center's spin read out is limited by the photon shot noise.

The spin echo signal is always measured by taking difference in the signal prepared in two different initial states by applying $(\pi/2)_{+y}$ and $(\pi/2)_{-y}$ pulses at the beginning. The $(\pi/2)_{+y}$ initial pulse leaves the NV center spin state in the dark state ($m_s = \pm 1$) at the end of the echo sequence, whereas the $(\pi/2)_{-y}$

initial pulse leaves in the bright state ($m_s = 0$). Define $S^+(\tau)$ and $S^-(\tau)$ to be the photon counts corresponding to the $(\pi/2)_{+y}$ and $(\pi/2)_{-y}$ initial pulses after the total echo time τ. In order to minimize systematic measurement error, these spin signals $S^{\pm}(\tau)$ are normalized by the reference signal $R^{\pm}(\tau)$ that are measured simultaneously during the spin read out pulse (Fig. 5.5). The spin echo contrast is therefore calculated by

$$\tilde{S}(\tau) = \frac{S^-(\tau) - S^+(\tau)}{\frac{1}{2}\left[R^-(\tau) + R^+(\tau)\right]}, \tag{5.17}$$

and the normalized spin echo signal is defined as

$$\xi(\tau) = \frac{\tilde{S}(\tau)}{\tilde{S}_0}, \tag{5.18}$$

where $\tilde{S}_0 = \tilde{S}_0(0)$ is the spin echo contrast for fully polarized bright and dark states of the NV center (typically ~ 0.30) and $\tilde{S}_0(\tau)$ is the spin echo contrast in the absence of proton magnetic field ($B_{rms} = 0$). $\xi(\tau)$ is sometimes referred as "coherence", which is ~ 1 for the short echo time and goes to zero for $\tau \gg T_{2e}$. The spin echo signal in the absence of proton field, $\xi_0(\tau)$ is plotted in Fig. 5.3. Combining Equations (5.17) and (5.18), the spin echo signal can be written as

$$\xi(\tau) = \frac{S^-(\tau) - S^+(\tau)}{\frac{1}{2}\left[R^-(\tau) + R^+(\tau)\right]} \frac{\frac{1}{2}\left[R_0^-(0) + R_0^+(0)\right]}{S_0^-(0) - S_0^+(0)}. \tag{5.19}$$

Assuming that $R^{\pm}$ are photon counts for the NV center spin fully polarized during the read out pulse to $m_s = 0$ state, which is independent of τ and B_{rms}, the spin echo signal can be reduced to

$$\xi(\tau) = \frac{S^{-}(\tau) - S^{+}(\tau)}{S_0^{-}(0) - S_0^{+}(0)}, \tag{5.20}$$

and

$$\xi_0(\tau) = \frac{S_0^{-}(\tau) - S_0^{+}(\tau)}{S_0^{-}(0) - S_0^{+}(0)}, \tag{5.21}$$

leading to the normalized signal in the presence of proton field,

$$\frac{\xi_0(\tau) - \xi(\tau)}{\xi_0(\tau)} = 1 - \frac{S^{-}(\tau) - S^{+}(\tau)}{S_0^{-}(0) - S_0^{+}(0)}. \tag{5.22}$$

In order to compute statistical uncertainty in the normalized signal, the effect of the denominator in Equation (5.22), $S_0^{-}(0) - S_0^{+}(0)$, can be ignored as it is assumed to be a constant normalization factor that has been well calibrated. Hence the uncertainty in $S^{\pm}(\tau)$ is analyzed assuming that they are limited by the photon shot noise. In the limit of small B_{rms},

$$\Delta S^{\pm}(\tau) = \sqrt{S^{\pm}(\tau)} \approx \sqrt{S_0^{\pm}(\tau)}, \tag{5.23}$$

leading to an overall noise

$$\frac{\sqrt{(\Delta S^-(\tau))^2+(\Delta S^+(\tau))^2}}{S_0^-(\tau)-S_0^+(\tau)}=\frac{\sqrt{S_0^-(\tau)+S_0^+(\tau)}}{S_0^-(\tau)-S_0^+(\tau)}. \tag{5.24}$$

According to Equation (5.15), the normalized signal caused by a proton magnetic field of B_{rms} can be written as

$$\frac{\xi_0(\tau)-\xi(\tau)}{\xi_0(\tau)}=\frac{1}{2}\gamma^2 B_{rms}^2\tau^2, \tag{5.25}$$

where $\gamma=2\pi\times 28$ GHz/T is the gyromagnetic ratio of the NV center electronic spin. In order to compute minimum detectable rms proton magnetic field, B_{min} (i.e. SNR = 1), setting the signal equal to the noise gives

$$\frac{1}{2}\gamma^2 B_{rms}^2\tau^2=\frac{\sqrt{S_0^-(\tau)+S_0^+(\tau)}}{S_0^-(\tau)-S_0^+(\tau)}. \tag{5.26}$$

Assuming that $S_0^-(0)+S_0^+(0)$ is independent of τ such that $S_0^-(\tau)+S_0^+(\tau)=S_0^-(0)+S_0^+(0)$, then,

$$\begin{aligned} B_{min}^2 &= \frac{2}{\gamma^2\tau^2}\frac{\sqrt{S_0^-(0)+S_0^+(0)}}{S_0^-(\tau)-S_0^+(\tau)} \\ &= \frac{2}{\gamma^2\tau^2\xi_0(\tau)}\frac{\sqrt{S_0^-(0)+S_0^+(0)}}{S_0^-(0)-S_0^+(0)}. \end{aligned} \tag{5.27}$$

In order to derive an expression of B_{rms} in terms of total acquisition time T_a, define α_0 and β_0 to be the average counts per echo sequence in the bright ($m_s=$

0) and the dark ($m_s = \pm 1$) states as $\alpha_0 = S_0^-(0)/N_E$ and $\beta_0 = S_0^+(0)/N_E$, where N_E is the total repetition number of the echo sequence. The total acquisition time is then defined as $T_a = 2N_E\tau$, where a factor of 2 arises from the separate measurements for S^- and S^+ in the one measurement cycle. Combining all these parameters into Equation (5.27) leads to a final expression,

$$B_{min}^2 = \frac{2\sqrt{2}}{\gamma^2\tau^{3/2}\xi_0(\tau)} \frac{\sqrt{\alpha_0+\beta_0}}{\sqrt{T_a}(\alpha_0-\beta_0)}. \tag{5.28}$$

Under experimental parameters of $\alpha_0 = 0.02$, $\beta_0 = 0.014$, $\tau = 440$ μs and $\xi_0(\tau) = 0.60$ as well as setting a reasonable acquisition time of $T_a = 1$ s, the NV center's proton magnetic field sensitivity is calculated to be $B_{min} = 8$ nT-rms.

The calculated sensitivity is comparable to the proton magnetic signal B_{rms} = 12 nT-rms estimated by the experimental results, suggesting that the measurement is effective.

5.4.3 Detection volume

It is important to calculate the detection volume as it leads to the number of protons contributing to the signal detected by the NV center. The goal of this subsection is to calculate a volume corresponding to the estimated proton magnetic signal $B_{rms} = 12$ nT (Section 5.4.1) or proton sensitivity $B_{min} = 8$ nT

(Section 5.4.2). First, an expression for the magnetic field from a proton at a point $\mathbf{r}$ is derived, which is integrated over a volume to calculate the total proton field on the NV center. Ideal cases are analyzed assuming that the signal from a half-infinite space of protons in the polymer layer is detected by the NV center with infinitely small sensitivity, and then a more realistic case is examined by setting finite sensitivity of the NV center resulting in a finite detection volume.

Assuming that the quantization axis of the proton spin $\hat{\mathbf{q}}$ is aligned to the external magnetic field, which is parallel to the NV center symmetric axis along $\langle 111 \rangle$ direction, the component of the proton magnetic field at the NV center along the symmetry axis ($\| \hat{\mathbf{q}}$) can be written as

$$B_q(\mathbf{r}) = \hat{\mathbf{q}} \cdot \mathbf{B} = \pm \frac{\mu_0 \mu_p}{4\pi} \left[\frac{3\left(\mathbf{q}\hat{\cdot}\mathbf{r}\right)^2 - 1}{r^3} \right], \tag{5.29}$$

where $\mathbf{r}$ is the vector from the proton to the NV center, $\hat{\mathbf{r}}$ is the unit vector along $\mathbf{r}$, $\mu_0 = 4\pi \times 10^{-7}$ Vs/Am is the vacuum permeability and $\mu_p = 1.41 \times 10^{-26}$ J/T is the magnetic moment of the proton. A root-mean-square (rms) field from an ensemble of proton spins is

$$\begin{aligned} B_{rms}^2 &= \left\langle \left[\sum_i B_q(\mathbf{r}_i) \right]^2 \right\rangle \\ &= \left\langle \sum_{i,j,i \neq j} B_q(\mathbf{r}_i) B_q(\mathbf{r}_j) + \sum_i B_q^2(\mathbf{r}_i) \right\rangle. \end{aligned} \tag{5.30}$$

The first summation of Equation (5.30) is zero for random, uncorrelated spins,

therefore,

$$B_{rms}^2 = \sum_i B_q^2(\mathbf{r}_i). \tag{5.31}$$

Assuming that protons in polymer are continuous with a constant density of ρ_N, the summation can be converted to an integral,

$$B_{rms}^2 = \rho_N \int_V \left[B_q(\mathbf{r})\right]^2 dV. \tag{5.32}$$

As a first step, the integral in Equation (5.32) is taken over the half-infinite space of polymer, which represents a relatively thick polymer layer on the surface. Specifically, two cases where the diamond film is grown on the (111) and (100) planes are considered. For the case of the (111) plane, where $\hat{\mathbf{q}}$ is perpendicular to the sample surface, the integral is taken in spherical coordinates as

$$B_{rms}^2 = 2\pi \left(\frac{\mu_0 \mu_p}{4\pi}\right)^2 \rho_N \int_0^{\pi/2} \int_{d/\cos\theta}^{\infty} \left(\frac{3\cos^2\theta - 1}{r^3}\right)^2 r^2 \sin\theta \, dr d\theta, \tag{5.33}$$

where d is the depth of the NV center and θ is the polar angle measured from the normal to the sample plane. The result is

$$\begin{aligned} B_{rms} &= \frac{1}{8\sqrt{\pi}} \mu_0 \mu_p \frac{\rho_N^{1/2}}{d^{3/2}} \\ &\approx 0.071 \mu_0 \mu_p \frac{\rho_N^{1/2}}{d^{3/2}}. \end{aligned} \tag{5.34}$$

For the (100) plane case representing the experiment, where $\hat{\mathbf{q}}$ is tilted 54.7° (the angle between $\langle 111 \rangle$ and $\langle 100 \rangle$ direction) from the axis normal to

the surface, the integral in spherical coordinates will be calculated by substituting $\hat{\mathbf{q}} = 1/\sqrt{3}\begin{pmatrix} 1 & 1 & 1 \end{pmatrix}$ and $\hat{\mathbf{r}} = \begin{pmatrix} \sin\theta\cos\phi & \sin\theta\sin\phi & \cos\theta \end{pmatrix}$ into Equations (5.29) and (5.32), leading to

$$B_{rms}^2 = \left(\frac{\mu_0\mu_p}{4\pi}\right)^2 \rho_N \int_0^{\pi/2} \int_{d/\cos\theta}^{\infty} \int_0^{2\pi} \left(\frac{2\sin^2\theta\cos\phi\sin\phi + 2\sin\theta\cos\theta\cos\phi + 2\sin\theta\cos\theta\sin\phi}{r^3}\right)^2 r^2 \sin\theta d\phi dr d\theta. \tag{5.35}$$

The result is

$$\begin{aligned} B_{rms} &= \frac{1}{8\sqrt{2\pi}} \mu_0\mu_p \frac{\rho_N^{1/2}}{d^{3/2}} \\ &\approx 0.050\mu_0\mu_p \frac{\rho_N^{1/2}}{d^{3/2}}, \end{aligned} \tag{5.36}$$

leading to $B_{rms,ideal}^{(100)} = 75$ and 598 nT by substituting $d = 20$ and 5 nm into Equation (5.36). These results are the ideal proton magnetic field contributed by all protons in the half-infinite space of the polymer layer, which are detected by the NV center with infinitely small sensitivity.

In reality, only protons in a small volume of the polymer near the surface are detected since the NV center has a finite sensitivity. To estimate the detection volume, proton fields $B_q(\mathbf{r})$ are calculated for each small volume dV at point $\mathbf{r}$, sorted in descending order and integrated using Equation (5.32) until the integration reaches a certain magnetic field $B_{detection}$. Detection volume is calculated for the case of $d = 20$ nm and the surface parallel to the (100) plane,

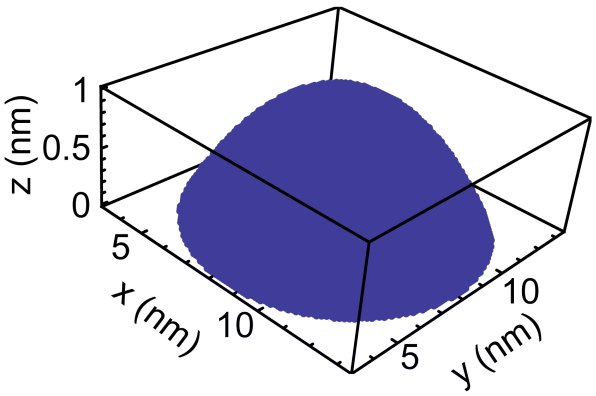


Figure 5.8: Three-dimensional plot of positions of protons (blue dots) that collectively contributes to a magnetic signal of 8 nT on the NV center. The *xy* plane corresponds to the (100) plane and the NV center is located 20 nm below the origin.

representing the experiment.

If $B_{detection}$ is set equal to the estimated proton magnetic signal $B_{rms} = 12$ nT, the detection volume is estimated to be $(4.8\text{ nm})^3$, corresponding to a number of proton spins $N \sim 6100$. Furthermore, setting $B_{detection} = B_{min} = 8$ nT leads to a detection volume of $(3.5\text{ nm})^3$, corresponding to $N \sim 2400$, leading to a conclusion that the presented nanoNMR scheme detects spin signals from the number of protons on the order of $\sim 10^3$. The three-dimensional positions of protons on the surface contributing to a collective signal of $B_{detection} = 8$ nT is plotted in Fig. 5.8.

5.4.4 Towards single proton spin detection

In order to give an insight into directions towards the single proton spin

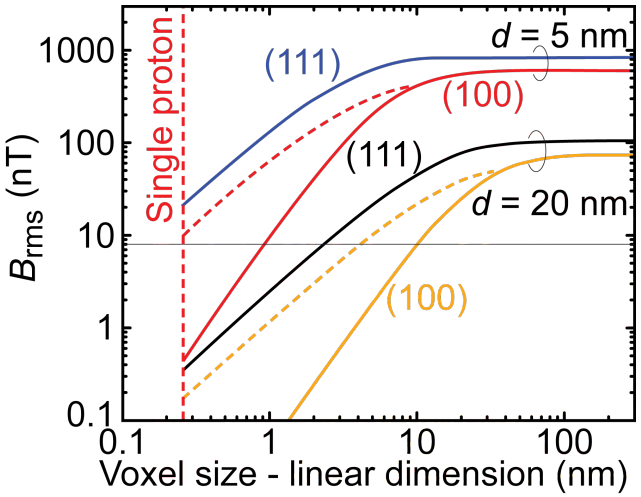


Figure 5.9: Root-mean-square field (B_{rms}) from a cubic volume (voxel) of proton as a function of its side length. Curves in orange and black are calculated results for a NV center 20 nm deep with the sample surface parallel to the (100) and (111) plane. Curves in red and blue are the (100) and (111) results for a 5-nm deep NV center. Solid lines are for the results assuming that the voxel is located on the surface immediately above the NV center. Dotted lines in orange and red are for the results of a NV center 20 and 5 nm deep with the optimized voxel position on the (100) surface. A vertical dotted line represents a voxel size corresponding to a single proton, and a horizontal line corresponds to $B_{rms} = 8$ nT. Original data presented in Ref. [102].

detection, the rms magnetic field from a cubic volume of protons ("voxel") is calculated as a function of the length of its side as shown in Fig. 5.9. Four plots are for each of combinations of NV center depth ($d = 5$ and 20 nm) and the surface planes ((111) and (100)). The solid curves are for voxels assumed to be placed on the surface right above the NV center, whereas dashed curves are for the optimized position of the voxel on the (100) surface. This consideration is necessary as NV centers is insensitive to the proton spins immediately above

on the (100) plane due to a vanishing angular term of the proton magnetic field $3\left(\hat{\mathbf{q}}\cdot\hat{\mathbf{r}}\right)^2-1=0$ (so-called the "magic angle").

As discussed in the previous subsection, proton sensitivity of 8 nT-rms for $d=20$ nm on the (100) surface corresponds to a proton volume of $(3.5\text{ nm})^3$ at the optimized position, which can be read from the dashed curve in orange in the figure. The proton volume can be reduced to $\sim(2\text{ nm})^3$ for the (111) plane at the same depth.

From Equation (5.28), the proton sensitivity B_{min} is roughly proportional to $(T_{2e})^{-3/4}$. As discussed in Section 4, a shallow NV center at $d=5$ nm grown on the (100) plane display $T_{2e}\sim 200\ \mu$s, resulting in an estimated sensitivity of 18 nT for such an NV center corresponding to a proton volume of $\sim(0.4$ nm$)^3$ at the optimized position (dashed curve in red in Fig. 5.9). The proton volume reaches the single proton limit assuming a similar T_{2e} for $d=5$ nm sample grown on the (111) plane.

5.5 Conclusion

A shallowly doped NV center is used to demonstrate the nanoNMR scheme. The NV center spin is coupled to the statistical polarization of the longitudinal magnetization of proton spins. In order to make the most of a long spin-lattice relaxation time T_{1n} associated with the longitudinal polarization, proton

spins are actively manipulated by RF pulses in synchronous with the Hahn echo pulses for NV center spin control. By sweeping the RF frequency, the NV center spin echo response displays dip when the RF frequency is in resonance with the proton Larmor frequency at a given external magnetic field, allowing for a spectroscopic detection of nanoNMR. The dip disappears when the polymer layer is removed from the surface, confirming that the proton signal is originated *external* to the diamond crystal. By analyzing the data, the proton magnetic field signal is calculated to be 12 nT-rms and corresponding detection volume is (4.8 nm)^3, equivalent to $\sim$6100 protons contributing to the signal, demonstrating the nanometer-scale detection of NMR.

This experiment sets an important milestone towards the ultimate goal of the NV-based nanoMRI technique, which is expected to be operated at room temperature. For the realization of nanoMRI, reduction of the acquisition time is necessary in order to sample many points to construct 2D or 3D images. Continuous efforts to increase the proton signal via creating even shallower NV centers with persisting coherence time is still required, which is also important for the outstanding challenge of the single proton spin sensing.

Despite these challenges, the NV-based nanoMRI is potentially capable of room-temperature operation, no radiation damage and elemental selectivity, which can be useful for imaging a certain type of molecules [151], ulti-

mately providing a complementary tool for protein structure determination, an outstanding challenge of the modern structural biology.

Chapter 6

Three-dimensional position control of a single NV center

6.1 Introduction

Diamond-based, nanoscale engineering has drawn extensive interests as it facilitates enhancement of NV center functionalities by coupling NV centers to the nanoscale structures. Examples include photonic crystals [152, 153] and plasmonic cavities [154] to improve photon collection efficiencies, scanning probe devices to increase spatial resolution of magnetic imaging [41], and mechanical resonators to enable a phonon-mediated coherent spin coupling [66, 69]. A critical challenge to enabling scalable creation of these NV-based diamond nanostructures is to maintain spin coherence of an NV center localized at a deterministic position with nanometer scale precision. In this chapter,

a method for three-dimensional (3D) localization of a single NV center is presented, which combines the nitrogen delta-doping technique with post-growth ^{12}C ion implantation. Section 6.2 describes challenges to control NV density by a current existing technique. The concept and the sample preparation process of the ^{12}C implantation technique are described in Section 6.3. Experimental results showing doped NV center activation via vacancy diffusion is presented in Section 6.4. The effects of ^{12}C implantation dose and $^{15}N_2$ doping gas flow is discussed in Section 6.5. 3D localization of a NV center by implanting through nanometer-scale apertures is presented in Section 6.6. Section 6.7 describes a theoretical model of vacancy diffusion leading to an estimation of the localization volume and the nitrogen to NV center conversion efficiency. Another approach for 3D localization using nanometer-scale pillars is presented in Section 6.8. Finally, conclusion and outlook are discussed in Section 6.9.

6.2 Challenges

The nitrogen delta-doping technique enables separate creation of nitrogen incorporation and vacancy creation, which opens up a degree of freedom for post-growth vacancy engineering. A previous approach to vacancy engineering in the delta-doped films uses a high-energy (2 MeV) electron irradiation to create vacancies followed by annealing to diffuse them. However, a drawback

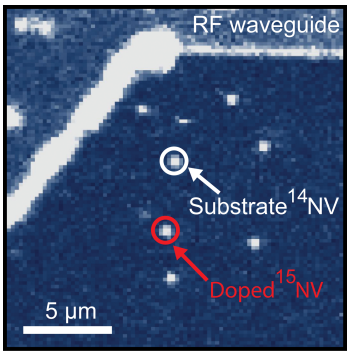


Figure 6.1: Surface confocal scan of an electron irradiated sample ($d = 21$ nm). Sparse bright spots correspond to single NV centers. A doped NV center is circled in red and a substrate NV center is in white. A feature on the top of the figure is a co-planar waveguide.

to the electron irradiation technique is that it results in a low density of doped NV centers, which prevents further incorporation to the device structures. As an example of a low-yield NV center creation via electron irradiation, Fig. 6.1 shows a surface confocal scan of one of the irradiated samples (depth $d = 21$ nm, nitrogen doped layer thickness $t = 1.3$ nm), in which only one doped NV center is found over a 20×20 μm scanned area as circled in red.

Since substitutional nitrogen (P1 centers) are a source of decoherence to NV center spins, the doped NV density must be increased without increasing the nitrogen incorporation [23]. This requirement necessitates vacancy engineering that enhances the conversion efficiency of nitrogen atoms within the nitrogen-doped layers turning into NV centers.

One would think that more nitrogen could turn into NV centers by sim-

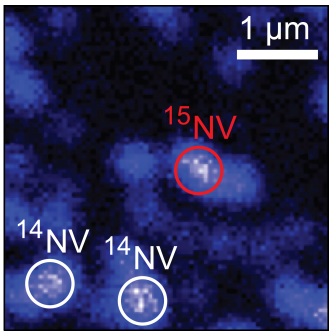


Figure 6.2: Surface confocal scan of an electron irradiated sample, showing not only a doped ^{15}NV center but also dense ^{14}NV centers from the substrate.

ply increasing the electron irradiation dose, as it would create more vacancies. However, this scheme would not work well as it would create a significant amount of background NV centers in the substrate since high-energy electron beam penetrates the diamond crystal (Fig. 6.2).

A key to increase the doped NV density without increasing the nitrogen incorporation and the background NV centers is to localize vacancies near the nitrogen doped layer. Since NV center formation is a probabilistic process that vacancies diffuse to the lattice cite adjacent to nitrogen atoms, localizing vacancies near the nitrogen doped layer will enhance the probability of NV center formation, leading to an increase of the nitrogen to NV center conversion efficiency, and ultimately the doped NV density. In the following sections, a ^{12}C ion implantation technique is described as a method to localize vacancies near the nitrogen delta-doped layer. The use of ^{12}C implantation is inspired by a

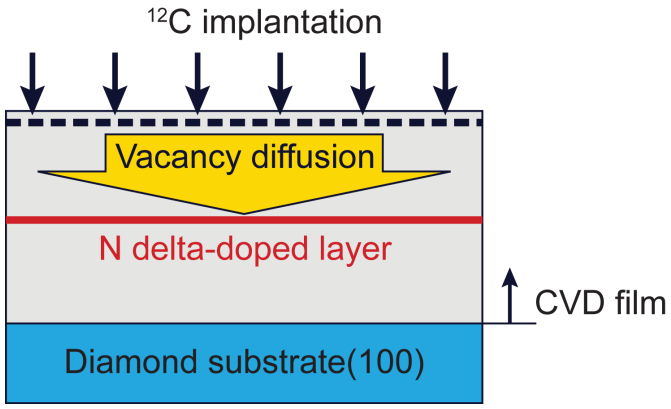


Figure 6.3: Concept of ^{12}C implantation technique and the sample structure. Original data presented in Ref. [156].

previous report that co-implantation of ^{15}N and ^{12}C ions results in an enhanced NV density [155]. The ^{12}C implantation technique is used in combination with the nitrogen delta-doping technique.

6.3 ^{12}C implantation technique: concept and sample preparation

Figure 6.3 illustrates the concept of the ^{12}C implantation technique and the sample structure [156]. After the growth, ^{12}C ions are implanted shallower ($\leq$ 8 nm) than the nitrogen delta-doped layer 51 nm deep from the surface to create a localized layer of vacancies. These vacancies diffuse into the nitrogen delta-doped layer during a subsequent annealing process to form NV centers. Since ^{12}C has no nuclear spin, the NV center spin coherence is not limited by

the carbon nuclear spin bath [26, 155].

A more detailed description of the sample preparation process is as follows. All the samples are grown by the plasma-enhanced chemical vapor deposition (PE-CVD) system using a growth temperature of 800 ^{o}C, microwave power of 750 W, pressure of 25 Torr, H_2 flow of 400 sccm and $^{12}CH_4$ (99.998 %) flow of 0.1 sccm. A ^{12}C buffer layer of 51 or 103 nm thick is first grown, followed by a 6-nm thick ^{15}N delta-doped layer (with $^{15}N_2$ doping gas flow of either 0.1 or 10 sccm) and a ^{12}C cap layer (51 nm), on top of a commercially available electronic grade single crystal diamond (100) substrate from *Element 6*. All the samples are mechanically polished by *Syntek Co.,Ltd* prior to the growth. Isotopically purified $^{15}N_2$ gas (> 98 %) is used to discriminate doped ^{15}NV centers from substrate ^{14}NV centers. After the growth, the sample is ^{12}C ion implanted by *Cutting Edge Ions, LLC* at an implantation energy of either 2 or 7 keV. According to the SRIM calculation [118] these implantation energies create vacancies at 2.4 ± 2.2 nm or 8.0 ± 6.1 nm from the surface, respectively. The incident angle of ^{12}C ions is tilted 7 degrees normal to the surface in order to mitigate ion channeling effects [33]. A ^{12}C implantation dose is selected from a range of 10^9 to 10^{13} cm^{-2} depending on the experiments. After the implantation process, the sample is annealed at either 800 ^{o}C or 850 ^{o}C in a H_2/Ar forming gas atmosphere in order to diffuse vacancies to activate NV cen-

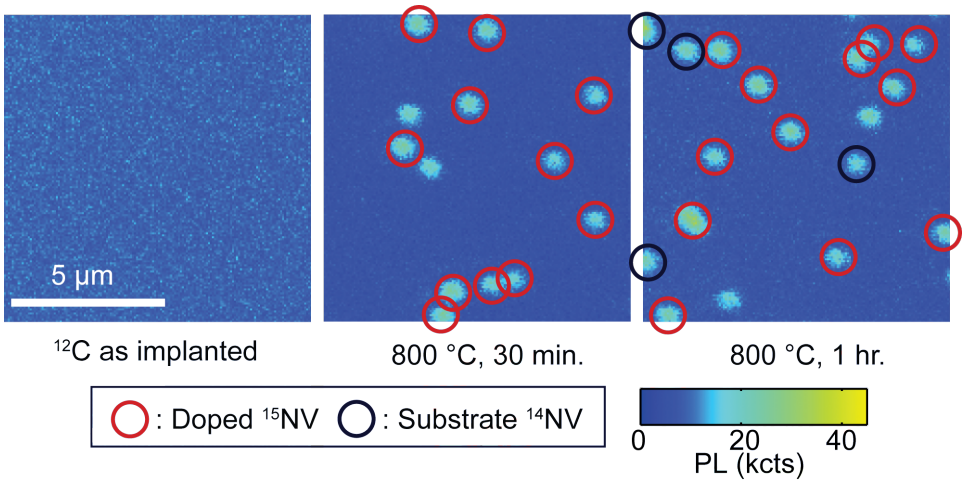


Figure 6.4: Confocal scans of the diamond surface as-implanted (left), after annealed at 800 ^{o}C for 30 min. (center), and 1 hour (right). Doped ^{15}NV centers are circled in red and substrate ^{14}NV centers are in black. PL spots indicative of containing multiple NV centers are not circled. Original data presented in Ref. [156].

ters. Then, the sample surface is cleaned using perchloric acid mixture ($HClO_4$: H_2SO_4 : HNO_3 = 10 mL : 10 mL : 10 mL, at 190 ^{o}C for 30 min.) in order to remove a graphitic layer on the surface as well as to make the surface oxidized to promote the negatively charged NV^- state [95, 96]. All the measurements are carried out using a confocal measurement system (similar to the one described in Section 4.5) under ambient conditions.

6.4 NV center activation via vacancy diffusion

In this section, experimental results showing NV center activation in the nitrogen delta-doped layer via vacancy diffusion are presented. Figure 6.4

shows surface confocal microscope scans of the as-implanted sample (left), after annealed at 800 ^{o}C for 30 min. (center) and 1 hour (right). In this sample, the ^{12}C buffer layer thickness is 103 nm, and an implantation energy of 2 keV and a ^{12}C dose of 10^{10} cm^{-2} are used. The same sample is used for this cumulative annealing study. For each annealing step, three areas on the surface are randomly selected and imaged to count the number of formed NV centers. Continuous wave electron spin resonance (CWESR) is used to discriminate doped ^{15}NV (circled in red in the figures) and substrate ^{14}NV centers (black) by measuring their hyperfine signatures. Some photoluminescence (PL) spots showing CW-ESR signatures of containing multiple NV centers are not circled in the figures.

The as-implanted sample shows no trace of NV-center activation, whereas more than 90 % of all measured NV centers are doped ^{15}NV centers after 30 minutes of the annealing. When the sample is further annealed for total 1 hour, a mixture of doped ^{15}NV centers ($\sim$ 70 % of all measured NV centers) and substrate ^{14}NV centers are observed. This result is consistent with a picture that shallow vacancies created by the ^{12}C ion implantation are diffused into the nitrogen doped layer to activate doped ^{15}NV centers during the annealing process, and they ultimately diffuse deeper to activate ^{14}NV centers in the substrate (See Fig. 6.3). A quantitative analysis of the vacancy diffusion is discussed in

Section 6.7 by applying the one-dimensional (1D) vacancy diffusion model.

6.5 Effects of ^{12}C implantation dose and $^{15}N_2$ doping gas flow

6.5.1 Effects on the NV density

In this section, effects of the process parameters such as ^{12}C implantation dose and $^{15}N_2$ doping gas flow on the doped NV density are discussed. Two samples of nominally identical structure (both have ^{12}C buffer layer thickness of 51 nm) are grown and used for this study. The only difference is the $^{15}N_2$ doping gas flow: 10 sccm and 0.1 sccm are used respectively for each sample. Both samples are ^{12}C implanted at 7 keV on three different quadrants with different ^{12}C doses (10^9, 10^{10}, and 10^{11} cm^{-2}), followed by annealing at 850 ^{o}C for 30 minutes. Six figures shown in Fig. 6.5 are surface confocal scans of each quadrant. For 10^9 and 10^{10} cm^{-2} dose cases, doped ^{15}NV and substrate ^{14}NV centers are isotropically discriminated and circled in red and black, respectively (some NV centers showing inconclusive results due to low CWESR contrasts are left uncircled). Three random areas within each quadrant are measured and NV centers are counted. The average number of doped NV centers found over the scanned 10 μm $\times$ 10 μm area is computed, which is translated to the doped

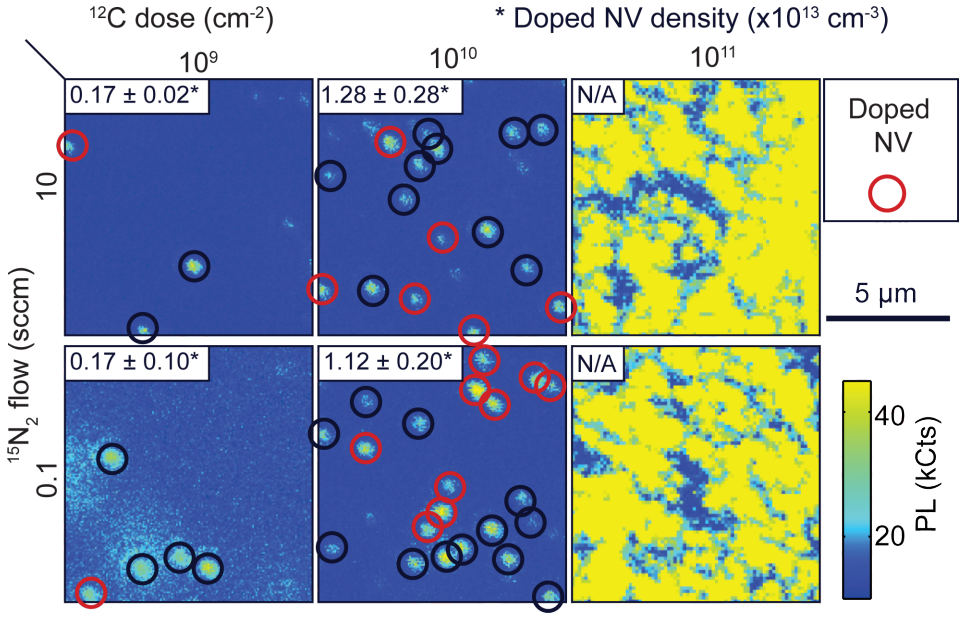


Figure 6.5: Surface confocal scans of six different parameter areas. The two rows correspond to different $^{15}N_2$ doping gas flows of 10 (top) and 0.1 (bottom) sccm. Three columns are for ^{12}C implantation doses of 10^9 (left), 10^{10} (center) and 10^{11} (right) cm^{-2}. The numbers on the left top of each figure correspond to the doped NV density in the units of 10^{13} cm^{-3} (for 10^{11} cm^{-2} dose cases, doped NV center cannot be measured as NV density is too high to isolate single NV centers). Doped NV centers are circled in red, and susbtrate NV centers are in black. PL spots showing inconclusive results due to low CWESR contrast are not circled. Original data presented in Ref. [156].

NV density assuming a thickness of the nitrogen delta-doped layer of 6 nm. The calculated doped NV density for each quadrant is shown on the left top of each figure in the unit of 10^{13} cm^{-3}.

For both $^{15}N_2$ flow cases, the doped NV density increases from ~ 0.1 to $\sim 1 \times 10^{13}$ cm^{-3} when ^{12}C implantation dose is increased from 10^9 to 10^{10} cm^{-2}, suggesting that doped NV density can be controlled by ^{12}C implantation dose. According to secondary ion mass spectrometry (SIMS) measurements, the nitrogen dopant concentration is estimated to be $(0.8 \pm 0.6) \times 10^{16}$ cm^{-3} (see Section 4.4) for a 10 sccm $^{15}N_2$ doping gas flow, which is consistent with the nitrogen spin bath concentration probed by spin coherence measurements of NV centers in a similar nitrogen-doped film [132]. The nitrogen to NV center conversion efficiency ([NV]/[N]) is calculated using the estimated nitrogen dopant concentration ([N]) and the measured doped NV density for the 10 sccm cases ([NV]) resulting in 0.02 % and 0.16 % for the 10^9 and 10^{10} cm^{-2} ^{12}C dose cases, respectively. The resulting low conversion efficiencies suggest that the doped NV density is limited by the vacancies in these ^{12}C dose cases. For the 10^{11} cm^{-2} dose case, NV density is too high to isolate single NV centers, however, the doped NV density should keep increasing with the ^{12}C implantation dose as the integrated PL over the scanned areas increase by roughly 20 - 40 times (which varies with measured positions) compared to the 10^{10} cm^{-2}

dose cases.

On the other hand, there is no noticeable difference of the doped NV density between two different $^{15}N_2$ flow samples even though the doping gas flow is varied over two orders of magnitude. This result indicates that the nitrogen incorporation is very weakly dependent on the $^{15}N_2$ doping gas flow, leading to a speculation that the nitrogen incorporation to diamond is limited and it is already saturated at a relatively small $^{15}N_2$ flow of 0.1 sccm. This result is quite interesting as it challenges prior assumptions in Chapter 4 that nitrogen dopant concentration can be controlled by the doping gas flow, and this speculation is further investigated from the spin coherence point of view in the following section.

6.5.2 Effects on the spin coherence

The effects of ^{12}C implantation dose and $^{15}N_2$ doping gas flow on the NV center spin coherence are investigated by using the same samples. Figure 6.6 shows spin coherence times T_2 measured using Hahn echo sequences of the NV centers within 10^{10} (left) and 10^9 (right) cm^{-2} ^{12}C dose quadrants of the 10 (red) and 0.1 (blue) sccm samples. Each data point corresponds to a T_2 result of an individual single NV center. Uncertainties in T_2 are quoted at 95 % confidence. The resulting T_2 are reproducibly long on the order of hundreds of

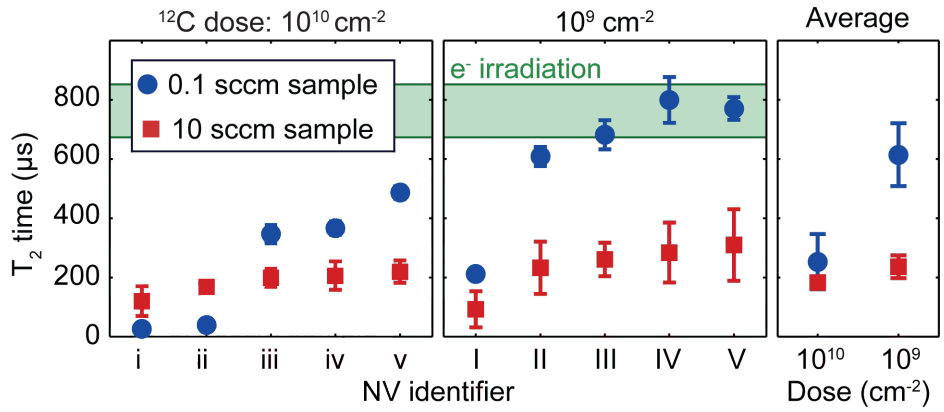


Figure 6.6: Spin coherence times T_2 of single NV centers from 10^{10} (left) and 10^{9} (center) cm^{-2} dose areas. Data from 0.1 (10) sccm samples are denoted by blue circles (red squares). Each data point represents a result of a single NV center. The errors are quoted at 95 % confidence. Measured T_2 ranges of the electron irradiated samples are shown in a green belt in the figure for comparison. The average T_2 times of the five NV centers from each combination of the process parameters are shown in the right panel. Original data presented in Ref. [156].

microseconds except only two NV centers showing $T_2 < 50$ μs (both from the 10^{10} cm^{-2} dose area in the 0.1 sccm sample). The longest T_2 of a single NV center, (799 ± 77) μs, is measured from the 10^{9} cm^{-2} dose quadrant of the 0.1 sccm sample, which encouragingly is comparable to the T_2 times of the electron irradiated samples presented in Chapter 4 (shown as a green belt in the figures). Some outliers (e.g. NV i, ii and I of the 0.1 sccm sample) are likely due to a non-uniform distribution of vacancy-related paramagnetic defects originated from the implantation process, which are not fully removed during the subsequent annealing process [157]. Although T_2 results seem to deviate in a wider range in the 0.1 sccm sample, whether it is a real effect or just by the limited

sampling size is inconclusive.

The means and standard deviations of T_2 of five single NV centers for the each combination of parameters (^{12}C dose and $^{15}N_2$ flow) are shown in the right panel of Fig. 6.6. The average T_2 times increase from 252 ± 93 (182 ± 18) μs to 614 ± 106 (235 ± 38) μs for the 0.1 (10) sccm sample when ^{12}C dose is changed from 10^{10} to 10^9 cm^{-2}. In order to investigate the effects of ^{12}C dose and $^{15}N_2$ flow on T_2 times, a two-way analysis of variance (ANOVA) is carried out, showing a statistically significant main effect for the ^{12}C implantation dose ($F(1,16) = 4.7, p < 0.05$), whereas the main effect for the $^{15}N_2$ flow and the interaction between the two parameters are not statistically significant ($F(1,16) = 1.0, p > 0.05$ and $F(1,16) = 2.6, p > 0.05$, respectively). It is hard to determine the sole effect of nitrogen on the spin decoherence from the limited number of sample, since vacancies coexist as another source of decoherence. However, if the nitrogen were incorporated proportionately to the $^{15}N_2$ doping gas flow, T_2 times would result in two orders of difference between the samples assuming that T_2 are inversely proportional to the nitrogen concentration [158]. The measured T_2 times differ only within the same order, suggesting that the nitrogen incorporation is indeed very weakly dependent on the $^{15}N_2$ doping gas flow, which is consistent with the NV density results discussed in the previous section.

It is interesting to investigate an even lower $^{15}N_2$ doping gas flow regime, which may show different results of the doped NV density and T_2 times, providing a deeper insight in the solubility of nitrogen into diamond. Also, it remains unclear whether an excess amount of nitrogen is not incorporated into the crystal or becomes a different form of crystal defects in the diamond, such as interstitials. Answering to these questions is a key to understand the nitrogen doping mechanism, leading to a better control of the NV density and T_2 times using the nitrogen doping technique.

6.6 3D localization of a single NV center using nanoscale apertures

The ^{12}C implantation technique is further utilized to demonstrate 3D localization of a single NV center. The nitrogen delta-doped layer constrains the depth direction of NV centers at nanometer scale, and the ^{12}C implantation through electron beam (EB) lithographically patterned, nanometer-scale apertures localizes vacancies to control the in-plane position of NV centers, thus leading to full 3D localization. This approach would also benefit to preserve spin coherence times of the localized NV centers, since the ^{12}C implantation technique would yield sustained T_2 times as seen in the previous section. In this section, the 3D localization of a single NV center with maintained spin

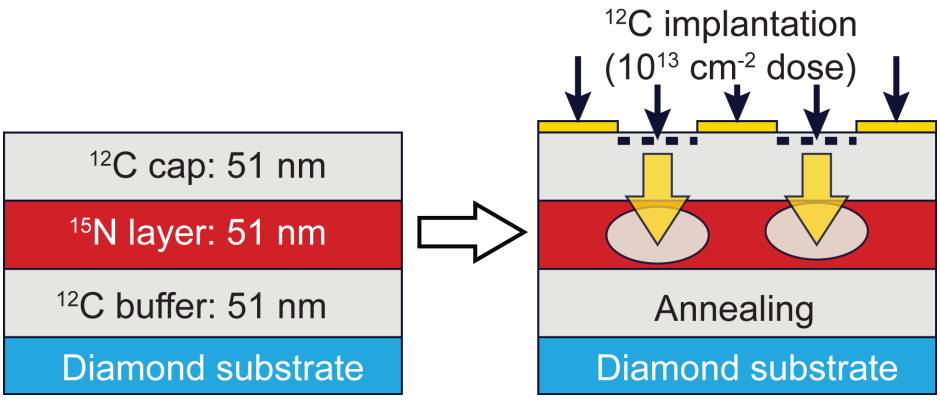


Figure 6.7: Schematic of the sample structure and the process flow of the aperture implantation sample. Original data presented in Ref. [156].

coherence is presented by implanting through nanometer-scale apertures. The sample preparation process, as well as the average number and spin coherence measurements of localized NV centers are discussed.

6.6.1 Aperture sample preparation

Figure 6.7 shows a sample preparation process of the aperture implantation approach. The sample consists of a 51-nm thick ^{12}C buffer layer, a ^{15}N doped layer 51 nm thick and a ^{12}C cap layer (51 nm). The ^{15}N doped layer is made relatively thick in order to increase the probability of finding NV centers in a localized volume of sub-diffraction limit length scale. A $^{15}N_2$ doping gas flow of 10 sccm is used for doping. After the growth, the sample is spin coated with positive EB resist (PMMA 950 A4) at 3000 rpm for 30 seconds, baked at

185 ^{o}C on a hot plate for 30 min. and then a 30-Å thick Cr layer is deposited using a thermal evaporator in order to make a conductive layer for EB patterning. An EB pattern is drawn using the nanometer pattern generation system (NPGS) integrated in a FEI Sirion field emission scanning electron microscope (SEM) equipped in the Nanofab, using an acceleration voltage of 30 kV and a spot size of either 3 or 5. The EB pattern consists of a two-dimensional (2D) array of apertures (2 μm spacing in both directions) patterned over a 100 μm $\times$ 100 μm area with various nominal diameters from 50 to 450 nm. At four corners of the array, a 25 μm $\times$ 25 μm square marker is patterned to find positions of the apertures during PL measurements. These patterns are repeatedly drawn at different places across the sample with varying EB dose from 1000 to 8000 μC/cm^2. The best dose to resolve small features is 2000 μC/cm^2. The sample is then ^{12}C implanted at an implantation energy of 7 keV and a dose of 10^{13} cm^{-2} with the incident angle 7 degrees tilted normal to the sample surface. ^{12}C implantation dose is increased in order to increase the NV density. After the implantation, the EB resist is stripped off and the sample is annealed in a tube furnace at 850 ^{o}C for 30 min. in a H_2/Ar atmosphere. The sample surface is cleaned using perchloric mixture prior to measurements.

6.6.2 Localized NV center number vs aperture diameter

Figure 6.8 shows a surface confocal scan of the processed sample, displaying patterned spots of PL from NV centers localized by the apertures. The 2D array pattern consists of ten columns of apertures (columns A - J) with varying their diameters; column A has the largest nominal diameter of 450 nm and column J has the smallest of 50 nm. The columns of smaller diameter H - J are not fully developed and only columns A - G (from left to right) are seen in the figure. The difference in PL of columns in the figure reflects the difference in their aperture diameter (larger apertures on the left). In this section, the average number of localized NV centers per aperture is discussed as a function of their measured diameter.

The aperture diameter is measured from SEM images, which are taken from a separate sample processed simultaneously in the same recipe (inset of Fig. 6.8). Ten apertures are selected from each column and measured to compute an average diameter. For example, the diameter of column A is 239 ± 19 nm, and the two smallest columns (F and G) in Fig. 6.8 have diameters of 123 ± 17 nm and 114 ± 21 nm, respectively.

The number of NV centers localized in an aperture is counted based on the PL intensity of the apertures. Several surface confocal scans are taken from the array to image total 90 apertures for each column to build up statistics. Each

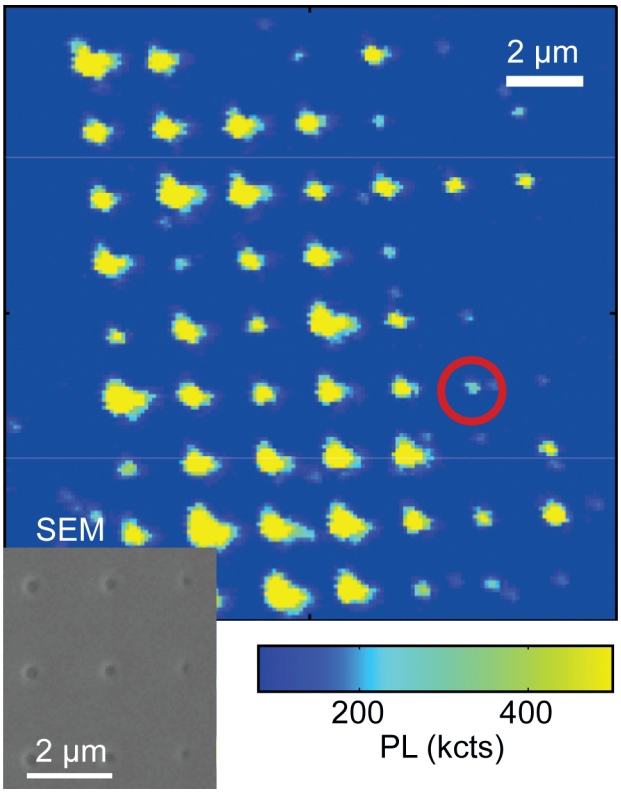


Figure 6.8: Surface confocal scan of the aperture implantation sample, showing a patterned PL of the NV centers localized in an array. One of the single NV centers is circled in red. (inset) SEM image of the processed apertures. Original data presented in Ref. [156].

scan is repeated four times with different excitation laser polarization (two orthogonal polarizations and another two polarization angles between them) and an average PL is computed for these four polarizations. In this way, differences of PL due to each single NV center's axis orientations relative to the magnetic field direction are compensated, as well as PL fluctuations caused by any polarization-dependent effects of optical components in the setup are minimized. In these scans, positions of the apertures are identified and PL is

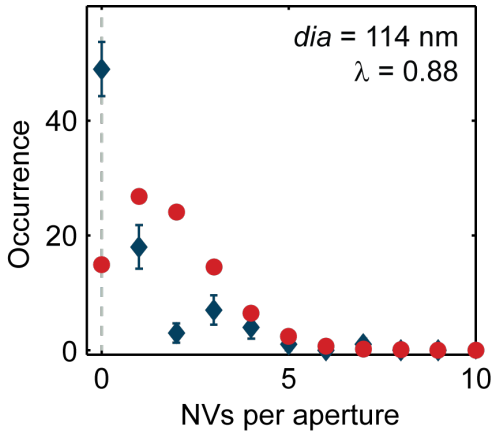


Figure 6.9: Histogram of the number of NV centers localized per aperture measured by 90 apertures in column G. Data are shown in blue, and a fit to a Poisson distribution using maximum likelihood method is shown in red. Original data presented in Ref. [156].

integrated over a circle of 0.9 μm radius around the apertures. After subtraction of background PL, which is taken from the area away from the aperture, the integrated PL is normalized by the PL from a single NV center (which is verified later) in order to measure the number of NV centers per aperture. A histogram of the number of NV centers per aperture is made for each column and the distribution is fitted by a Poisson distribution using a maximum likelihood estimation (MLE) method. In order to get rid of spurious PL from darts on the surface, an iterative method is used to set a reasonable cutoff. To begin with, any apertures showing more than 50 times brighter than single NV center PL is removed. Then, the data is fitted by a Poisson distribution and the next cutoff is set at the NV center number where there is a 1/1000 chance of occurrence

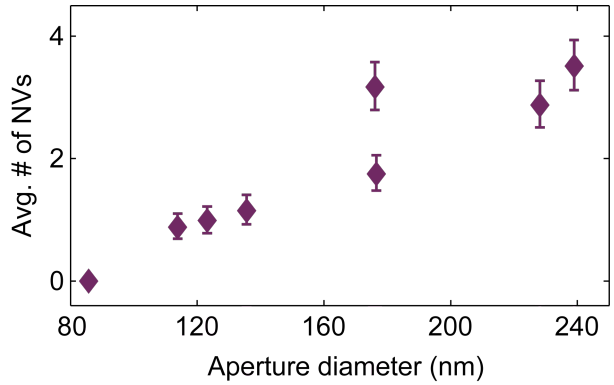


Figure 6.10: Average number of NV centers per aperture as a function of measured diameter. Original data presented in Ref. [156].

according to the fit. This process is iterated for a couple of times until the cutoff is converged (typically at the NV center number of 10 – 15) and the mean value of localized NV centers per aperture is extracted from the final fit.

Figure 6.9 is an example histogram of the number of localized NV center in column G (the data are shown in blue and the fit is in red), showing that 18 % of the measured apertures display PL consistent with a single NV center, and the mean value of $\lambda = 0.88$ NV centers are localized per aperture from the fit.

Figure 6.10 shows the mean values of localized NV centers as a function of their measured diameter, showing that the average number of localized NV center can be controlled from $0.88^{+0.22}_{-0.19}$ to $3.51^{+0.43}_{-0.39}$ by changing the aperture diameter from 114 ± 21 nm (column G) to 239 ± 19 nm (column A).

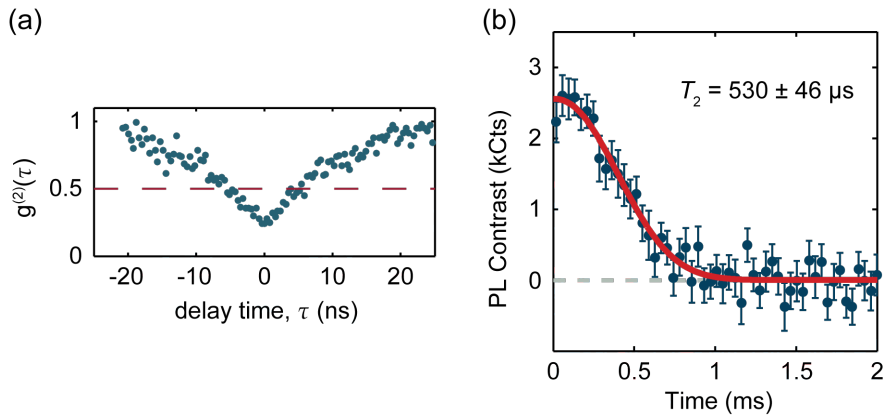


Figure 6.11: (a) Photon auto-correlation function $g^{(2)}\tau$ as a function of a delay time τ in the NV center circled in red in Fig. 6.8. (b) Hahn echo decay data (blue) and a fit (red) of one of the single NV centers showing longest $T_2 = 530 \pm 46$ μs. Uncertainties are quoted by 95 % confidence. Original data presented in Ref. [156].

6.6.3 Spin coherence of a localized single NV center

In order to test the validity of the PL-based NV center counting method, four NV centers showing PL consistent with a single NV center are tested using photon anti-bunching measurements. Figure 6.11(a) shows a normalized photon autocorrelation function $g^{(2)}(\tau)$ as a function of delay time τ measured in the NV center circled in red in Fig. 6.8, displaying $g^{(2)}(0) < 0.5$, which confirms PL from a single NV center. This single NV center signature is observed in all of the four measured NV centers.

Spin coherence times T_2 are measured in these four single NV centers using the Hahn echo sequences. The results show a scattering of T_2 times between 60 to 530 μs, due to non-uniform nature of vacancy creation in the ion implan-

tation process. However, the average T_2 time of four single NV center is ~ 340 μs, and two of these show long $T_2 \sim 500$ μs. The Hahn echo result of the NV center displaying the longest $T_2 = 530 \pm 46$ μs is shown in Fig. 6.11(b). The measured T_2 times for localized NV centers result in about an order of magnitude improvement compared to a previously reported complementary approach using ^{15}N implantation through nanometer scale aperture [33].

6.7 Localization volume estimation

In this section, the localization volume for a single NV center in the aperture sample is discussed. First, the vacancy diffusion length is estimated by a one-dimensional diffusion model using the results of the isotopic doped/substrate NV center discrimination in the confocal scans probing the diffusion depth of vacancies. Then, an isotropic expansion of vacancy diffusion is taken into account to calculate a three-dimensional volume where a single NV center is localized beneath the apertures. Finally, the NV center conversion efficiency is discussed based on the estimated localization volume.

6.7.1 Vacancy diffusion length

Assuming that vacancies are initially well localized near the surface by using a low energy implantation compared to the vacancy diffusion length after

the annealing, and that the total number of vacancies is constant N, a drive-in diffusion model can be applied [158]. Under this model, the vacancy concentration at depth z after an annealing time t can be expressed as

$$C(z,t) = \frac{N}{\sqrt{\pi Dt}} \exp\left(-\frac{z^2}{4Dt}\right), \tag{6.1}$$

where D is a diffusivity. Since only a static vacancy distribution after a certain annealing time is considered, $C(z,t) \approx C(z)$, and the equation can be simplified as

$$C(z,t) = 2N \cdot G(z), \tag{6.2}$$

where $G(z)$ is a form of the normal distribution function,

$$G(z) = \frac{1}{\sigma\sqrt{2\pi}} \exp\left(-\frac{z^2}{2\sigma^2}\right), \tag{6.3}$$

and

$$\sigma = \sqrt{2Dt} \tag{6.4}$$

is a normalized vacancy diffusion length that is to be calculated. The NV center density at depth z, $[NV](z)$, is proportional to a product of the nitrogen concentration at z, $[N](z)$, and a total amount of vacancies that diffuse through z, $F(z)$, which can be written as

$$[NV](z) = P \cdot [N](z) \cdot F(z), \tag{6.5}$$

where P is a probability that a pair of a nitrogen and a vacancy forms a NV center (assuming that there is a sufficient amount of both nitrogen and vacancy

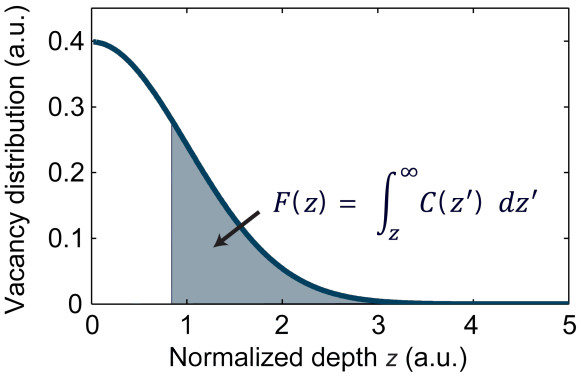


Figure 6.12: Vacancy distribution $C(z)$ at a certain annealing time. The total amount of vacancies that diffuse at depth z, $F(z) = \int_z^\infty C(z')dz'$ is shown as a shaded area. Original data presented in Ref. [156].

in the diamond, and that neither of them is a limiting factor for the NV center formation). From definition, $F(z)$ can be expressed as (see Fig. 6.12)

$$\begin{aligned} F(z) &= \int_z^\infty C(z')dz' \\ &= 2N \int_z^\infty G(z')dz' \\ &= N \cdot Erfc\left(\frac{z}{\sigma\sqrt{z}}\right), \end{aligned} \tag{6.6}$$

where $Erfc$ is a complementary error function. Define n as the number of NV centers (per unit scanned area) in a layer between the bottom depth at z_2 and the top depth at z_1, which can be calculated by taking an integral of Equation (6.5)

from z_1 to z_2,

$$\begin{aligned} n &= \int_{z_1}^{z_2} [NV](z')dz' \\ &= P \cdot [N] \int_{z_1}^{z_2} F(z')dz' \\ &= P \cdot [N] \left(H(z_1) - H(z_2) \right), \end{aligned} \tag{6.7}$$

where the nitrogen concentration is assumed to be constant in the layer ($[N](z) \approx [N]$) and $H(z)$ is an integral of $F(z)$,

$$H(z) = \int_{z}^{\infty} F(z')dz'. \tag{6.8}$$

Solving the integral of Equation (6.8) is non-trivial and it should be solved numerically. As the nitrogen concentration in the ^{15}N doped layer is estimated to be 0.8×10^{16} cm^{-3} by the experimental results of the SIMS measurements, and the specification of the substrate nitrogen concentration is 5 ppb given by *Element 6*,

$$[^{15}N] = 0.8 \times 10^{16} \text{ cm}^{-3} \tag{6.9}$$

$$[^{14}N] = 5\text{ppb} = 0.8 \times 10^{16} \text{ cm}^{-3}. \tag{6.10}$$

Since the sample contains a ^{15}N doped layer between depths of 51 nm and 102 ($= 2 \times 51$) nm, and the depth of the substrate being 153 ($= 3 \times 51$) nm, the number of doped NV centers (^{15}n) and substrate NV centers (^{14}n) per unit

scanned area can be expressed as,

$$^{15}n = P \cdot [^{15}N]\,(H(z_0) - H(2z_0)) \tag{6.11}$$

$$^{14}n = P \cdot [^{14}N]\,(H(3z_0))\,, \tag{6.12}$$

where

$$z_0 = \frac{51\text{ nm}}{\sigma\sqrt{2}} \tag{6.13}$$

is the normalized depth. Of 26 NV centers measured in column F and G of the aperture sample, 23 NV centers (88 %) are doped ^{15}NV centers. This result is used to form an equation that links Equations (6.11) and (6.12), which is

$$^{15}n :^{14} n = 88 : (100 - 88). \tag{6.14}$$

Solving this equation by substituting Equations (6.6) and (6.8) - (6.13), the normalized depth is calculated to be

$$z_0 = 0.27, \tag{6.15}$$

which leads to a vacancy diffusion length of

$$\sigma = 134\text{ nm}. \tag{6.16}$$

Now, errors in the vacancy diffusion length are estimated, which arise from the error of finding doped ^{15}NV centers due to a limited number of scanned NV centers. The average probability, p, of finding a doped NV center is estimated from the posterior distribution of p for 23 doped and 3 substrate NV

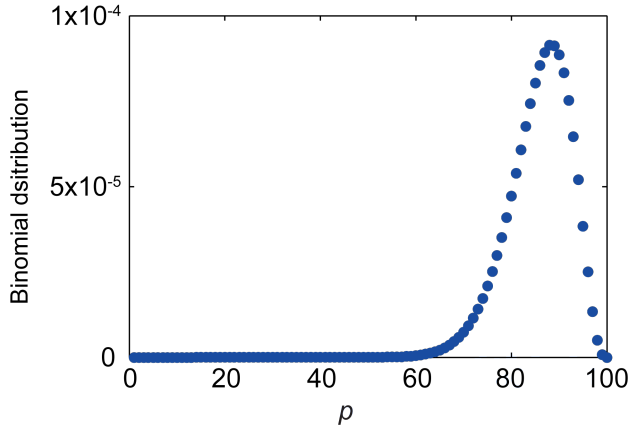


Figure 6.13: Calculated distribution of probability p of finding doped NV center, estimated by measurement results of 23 doped and 3 substrate NV centers. The distribution takes a form of a binomial distribution. Original data presented in Ref. [156].

centers assuming a uniform prior distribution, which takes a form of the binomial distribution (Fig. 6.13),

$$B(p) = \binom{26}{23} p^{23}(1-p)^{(26-23)}, \tag{6.17}$$

where $\binom{n}{k} = \frac{n!}{k!(n-k!)}$. From this distribution, p is inferred to be 88^{-18}_{+10} % where the errors are quoted as the 95 % confidential interval. The distribution of p, $B(p)$, is projected to a distribution of vacancy diffusion length σ, $D(\sigma)$ by the following procedure. First, a sample size of M of numbers for p are generated whose occurrence is weighted by $B(p)$ using the inverse transform sampling. Then, the corresponding vacancy diffusion length σ is calculated for each p, resulting in a distribution for σ, $D(\sigma)$, as shown in Fig. 6.14 (a sample size $M = 1.2 \times 10^6$ is used). The mean (σ_{mean}) and errors (σ_{upper} , σ_{lower}) of the

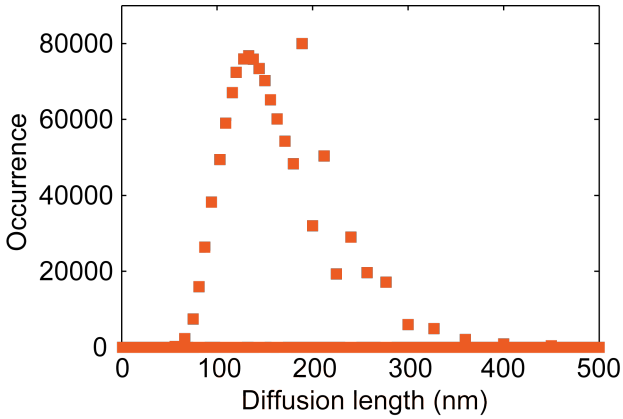


Figure 6.14: Distribution of diffusion length projected using the distribution of finding doped NV center (p). The sample size used for this calculation is $M = 1.2 \times 10^6$. Original data presented in Ref. [156].

vacancy diffusion length are calculated from this distribution by the following equations,

$$\sigma_{mean} = \frac{\sum_{0}^{\sigma_{max}} \sigma D(\sigma)}{\sum_{0}^{\sigma_{max}} D(\sigma)}, \tag{6.18}$$

$$\frac{\sum_{0}^{\sigma_{upper}} D(\sigma)}{\sum_{0}^{\sigma_{max}} D(\sigma)} \geq 97.5\ \%, \tag{6.19}$$

$$\frac{\sum_{0}^{\sigma_{lower}} D(\sigma)}{\sum_{0}^{\sigma_{max}} D(\sigma)} \leq 2.5\ \%, \tag{6.20}$$

where σ_{max} is a cut off length, for which a reasonably large number should be chosen (500 nm for this plot). The results are converged with a large number of M, and for the distribution shown in Fig. 6.14, they are $\sigma_{mean} = 153$ nm,

$\sigma_{upper} = 276$ nm and $\sigma_{lower} = 86$ nm, or in another expression, the estimated vacancy distribution is $\sigma = 153^{+123}_{-67}$ nm. A relatively large error is due to the limited number of NV centers measured, which makes a large error in estimating p.

As a cross check, the calculated vacancy diffusion length is much larger than the initial depth of vacancies by ^{12}C implantation (8.0 ± 6.1 nm for the 7 keV acceleration voltage), which confirms the assumption that the vacancies are initially localized near the surface.

6.7.2 Localization volume

A three-dimensional volume beneath the apertures wherein NV centers are localized is calculated using the estimated vacancy diffusion length. Assuming that the vacancies diffuse isotropically in the diamond crystal, the volume into which the vacancy can diffuse is defined as a downward hemisphere with a radius of the vacancy diffusion length σ and its center located at the surface where the vacancy is initially created by the implantation (see Fig. 6.15(a)). For a case of implanting through an aperture of radius r_0, vacancies are initially created uniformly inside the aperture and the volume that the vacancies can diffuse is a superposition of the hemispheres. The localization volume of NV centers by the aperture implantation is therefore the overlapping volume of the

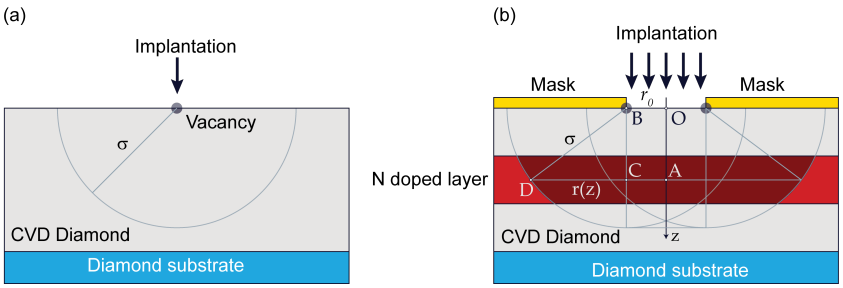


Figure 6.15: (a) Schematic of the volume that vacancy can diffuse assuming the isotropic diffusion and the diffusion length of σ. The vacancy is assumed to be initially created at the surface by the implantation. (b) Schematic describing the localization volume of the aperture implantation technique (dark red). The nitrogen doped layer is denoted by red and the surface mask is yellow. See main text for the definition of five points, $O, A-D$. Original data presented in Ref. [156].

hemispheres and the nitrogen doped layer, shown as a dark red region in Fig. 6.15(b).

For a detailed analysis, define z axis normal to the sample surface pointing deeper in the diamond crystal with its origin O locating at the center of the aperture at the surface. Other four points are defined as A: straight below O at depth z, B: the edge of the aperture in the considered plane, C: straight below B at depth z, D: $BD = \sigma$ at depth z (see Fig. 6.15(b)), which lead to

$$CD = r(z) = \sqrt{\sigma^2 - z^2}, \tag{6.21}$$

$$AC = OB = r_0, \tag{6.22}$$

$$AD = R(z) = \sqrt{\sigma^2 - z^2} + r_0. \tag{6.23}$$

The localization volume V can be calculated by taking an integral of a circle

of radius $R(z)$ over the depth of the nitrogen doped layer between z_1 and z_2 $(z_1 < z_2)$,

$$V = \pi \int_{z_1}^{z_2} R(z)^2 dz, \tag{6.24}$$

where $z_1 = 51$ nm and $z_2 = 102$ nm for the specific sample structure (*n.b.* the integral is taken up to σ when $\sigma \leq z_2$). Substituting σ with the estimated $\sigma_{mean} = 153$ nm, the localized volume for column G is calculated to be $V = 5.6 \times 10^6$ nm^3, or (179 nm)^3.

The corresponding nitrogen to NV center conversion efficency ([NV]/[N]) can be calculated by the following equation,

$$\frac{[NV]}{[N]} = \frac{\lambda}{[^{15}N] \times V}, \tag{6.25}$$

where $[^{15}N] = 0.8 \times 10^{16}$ cm^{-3} is the dopant concentration in the nitrogen doping layer (Equation (6.9)), $\lambda = 0.88$ is the mean number of localized NV centers for column G. The conversion efficiency is calculated to be 1.9 % using the localization volume V calculated above.

The results presented in Section 6.5.1 suggests that the conversion efficiency increases with the ^{12}C implantation dose. Although the implantation dose is increased by three orders of magnitude from 10^{10} cm^{-2} (see Fig. 6.5) to 10^{13} cm^{-2} (the aperture sample), the conversion efficiency increases only by an order of magnitude from 0.16 % to 1.9 %. This discrepancy can be partially explained by the shadowing effect of the masks as the incident angle of the ^{12}C

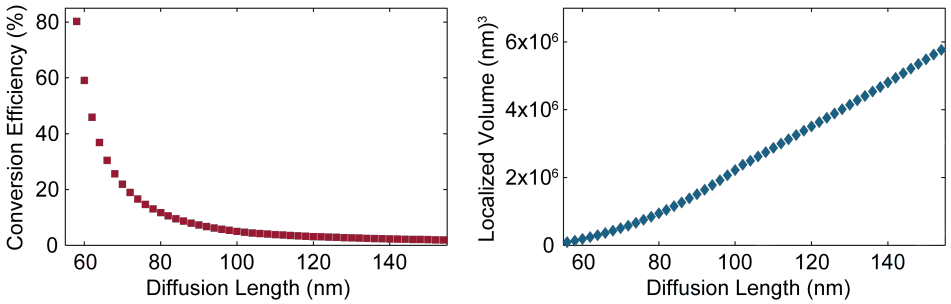


Figure 6.16: Calculated conversion efficiency (left) and localization volume (right) as a function of vacancy diffusion length. Original data presented in Ref. [156].

ions is 7 degrees tilted normal to the surface, but more importantly due to the estimation of the localization volume, which is sensitively affected by the errors in the vacancy diffusion length.

In order to see the error range of the conversion efficiency, Fig. 6.16 shows plots of the conversion efficiency (left) and the localization volume (right) as a function of vacancy diffusion length. The calculation is based on Equations (6.23) - (6.25), using fixed values of $r_0 = 114/2$ nm, and $\lambda = 0.88$ to show an example for column G. The conversion efficiency saturates below 10 % when the diffusion length σ is greater than 90 nm, but it rapidly increases up to several tens of percent when $\sigma < 70$ nm due to a monotonic decrease of localization volume. These results suggest that a precise estimation of the vacancy diffusion length is important to calculate the conversion efficiency, which is constrained by the limited number of measured NV centers in the aperture implantation approach. In order to give more precise estimation of the conversion efficiency,

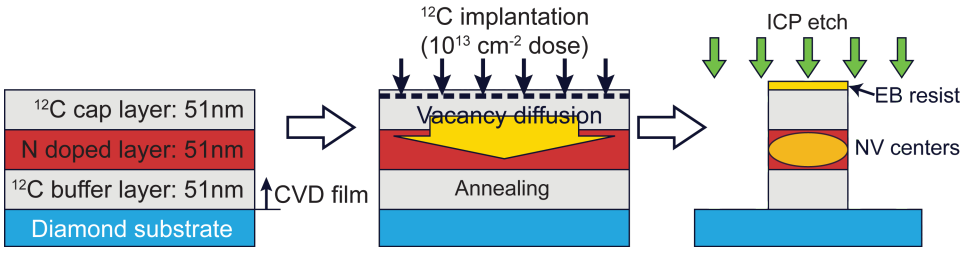


Figure 6.17: Sample structure and process flow of the nanometer-scale pillar sample. Original data presented in Ref. [156].

NV centers should be localized within a more definitive volume such as inside the nanometer-scale pillars, which is further explored in the next section.

6.8 Nanopillar approach for 3D localization

6.8.1 Nanoplillar sample preparation

As an alternative approach for the 3D localization, a single NV center is localized within a nanometer-scale pillar. Figure 6.17 shows a process flow of the nanopillar sample. The sample consists of a 51-nm thick ^{12}C buffer layer, a nitrogen doped layer of 51 nm thick (doping gas flow: 50 sccm), and a ^{12}C cap layer (also 51 nm). It should be noted that natural N_2 gas (^{14}N = 99.6 %) is used to dope for this sample. The use of natural nitrogen doping gas leaves questions whether measured NV center is located within the pillar or in the substrate. After the growth, the entire surface is ^{12}C implanted at an implantation energy of 7 keV and a dose of 10^{13} cm^{-2} with the incident angle 7 degrees tilted normal

to the surface. The sample is then annealed at 850 ^{o}C for 2 hours in a H_2/Ar forming gas atmosphere, followed by a perchloric acid mixture cleaning process before fabricating Ti/Pt coplanar waveguide using a standard optical lithography technique. Subsequently, the sample is spin coated by negative EB resist hydrogen silsesquioxane (HSQ) diluted by an equal volume of methyl isobutyl ketone (MIBK) at 4000 rpm for 30 seconds, followed by a 3-minute bake at 95 ^{o}C. A 30 Å of Cr layer is deposited prior to the EB patterning. The EB lithography process is done by NPGS of the FEI Sirion SEM in the Nanofab, using an acceleration voltage of 30 kV, a dose of 650 μC/cm^2, and a spot size of 3. The EB pattern consists of a 2D array of circles of nominally 200 (and 150) nm in diameter spaced by 1 μm in each direction. The 2D array spreads over a 60 μm $\times$ 60 μm area in a crook of the coplanar waveguide [10] in order to couple NV centers with AC magnetic field generated by microwave to manipulate spins (one crook is for the 200-nm diameter array and another crook for the 150 nm). After developing the pattern using Tetramethylammonium hydroxide (TMAH), nanopillars are formed by O_2 plasma etching for 5 min. using a standard recipe of an induction-coupled plasma reactive ion etching (ICP-RIE) system.

Figure 6.18 shows SEM images of the processed nanopillars. From these images, the diameter of nanopillars is measured to be 150 and 80 nm for the nominal design of 200 and 150 nm, respectively, and their height is measured

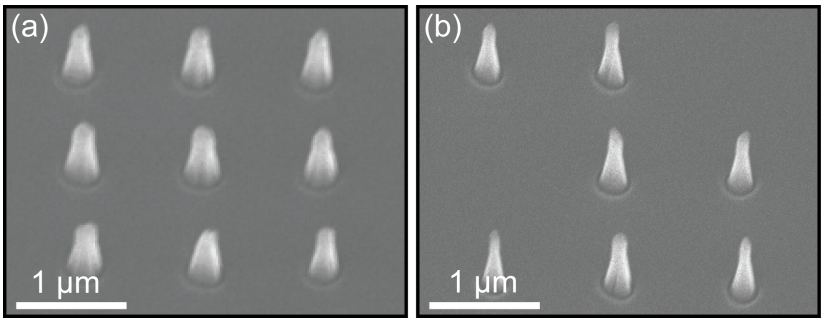


Figure 6.18: SEM image of an array of 150 nm (a) and 80 nm (b) nanopillars. Data adapted from Ref. [156].

to be 400 nm. These two types are called 150 nm (80 nm) nanopillars hereafter. The nanometer-scale masks on top of the pillars are removed using buffered HF prior to measurements.

6.8.2 Average NV center number localized in the nanopillar

Figure 6.19 shows a surface confocal image of an array of the 150 nm nanopillars, displaying a patterned PL from NV centers confined in the nanopillars. The dark area on the left bottom and top of the figure is the coplanar waveguide. The numbers of NV centers localized in each nanopillars are counted by measuring the number of characteristic dips in CWESR scans. The results of finding n NV centers per nanopillar $(n = 0, 1, 2, 3)$ measured from 49 of 150 nm nanopillars are shown in Fig. 6.20(a). The data are shown in blue and a fit to Poisson distribution is shown in red. The mean value of $\lambda = 1.33$ NV centers are localized per nanopillar.

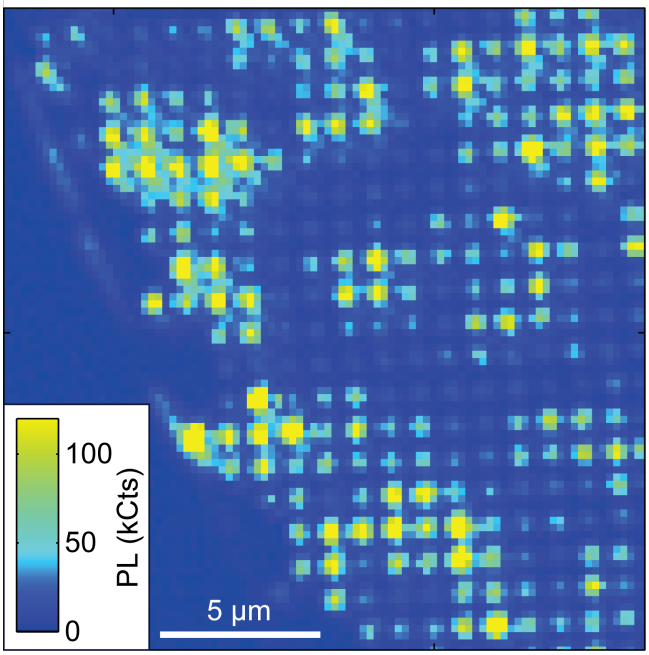


Figure 6.19: Surface confocal scan of 150 nm nanopillars, showing a patterned PL from NV centers localized in nanopillars. The featureless area in the left bottom of the image corresponds to a co-planar waveguide. Original data presented in Ref. [156].

The localization volume is calculated to be 8.8×10^5 nm^3, or (96 nm)^3, based on the diameter of the nanopillar of 150 nm and the thickness of the nitrogen doped layer of 51 nm. Assuming that the nitrogen dopant concentration is independent of nitrogen doping gas flow and is 0.8×10^{16} cm^{-3} (see Section 6.5.1), the nitrogen to NV center conversion efficiency is calculated to be 19 %, which is about an order of magnitude larger compared to the result of the aperture approach (1.9 %). The discrepancy between these results is likely due to an overestimation of localization volume in the aperture approach.

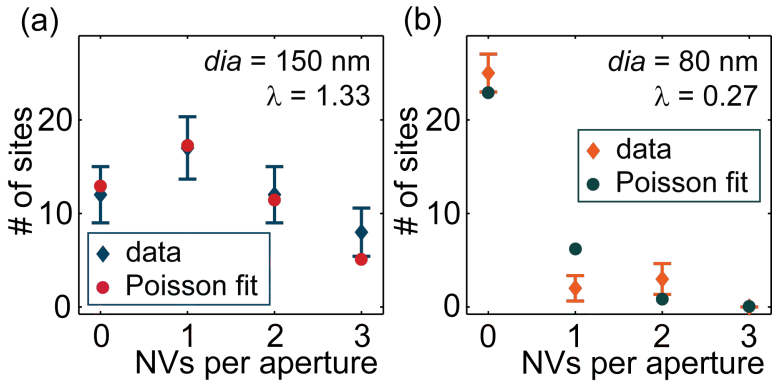


Figure 6.20: Histogram of NV centers per nanopillar for 150 nm (a) and 80 nm (b) nanopillars. Fits to a Poisson distribution of each data are also shown. Original data presented in Ref. [156].

In order to obtain a deep insight of the NV localization volume in the nanopillar sample, the measurements are repeated for the 80 nm nanopillars. Figure 6.20(b) shows a histogram of the number of NV center localized per nanopillar, measured from 30 of the 80 nm nanopillars. The results are again fitted by Poisson distribution and a mean value of $\lambda = 0.27$ NV centers are localized per nanopillar of the smaller diameter. The estimated localization volume and the conversion efficiency are 2.5×10^5 nm^3, and 14 %, respectively. If the number of localized NV center (n_{NV}) is proportional to their localization volume (V_{NV}), the conversion efficiency is independent of V_{NV}. However, the conversion efficiency of the 80 nm nanopillars is smaller than that of the 150 nm pillars. Moreover, the resulting number of localized NV centers for the 80 nm

nanopillars are smaller than an expected value assuming this proportionality,

$$\begin{aligned} n_{NV}^{80nm} &= 0.27 \\ &< n_{NV}^{150nm} \frac{V_{NV}^{80nm}}{V_{NV}^{150nm}} \\ &= 1.33 \, \frac{2.5 \times 10^5 \text{ nm}^3}{8.8 \times 10^5 \text{ nm}^3} = 0.38. \end{aligned} \tag{6.26}$$

These results suggest that NV centers near the sidewall of the nanopillars are depleted either due to charge instability near the surface or the process damage. The thickness of the depleted area (x) can be estimated using the proportionality assumption ($n_{NV} \propto V_{NV}$),

$$\pi(150/2-x)^2 \times 51 : \pi(80/2-x)^2 \times 51 = 1.33 : 0.27. \tag{6.27}$$

Solving this equation with a reasonable assumption that $x < 40$, the depleted area thickness is estimated to be 11 nm, which is consistent with the depth that the NV center spin coherence properties are subject to the surface effects [132]. If the depleted area is taken into account, the effective localized volume is calculated to be 6.4 (1.3) $\times 10^5$ nm^3 for the 150 (80) nm nanopillars, resulting in a converged value of the conversion efficiency of 26 %. As seen, the conversion efficiency is very sensitive to the estimation of the localized volume. However, the results suggest that the nitrogen doping technique combined with the ^{12}C implantation could lead to a high yield creation of localized NV centers.

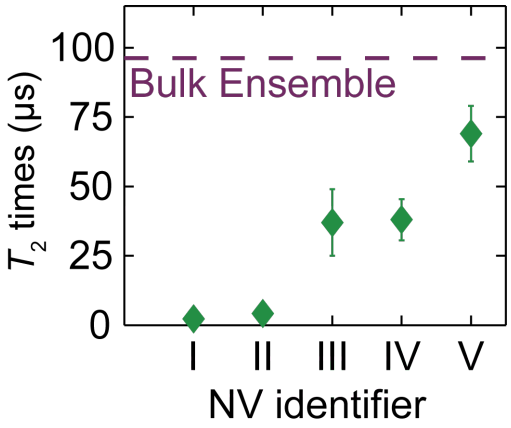


Figure 6.21: Spin coherence times T_2 of five NV centers localized within nanopillars. Each data set corresponds to NV center from a single pillar. Uncertainties are quoted at 95 % confidence. The bulk ensemble T_2 measured prior to the sample fabrication process is shown as a dotted line. Original data presented in Ref. [156].

6.8.3 Spin coherence of NV centers localized in the nanopillar

Figure 6.21 shows spin coherence times T_2 of five NV centers localized within the 150 nm nanopillars, measured using the Hahn echo sequences. These NV centers are selected from the nanopillars showing a single pair of dip characteristic to NV centers in CWESR scans. The longest $T_2 = 69 \pm 10$ μs is measured, along with two very short T_2 times of 4 ± 1 and 2 ± 1 μs. The scattering of T_2 results may be explained by the non-uniform nature of the ion implantation, but may also be caused by the uncontrolled proximity of NV centers to the sidewall within the nanopillar. However, the bulk ensemble measurement

prior to the nanopillar fabrication results in $T_2 = 96 \pm 20$ μs, suggesting that the substrate quality variation could also affect the T_2 times.

6.9 Conclusion and outlook

Three-dimensional localization of a single NV center with sustained spin coherence is presented. The nitrogen delta-doping technique is used to define the depth direction of NV centers, while ^{12}C ion implantation through nanometer-scale apertures creates spatially localized vacancies to control the in-plane position of NV centers. The vacancies diffuse during a subsequent annealing process to activate NV centers. In this way, a single NV center is localized in a nanometer-scale volume of $\sim$ (180 nm)^3 at the three-dimensionally deterministic position. The localized single NV centers show spin coherence times, T_2, longer than 300 μs on their average, and reach as long as $\sim$ 500 μs.

The presented localization volume is comparable to the scale of many kinds of NV-based diamond nanostructures, encouraging the integration into these devices. For example, the mode volume of diamond photonic cavities is reported to be a fraction of $(\lambda/n)^3$, where $\lambda = 637$ nm is the wavelength of the zero phonon line of NV centers, and $n = 2.4$ is the refractive index of diamond [152, 153]. The deterministic position control of the NV center photon source is a very important challenge to improve photonic cavity performances,

and the growth-based localization technique is promising as it is compatible to the monolithic diamond approach, although optical coherence measurements of the localized NV centers are the important next step for this application.

Moreover, scaling down diamond-based mechanical resonators to sub-μm size is an important challenge towards demonstrating coherent spin couplings mediated by phonons [66, 69]. The localization technique presented in this chapter is particularly promising for this application as the delta-doping is capable of controlling the depth of NV centers at nanometer scale, which is critically important to maximize the strain induced onto the NV center in the resonator.

The nitrogen to NV center conversion efficiency is calculated to be 1.9 % for the aperture localization method, and it is shown that the estimation is sensitive to the errors in vacancy diffusion length due to a limited number of NV centers measured to probe the vacancy diffusion depth. Localization of NV centers into nanometer-scale pillars gives a more precise way to estimate the conversion efficiency as the localization volume is well defined by the sidewall of the pillars. The conversion efficiency in the nanopillar is calculated to be 26 %, suggesting that the ^{12}C implantation technique could result in a high yield creation of NV centers.

Although results presented in this chapter are mainly focused on the single NV center applications, the resulting highly efficient creation of NV centers

could lead to a multiple NV-center spin entanglement through a proximal magnetic dipole interaction. Several approaches for this goal were demonstrated including using a high energy (2 MeV) nitrogen ion implantation with nanometer-scale apertures [55], and nitrogen ion implantation (20 keV) in combination with ^{12}C implantation [159]. The technique presented in this chapter could provide a complementary approach with the sustained spin coherence of NV centers facilitated by using the nitrogen-delta doping technique, which is a critical requirement to achieve better coupling between multiple spins.

Finally, the nitrogen incorporation and vacancy diffusion in diamond are discussed in this chapter. Although some questions are addressed, understanding these mechanisms requires further studies as it is critically important to control the 3D localization volume and the conversion efficiency. Some of the important questions yet addressed are: In what N_2 doping gas flow regime, can the nitrogen incorporation be controlled by the flow rate? Can spin coherence times be extended by reducing the nitrogen incorporation using an extremely low N_2 doping gas flow? Can any important parameters for vacancy diffusion such as diffusivity be estimated [160]? Can the vacancy diffusion length be controlled such that only NV centers in the nitrogen doped layer are activated? These engineering questions have to be answered in order to enable better control of materials using the ^{12}C implantation technique.

Chapter 7

Recent results

7.1 Nanometer-scale magnetic resonance imaging (nanoMRI)

The nanoNMR technique discussed in Chapter 5 is extended to two-dimensional nanometer-scale magnetic resonance imaging (2D nanoMRI). An organic sample containing an ensemble of protons is attached to a quartz tuning fork and scanned over a diamond sample containing a near-surface NV center. An in-plane spatial resolution of 12 nm is demonstrated [161].

7.1.1 Sample preparation

A 50-nm thick ^{12}C diamond film is grown on top of an electronic grade (100) diamond substrate. The diamond substrate is thinned down to 160 μm and polished prior to the growth in order to compensate the spherical aberration

for the optical access from the backside of the sample. To create shallow NV centers, ^{15}N ions are implanted at an energy of 2.5 keV followed by an annealing process for six hours at 850 ^{o}C in vacuum. The sample is then treated by an perchloric acid treatment and heated at 425 ^{o}C in pure oxygen for two hours [162] in order to remove the graphitic layer and to oxygen-terminate the surface. The NV centers used in the measurements are located between 5 to 10 nm below the surface, displaying T_2 ranging from 7 to 15 μs.

Reducing the organic sample volume is important to minimize the background luminescence from the contamination on the organic sample. For this purpose, a fiber of poly(methyl methacrylate) (PMMA, molecular weight $\sim$ 996k) is used as an organic sample containing dense protons ($\rho_N \sim 57$ nm^{-3}). The 10 μm-long PMMA fiber terminating with an end radius of curvature below 1 μm is formed at the end of a tapered glass capillary (4 μm in diameter), which is glued to one prong of a commercially available quartz tuning fork (Fig. 7.1).

7.1.2 Scanning the sample

The mechanical positioning of the sample is controlled by piezoelectric devices (Attocube ANPx51 and ANPz51), enabling sub-nanometer scan resolution according to the product specification. In reality, the spatial resolution

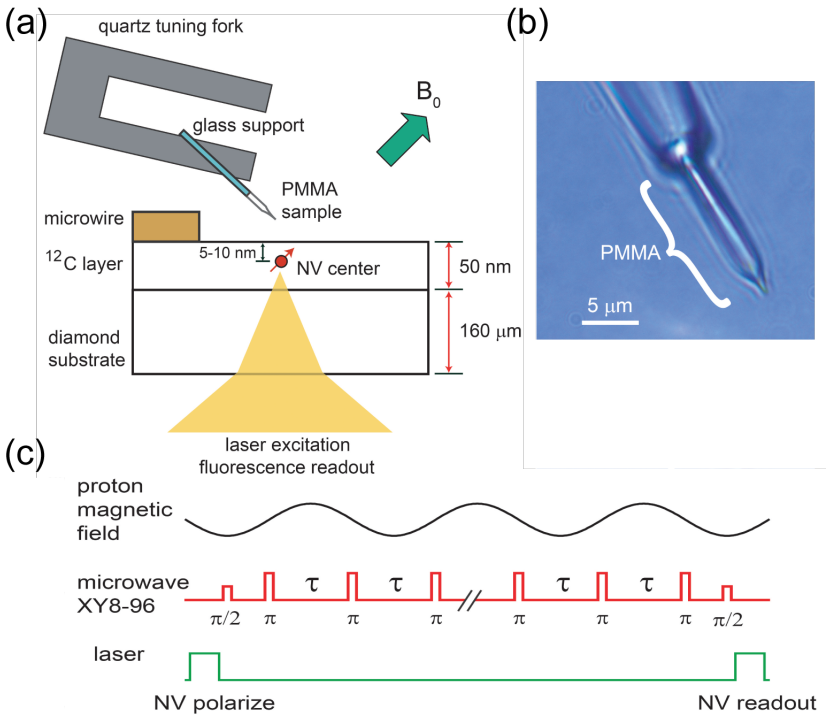


Figure 7.1: Experimental setup for 2D nanoMRI. (a) Schematic of the sample structure and the scanning system. An organic PMMA fiber sample is formed at the end of a tapered glass capillary, which is glued to one prong of a quartz tuning fork. (b) Optical micrograph of the PMMA sample. (c) Schematic of the multi-pulse spin echo XY8-96 sequence. When the inter-pulse period τ coincides with a half period of the proton Larmor frequency, the proton magnetic field is constructively accumulated to disturb the NV center's spin coherence signal. Original data presented in Ref. [161]

of the measurement is $\sim$ 12 nm limited by the thermal drift and creep during the long duration of the scans. In order to minimize the positioning error, the system is placed in a box to carefully control the temperature within 0.1 ^{o}C. Additionally, the sample position with respect to the NV center is periodically monitored by taking reflection images of the diamond surface showing a dark dot where the sample is in contact with the surface. These reflection images are correlated with the fluorescence images of the NV center, enabling to monitor the relative sample position to the NV center with a precision of about 10 nm. The proton spin signal from the PMMA sample is measured by the single NV center as a function of the sample position while the sample is stepped in a raster pattern on the diamond surface within a 1μm $\times$ 1μm area near the NV center.

Precise measurements of the tuning fork frequency allow for careful monitoring of the distance between the PMMA sample and the diamond surface. During the NMR measurement at each position, the PMMA sample is in a gentle contact to the surface, and then the sample is lifted up before moving to the next measurement position and reapproached to the surface at the new position. In this way, the wear of the organic sample and the diamond surface contamination are minimized. It takes 4 minutes to take data at each point including 3 minutes of the NMR signal acquisition and 1 minute for monitoring the sample

position and the approach-retraction process.

7.1.3 Spin echo measurements

The proton magnetic field signal originated from the Larmor precession of the ensemble proton spins is detected by the multi-pulse XY8-96 spin echo sequence [163]. The coherence signal of the NV center $C(\tau)$ is optically detected while the inter-π-pulse period τ is swept. The proton magnetic field signal is constructively accumulated to disturb the NV center coherence when τ is matched to the half of the Larmor precession period,

$$\tau = \tau_L \equiv 1/(2f_L), \tag{7.1}$$

where $f_L = (\gamma_n/2\pi)B_0$ is the Larmor frequency with $\gamma_n/2\pi = 42.56$ MHz/T being the gyromagnetic ratio of the proton spin. Under the external magnetic field of $B_0 = 36.6$ mT applied along the NV center symmetry axis, $f_L = 1.64$ MHz and $\tau_L = 305$ ns.

7.1.4 Proton NMR measurements

The proton NMR results when the PMMA sample is in contact (blue) and retracted (black) are shown in Fig. 7.2. The NV center coherence dip is observed at the expected $\tau \sim \tau_L$, suggesting that the proton signal is acquired. The dip position is shifted as expected when the external field is changed (data not

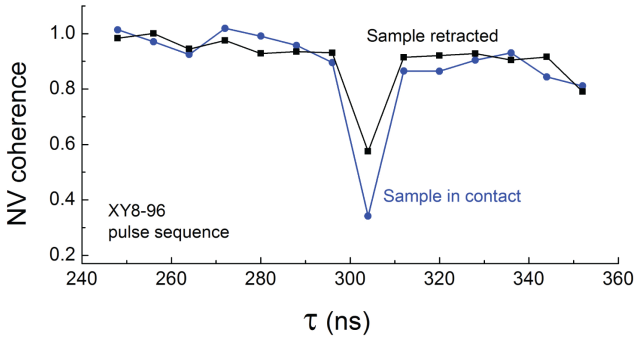


Figure 7.2: Proton NMR measurements. The NV coherence signal is measured as a function of the inter-pulse period τ when the sample is in contact with (blue) and retracted from (black) the diamond surface. A clear NMR dip is observed for the both cases when τ is matched with a half period of the proton Larmor frequency under the external magnetic field of $B_0 = 36.6$ mT. Original data presented in Ref. [161]

shown), which further confirms that the signal is originated by the proton spins. Interestingly, the coherence dip is also observed at the same τ when the sample is retracted, suggesting that the diamond surface is permanently covered by a thin layer containing protons, likely due to adsorbed water or hydrocarbons. Still, the difference in the coherence dip is clearly observed, which is attributed to the magnetic signal from protons in the PMMA sample. The sharpness of the observed dip is due to the narrow bandwidth of the proton spin precession, typically on the range of 10 - 50 kHz for organic solids at room temperature. In addition, the effective filter bandwidth of the multi-pulse sequence is inversely proportional to the number of π pulses N ($\sim 1/N\tau$, where $N = 96$), allowing for a narrow frequency selectivity.

Another advantage of the use of the multi-pulse sequence is that it decouples the NV center spin from the spin noise of the environment, resulting in an extension of T_2 from 7-15 μs to ~ 50 μs, allowing for the total echo sequence time increased up to $N\tau \sim 30$ μs

7.1.5 2D nanoMRI

In order to distinguish the proton magnetic signal from other sources of spin decoherence, such as randomly fluctuating electron spins on the surface of the diamond [132] or the PMMA sample, the background spin decoherence signal is computed by taking an average of two NV center coherence signals measured at $\tau_L \pm \Delta\tau$,

$$C_0(\tau_L) = \frac{1}{2}\left[C(\tau_L + \Delta\tau) + C(\tau_L - \Delta\tau)\right], \tag{7.2}$$

where $\Delta\tau = 32$ ns is selected to be large enough such that the additional measurement points are outside of the bandwidth of the proton NMR signal.

The nanoMRI data is acquired by measuring the proton signal as a function of the point (x,y), defined by

$$s(x,y) = 1 - \frac{C(\tau_L)}{C_0(\tau_L)}. \tag{7.3}$$

Line scans of NMR signal as a function of the lateral position are shown in Fig. 7.3. A step-wise function of the NMR signal is clearly observed when

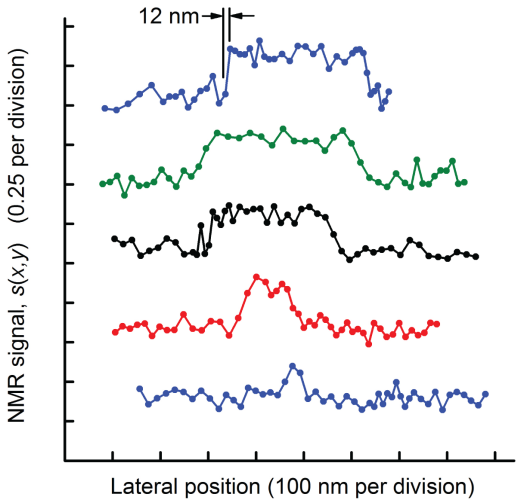


Figure 7.3: Line scans of the NMR signal as a function of the lateral position (100 nm per division). Plateau features are observed when the sample is passed above the NV center. Step heights corresponds to a proton field of $\sim (300\ \mathrm{nT})^2$. The in-plane resolution is 12 nm based on the sharpness of the single step. Successive scans in the figure are displaced vertically by two divisions. Original data presented in Ref. [161]

the sample passes above the location of the NV center. Plateau features seen in some of the scans are because of the large volume of the PMMA sample compared to the detection volume of the NV center (roughly 10 nm $\times$ 20 nm $\times$ 5 nm). From the height of the steps compared to the standard deviation of the baseline, the signal-to-noise is estimated to be ~ 6, limited by the photon shot noise. The spatial resolution is estimated to be 12 nm from the sharpness of the signal step, limited by the thermal drift and creep of the scanning system becoming worse due to the long duration of the scans (taking 3 hours for one line scan).

2D NMR images are taken by repeating the line scans with a small displacement in the orthogonal direction. Shown in Fig.7.4 are two images from two different PMMA samples with two different NV centers. Height in the images is proportional to $s(x,y)$. These images demonstrate the 2D nanoMRI operating at room temperature.

7.1.6 Proton magnetic signal

In this subsection, the proton magnetic signal is estimated based on the data shown in Fig. 7.2 for both cases when the PMMA sample is in contact to and retracted from the diamond surface.

For the multi-pulse echo sequence, the loss of spin coherence in the presence of Gaussian randomly fluctuating magnetic field can be expressed as

$$C(\tau) = \exp\left[-\chi(\tau,N)\right], \tag{7.4}$$

where τ is the inter-π-pulse period, N is the number of π-pulses and χ is the decoherence functional [164] given by

$$\chi(\tau,N) = \frac{\gamma^2}{2}\int_0^\infty d\omega S(\omega)\frac{F(\omega;\tau,N)}{\omega^2}, \tag{7.5}$$

where $\gamma/2\pi = 28$ GHz/T is the gyromagnetic ratio of the NV center, $S(\omega)$ is the power spectral density of the magnetic noise and $F(\omega;\tau,N)$ is the filter function describing the bandpass filter profile specific to the echo sequence, which can

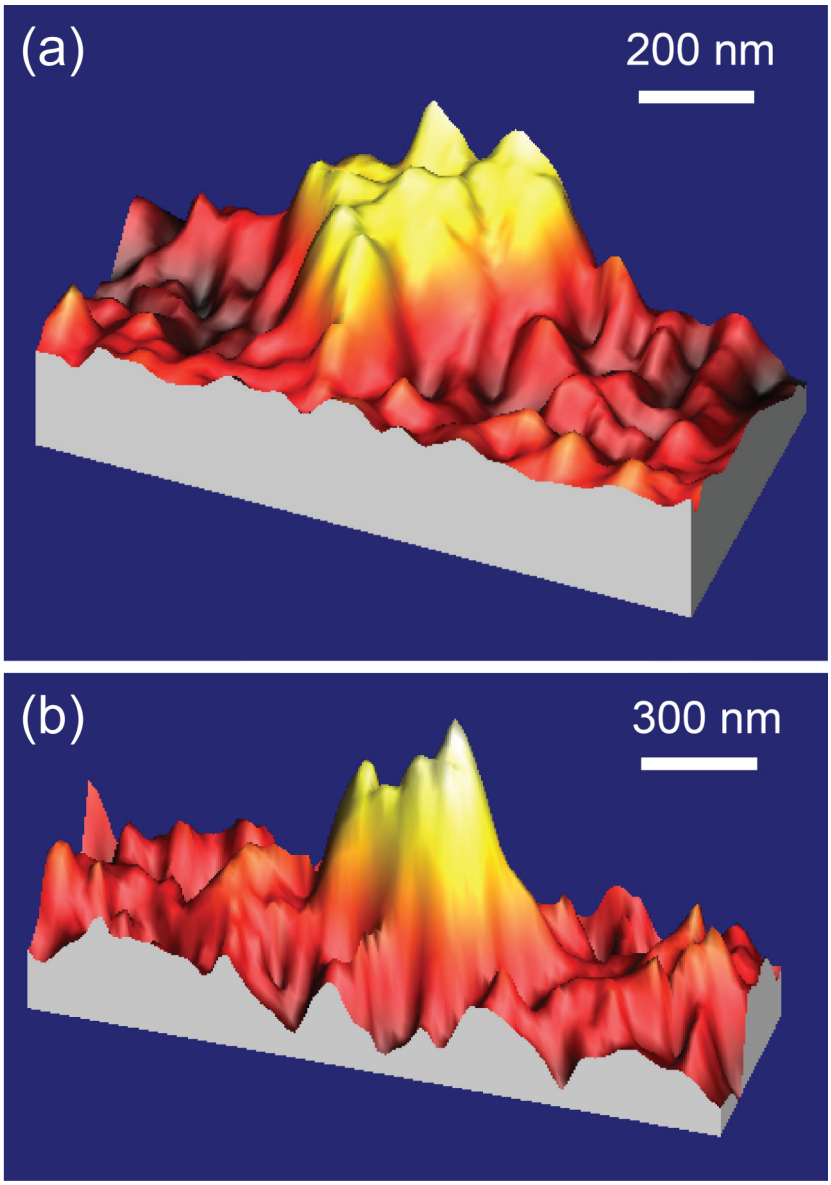


Figure 7.4: Two-dimensional NMR images. Images in (a) and (b) are taken for different PMMA samples by different single NV centers. Height in the image is proportional to $s(x,y)$. Images are rendered using the commercially available software (VXsM, from *Nanotec*). Original data presented in Ref. [161]

be written as

$$F(\omega;\tau,N) = 8\sin^2\left(\frac{\omega N\tau}{2}\right)\frac{\sin^4(\omega\tau/4)}{\cos^2(\omega\tau/2)} \tag{7.6}$$

for the XY8-96 sequence.

The decoherence of the NV center spin is caused by the proton magnetic signal and the background noise, which can be written as

$$\chi(\tau,N) = \chi_n(\tau,N) + \chi_{bg}(\tau,N), \tag{7.7}$$

where $\chi_n(\tau,N)$ is the contribution from the proton spin and $\chi_{bg}(\tau,N)$ represents the all background contribution. Combining Equations (7.3), (7.4) and (7.7), and assuming that the $\chi_n(\tau,N)$ is small, the proton NMR signal is given by

$$\begin{aligned} s(x,y) &= 1 - \frac{C(\tau_L)}{C_0(\tau_L)} \\ &= 1 - \frac{\exp\left[-\left[\chi_n(\tau,N)+\chi_{bg}(\tau,N)\right]\right]}{\exp\left[-\chi_{bg}(\tau,N)\right]} \\ &= 1 - \exp\left[-\chi_n(\tau,N)\right] \\ &\approx \chi_n(\tau,N), \end{aligned} \tag{7.8}$$

where $\chi_n(\tau,N)$ can be calculated by substituting the following equation into Equation (7.5),

$$S(\omega) = B_{rms}^2\sqrt{\frac{\pi}{2\sigma^2}}\left(\exp\left[-\frac{(\omega-\omega_L)^2}{2\sigma^2}\right] + \exp\left[-\frac{(\omega+\omega_L)^2}{2\sigma^2}\right]\right), \tag{7.9}$$

where $S(\omega)$ is the proton spectral density, B_{rms} is the root-mean-square (rms) proton magnetic field, ω_L is the proton Larmor frequency. The Larmor pre-

cession of the ensemble proton spin is assumed to have a Gaussian spectrum characterized by the parameter σ that is related to the FWHM linewidth of the proton NMR Δf through an equation,

$$\sigma = \frac{\pi \Delta f}{\sqrt{2 \ln 2}} \approx 2.67 \Delta f. \tag{7.10}$$

Plugging in measurement parameters of $N = 96$, $\tau = 304$ ns, $f_L = 1.645$ MHz, and $\Delta f = 20$ kHz, the rms proton magnetic field for the in-contact ($s \sim 0.65$) and the retracted ($s \sim 0.4$) cases are calculated to be 485 nT and 330 nT, respectively. The larger signal compared to the nanoNMR results discussed in Chapter 5 ($B_{rms} = 12$ nT) is mainly due to the closer proximity of the NV center to the surface in this experiment.

7.1.7 Thickness of the proton containing layer

The calculated rms proton magnetic signal is used to estimate the depth of the NV center and the thickness of the proton containing layer.

Proton spins are assumed to precess about the external magnetic field axis $\hat{\mathbf{z}}'$, which is applied parallel to the NV center symmetry axis // $\langle 111 \rangle$. The multi-pulse echo sequence measures the proton magnetic field caused by the perpendicular components of the proton moment ($m_{x'}$ and $m_{y'}$) precessing at the Larmor frequency. For the NV center located at $(0, 0, -d)$, the NV center symmetry axis component of the magnetic field caused by a proton located at

(x,y,z) can be written as

$$\mathbf{B}\cdot\hat{\mathbf{z}}' = \frac{\mu_0}{4\pi r^5}\left[\left(\hat{\mathbf{x}}' m_{x'}(t) + \hat{\mathbf{y}}' m_{y'}(t)\right)\cdot\mathbf{r}\right]\left(\mathbf{r}\cdot\hat{\mathbf{z}}'\right), \tag{7.11}$$

where $\mu_0 = 4\pi\times 10^{-7}$ Vs/Am is the vacuum permeability, $\hat{\mathbf{x}}'$, $\hat{\mathbf{y}}'$ and $\hat{\mathbf{z}}' = \left(1/\sqrt{3}\right)(\hat{\mathbf{x}}+\hat{\mathbf{y}}+\hat{\mathbf{z}})$ constitute an orthonomal basis, $\hat{\mathbf{r}} = -(x\hat{\mathbf{x}}+y\hat{\mathbf{y}}+(z+d)\hat{\mathbf{z}})$ is the vector from the proton to the NV center and r is the distance between two. For the random, unpolarized protons, the mean square field is given by

$$B_{rms}^2 \equiv \left\langle\left(\mathbf{B}\cdot\hat{\mathbf{z}}'\right)^2\right\rangle = \left(\frac{\mu_0}{4\pi r^5}\right)^2\left(\mathbf{r}\cdot\hat{\mathbf{z}}'\right)^2\left[\left\langle m_{x'}^2\right\rangle\left(\hat{\mathbf{x}}'\cdot\mathbf{r}\right)^2 + \left\langle m_{y'}^2\right\rangle\left(\hat{\mathbf{y}}'\cdot\mathbf{r}\right)^2\right]. \tag{7.12}$$

From the quantum mechanics, the expectation value for $\left\langle m^2\right\rangle$ is

$$\left\langle m^2\right\rangle = \hbar^2\gamma_n^2\left\langle\tilde{I}^2\right\rangle = \hbar^2\gamma_n^2 I(I+1), \tag{7.13}$$

where $\tilde{I}$ is the spin angular momentum operator. Since the proton has $I = 1/2$,

$$\left\langle m^2\right\rangle = \frac{3}{4}\hbar^2\gamma_n^2. \tag{7.14}$$

For unpolarized nuclei, each orthogonal component takes 1/3 of this value, leading to

$$\left\langle m_{x'}^2\right\rangle = \left\langle m_{y'}^2\right\rangle = \frac{1}{3}\left\langle m^2\right\rangle = \frac{1}{4}\hbar^2\gamma_n^2. \tag{7.15}$$

Substituting this equation to Equation (7.12) leads to a point spread function,

$$B_{rms}^2(x,y,z) = \\ 2\left(\frac{\mu_0\mu_n}{4\pi}\right)^2 \frac{(x+y+z+d)^2}{\left(x^2+y^2+(z+d)^2\right)^5}\left(x^2+y^2+(z+d)^2-xy-(x+y)(z+d)\right), \tag{7.16}$$

where $\mu_n = \hbar\gamma_n/2 = 1.41\times10^{-26}$ J/T is the magnetic moment of the proton spin.

The mean square proton field from the surface proton layer of thickness h can be calculated by taking an integral of Equation (7.16),

$$\begin{aligned} B_{rms}^2 &= \rho_N \int_0^h dz \int_0^\infty dy \int_0^\infty dx B_{rms}^2(x,y,z) \\ &= \frac{5}{24\pi}\left(\frac{\mu_0\mu_n}{4\pi}\right)^2 \rho_n \left[\frac{1}{d^3} - \left(\frac{1}{(d+h)^3}\right)\right], \end{aligned} \tag{7.17}$$

where $\rho_N = 57$ nm^{-3} is the proton density. Figure 7.5 plots the rms proton magnetic signal B_{rms} as a function of the NV center depth, d. The red curve shows the result of an infinitely thick layer ($h\to\infty$) corresponding to the case of the PMMA sample in contact with the diamond surface. As discussed in the previous subsection, the in-contact rms proton signal is $B_{rms}^{in-contact} = 485$ nT, which corresponds to $d = 6.8$ nm according to the plot. The calculated NV center depth is within the expected range of 5 - 10 nm based on the nitrogen implantation energy. The curve is shifted downwards with a smaller finite value of h. The parameter h can be varied to find a value corresponding to the retracted

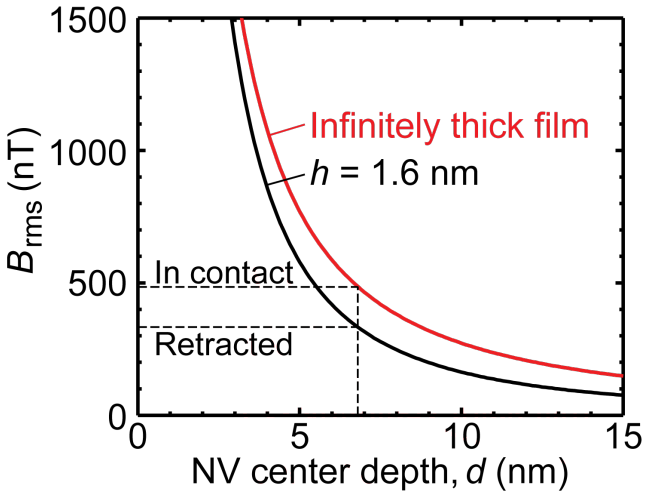


Figure 7.5: RMS proton magnetic signal B_{rms} as a function of NV center depth (d). Two curves are for a proton containing layer on the surface infinitely thick (red) and $h = 1.6$ nm thick (black). From the proton NMR measurements shown in Fig. 7.2, B_{rms} is calculated to be 485 and 330 nT for the in-contact and retracted cases, represented by the horizontal dotted lines. The NV center depth is estimated to be d =6.8 nm (represented by the vertical dotted line) from the intersection of the in-contact dotted line and the red curve. Data adapted from Ref. [161]

rms proton signal $B_{rms}^{retracted} = 330$ nT at $d = 6.8$ nm, resulting in a proton layer thickness of $h = 1.6$ nm.

7.1.8 Outlook

Towards the ultimate goal of 3D nanoMRI, reduction of the data aquisition time is a critical challenge, as the increase of the dimension of MRI requires more data points. One approach to reduce the acquisition time is to take advan-

tage of the $S = 1$ nature of the NV center spin [165]. The use of a superposition state of m_s = -1 and +1 can accumulate a spin phase from the external field twice as fast compared to the conventional magnetometry schemes using a superposition state of m_s = 0 and +1 (or -1). Using this double quantum method, the signal-to-noise (SNR) ratio of the detection of proton NMR signals is improved by a factor of 2, corresponding to a $4\times$ reduction of the data acquisition time. The SNR is predicted to be as large as a factor of 4, implying a potential averaging time reduction by a factor of 16.

Further reduction of the NV center depth with preserved spin coherence is an everlasting desire for increasing proton NMR signals. Some preliminary results of extremely shallowly doped NV centers are presented in the next subsection.

It is also important to understand the origin and the mechanism of the surface spin noise that degrades the spin coherence of near-surface NV centers. A recent experimental work shows that the bath of electron spins on the surface has a correlation rate much faster than the bulk nitrogen electron spin bath, and that the surface spin noise can be decoupled by a multi-pulse echo sequence with a shorter inter-π-pulse period [132]. Combining shallow NV center creation with the effective decoupling technique will be a promising approach to further improve the proton magnetic field sensitivity.

Finally, the existence of a proton containing layer on the surface is revealed, opening up new questions of its origin and the way to get around these background proton spins, an interesting topic in the field of surface physics and chemistry of diamond.

7.2 Extremely shallowly doped NV centers

Since shallow and coherent NV centers are one of the critical requirements for extending the proton imaging capabilities, it is important to explore the limit of depth d and T_2 of shallow NV centers. In this section, spin properties of extremely shallowly doped NV centers with $d \leq 3$ nm are investigated.

7.2.1 Sample preparation

Four ^{12}C diamond samples each containing a single nitrogen delta-doped layer are grown. Their cap layer thickness is either $c = 0.5 \pm 0.2$ or 2.1 ± 0.8 nm (two samples are grown for each c). After the ^{12}C buffer layer growth for 4 hours, nitrogen is doped using a $^{15}N_2$ doping gas flow of 30 sccm for 15 minutes, corresponding to the nitrogen delta-doped layer thickness $t = 2.1 \pm 0.8$ nm. The average depth of the doped NV centers are therefore $d = 1.5 \pm 0.6$ or 3.1 ± 1.2 nm, where $d = c + t/2$. For simplicity, these samples are hereafter called the 1.5 and 3 nm samples, respectively. All thickness is computed

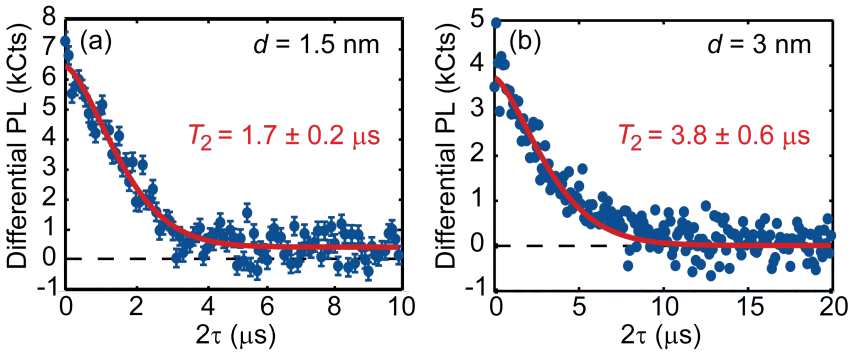


Figure 7.6: Hahn echo decay curves of extremely shallowly doped NV centers. (a) $d = 1.5$ nm and (b) $d = 3$ nm. Red lines are the fitting curves.

by using the calibrated growth rate discussed in Chapter 3. In order to form NV centers, the samples are electron irradiated after the growth, followed by annealing and acid cleaning with the standard recipe described in Chapter 4.

7.2.2 Spin coherence of extremely shallow NV centers

Despite an extreme proximity to the surface, doped NV centers in these samples display fairly stable optical properties similar to the ones at $d \geq 5$ nm. The blinking phenomena are not observed and the CWESR spectra of these extremely shallow NV centers show the characteristic hyperfine dips similar to the one shown in Fig. 4.7(b).

Figure 7.6 show typical Hahn echo data for the (a) 1.5 nm and (b) 3 nm samples. From the fits to these Hahn data, $T_2 = 1.7 \pm 0.2$ and 3.8 ± 0.6 μs are measured, respectively. Given the $d = 5$ nm sample consistently shows $T_2 > 100$

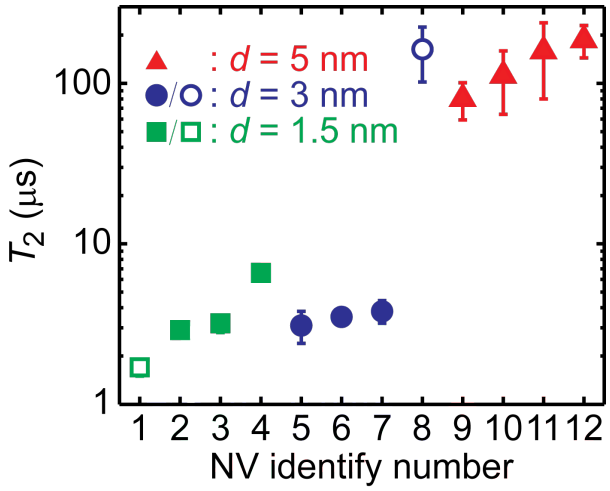


Figure 7.7: Summary of T_2 for extremely shallowly doped NV centers. Each data point corresponds to a T_2 result from a single NV center. Green and blue data points represent results from the $d = 1.5$ and 3 nm samples, respectively. Results from the $d = 5$ nm sample are also shown in red (replotted from Fig. 4.17). Open and closed symbols represent data from separate samples at the same depth.

μs, a sharp T_2 decrease of almost two orders of magnitude is observed with a small change of the depth, suggesting that the spin coherence of extremely shallow NV centers is severely degraded by the surface effect.

In order to derive more statistical information about the spin coherence of extremely shallow NV centers, T_2 times of four different NV centers are measured for each depth, as plotted in Fig. 7.7. The open and closed symbols for each color represent the data from separate samples of the identical NV center depth. For comparison, the T_2 results of the $d = 5$ nm sample are also shown. A sharp drop of T_2 is distinct between $d = 3$ and 5 nm. One outlier

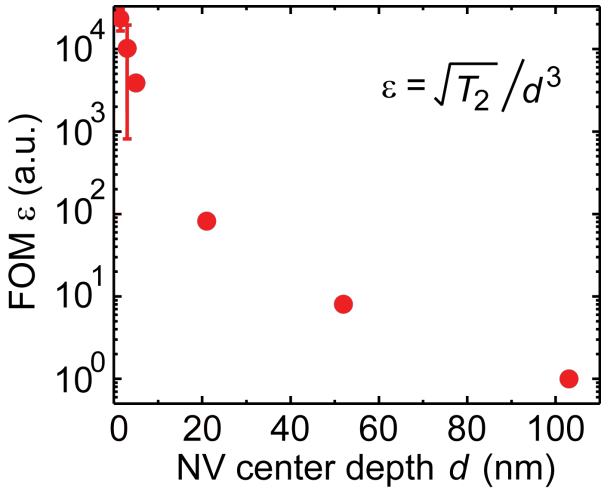


Figure 7.8: Figure of merit ε as a function of d. An average T_2 is computed from results of multiple NV centers at each depth. Error bars are calculated by their standard deviation and appropriately propagated. The ε values are normalized by the result of the $d = 103$ nm sample.

in the 3 nm sample shows $T_2 = 163 \pm 61$ μs, which may be due to this NV center being located close to the deeper limit of the nitrogen doped layer at 4.3 nm from the surface displaying more similar T_2 observed in the $d = 5$ nm sample. These results suggest that there may be a critical depth between $d = 3$ and 5 nm within which another mechanism of the surface effect dominates the drastic T_2 reduction in addition to the first reduction of T_2 observed around $d \sim 20$ nm (see Fig. 4.16) [120, 132]. Excluding this outlier of the 3 nm sample from calculation, the average T_2 for the 1.5 and 3 nm samples are 3.5 ± 0.2 and 3.6 ± 0.2 μs, respectively showing a similar value, which may be due to the depth of these NV centers being overlapped within the error.

7.2.3 Figure of merit

It is instructive to define a figure of merit (FOM) ε, which can be used to measure the performance of NV centers for the external spin sensing applications and that should be

$$\varepsilon = \frac{\sqrt{T_2}}{d^3}, \tag{7.18}$$

as the minimum detectable field of NV centers is proportional to $1/\sqrt{T_2}$ and the external magnetic field decreases with depth by d^3. Figure 7.8 plots this FOM as a function of the depth of NV centers. Average T_2 is computed from results of multiple NV centers at each depth and the vertical error bars are due to their standard deviation. The average depth is plotted in the horizontal direction and the data is normalized by the value of the $d = 103$ nm sample. The plot shows a monotonic increase of ε as depth is decreased despite monotonic decrease of T_2 with depth, suggesting that the depth factor d^3 in the denominator is much more dominant than the spin coherence factor. As the extension of T_2 by using the dynamical decoupling techniques becomes more established and popular, using a very shallow NV center in combination with the dynamical decoupling technique should provide a promising way to improve the external spin sensitivity, ultimately towards the 3D nanoMRI.

7.3 Deterministic depth control of NV emitters in photonic cavities

The nitrogen delta-doping technique is used for the deterministic vertical placement of NV center emitters in photonic cavities. The Purcell enhancement of NV center PL with a factor greater than 20 is observed using a photonic crystal nanobeam of 200 nm thick containing a nitrogen delta-doped layerat controlled depth [166].

7.3.1 Sample preparation

The sample fabrication process consists of membrane fabrication using He ion implantation, diamond overgrowth, and electrochemical etching techniques.

An electronic-grade (100) diamond substrate is He-implanted at an energy of 1 MeV and a dose of 5×10^{16} cm^{-2} to create a damaged layer at 1.7 μm from the surface. Then, a diamond film is overgrown using a standard PE-CVD recipe, consisting of a ^{12}C buffer layer of 100 nm thick followed by a 6 nm-thick ^{15}N doped layer ($^{15}N_2$ flow: 10 sccm) and a ^{12}C cap layer (100 nm). To form NV centers inside the nitrogen delta-doped layer, the sample is electron irradiated after the growth (2 MeV, 5×10^{14} cm^{-2}) followed by the standard annealing and acid cleaning process. A subsequent electrochemical etching process in pure water selectively attacks the He ion-damaged layer, resulting in

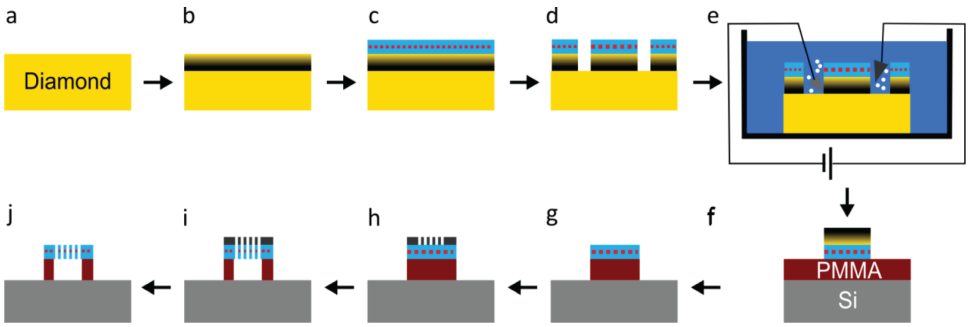


Figure 7.9: Schematic of the sample preparation process for the photonic crystal nanobeam. (a and b) A diamond substrate is He implanted creating a damaged layer ~ 1.7 μm deep. (c) The diamond film containing a single nitrogen delta-doped layer is overgrown. (d) A Mesa structure is defined by photolithography and ICP-RIE. (e) Electrochemical etching results in lift-off of a thin membrane. (f) The membrane is stamped on a PMMA-coated Si substrate with the grown film in contact with the PMMA layer. (g) The membrane is thinned down to ~ 200 nm using ICP-RIE. (h) The photonic crystal pattern is drawn using EB lithography on negative photoresist HSQ. (i) The suspended photonic crystal structure is formed using ICP-RIE. (j) The photomask is etched off. Original data presented in Ref. [166]

lift-off of a ~ 1.7 μm-thick thin diamond membrane from the substrate [167].

For photonic crystal fabrication, the diamond membranes are stamped on a poly(methyl methacrylate) (PMMA)-coated Si substrate with the overgrown surface in contact with PMMA. The membrane is then thinned using O_2 inductively-coupled plasma reactive ion etching (ICP-RIE) down to a thickness of ~ 200 nm leaving mostly the grown film on top of the PMMA layer. The photonic crystal pattern is drawn by using electron-beam (EB) lithography on negative resist (hydrogen silsesquioxane, HSQ), which serves as an etch mask during a subsequent ICP-RIE etching step. The ICP-RIE process also undercuts

the PMMA layer, leaving a suspended diamond photonic crystal nanobeam. The sample fabrication process is schematically shown in Fig. 7.9.

7.3.2 Photonic cavity design

The cavity design used in the experiment is a nanobeam with linearly tapered lattice constants in the middle of the cavity, sandwiched by a Bragg mirror on each side. This design allows for a high Q and a small mode volume (V) simultaneously. Figure 7.10(a) shows a scanning electron microscopy (SEM) image of the fabricated nanobeam. The width and length of the beam are measured to be 260 nm and 8 μm, respectively from this image. The electric field intensity profile for the fundamental transverse electric (TE) mode is plotted in Fig. 7.10(b) and (c) using a finite-difference time-domain (FDTD) simulation. According to the simulation, $Q \sim 270,000$ is predicted for the fundamental TE mode of the cavity and the mode volume is calculated to be $V \sim 0.47(\lambda/n)^3$. The measured Q value from the processed device used in the experiment is as low as 7,000 based on the photoluminescence (PL) linewidth of the cavity mode. The discrepancy is likely due to imperfection of the device process. It should be noted that $Q \sim 24,000$ is measured in a separate cavity. Despite reduction of the measured Q values, this nanobeam design still makes use of its small mode volume.

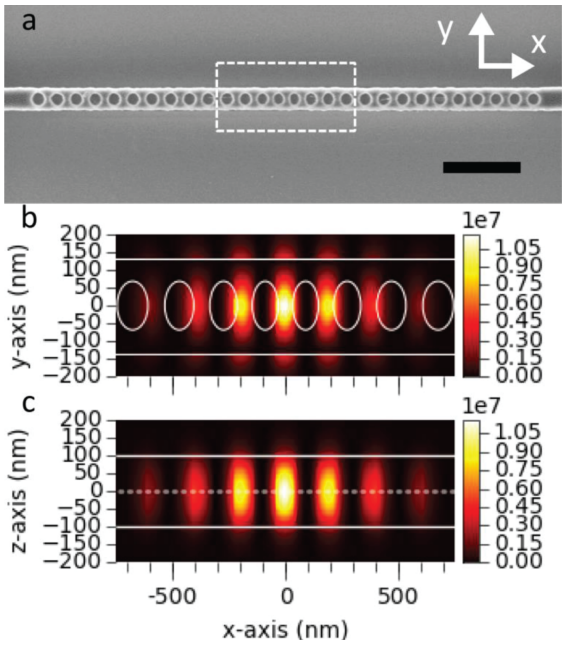


Figure 7.10: (a) SEM image of the fabricated photonic crystal nanobeam. The black line corresponds to 1 μm. FDTD simulations of the (b) in-plane and (c) vertical electric field profile of the fundamental transverse electric (TE) mode of the nanobeam. Original data presented in Ref. [166]

7.3.3 Estimation of the Purcell enhancement

PL emission of NV centers in a photonic cavity can be resonantly enhanced through increasing their spontaneous emission rate by coupling NV centers with the cavity mode. For an ideal spatial and spectral overlap of NV centers to the cavity mode, the PL emission enhancement is proportional to the Purcell factor,

$$F \approx \frac{3}{4\pi^2}\left(\frac{\lambda}{n}\right)^3 \frac{Q}{V}, \tag{7.19}$$

where $\lambda = 637.8$ nm is the NV center's zero phonon line (ZPL) wavelength,

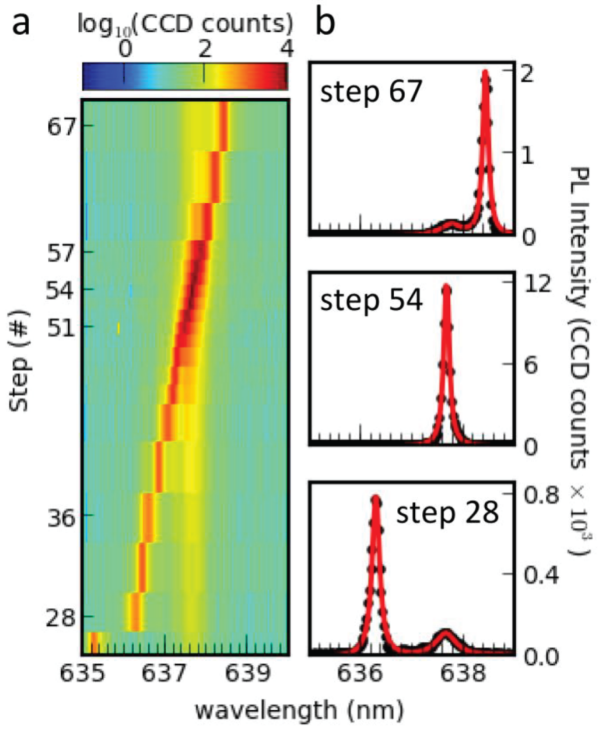


Figure 7.11: Two-dimensional plot of PL scans as a function of the nitrogen gas injection step (vertical axis). The cavity mode red-shifts across the NV center's ZPL wavelength (637.8 nm) during the multiple steps of the nitrogen gas injection. Single PL scans of the step 28 (off resonance), 54 (on resonance) and 67 (off resonance) are shown to the right. Original data presented in Ref. [166]

$n = 2.4$ is the refractive index of diamond.

PL enhancement at the ZPL wavelength is observed by tuning the cavity mode frequency via injecting nitrogen gas into the cryostat. By carefully controlling the nitrogen gas flow, the red-shift of the cavity mode wavelength can be tuned by ~ 0.07 nm per injection step. Figure 7.11 shows cavity mode shift passing across the ZPL wavelength as a function of the injection step. When the

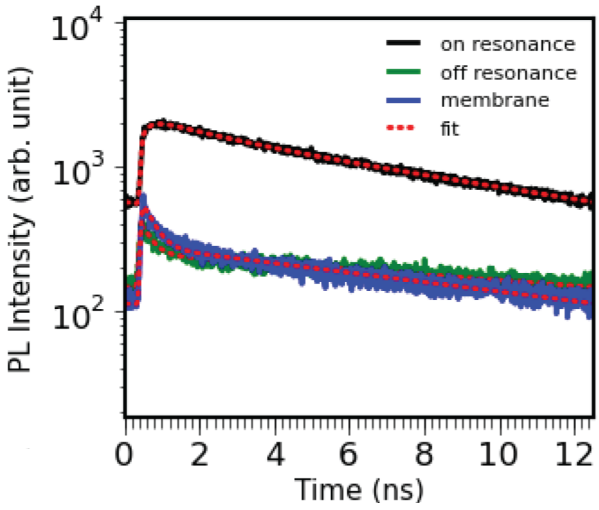


Figure 7.12: Time-resolved PL intensity of the NV centers on resonance (black) and off resonance (green) to the cavity mode. The blue curve is for the NV centers in the membrane without photonic structure fabrication. Red dotted lines are fitting curves according to the double exponential decay model. The longer decay component of each fit curve is used to estimate the photon lifetime. Original data presented in Ref. [166]

cavity mode is in resonance with the ZPL (step 54), the PL intensity at the ZPL is enhanced by a factor of 27 compared to the off-resonance case (step 28).

In order to verify if this ZPL enhancement is caused by the Purcell effect, NV center's photon lifetime is measured when the cavity mode is on (τ_{on}) and off (τ_{off}) resonance to the ZPL as well as from a diamond membrane without photonic crystal structure (τ_0). The time-resolved fluorescence curves are fitted with the double exponential decay model. The long decay component is used to calculate the lifetime for each case, which are $\tau_{on} = 10.43^{+0.56}_{-0.22}$ ns, $\tau_{off} = 22.34^{+1.19}_{-1.03}$ ns and $\tau_0 = 12.96^{+0.68}_{-0.67}$ ns (Fig. 7.12). As expected, the

on-resonance lifetime is reduced compared to the off resonance case due to an increase of spontaneous emission rate originated from the Purcell effect. From these measured values, the Purcell factor can be calculated by the following equation,

$$F = \frac{\tau_0}{\xi_{ZPL}} \left(\frac{1}{\tau_{on}} - \frac{1}{\tau_{off}} \right), \tag{7.20}$$

where $\xi_{ZPL} \sim 0.03$ is the zero-phonon spontaneous emission fraction in bulk diamond [152]. Plugging in the measured lifetimes into Equation (7.20), the Purcell factor is calculated to be $F = 22$, which is comparable to the PL enhancement factor of 27 discussed above, confirming that both of the PL enhancement and lifetime reduction are caused by the Purcell effect.

7.3.4 Outlook

PL intensity enhancement due to the Purcell effect is observed from NV centers embedded in the nitrogen delta-doped layer within a diamond-based photonic crystal cavity. Despite a high Q/V ratio of the nanobeam design, with a measured $Q \sim 7000$ and a calculated $V = 0.47(\lambda/n)^3$, the resulting Purcell factor of $F = 22$ is not as high as expected. For example, Faraon *et al.*, [152] measured $F = 70$ from the diamond-based 2D photonic cavity with a measured $Q \sim 3000$, and a calculated $V = 0.88(\lambda/n)^3$. The observed decrease of the Purcell factor may be due to the cavity mode coupled to a broad peak from an

ensemble of NV centers. The FWHM of the NV center PL is measured to be 0.2 - 0.35 nm, much broader than the cavity mode resulting in a reduction of the coupling between NV centers and the cavity.

Nevertheless, this experiment demonstrates a first important step of a photonic cavity that contains a photon emission source at a deterministic position, a critical requirement for the maximized performance of photonic cavities. As discussed in Chapter 6, the nitrogen delta-doping technique can be extended to the 3D position control of the NV center using the aperture implantation. The compatibility of the nitrogen delta-doping technique with the photonic crystal fabrication demonstrated here paves a way towards the full 3D position control of a photon emitter within diamond-based photonic cavities.

7.4 Sub-micron-scale diamond particle sensor in fluidic environment

Carefully designed sub-micron-scale diamond particles (DPs) can hold their position and motion stable in a fluidic environment using an optical tweezer technique [168], which can be potentially used for an *in-situ* temperature and magnetic sensor in a fluidic channel [169].

7.4.1 Sample preparation

Cylindrical-shape DPs of $\sim$ 500 nm in diameter and $\sim$ 2 μm in length are fabricated using diamond membranes made by a combination of He implantation, diamond overgrowth and electrochemical etching techniques described in the previous section. For the diamond overgrowth, a diamond film of 1 μm thick is grown by the high-power growth mode (see Section 3.8) using a microwave power of 2000 W, pressure of 165 Torr, and CH_4/H_2 ratio of 1 % for 20 minutes. During the diamond growth, $^{15}N_2$ flow of 0.1 sccm is added allowing for uniform nitrogen doping for the entire film. Due to the increased growth rate, nitrogen is easily incorporated into the film, resulting in a nitrogen concentration $> 10^{18}$ cm^{-3} and also a high NV center density showing a bright PL from the film. After the growth, the membrane is lifted-off from the substrate by the electrochemical etching process and is stamped on a PMMA-coated Si substrate with the grown film in contact with PMMA. Subsequently, sub-micron-scale cylindrical DPs are fabricated using EB lithography on negative photoresist (HSQ) and O_2 ICP-RIE. This process allow for mass production of the cylindrical DPs (6.3×10^5 DPs per process) as demonstrated by an SEM image shown in Fig. 7.13. Furthermore, if an ICP-RIE condition is carefully tuned, the DPs are anchored by thinned PMMA to the Si substrate, allowing for release of DPs in solvent and their easy introduction to microfulidic channels.

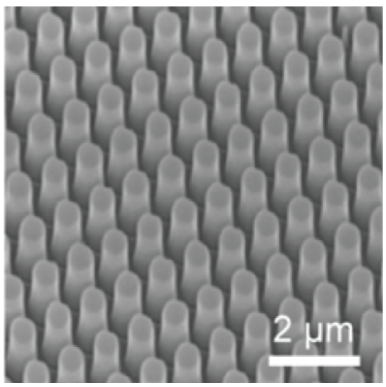


Figure 7.13: SEM image of an array of the fabricated cylindrical diamond particles (DPs). Original data presented in Ref. [169]

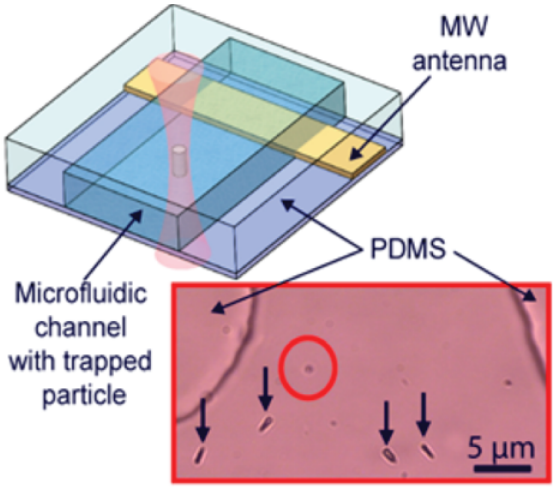


Figure 7.14: Schematic of the polydimethylsiloxane (PDMS) microfluidic channel with a single DP trapped in the focal volume of a 1064 nm infrared laser. A microwave (MW) antenna used for the ODMR measurements are shown in yellow. A CCD image of the microfluidic channel is shown in the inset. A trapped DP is circled in red, whereas DPs stuck at the bottom of the channel are indicated by the black arrows. Original data presented in Ref. [169]

7.4.2 Position and motion stability of diamond particles in microfluidic channel

Figure 7.14 shows a schematic of a polydimethylsiloxane (PDMS) microfluidic channel with a trapped particle using a 1064 nm infrared laser. A careful control of the size of the DPs allows for a stable trapping of a single DP within the trapping volume of the focused laser. Moreover, their cylindrical shape enables a deterministic orientation control of the DPs during trapping with their longitudinal axis (// $\langle 100 \rangle$ crystal axis) along with the laser's optical axis. The inset of Fig. 7.14 shows a charge-coupled device (CCD) image of the microfluidic channel displaying a single trapped DP (circled in red) with its axis aligned on the laser axis. Single DPs can be trapped for up to 30 hours before purposely releasing them, demonstrating stability of the engineered DPs within a fluidic channel, allowing for long data acquisition using ODMR or spin echo techniques.

A microwave antenna is used for ODMR measurements of trapped DPs in the microfluidic channel. Figure 7.15 shows ODMR spectra for commercially available DPs (top) and the engineered DPs (bottom). The external magnetic field of $\sim$ 10 G is applied parallel to the laser axis. The commercial DPs of their diameter less than 100 nm without control of their shape, showing relatively broad ODMR dips with a FWHM of $\sim$ 30 MHz due to uncontrolled

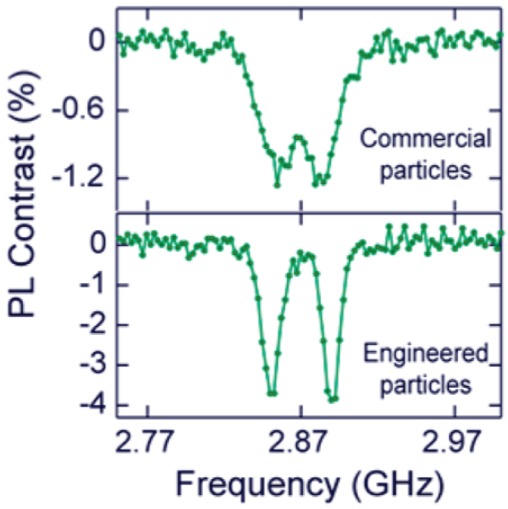


Figure 7.15: ODMR spectra for commercially available DPs (top) and the engineered DPs (bottom). The external magnetic field of $\sim$ 10 G is applied parallel to the optical axis of the laser, which is along the $\langle 100 \rangle$ crystal axis for the engineered DPs. Original data presented in Ref. [169]

rotational dynamics within the trapped volume. On the other hand, the engineered DPs show sharper dips with a FWHM of $\sim$ 10 MHz because of their suppressed rotational motion aligning parallel to the laser axis. Furthermore, the observation of the two distinct dips suggests that their precession around their main axis is also suppressed, demonstrating an excellent position and motion stability of the engineered DPs in the fluidic environment for a time scale of 400 seconds.

7.4.3 Outlook

The position and motion stability as well as compatibility to the ODMR

technique of the engineered DPs hold a promise for the DP-based sensing in a fluidic environment. Although temperature sensing in living cells using diamond nanoparticles is already demonstrated [48], the engineered DP sensors possess additional capabilities to control their locations inside cells by scanning the the optical tweezers laser and to enhance their sensitivity using the spin echo technique. Temperature sensing applications of these engineered DPs may be more feasible than magnetic sensing because of high thermal conductivity of diamond and mitigated size requirement for thermometry. Careful position control of NV centers within a DP to protect their spin coherence is an important challenge for their magnetic sensing applications in a fluidic environment.

7.5 Conclusion

Recent results that extend the applications of NV centers in PE-CVD grown diamond films are reviewed.

A shallowly implanted single NV center in a ^{12}C-enriched diamond film is used to demonstrate two-dimensional nanometer-scale magnetic resonance imaging (2D nanoMRI) with spatial resolution of 12 nm. Further extension of this technique to the 3D nanoMRI requires reduction of the data acquisition time, as the resolution is currently limited by the thermal drift of the scanning system exacerbated by the long averaging time. Creating even shallower

NV centers with maintained coherence is one of the approaches to enable 3D nanoMRI. In order to study limitations of shallow NV centers, spin properties of extremely shallowly doped NV centers ($d \leq 3$ nm) are investigated. Although significant reduction of $T_2 \sim$ a few μs is observed, the extremely shallow NV centers still maintain their optical properties without showing blinking.

The nitrogen delta-doped diamond films are compatible to the diamond-based nanometer scale device engineering, enabling to fabricate photonic crystal nanobeams with deterministic depth control of NV center emitters. A full 3D position control of NV emitters could be possible using a combination of the nitrogen delta-doping technique and the aperture implantation discussed in Chapter 6. The position engineering of NV centers inside the diamond nanostructures is one of the most important challenges for the NV-based quantum processing and metrology applications.

Sub-micrometer-scale diamond particle engineering allows for position and motion stability in a microfluidic channel, an important first step for thermal and magnetic sensing applications with location-controlled sensors within biological and chemical environments.

Chapter 8

Conclusion

A crystal growth technique that enables to control the depth of a single NV center at nanometer scale is developed. This nitrogen delta-doping technique enables to create shallow NV centers whose depth ranging from about 100 nm down to less than 2 nm while preserving their spin coherence. The T_2 times of these doped NV centers are measured to be $T_2 > 600$ μs for $d > 50$ nm and $T_2 > 100$ μs at $d = 5$ nm.

These shallowly doped, long-coherence NV centers are used as an atomic-scale magnetic sensor enabling nanometer-scale volume detection of nuclear spins *external* to the diamond crystal. This nanometer-scale nuclear magnetic resonance (nanoNMR) technique is further extended to two-dimensional magnetic resonance imaging (2D nanoMRI) with spatial resolution of 12 nm. Realization of ultimate 3D nanoMRI will require to create even shallower and

long-coherence NV centers, necessitating understanding the mechanism of surface spin noise.

The nitrogen delta-doping technique is combined with shallow ^{12}C ion implantation through lithographically-patterned apertures enabling 3D localization of NV centers at a nanometer scale. By controlling the implantation dose and the annealing conditions, the localization volume for a single NV center is estimated to be $\sim$ (180 nm)^3. Moreover, by separating nitrogen incorporation from the vacancy creation, the local crystal damage around the NV center is minimized, leading to the preserved spin coherence of $T_2 > 300$ μs for the 3D-localized NV centers. The localization volume is comparable to the diamond-based nanostructures, holding a promise for quantum applications by maximizing coupling between NV centers and these nanostructures. As an example of a deterministic placement, the delta-doped NV centers are incorporated into a photonic crystal nanobeam displaying a Purcell enhancement of their PL emission. An ultimate 3D position control of the NV center emitter in the cavity will further enhance the NV center photon emission.

As presented in this dissertation, a nanometer-scale materials engineering technique enabling to control a "single atom" in the solid state opens up wide applications ranging from nanometer-scale imaging to quantum information processing. Despite an outstanding challenge, pushing the boundaries of

the nanometer-scale engineering into atomic scale will further enable broad technological capabilities and provide intriguing problems for the science community.

Appendix A

Seki AX6300 Diamond CVD Operation Procedure with 1.5 kW Microwave Head

(A) Initial check

1. Sign up and write down the date and the description of the process in the Diamond CVD machine check list.
2. Check if the chamber is being pumped down with the turbo pump by checking all the icons in the main panel of the AX6300-1500 software representing the gate valve (GATE), turbo pump (TURBO), the valve backside of the turbo pump, and the dry pump (PUMP) are red.
3. Check the pressure at the Anelva Ionization Gauge on the rack. It should read on the order of 1e-5 Pa or lower after pumping down for 2.5 hours.

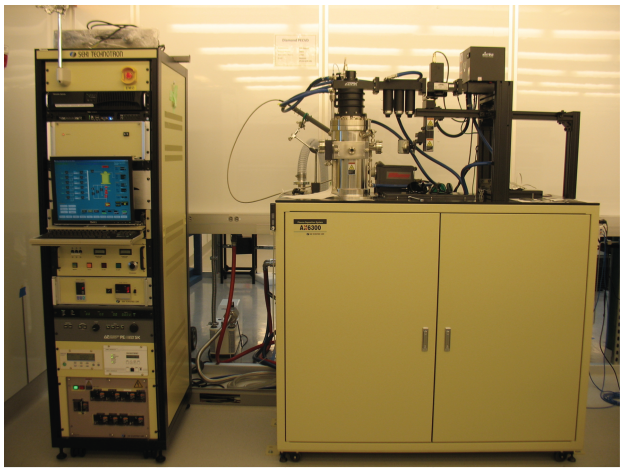


Figure A.1: Photo of the diamond CVD system.

Record this value on the Diamond CVD machine check List.

4. Turn the valve at the Ar flow meter attached to the CVD machine to the left. Set the flow value around 5 SCFH. The Ar gas line is connected to the gas ballast port in the dry pump. The Ar gas improves the pumping of hydrogen.

(B) Starting up and verifing the gas lines

1. Go to the chase, and turn on the hydrogen purifier following the Hydrogen Purifier Activation Procedure, which is located in the case on the side of the hydrogen gas cage.

2. While turning on the hydrogen purifier, check the hydrogen gas remaining by reading the upside pressure of the gas regulator of the hydrogen bottle

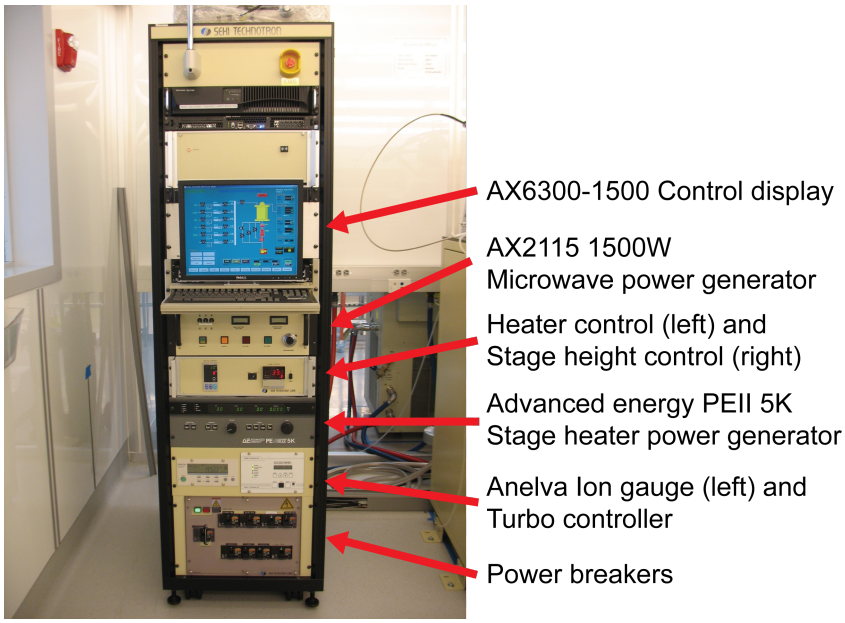


Figure A.2: Photo of the Diamond CVD rack.

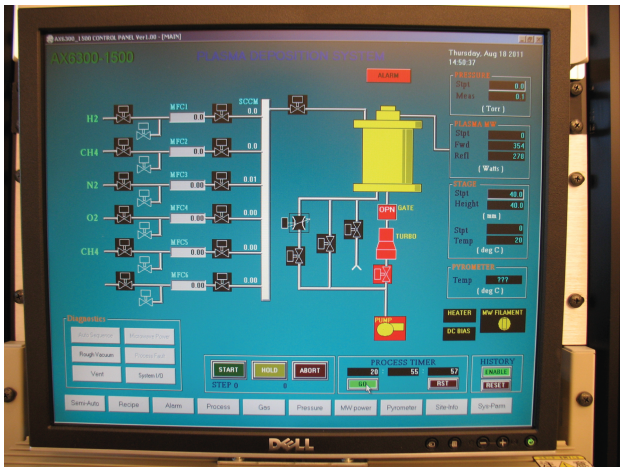


Figure A.3: Photo of the display showing the main panel of the CVD control software.



Figure A.4: Photo of the chase.

(the left bottle inside the cage). Record this value in the Diamond CVD machine check list.

3. Verify that the hydrogen gas and the methane gas are online by checking the gas monitor sitting on top of these gas cages. Check all the valves in the gas lines in use are open.

4. Turn on the chiller unit. Go back to the in front of the CVD machine. Go to the Alarm Panel on the control software and click the RESET button. The alarm message will disappear and the signal on top of the rack will turn green. Usually the signal is covered with aluminum foil.

(C) Before starting the process

1. Turn off the ion gauge filament by pushing the FILAMENT button on the

Anelva Ionization Gauge on the rack. Turn off the ion gauge by pressing the green power button on the ion gauge.

2. Close the turbo pump line by clicking the icons of the gate valve (GATE), turbo pump (TURBO) and the valve back at the turbo pump in this order in the main panel of the control software. They should become black after clicking. Reset the process timer in the main panel.

3. Turn on the microwave power generator by lifting up the white lever switch at AX2115 1500W MICROWAVE POWER GENERATOR. After seconds, the MW FILAMENT icon in the main panel of the control software turns red. Make sure that the indicator on the READY of the power generator is lit at REMOTE. If not (the indicator is lit at LOCAL), push this button once.

4. Go to the Semi-Auto panel in the control software. Set 8.0 in the box at the PRES row and 100 in the box at the H2 (MFC1) row in the SP_MAIN column, and click Start in the both rows. Now the hydrogen gas is led to the chamber with the gas flow at 100 sccm controlled by the MFC1, and the chamber pressure is maintained at 8 Torr by adjusting the throttle valve automatically. It takes a couple of minutes for the chamber pressure to get stabilized (the orange indicator in the PRES row moves to the DONE column).

5. Check if the sample is sitting in the pocket of the top face of the sample holder and if the sample holder is located roughly at the center inside the chamber by looking inside the chamber through the top window. Use a small ladder to climb up to the machine. Aim the laser of the pyrometer at the sample by tweaking the screws on the gray, cylindrical laser mount

6. Open the cage at the lower part of the CVD machine, and check the water flow of the flow meters located on the wall inside. These should read around 4.1 (upper meter) , 8.7 (middle meter) and 0.7 (lower meter). Record these values in the Diamond CVD check list.

7. Set the values at the three tuners hanging down from the waveguide to the proper numbers. The appropriate values could change and need to be adjusted for each operation time. You can refer to the values which work best for the last time as a start point. Record these tuner reads in your notebook.



Figure A.5: Photo of the display showing the Semi-auto panel of the CVD control software.

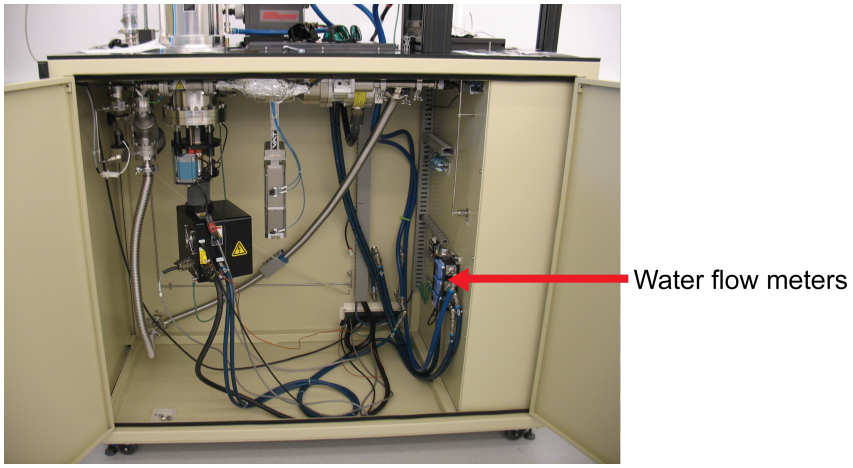


Figure A.6: Photo of the cage at the bottom of the diamond CVD system.

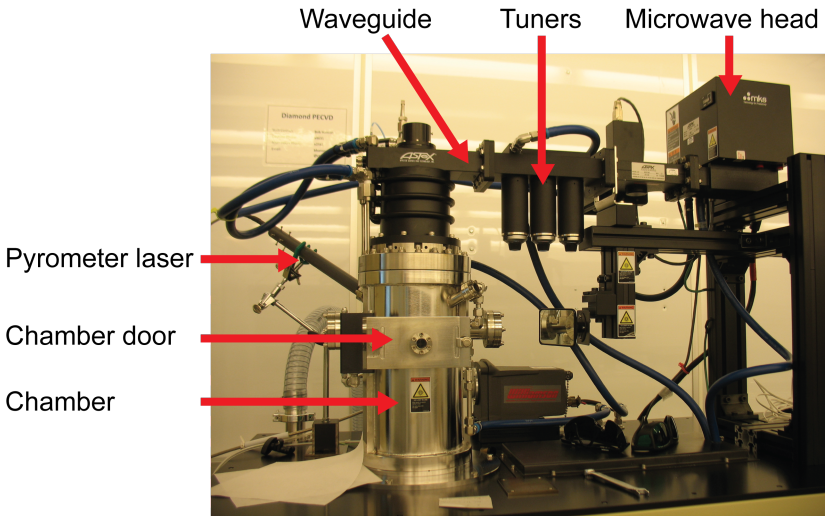


Figure A.7: Photo of the top part of the diamond CVD system.

(D) Plasma ignition and Ramping up temperature

1. After confirming that the chamber pressure is stabilized, set 400 in the box (next to the letter "F") at the MWAVE row in the SP_MAIN column and push the Replace button next to the box.

2. Push the Start button at the MWAVE row. The microwave power generator turns on by this action. Look carefully where a plasma ball shows up inside the chamber. If the chamber (this also works as a cavity for the microwave) is tuned correctly, a plasma ball shows up above the sample holder when the REFLECTED WATTS value at the AX2115 1500W MICROWAVE POWER GENERATOR reaches about 100 and suddenly drops down below 50. If a plasma ball shows up at the quartz window on

top of the chamber or at the side of the stage below the sample holder, cut off the microwave immediately by pushing the Start button at the MWAVE row in the Semi-Auto panel. The plasma ball showing up at wrong places can cause an arcing damage to the equipment. Cut off the microwave also if the REFLECTED WATTS remains at the high value around 200 and never drops. In these cases, tweak the tuner tabs and try again until the plasma ball shows up above the sample holder. Setting the pressure to the lower value (about 5 Torr) might help you turning on the plasma in a correct place.

3. After confirming the plasma turns on correctly, minimize the read at the REFLECTED WATTS by tweaking the three tuner tabs. The value can reach to the 0. Usually, the center tab affects most, followed by the left and the right ones. The REFLECTED WATTS indicates the reflected microwave power back to the microwave source due to the impedance mismatch of the cavity consisting of the chamber and the waveguide. You can tune the cavity condition by adjusting these three tuners.

4. If you feel comfortable with the plasma ignition, increase the pressure and the hydrogen flow by setting 25.0 and 400 in the boxes at the PRES and the H2 (MFC1) rows in the SP_MAIN column respectively and click Replace button next to these boxes. The hydrogen MEAS value will soon turn to

the 400 (sccm), while it takes a couple of minutes for the chamber pressure to reach and get stabilized at 25 Torr.

5. While chamber pressure increases, the REFLECTED WATTS value may also increase. Tweak the tuner tabs to minimize this value when it starts to increase. Do not exceed 100, otherwise the plasma ball may disappear inside the chamber. If this happens, turn off the plasma by hitting the Start button at the MWAVE row, set pressure and the hydrogen flow at 8 Torr and 100 sccm again, and repeat the plasma ignition procedure (D.2).

6. When the chamber pressure get stabilized at 25 Torr (the orange indicator moves to the DONE column in the PRES row), with stable plasma condition, set 750 in the box at the MWAVE row in the SP_MAIN column and click Replace next to the box. Now the microwave power turns up to 750 W. The REFLECTED WATTS may increase when the microwave power jumps up. Tweak the tuner tabs again to minimize the reflected power.

7. After minimizing the reflected power, set 800 in the box at the HEATER row in the SP_MAIN column. Bring a timer, and start counting up when you hit the Start button at the HEATER row. Make sure that the stage heater power generator outputs the power by checking the Setpoint on the ADVANCED ENERGY PEII 5K reads about 3.7. The Setpoint number will keep fluctuating. Now, the stage heater ramps up until the thermo-

couple temperature beneath the stage inside the chamber reaches and get stabilized at 800 ^{o}C. The output power is automatically adjusted.

8. Go to the Main panel and then Pyrometer panel in the control software. Adjust the temperature range by clicking the top and the bottom number at the vertical axis and input the appropriate number. Adjust also the time range by clicking the horizontal axis. You have 1 min, 30 min, 8 hours, 24 hours, and 100 hours options. 30 min range is typically used when ramping up.
9. Adjust Ar flow at around 3 SCFH.
10. Keep watching the pyrometer readout, CH_PRES (chamber pressure), Set-point at the ADVANCED ENERGY PEII 5K and the heater PV at the HEATER CONTROL on the rack while ramping up. Record these values each minute. The pyrometer readout reaches at the maximum about 5min after you turn on the heater.
11. Wait 6 min after you click the Start button at the HEATER row in the Semi-Auto panel. Bring another timer and start counting up when the first timer counts 6min. At this moment, you move onto the hydrogen etching process, which prepares better interface before diamond growth. The typical hydrogen etching condition is the microwave power of 750 W, the pressure of 25 Torr, the thermocouple temperature of 800 ^{o}C, hydrogen

flow of 400 sccm. The hydrogen etching process typically lasts 15 min. You need not to do anything except starting another timer on moving to the hydrogen etching process.

(E) Diamond growth

1. Keep recording the pyrometer readout, CH_PRES (chamber pressure), Setpoint at the ADVANCED ENERGY PEII 5K (stage heater output) and the heater PV at the HEATER CONTROL on the rack (thermocouple temperature) each minute and each 5 minutes after 5 minutes during the hydrogen etching process. Occasionally check the plasma shape inside the chamber. Do not stare at the plasma ball for a long time, though, since the plasma emits the UV light. You may use a sunglass.
2. Reset the first timer. Go to the Semi-Auto panel at the control software at least one minute before the hydrogen etching process is done.
3. After 15 minutes of the hydrogen etching, diamond growth starts by introducing methane gas into the chamber while other parameters are maintained. Set (typically) 0.1 (sccm) in the box at CH4 (MFC2) row in the SP_MAIN column.
4. When the second timer counts 15 minutes, Click Start button at the CH4 (MFC2) row. Start a new timer simultaneously. This third timer counts

the growth time. Make sure that an orange indicator shows up at the ACT column in the CH4 (MFC2) row and moves to the DONE column when the methane gas flow reaches the setpoint. Make sure that the MEAS value at the CH4 (MFC2) row shows around the input value.

5. Keep recording the pyrometer readout, CH_PRES (chamber pressure), Setpoint at the ADVANCED ENERGY PEII 5K (stage heater output), the Ar flow level and the PV at the HEATER CONTROL (thermocouple temperature) each minute and each 5 minutes after 5 minutes in the first 15 minutes of the diamond growth. You don't have to stay in front of the machine all the time, but always pay attention about the machine condition during the growth. Come back and record theses values at least every hour to make sure the growth runs with no problem.

(F) Finishing up growth

1. After a certain time (typically 6 hours), finish the diamond growth by shutting off the methane flow by clicking the Start button at the CH4 (MFC2) row in the Semi-Auto panel. You may proceed to the hydrogen termination process by keeping all the parameters in this state for 5 minutes without methane flow.

2. Either immediately after the diamond growth or after the hydrogen termi-

nation process, turn off the microwave, heater, and the hydrogen flow by clicking the Start button at the MWAVE, HEATER, PRES, and H2 (MFC1) rows. All the orange light at the DONE column should turn off after clicking.

3. Turn off the microwave power generator by lifting down the white lever switch at AX2115 1500W MICROWAVE POWER GENERATOR. Go back to the Main panel at the control software and make sure that the MW FILAMENT icon turns black. Check at the "MW Shut off?" column in the Diamond CVD check list.

4. Turn the valve at the Ar flow meter toward the further right. Although the Ar flow may not get to the 0, this is fine.

5. Leave the machine at this state for 38 minutes to cool down.

6. While cooling down, turn off the hydrogen purifier by following the Hydrogen Purifier Standby Procedure. This is on the backside of the Hydrogen Purifier Activation Procedure.

7. Check the hydrogen gas remaining by reading the upstream pressure of the regulator on the hydrogen gas bottle in the gas cage. Record the gas remaining as well as the process time in the Diamond CVD check list.

8. After the completion of hydrogen purifier standby procedure, check at the

"H2 gas shut down?" column in the Diamond CVD check list.

(G) Unloading the sample

1. Make sure that the thermocouple temperature (the PV at the HEATER CONTROL on the rack) is less than 50 ^{o}C.
2. Go to the Main panel in the control software. Set 0 in the box at Stpt in the PRESSURE square at right top of the panel. Open the throttle valve by clicking the valve icon at the bottom in the further left line (connecting the chamber icon and the PUMP icon).
3. Turn left the Ar flow meter valve and set the Ar flow at 5 SCFH.
4. Lower the stage height to the loading position by setting 10 in the Stpt box in the STAGE square at the right side of the Main panel.
5. Wait until the chamber pressure is less than 2.0 Torr by reading the Meas in the PRESSURE indicator.
6. When the chamber pressure gets below 2.0 Torr, open the rough valve by clicking the valve icon in the second line from the left (connecting the chamber icon and the PUMP icon). Wait until the chamber pressure is less than 0.1 Torr.
7. Loosen the two hex bolts on the chamber door by a wrench.

8. Purge the chamber by the Ar vent gas though clicking the valve icon at the third line from the left (hanging from the chamber icon and an arrow at the other end).
9. When the chamber pressure is over 200 Torr, the ALARM indicator turns red. Go to the Alarm panel and click the RESET button at the top. The alarm message will disappear and the ALARM indicator in the Main panel becomes dark again.
10. When the chamber pressure reaches 750 Torr (the atmospheric pressure), the chamber window pops open.
11. Change your glove to a new one. Grab and take out the sample holder. Take the sample out from the pocket of the sample holder by a tweezer.
12. You may load a new sample in the pocket of the sample holder.
13. Return the sample holder into the chamber by fitting it into the centering plate. Make sure the sample holder is sitting roughly at the center of the stage by checking all around the edge of the centering plate is equally separated from the edge of the stage.
14. Take out and sweep the O ring at the chamber door by IPA.
15. Close the chamber door, stop the Ar vent gas. Start pumping down the chamber using the throttle valve line by clicking the corresponding icon.

Push the chamber door for a little while until the chamber pressure goes down ($\sim$ 700 Torr) such that it automatically pulls the door.

16. Tighten two hex bolts on the chamber door by a wrench.

17. Pump down the chamber through the throttle valve. Wait for the chamber pressure being below 2.0 Torr. It takes about 12 minutes.

18. When the chamber pressure becomes below 2.0 Torr, open the rough valve by clicking the corresponding icon in the Main panel.

19. Wait until the chamber pressure is lower than 0.1 Torr. Then, push the green power button on the Anelva Ionization Gauge on the rack. Wait until the pressure reads below 1e-0 Pa. Do not push the FILAMENT button at this point. You will read "TC" on the panel, suggesting the pressure reads by the thermocouple.

20. Close the throttle valve and the rough valve by clicking the corresponding icons. These icons should turn black.

21. Open the valve at the backside of the turbo pump by clicking the corresponding icons.

22. Turn on the turbo pump by clicking the TURBO icon. This icon starts blinking until the turbo pump reaches the normal operation state. Make sure that the green light at the ACCELERATION turns on and Rot Spd

keep increasing in the panel at the TURBO CONTROLLER on the rack. It takes about 2 minutes to get the normal operation.

23. Go to the chase and push the “ON/OFF” button on the chiller unit to stop the water flow. You don’t need to shut down the whole chiller system. After a few seconds, the alarm beep will come out from the diamond CVD machine. Go back to the rack of the CVD machine and click the BZ STOP button at the top of the Alarm panel. The alarm message remains in the Alarm panel and the signal at the top of the rack remains red even after you click the BZ STOP button. Just leave them. These signs will stay until you turn on the chiller unit for the next growth.

24. When the turbo pump rotation speed reaches 600 Hz, the TURBO icon in the Main panel stays red. At this point, open the gate valve by clicking the GATE icon in the Main panel. Click GO button in the PROCESS TIMER in the main panel to count the pumping time with the turbo pump.

25. The pressure read at the Anelva Ionization Gauge will increase to 2e+1Pa and start to decrease later. When this pressure read reaches 5e-0Pa, push the FILAMENT button to turn on the ion gauge. Make sure that you read “BA” on the panel of the ion gauge. Check at the “Turbo ON? ” and “IG ON?” column in the Diamond CVD check list.

26. When the pressure at the ion gauge reads below 1e-3Pa, turn the Ar flow

valve towards the further right. The flow meter may not reach to the 0. This is fine. Check at the "Ar purge shut off?" column in the Diamond CVD machine check list.

27. Make sure that you filled out all the items on the check list for your process today.

28. You are all set!

Appendix B

Growth resources

Table B.1 shows a list of samples presented in this dissertation. The thickness of layers in each sample is calculated by the calibrated growth rate. Three types of vacancy creation methods, electron irradiation, ^{12}C ion implantation, and ^{15}N ion implantation are denoted by e-, ^{12}C, and ^{15}N, respectively. The column on the far right shows the corresponding sections in the dissertation that discuss more details about the sample structure and the results.

Figure B1 shows a drawing of the molybdenum sample holder. Seen at the center of the holder is the sample pocket. The size of the pocket can be adjusted to the different sizes of the samples. The depth of the pocket should be same as the height of the sample otherwise the sample surface could be subject to the excessive plasma damage. The original design is from Ref. [83].

Sample Name	Project	Depth d (nm)	Layer thickness: Cap c (nm)	Layer thickness: N layer t (nm)	Layer thickness: Buffer (nm)	$^{15}N_2$ flow (sccm)	Vacancy creation: method	Vacancy creation: energy	Vacancy creation: dose $(cm)^{-2}$	Annealing: Temp. (^{o}C)	Annealing: Time (hr)	Dissertation Chapter
D200	Delta-doping	5	4	2	32	30	e-	2 M	10^{14}	850	2	4.8
D188	Delta-doping	21	21	1	32	10	e-	2 M	10^{14}	850	2	4.8, 5.2, 5.3
D206	Delta-doping	52	51	1	32	10	e-	2 M	10^{14}	850	2	4.8
D213	Delta-doping	103	103	1	32	10	e-	2 M	10^{14}	850	2	4.8
D212	$^{13}C/^{12}C/^{13}C$		103	1	32	10	e-	2 M	10^{14}	850	2	4.6, 4.7
D239	Shallow NV	1.5	0.5	2	32	30	e-	2 M	10^{14}	850	2	7.2
D247A	Shallow NV	1.5	0.5	2	32	30	e-	2 M	10^{14}	850	2	7.2
D234	Shallow NV	3	2	2	32	30	e-	2 M	10^{14}	850	2	7.2
D237B	Shallow NV	3	2	2	32	30	e-	2 M	10^{14}	850	2	7.2
D202	NV density	5	4	2	32	10	e-	2 M	10^{14}	850	2	4.8
D203	NV density	9	8	2	32	10	e-	2 M	10^{14}	850	2	4.8
D204	NV density	106	103	6	32	10	e-	2 M	10^{14}	850	2	4.8
D279	^{12}C-annealing	106	103	6	51	10	^{12}C	2 k	10^{10}	800	0.5, 1	6.4
D263	^{12}C-dose	54	51	6	51	0.1	^{12}C	7 k	10^{9}-10^{11}	850	0.5	6.5
D269	^{12}C-dose	54	51	6	51	10	^{12}C	7 k	10^{9}-10^{11}	850	0.5	6.5
D280	3D control		51	51	51	10	^{12}C	7 k	10^{13}	850	0.5	6.6
D255	3D nanopillar		51	51	51	50 (N_2)	^{12}C	7 k	10^{13}	850	2	6.6
D266	nanoMRI				51	undoped	^{15}N	2.5 k	10^{10}	850	6	7.1
C006	Phtonic cavity	105	103	5	103	10	e-	2 M	5×10^{14}	850	2	7.4

Table B.1: List of samples

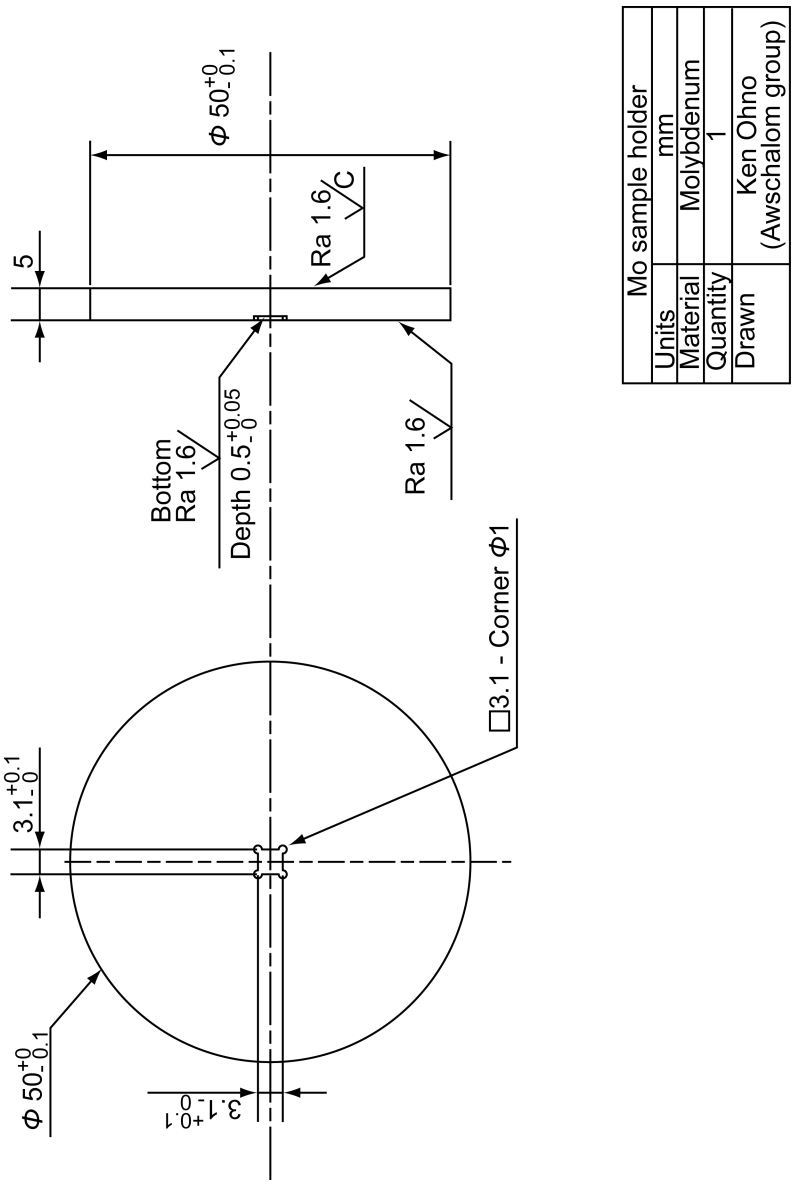


Figure B.1: Molybdenum sample holder design

References

[1] G. E. Moore, Electronics **38**, 114 (1965).

[2] International Roadmap Committee, editor. *The International Technology Roadmap for Semiconductors* (2013).

[3] A. Cho, eds., *Molecular Beam Epitaxy (Key Papers in Applied Physics)* (American Institute of Physics, New York, 1997).

[4] M. Desirant, and J. L. Michiels, eds., *Solid State Physics in Electronics and Telecommunications (Proc. Int. Conf., Brussels, 1958) Vol.1 Semiconductors part 1* (Academic Press, New York, 1960).

[5] G. Davis and M. F. Hamer, Proc. R. Soc. Lond. A **348**, 285 (1976).

[6] J. H. N. Lobser and J. A. van Wyk, Rep. Prog. Phys. **41**, 1201 (1978).

[7] N. Reddy, N. Manson, and E. Krausz, J. Lumin. **38**, 46 (1987).

[8] A. Gruber, A. Drabenstedt, C. Tietz, L. Fleury, J. Wrachtrup, and C. v. Borczyskowski, Science **276**, 2012 (1997).

[9] F. Jelezko, I. Popa, A. Gruber, C. Tietz, J. Wrachtrup, A. Nizovtsev, and S. Kilin, Appl. Phys. Lett. **81**, 2160 (2002).

[10] F. J. Heremans, *Engineering and manipulating single spins in diamond*, Ph.D. dissertation, University of California, Santa Barbara (2013).

[11] D. A. Redman, S. Brown, R. H. Sands, and S. C. Rand, Phys. Rev. Lett. **67**, 3420 (1991).

[12] R. T. Harley, M. J. Henderson, and R. M. Macfarlane, J. Phys. C: Solid State Physics **17**, L233 (1984).

[13] A. T. Collins, M. F. Thomaz, and M. I. B. Jorge, J. Phys. C: Solid State Physics **16**, 2177 (1983).

[14] N. B. Manson, J. P. Harrison, and M. J. Sellars, Phys. Rev. B **74**, 104303 (2006).

[15] J. Harrison, M. Sellars, and N. Manson, J. Lumin. **107**, 245 (2004).

[16] D. Redman, S. Brown, and S. C. Rand, J. Opt. Soc. Am. B **9**, 768 (1992).

[17] E. van Oort, N. B. Manson, and M. Glasbeek, J. Phys. C: Solid State Physics **21**, 4385 (1988).

[18] E. van Oort and M. Glasbeek, Phys. Rev. B **40**, 6509 (1989).

[19] E. van Oort, P. Stroomer, and M. Glasbeek, Phys. Rev. B **42**, 8605 (1990).

[20] F. Jelezko, T. Gaebel, I. Popa, A. Gruber, and J. Wrachtrup, Phys. Rev. Lett. **92**, 076401 (2004).

[21] R. Hanson, V. V. Dobrovitski, A. E. Feiguin, O. Gywat, and D. D. Awschalom, Science **320**, 352 (2008).

[22] S. Takahashi, R. Hanson, J. van Tol, M. S. Sherwin, and D. D. Awschalom, Phys. Rev. Lett. **101**, 047601 (2008).

[23] J. A. van Wyk, E. C. Reynhardt, G. L. High, and I. Kiflawi, J. Phys. D **30**, 1790 (1997).

[24] T. A. Kennedy, J. S. Colton, J. E. Butler, R. C. Linares, and P. J. Doering, Appl. Phys. Lett. **83**, 4190 (2003).

[25] P. L. Stanwix, L. M. Pham, J. R. Maze, D. Le Sage, T. K. Yeung, P. Cappellaro, P. R. Hemmer, A. Yacoby, M. D. Lukin, and R. L. Walsworth, Phys. Rev. B **82**, 201201(R) (2010).

[26] G. Balasubramanian, P. Neumann, D. Twitchen, M. Markham, R. Kolesov, N. Mizuochi, J. Isoya, J. Achard, J. Beck, J. Tissler,

V. Jacques, P. R. Hemmer, F. Jelezko, and J. Wrachtrup, Nat Mater **8**, 383 (2009).

[27] J. R. Maze, J. M. Taylor, and M. D. Lukin, Phys. Rev. B **78**, 094303 (2008).

[28] N. Mizuochi, P. Neumann, F. Rempp, J. Beck, V. Jacques, P. Siyushev, K. Nakamura, D. J. Twitchen, H. Watanabe, S. Yamasaki, F. Jelezko, and J. Wrachtrup, Phys. Rev. B **80**, 041201(R) (2009).

[29] G. de Lange, Z. H. Wang, D. Riste, V. V. Dobrovitski, and R. Hanson, Science **330**, 60 (2010).

[30] B. Naydenov, F. Dolde, L. T. Hall, C. Shin, H. Fedder, L. C. L. Hollenberg, F. Jelezko, and J. Wrachtrup, Phys. Rev. B **83**, 081201R (2011).

[31] C. A. Ryan, J. S. Hodges, and D. G. Cory, Phys. Rev. Lett. **105**, 200402 (2010).

[32] J. R. Rabeau, P. Reichart, G. Tamanyan, D. N. Jamieson, S. Prawer, F. Jelezko, T. Gaebel, I. Popa, M. Domhan, and J. Wrachtrup, Appl. Phys. Lett. **88**, 023113 (2006).

[33] D. M. Toyli, C. D. Weis, G. D. Fuchs, T. Schenkel, and D. D. Awschalom, Nano Lett. **10**, 3168 (2010).

[34] B. Naydenov, F. Reinhard, A. Lammle, V. Richter, R. Kalish, U. F. S. D'Haenens-Johansson, M. Newton, F. Jelezko, and J. Wrachtrup, Appl. Phys. Lett. **97**, 242511 (2010).

[35] F. H. L. Koppens, C. Buizert, K. J. Tielrooij, I. T. Vink, K. C. Nowack, T. Meunier, L. P. Kouwenhoven, and L. M. K. Vandersypen, Nature **442**, 766 (2006).

[36] G. Feher and E. A. Gere, Phys. Rev. **114**, 1245 (1959).

[37] A. M. Tyryshkin, S. A. Lyon, A. V. Astashkin, and A. M. Raitsimring, Phys. Rev. B **68**, 193207 (2003).

[38] W. F. Koehl, B. B. Buckley, F. J. Heremans, G. Calusine, and D. D. Awschalom, Nature **479**, 84 (2011).

[39] J. R. Maze, P. L. Stanwix, J. S. Hodges, S. Hong, J. M. Taylor, P. Cappellaro, L. Jiang, M. V. G. Dutt, E. Togan, A. S. Zibrov, A. Yacoby, R. L. Walsworth, and M. D. Lukin, Nature **455**, 644 (2008).

[40] J. M. Taylor, P. Cappellaro, L. Childress, L. Jiang, D. Budker, P. R. Hemmer, A. Yacoby, R. Walsworth, and M. D. Lukin, Nat Phys **4**, 810 (2008).

[41] P. Maletinsky, S. Hong, M. S. Grinolds, B. Hausmann, M. D. Lukin, R. L. Walsworth, M. Loncar, and A. Yacoby, Nat Nano **7**, 320 (2012).

[42] C. L. Degen, Appl. Phys. Lett. **92**, 243111 (2008).

[43] G. Balasubramanian, I. Y. Chan, R. Kolesov, M. Al-Hmoud, J. Tisler, C. Shin, C. Kim, A. Wojcik, P. R. Hemmer, A. Krueger, T. Hanke, A. Leitenstorfer, R. Bratschitsch, F. Jelezko, and J. Wrachtrup, Nature **455**, 648 (2008).

[44] M. S. Grinolds, S. Hong, P. Maletinsky, L. Luan, M. D. Lukin, R. L. Walsworth, and A. Yacoby, Nat Phys **9**, 215 (2013).

[45] M. S. Grinolds, P. Maletinsky, S. Hong, M. D. Lukin, R. L. Walsworth, and A. Yacoby, Nat Phys **7**, 687 (2011).

[46] M. S. Grinolds, M. Warner, K. D. Greve, Y. Dovzhenko, L. Thiel, R. L. Walsworth, S. Hong, P. Maletinsky, and A. Yacoby, Nat Nano **9**, 279 (2014).

[47] F. Dolde, H. Fedder, M. W. Doherty, T. Nobauer, F. Rempp, G. Balasubramanian, T. Wolf, F. Reinhard, L. C. L. Hollenberg, F. Jelezko, and J. Wrachtrup, Nat Phys **7**, 459 (2011).

[48] G. Kucsko, P. C. Maurer, N. Y. Yao, M. Kubo, H. J. Noh, P. K. Lo, H. Park, and M. D. Lukin, Nature **500**, 54 (2013).

[49] D. M. Toyli, D. J. Christle, A. Alkauskas, B. B. Buckley, C. G. Van de Walle, and D. D. Awschalom, Phys. Rev. X **2**, 031001 (2012).

[50] V. M. Acosta, E. Bauch, M. P. Ledbetter, A. Waxman, L.-S. Bouchard, and D. Budker, Phys. Rev. Lett. **104**, 070801 (2010).

[51] D. M. Toyli, C. F. de las Casas, D. J. Christle, V. V. Dobrovitski, and D. D. Awschalom, Proc. Nat. Acad. Sci. **110**, 8417 (2013).

[52] L. P. McGuinness, Y. Yan, A. Stacey, D. Simpson, L. T. Hall, D. Maclaurin, S. Prawer, P. Mulvaney, J. Wrachtrup, F. Caruso, R. D. Scholten, and L. C. L. Hollenberg, Nat Nano **6**, 358 (2011).

[53] T. Gaebel, M. Domhan, I. Popa, C. Wittmann, P. Neumann, F. Jelezko, J. R. Rabeau, N. Stavrias, A. D. Greentree, S. Prawer, J. Meijer, J. Twamley, P. R. Hemmer, and J. Wrachtrup, Nat Phys **2**, 408 (2006).

[54] P. Neumann, R. Kolesov, B. Naydenov, J. Beck, F. Rempp, M. Steiner, V. Jacques, G. Balasubramanian, M. L. Markham, D. J. Twitchen, S. Pezzagna, J. Meijer, J. Twamley, F. Jelezko, and J. Wrachtrup, Nat Phys **6**, 249 (2010).

[55] F. Dolde, I. Jakobi, B. Naydenov, N. Zhao, S. Pezzagna, C. Trautmann, J. Meijer, P. Neumann, F. Jelezko, and J. Wrachtrup, Nat Phys **9**, 139 (2013).

[56] G. D. Fuchs, G. Burkard, P. V. Klimov, and D. D. Awschalom, Nat Phys **7**, 789 (2011).

[57] L. Childress, M. V. Gurudev Dutt, J. M. Taylor, A. S. Zibrov, F. Jelezko, J. Wrachtrup, P. R. Hemmer, and M. D. Lukin, Science **314**, 281 (2006).

[58] M. V. G. Dutt, L. Childress, L. Jiang, E. Togan, J. Maze, F. Jelezko, A. S. Zibrov, P. R. Hemmer, and M. D. Lukin, Science **316**, 1312 (2007).

[59] P. Neumann, N. Mizuochi, F. Rempp, P. Hemmer, H. Watanabe, S. Yamasaki, V. Jacques, T. Gaebel, F. Jelezko, and J. Wrachtrup, Science **320**, 1326 (2008).

[60] P. C. Maurer, G. Kucsko, C. Latta, L. Jiang, N. Y. Yao, S. D. Bennett, F. Pastawski, D. Hunger, N. Chisholm, M. Markham, D. J. Twitchen, J. I. Cirac, and M. D. Lukin, Science **336**, 1283 (2012).

[61] P. Neumann, J. Beck, M. Steiner, F. Rempp, H. Fedder, P. R. Hemmer, J. Wrachtrup, and F. Jelezko, Science **329**, 542 (2010).

[62] L. Robledo, L. Childress, H. Bernien, B. Hensen, P. F. A. Alkemade, and R. Hanson, Nature **477**, 574 (2011).

[63] E. Togan, Y. Chu, A. S. Trifonov, L. Jiang, J. Maze, L. Childress, M. V. G. Dutt, A. S. Sorensen, P. R. Hemmer, A. S. Zibrov, and M. D. Lukin, Nature **466**, 730 (2010).

[64] B. B. Buckley, G. D. Fuchs, L. C. Bassett, and D. D. Awschalom, Science **330**, 1212 (2010).

[65] H. Bernien, B. Hensen, W. Pfaff, G. Koolstra, M. S. Blok, L. Robledo, T. H. Taminiau, M. Markham, D. J. Twitchen, L. Childress, and R. Hanson, Nature **497**, 86 (2013).

[66] S. D. Bennett, N. Y. Yao, J. Otterbach, P. Zoller, P. Rabl, and M. D. Lukin, Phys. Rev. Lett. **110**, 156402 (2013).

[67] S. Kolkowitz, A. C. Bleszynski Jayich, Q. P. Unterreithmeier, S. D. Bennett, P. Rabl, J. G. E. Harris, and M. D. Lukin, Science **335**, 1603 (2012).

[68] P. Rabl, P. Cappellaro, M. V. G. Dutt, L. Jiang, J. R. Maze, and M. D. Lukin, Phys. Rev. B **79**, 041302(R) (2009).

[69] P. Ovartchaiyapong, K. W. Lee, B. A. Myers, and A. C. B. Jayich, Nat Commun **5**, 4429 (2014).

[70] P. Rabl, S. J. Kolkowitz, F. H. L. Koppens, J. G. E. Harris, P. Zoller, and M. D. Lukin, Nat Phys **6**, 602 (2010).

[71] I. Akasaki, H. Amano, and S. Nakamura, *2014 Nobel Prize in Physics*.

[72] S. Koizumi, C. E. Nebel, M. Nesladek, eds., *Physics and Applications of CVD Diamond* (Wiley-VCH, Weinheim, 2008).

[73] J. Isberg, J. Hammersberg, E. Johansson, T. WikstrÃűm, D. J. Twitchen, A. J. Whitehead, S. E. Coe, and G. A. Scarsbrook, Science **297**, 1670 (2002).

[74] Course handouts, MATRL 205: *Introduciton to Wide Bandgap Semiconductors and Applications*, Winter 2010, University of California, Santa Barbara.

[75] F. P. Bundy, J. Geophys. Res. **85**, 6930 (1980).

[76] http : //www.ch.ic.ac.uk/rzepa/mim/century/html/diamond_text.htm.

[77] General catalog, *Synthetic Single Crystal Diamond SUMICAL*, Sumitomo Electric Industries.

[78] S. Yamanaka, H. W. Masai, D. Takeuchi, H. Okushi, and K. Kajimura, Jpn. J. of Appl. Phys. **37**, L1129 (1998).

[79] S. Koizumi, M. Kamo, Y. Sato, H. Ozaki, and T. Inuzuka, Appl. Phys. Lett. **71**, 1065 (1997).

[80] S. Koizumi, K. Watanabe, M. Hasegawa, and H. Kanda, Science **292**, 1899 (2001).

[81] N. Mizuochi, T. Makino, H. Kato, D. Takeuchi, M. Ogura, H. Okushi, M. Nothaft, P. Neumann, A. Gali, F. Jelezko, J. Wrachtrup, and S. Yamasaki, Nat Photon **6**, 299 (2012).

[82] H. Watanabe, C. E. Nebel, and S. Shikata, Science **324**, 1425 (2009).

[83] H. Watanabe, *On synthesis and optical properties of high-quality semiconductor diamond film*, Ph.D. dissertation, University of Tsukuba (2000).

[84] H. Okushi, H. Watanabe, S. Ri, S. Yamanaka, and D. Takeuchi, J. Cryst. Growth **237**, 1269 (2002).

[85] J. Y. Tsao, *Materials Fundamentals of Molecular Beam Epitaxy* (Academic Press, San Diego, 1993).

[86] H. Watanabe, D. Takeuchi, S. Yamanaka, H. Okushi, K. Kajimura, and T. Sekiguchi, Diamond Relat. Mater. **8**, 1272 (1999).

[87] K. Hayashi, S. Yamanaka, H. Watanabe, T. Sekiguchi, H. Okushi, and K. Kajimura, J. Appl. Phys. **81**, 744 (1997).

[88] R. E. Stallcup and J. M. Perez, Phys. Rev. Lett. **86**, 3368 (2001).

[89] S. Ri, H. Watanabe, M. Ogura, D. Tajeuchi, S. Yamasaki, and H. Okushi, J. Cryst. Growth **293**, 311 (2006).

[90] S.-G. Ri, H. Yoshida, S. Yamanaka, H. Watanabe, D. Takeuchi, and H. Okushi, J. Cryst. Growth **235**, 300 (2002).

[91] K. Hayashi, S. Yamanaka, H. Watanabe, T. Sekiguchi, H. Okushi, and K. Kajimura, Appl. Surf. Sci. **125**, 120 (1998).

[92] R. Rawles, S. Komarov, R. Gat, W. Morris, J. Hudson, and M. D'Evelyn, Diamond Relat. Mater. **6**, 791 (1997).

[93] M. I. Landstrass and K. V. Ravi, Appl. Phys. Lett. **55**, 975 (1989).

[94] F. Maier, M. Riedel, B. Mantel, J. Ristein, and L. Ley, Phys. Rev. Lett. **85**, 3472 (2000).

[95] K.-M. C. Fu, C. Santori, P. E. Barclay, and R. G. Beausoleil, Appl. Phys. Lett. **96**, 121907 (2010).

[96] M. V. Hauf, B. Grotz, B. Naydenov, M. Dankerl, S. Pezzagna, J. Meijer, F. Jelezko, J. Wrachtrup, M. Stutzmann, F. Reinhard, and J. A. Garrido, Phys. Rev. B **83**, 081304R (2011).

[97] L. J. Clarke, *Surface Crystallography: An Introduction to Low Energy Electron Diffraction* (John Wiley & Sons, Chichester, 1985).

[98] J. Zheng, X. Xie, A. Wee, and K. P. Loh, Diamond Relat. Mater. **10**, 500 (2001).

[99] R. E. Thomas, R. A. Rudder, and R. J. Markunas, J. Vac. Sci. Technol. A **10**, 2451 (1992).

[100] F. G. Celii and J. E. Butler, Ann. Rev. of Phys. Chem. **42**, 643 (1991).

[101] B. D. Thoms and J. E. Butler, Surf. Sci. **328**, 291 (1995).

[102] H. J. Mamin, M. Kim, M. H. Sherwood, C. T. Rettner, K. Ohno, D. D. Awschalom, and D. Rugar, Science **339**, 557 (2013).

[103] L. C. Bassett, F. J. Heremans, C. G. Yale, B. B. Buckley, and D. D. Awschalom, Phys. Rev. Lett. **107**, 266403 (2011).

[104] J. Michl, T. Teraji, S. Zaiser, I. Jakobi, G. Waldherr, F. Dolde, P. Neumann, M. W. Doherty, N. B. Manson, J. Isoya, and J. Wrachtrup, Appl. Phys. Lett. **104**, 102407 (2014).

[105] T. Fukui, Y. Doi, T. Miyazaki, Y. Miyamoto, H. Kato, T. Matsumoto, T. Makino, S. Yamasaki, R. Morimoto, N. Tokuda, M. Hatano, Y. Sakagawa, H. Morishita, T. Tashima, S. Miwa, Y. Suzuki, and N. Mizuochi, Appl. Phys. Exp. **7**, 055201 (2014).

[106] N. Tokuda, H. Umezawa, K. Yamabe, H. Okushi, and S. Yamasaki, Diamond Relat. Mater. **19**, 288 (2010).

[107] T. Teraji and T. Ito, J. Cryst. Growth **271**, 409 (2004).

[108] J. Achard, A. Tallaire, R. Sussmann, F. Silva, and A. Gicquel, J. Cryst. Growth **284**, 396 (2005).

[109] A. Tallaire, J. Achard, F. Silva, R. Sussmann, and A. Gicquel, Diamond Relat. Mater. **14**, 249 (2005).

[110] A. Tallaire, A. Collins, D. Charles, J. Achard, R. Sussmann, A. Gicquel, M. Newton, A. Edmonds, and R. Cruddace, Diamond Relat. Mater. **15**, 1700 (2006).

[111] A. Tallaire, J. Achard, F. Silva, R. S. Sussmann, A. Gicquel, and E. Rzepka, Phys. Stat. Sol. A **201**, 2419 (2004).

[112] C. J. Chu, R. H. Hauge, J. L. Margrave, and M. P. D'Evelyn, Appl. Phys. Lett. **61**, 1393 (1992).

[113] J. Cai, A. Retzker, F. Jelezko, and M. B. Plenio, Nat Phys **9**, 168 (2013).

[114] N. Zhao, J. L. Hu, S. W. Ho, J. T. K. Wan, and R. B. Liu, Nat Nano **6**, 242 (2011).

[115] R. Hanson, F. M. Mendoza, R. J. Epstein, and D. D. Awschalom, Phys. Rev. Lett. **97**, 087601 (2006).

[116] E. Cherepov, E. Tishkovsky, V. Obodnikov, J. Pal'yanov, A. Sokol, and N. Sobolev, Nucl. Instrum. Methods Phys. Res. B **183**, 301 (2001).

[117] B. K. Ofori-Okai, S. Pezzagna, K. Chang, M. Loretz, R. Schirhagl, Y. Tao, B. A. Moores, K. Groot-Berning, J. Meijer, and C. L. Degen, Phys. Rev. B **86**, 081406R (2012).

[118] J. F. Ziegler, Nucl. Instrum. Methods Phys. Res. B **219-220**, 1027 (2004).

[119] T. Ishikawa, K.-M. C. Fu, C. Santori, V. M. Acosta, R. G. Beausoleil, H. Watanabe, S. Shikata, and K. M. Itoh, Nano Lett. **12**, 2083 (2012).

[120] K. Ohno, F. Joseph Heremans, L. C. Bassett, B. A. Myers, D. M. Toyli, A. C. Bleszynski Jayich, C. J. Palmstrom, and D. D. Awschalom, Appl. Phys. Lett. **101**, 082413 (2012).

[121] J. Achard, F. Silva, O. Brinza, A. Tallaire, and A. Gicquel, Diamond Relat. Mater. **16**, 685 (2007).

[122] A. Chayahara, Y. Mokuno, Y. Horino, Y. Takasu, H. Kato, H. Yoshikawa, and N. Fujimori, Diamond Relat. Mater. **13**, 1954 (2004).

[123] D. M. Toyli, *Quantum control and engineering of single spins in diamond*, Ph.D. dissertation, University of California, Santa Barbara (2013).

[124] B. B. Buckley, *Coherent light-matter interactions of defect spins in solids*, Ph.D. dissertation, University of California, Santa Barbara (2013).

[125] R. J. Epstein, F. M. Mendoza, Y. K. Kato, and D. D. Awschalom, Nat Phys **1**, 94 (2005).

[126] B. Smeltzer, L. Childress, and A. Gali, New J. Phys. **13**, 025021 (2011).

[127] B. Smeltzer, J. McIntyre, and L. Childress, Phys. Rev. A **80**, 050302R (2009).

[128] M. Steiner, P. Neumann, J. Beck, F. Jelezko, and J. Wrachtrup, Phys. Rev. B **81**, 035205 (2010).

[129] L. G. Rowan, E. L. Hahn, and W. B. Mims, Phys. Rev. **137**, A61 (1965).

[130] P. C. Maurer, J. R. Maze, P. L. Stanwix, L. Jiang, A. V. Gorshkov, A. A. Zibrov, B. Harke, J. S. Hodges, A. S. Zibrov, A. Yacoby, D. Twitchen, S. W. Hell, R. L. Walsworth, and M. D. Lukin, Nat Phys **6**, 912 (2010).

[131] E. V. Oort and M. Glasbeek, Chem. Phys. **143**, 131 (1990).

[132] B. A. Myers, A. Das, M. C. Dartiailh, K. Ohno, D. D. Awschalom, and A. C. Bleszynski Jayich, Phys. Rev. Lett. **113**, 027602 (2014).

[133] B. Grotz, J. Beck, P. Neumann, B. Naydenov, R. Reuter, F. Reinhard, F. Jelezko, J. Wrachtrup, D. Schweinfurth, B. Sarkar, and P. Hemmer, New J. Phys. **13**, 055004 (2011).

[134] P. Mansfield, Angew. Chem. Int. Ed. **43**, 5456 (2004).

[135] J. B. Aguayo, S. J. Blackband, J. Schoeniger, M. A. Mattingly, and M. Hintermann, Nature **322**, 190 (1986).

[136] A. G. Webb, Proc. Nuc, Mag. Res. Spec. **31**, 1 (1997).

[137] L. Ciobanu, D. A. Seeber, and C. H. Pennington, J. Magn. Res. 158, 178 **158**, 178 (2002).

[138] K. R. Turber and R. Tycko, Chem. Phys. Phys. Chem. **12**, 5779 (2010).

[139] P. Glover and P. Mansfield, Rep. Prog. Phys. **65**, 1489 (2002).

[140] C. Branden and J. Tooze, *Introduction to Protein Structure* (Garland Publishing, Inc. New York, edn. 2, 1998).

[141] C. L. Degen, M. Poggio, H. J. Mamin, C. T. Rettner, and D. Rugar, Proc. Nat. Acad. Sci. U. S. A. **106**, 1313 (2009).

[142] C. Granata, E. Esposito, A. Vettoliere, L. Petti, and M. Russo, Nanotechnology **19**, 275501 (2008).

[143] G. Boero, P.-A. Besse, and R. Popovic, Appl. Phys. Lett. **79**, 1498 (2001).

[144] J. A. Sidles, J. L. Garbini, K. J. Bruland, D. Rugar, O. Züger, S. Hoen, and C. S. Yannoni, Rev. Mod. Phys. **67**, 249 (1995).

[145] D. Rugar, R. Budakian, H. J. Mamin, and B. W. Chui, Nature **430**, 329 (2004).

[146] H. J. Mamin, T. H. Oosterkamp, M. Poggio, C. L. Degen, C. T. Rettner, and D. Rugar, Nano Lett. **9**, 3020 (2009).

[147] S. Kolkowitz, Q. P. Unterreithmeier, S. D. Bennett, and M. D. Lukin, Phys. Rev. Lett. **109**, 137601 (2012).

[148] T. H. Taminiau, J. J. T. Wagenaar, T. van der Sar, F. Jelezko, V. V. Dobrovitski, and R. Hanson, Phys. Rev. Lett. **109**, 137602 (2012).

[149] N. Zhao, J. Honert, B. Schmid, M. Klas, J. Isoya, M. Markham, D. Twitchen, F. Jelezko, R.-B. Liu, H. Fedder, and J. Wrachtrup, Nat Nano **7**, 657 (2012).

[150] H. J. Mamin, M. H. Sherwood, and D. Rugar, Phys. Rev. B **86**, 195422 (2012).

[151] L. Gross, F. Mohn, N. Moll, P. Liljeroth, and G. Meyer, Science **325**, 1110 (2009).

[152] A. Faraon, C. Santori, Z. Huang, V. M. Acosta, and R. G. Beausoleil, Phys. Rev. Lett. **109**, 033604 (2012).

[153] B. J. M. Hausmann, B. J. Shields, Q. Quan, Y. Chu, N. P. de Leon, R. Evans, M. J. Burek, A. S. Zibrov, M. Markham, D. J. Twitchen, H. Park, M. D. Lukin, and M. Loncar, Nano Letters **13**, 5791 (2013).

[154] J. T. Choy, B. J. M. Hausmann, T. M. Babinec, I. Bulu, M. Khan, P. Maletinsky, A. Yacoby, and M. Loncar, Nat Photon **5**, 738 (2011).

[155] B. Naydenov, V. Richter, J. Beck, M. Steiner, P. Neumann, G. Balasubramanian, J. Achard, F. Jelezko, J. Wrachtrup, and R. Kalish, Appl. Phys. Lett. **96**, 163108 (2010).

[156] K. Ohno, F. J. Heremans, C. F. de las Casas, B. A. Myers, B. J. Aleman, A. C. Bleszynski Jayich, and D. D. Awschalom, Appl. Phys. Lett. **105**, 052406 (2014).

[157] T. Yamamoto, T. Umeda, K. Watanabe, S. Onoda, M. L. Markham, D. J. Twitchen, B. Naydenov, L. P. McGuinness, T. Teraji, S. Koizumi, F. Dolde, H. Fedder, J. Honert, J. Wrachtrup, T. Ohshima, F. Jelezko, and J. Isoya, Phys. Rev. B **88**, 075206 (2013).

[158] S. A. Campbell, *The Science and Engineering of Microelectronic Fabrication* (Oxford University Press, New York, 2001).

[159] T. Yamamoto, C. Müller, L. P. McGuinness, T. Teraji, B. Naydenov, S. Onoda, T. Ohshima, J. Wrachtrup, F. Jelezko, and J. Isoya, Phys. Rev. B **88**, 201201 (2013).

[160] C. Santori, P. E. Barclay, K.-M. C. Fu, and R. G. Beausoleil, Phys. Rev. B **79**, 125313 (2009).

[161] D. Rugar, H. J. Mamin, M. H. Sherwood, M. Kim, C. T. Rettner, K. Ohno, and D. D. Awschalom. arxiV:1406.2983 (2014).

[162] M. Kim, H. J. Mamin, M. H. Sherwood, C. T. Rettner, J. Frommer, and D. Rugar, Appl. Phys. Lett. **105**, 042406 (2014).

[163] T. Staudacher, F. Shi, S. Pezzagna, J. Meijer, J. Du, C. A. Meriles, F. Reinhard, and J. Wrachtrup, Science **339**, 561 (2013).

[164] N. Bar-Gill, L. Pham, C. Belthangady, D. Le Sage, P. Cappellaro, J. Maze, M. Lukin, A. Yacoby, and R. Walsworth, Nat Commun **3**, 858 (2012).

[165] H. J. Mamin, M. H. Sherwood, M. Kim, C. T. Rettner, K. Ohno, D. D. Awschalom, and D. Rugar, Phys. Rev. Lett. **113**, 030803 (2014).

[166] J. C. Lee, D. O. Bracher, S. Cui, K. Ohno, C. McLellan, X. Zhang, P. Andrich, B. J. Aleman, K. J. Russell, A. P. Magyer, I. Aharonovich, A. C. Bleszynski Jayich, D. D. Awschalom, and E. L. Hu. in preparation.

[167] A. P. Magyar, J. C. Lee, A. M. Limarga, I. Aharonovich, F. Rol, D. R. Clarke, M. Huang, and E. L. Hu, Appl. Phys. Lett. **99**, 081913 (2011).

[168] V. R. Horowitz, B. J. Aleman, D. J. Christle, A. N. Cleland, and D. D. Awschalom, Proc. Nat. Acad. Sci. U. S. A. **109**, 13493 (2012).

[169] P. Andrich, B. J. Aleman, J. C. Lee, K. Ohno, C. F. de las Casas, F. J. Heremans, E. L. Hu, and D. D. Awschalom, Nano Lett. **14**, 4959 (2014).